Advanced Electrochemical Analysis for Complex Electrode Applications

Feng Zheng

Department of Chemical Engineering and Biotechnology

University of Cambridge

This dissertation is submitted for the degree of

Doctor of Philosophy

Queens' College Jul 2018

Abstract

Advanced Electrochemical Analysis for Complex Electrode Applications

Feng Zheng

This thesis has investigated several complex situations that may be encountered in electrochemical studies. Three main situations have been examined, they include the formation of polymer films on electrode surfaces during measurements, a novel nanocatalyst modified electrode surfaces, and organised carbon nanotube (CNT) structures on electrode surfaces. These have been utilised for different electrochemical applications owing to their dissimilar properties. Voltammetric techniques of cyclic voltammetry (CV), square wave voltammetry (SWV) and Fourier transformed large amplitude ac voltammetry (FTACV) have been utilised to examine these reactions.

Chapter 3 reports the investigation of catechol oxidation and subsequent polymerisation through crosslinking with D-glucosamine or chitosan. Hydrogel can be formed on the electrode surface during the process, which changes the viscosity of the solution and thus affects the diffusion of chemical species. This process has been examined by several voltammetric techniques. A further examination of the chemical system has also been conducted using FTACV for the first time.

Chapter 4 describes the preparation of carbon microsphere supported molybdenum disulfide. The material has been utilised as electrocatalysts for hydrogen evolution reaction (HER) in acidic media, and the performance tested by traditional linear sweep voltammetry (LSV) and advanced FTACV techniques. The FTACV technique has been used for the first time for HER processes. In addition, the synthesised particles have also been used for thermal catalytic decomposition of hydrogen sulfide, which shows a significant improvement in the conversion rate over conventional examples.

Chapter 5 demonstrates the direct growth of vertically aligned CNT forests on a gold electrode. The electrochemical response of the fabricated electrode has also been examined with ferrocyanide as the redox species. Furthermore, the immobilisation of anthraquinone onto CNT forest has been attempted. The fabricated electrode was utilised as a pH sensor via CV and SWV, and both indicates a well correlated pH-potential relationship in the pH range of 2 to 12. The sensor has also been assessed by the FTACV technique.

I would like to dedicate this thesis to my loving parents.

Declaration

I hereby declare that except where specific reference is made to the work of others, the contents of this dissertation are original and have not been submitted in whole or in part for consideration for any other degree or qualification in this, or any other University. This dissertation is the result of my own work and includes nothing which is the outcome of work done in collaboration, except where specifically indicated in the text. This dissertation contains less than 65,000 words including appendices, bibliography, footnotes, tables and equations and has less than 150 figures.

Feng Zheng

Jul 2018

Acknowledgements

Many people have given me help and support throughout my PhD study. It would have been impossible for me to complete my PhD project without them.

Firstly, I would like to express my sincere gratitude to my supervisor, Dr Adrian Fisher, for his continual support of my research, for his intriguing and creative ideas, immense knowledge, and his patience. I am grateful for the intern opportunity at Schlumberger Gould Research Centre (SGR), and a research project at the Cambridge Centre for Advanced Research and Education in Singapore (CARES), and a collaboration project with the Institute of Manufacturing. I am also grateful to my colleagues, especially Dr Kamran Yunus, Dr Peng Song, Dr Chencheng Dai, Dr Hongkai Ma, Dr Minyu Zeng, Dr Viet Nguyen, Dr Arely Gonzalez, Xiangming Gao, Aazraa Pankan, Yian Wang, and Luwen Meng.

I would also like to acknowledge Dr Nathan Lawrence for his supervision and support during my time at SGR and afterwards. I would like to thank my colleagues at SGR, Dr Emma Corcoran, Dr Linhongjia Xiong, Dr Shen Chao, Dr Shiwei Fan and William Barrow.

I also acknowledge Prof Hua Chun Zeng for his support and guidance during my time at the Department of Chemical and Biomolecular Engineering, National University of Singapore, under the collaboration project with CARES. I sincerely thank Kelvin Kwok for conducting the catalytic decomposition test at the Institute of Chemical and Engineering Sciences. I would also like to thank Dr Kamal Elouarzaki, Dr Yao Zhou, Dr Ping Li, Jingjing Wang and Runze Qin for their help and companions.

I would also like to acknowledge my collaborators at the Institute of Manufacturing, Dr Michael De Volder for his kind support and creative ideas, and Chris Valentine for the synthesis experiments and fruitful discussions.

I also want to thank all the supporting staff at these institutions. I appreciate the companion of my relatives and friends during my PhD, especially Yimin Chen, Yonglie Chen, Yao Du, Yushu Geng, Chao Li, Zhipeng Li, Haochen Sun, Andi Tao, Qian Xu, Ziyan Zhao, Danni Zheng, Yaoyao Zheng.

Finally, I wish to express my sincerest gratitude and love to my father Zhongliang Zheng and mother Julian Zheng for supporting me through my life.

Publications

1. **F. Zheng**, N. S. Lawrence, R. S. Hartshorne, and A. C. Fisher, "Voltammetric and Electrosynthetic Triggered Gel Formation," Electrochimica Acta, 2018.
2. J. Chen, **F. Zheng**, S. Zhang, A. C. Fisher, Y. Zhou, Z. Wang, Y. Li, B. Xu, J. Li and S. Sun, "Interfacial Interaction between FeOOH and Ni-Fe LDH to Modulate the Local Electronic Structure for Enhanced OER Electrocatalysis," ACS Catalysis, 2018.
3. **F. Zheng**, N. S. Lawrence, R. S. Hartshorne, and A. C. Fisher, "Electrochemically Initiated Crosslinking of Chitosan," ChemElectroChem, pp. 1–7, 2018.
4. **F. Zheng**, C. J. Valentine, P. Song, N. S. Lawrence, M. De Volder, A. C. Fisher, "Vertically Aligned and Anthraquinone Functionalised CNT Forests Synthesised on Gold Electrode for Electrochemical pH Sensing," (Manuscript prepared, under review by co-authors, planning submits to Angewandte Chemie)
5. **F. Zheng**, J. J. Varghese, K. M. Kwok, H. C. Zeng, A. C. Fisher, "Carbon Microspheres Supported Molybdenum Disulfide for Hydrogen Sulfide Decomposition," (Manuscript written, awaiting DFT modelling results from collaborator)
6. **F. Zheng**, K. M. Kwok, H. C. Zeng, A. C. Fisher, "Fourier Transform Large Amplitude Alternating Current Voltammetry Investigations of the Electron Transfer Processes in Hydrogen Evolution Reaction," (In Preparation)

Contents

List of Figures

List of Tables

Nomenclature

Symbols

Symbol	Definition	Unit
A	Electrode area	cm^2
C	Concentration of a substance	mol cm^{-3}
C_d	Differential capacitance	F
C_{dl}	Capacitance of a double layer	F
$C_O(0, t)$	Surface concentration at time t for the oxidant	mol cm^{-3}
$C_O(\infty, t)$	Bulk concentration at time t for the oxidant	mol cm^{-3}
$C_R(0, t)$	Surface concentration at time t for the reductant	mol cm^{-3}
$C_R(\infty, t)$	Bulk concentration at time t for the reductant	mol cm^{-3}
D	Diffusion coefficient	cm^2 s^{-1}
e^-	Electron	N/A
E	Electrode potential	V
E^0	Electron energy corresponding to the standard potential of a couple	eV
$E^{0'}$	Formal potential	V
E_{ac}	Alternating potential	V
E_b	Binding energy	eV
E_{dc}	Linear potential	V
E_F	Fermi energy	eV
E_{kin}	Kinetic energy	eV
E_m	Maximum amplitude	V
f	Frequency	Hz
F	Faraday constant, 96487	C mol^{-1}
i_0	Standard exchange current	A

i_b	Backward current	A
i_f	Forward current	A
i_{net}	Overall current	A
I_p	Peak current	A
I_p^a	Oxidative peak current	A
I_p^c	Reductive peak current	A
J	Flux of the electroactive species reaching the electrode surface	mol s^{-1} cm^{-2}
J_b	Backward (oxidative) flux	mol s^{-1} cm^{-2}
J_f	Forward (forward) flux	mol s^{-1} cm^{-2}
J_m	Migration flux	mol s^{-1} cm^{-2}
j_0	Exchange current density	A cm^{-2}
k	Heterogeneous rate constant	cm s^{-1}
k^0	Standard heterogeneous charge transfer rate constant	cm s^{-1}
k_f	Forward heterogeneous rate constant	cm s^{-1}
k_b	Backward heterogeneous rate constant	cm s^{-1}
k_e	Electron transfer rate constant	cm s^{-1}
k_{EC}	Homogeneous reaction rate constant	cm s^{-1}
L_a	Mean graphitic microcrystallite size along a-axis	Å
L_c	Interplanar microcrystallite size along graphite plane	Å
n	Number of electrons	N/A
q^m	Charge density on metal side	C cm^{-3}
q^s	Charge density on solution side	C cm^{-3}
R	Universal gas constant	J K^{-1} mol^{-1}
R_u	Uncompensated resistance	Ω
T	Temperature	K

t	Time	s
t_p	Pulse width	s
u	Ionic mobility	$m^2\ V^{-1}\ s^{-1}$
$v(x)$	The velocity of a substance	$m\ s^{-1}$
x	One-dimensional Cartesian coordinate	N/A
z	Charge of a substance	C
Z	Impedance	Ω
Z_{Im}	Imaginary part of impedance, or Z'	Ω
Z_{Re}	Real part of impedance, or $-Z''$	Ω
α	The charge transfer coefficient	N/A
η	Overpotential	V
Γ_O^*	Concentration of absorbed O on electrode surface	$mol\ cm^{-3}$
Ψ_b	Backward current	A
Ψ_f	Forward current	A
Ψ_n	Net current	A
θ	Phase shift	rad
ω	Angular frequency	$rad\ s^{-1}$
λ	Wavelength	nm
$\partial C(x, t)/\partial x$	The concentration gradient at distance x	N/A
$\partial \phi(x, t)/\partial x$	The potential gradient at distance x	N/A
ΔE	Amplitude	V
ΔE_p	Peak-to-peak separation	V
ΔE_s	Step height in SWV	V
ΔE_{swv}	Amplitude in SWV	V
ΔE_{swv}	Potential amplitude in SWV	V

Abbreviations

Abbreviation	Meaning
ac	Alternating current
BE	Binding energy
BPPG	Basal-plane pyrolytic graphite
CNTs	Carbon Nanotubes
CV	Cyclic voltammetry
CVD	Chemical vapour deposition
DFT	Density functional theory
DPV	Differential pulse voltammetry
dc	Direct current
EC	Heterogeneous electron transfer with homogeneous chemical reaction
ECE	Heterogeneous electron transfer, homogeneous chemical reaction and heterogeneous electron transfer in sequence
EC’	Heterogeneous electron transfer followed by homogeneous catalytic regeneration of the electroactive species
EDX	Energy dispersive X-ray spectroscopy
EPPG	Edge-plane pyrolytic graphite
EIS	Electrochemical impedance spectroscopy
FT	Fourier transform
FTACV	Fourier transformed large amplitude ac voltammetry
GC	Gas chromatography, or glassy carbon
GCE	Glassy carbon electrode
HACNT	Horizontally aligned CNT
HER	Hydrogen evolution reaction
HOMOs	Highest occupied molecular orbital

HOPG	Highly ordered pyrolytic graphite
HRTEM	High resolution transmission electron microscopy
ICP	Inductively coupled plasma – optical emission spectrometry
IHP	Inner Helmholtz plane
iFT	Inverse Fourier transform
NPV	Normal pulse voltammetry
LUMOs	Lowest unoccupied molecular orbital
LSV	Linear sweep voltammetry
MS	Mass spectrometry
MWCNT	Multi wall carbon nanotube
OER	Oxygen evolution reaction
OHP	Outer Helmholtz plane
PCET	Proton-coupled electron transfer
RHE	reversible hydrogen electrode
RPV	Reverse pulse voltammetry
SCE	Saturated calomel electrode
SEM	Scanning electron microscopy
SWCNT	Single wall carbon nanotube
SWV	Square wave voltammetry
VACNT	Vertically aligned carbon nanotube
TEM	Transmission electron microscopy
XPS	X-ray photoelectron spectroscopy
XRD	X-ray diffraction

Chapter 1 Introduction

Abstract

This chapter introduced the background and theories of the topics employed in the thesis. The investigated topics vary from the electrochemically initiated gelation process, to catalytic hydrogen evolution reaction, and to aligned and functionalised carbon nanotubes pH sensor. They have been all been examined by voltammetry techniques and utilised for electrochemical applications. Therefore, the fundamentals of electrode reactions, behaviours of voltammetric responses, coupled electrode mechanisms and electrode materials have been reviewed and discussed.

1.1 Introduction

This thesis describes the utilisation of advanced electrochemical techniques to investigate several complex electrochemical systems. These systems range from homogeneous reactions, to nanocatalyst modified electrode surface, to organised electrode structures. In each system, there remains some challenges to either identify the mechanism or improve the performance for certain applications. The first system involves the viscosity change of the solution upon the application of an external differential potential to the system. This thickening effect appeares as a result of the crosslinking between catechol and chitosan. The mechanism of electrochemical oxidation of catechol has been studied in the presence of D-glucosamine and chitosan using several voltammetric techniques. The second system studied is hydrogen production from hydrogen evolution reaction. Hydrothermal synthesised molybdenum disulfide have been examined as the catalysts for the reaction. Both regular linear sweep voltammetry and innovative Fourier transformed large amplitude ac voltammetry have been adopted to study the catalytic performance of the materials. The last system concerns the modification of electrode surface by carbon nanotubes (CNTs). CNT forest has been

synthesised directly on gold surface by a chemical vapour deposition process. The self-fabricated electrode served as a working electrode for some well-known electrochemical reactions. The deposition of anthraquinone onto the CNT forest has also been explored, and its performance as a pH sensor has been examined. All of these complex electrochemical systems will be discussed in later chapters.

In this chapter, the fundamentals of the electrochemical theories and techniques employed are introduced and discussed. The selection of electrode materials and modification of electrode surface have also been reviewed.

1.2 Electrochemical Fundamentals

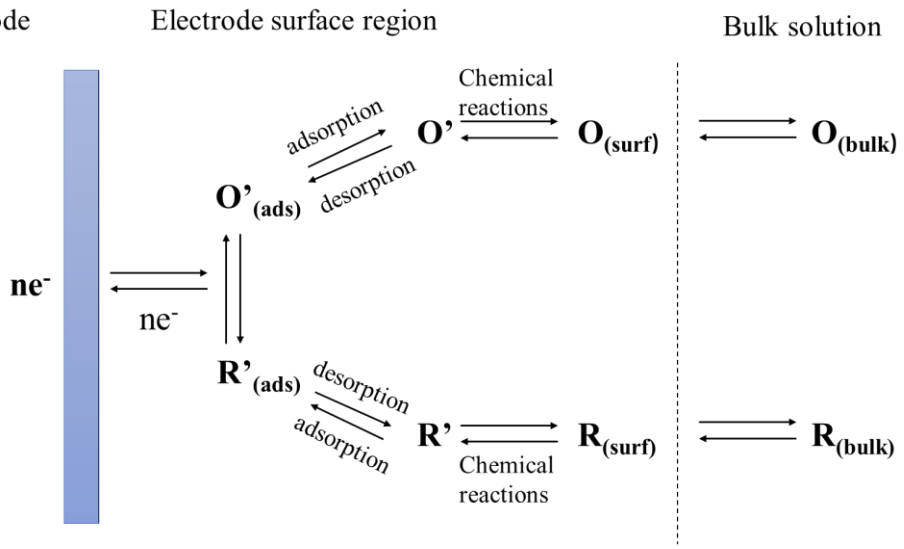

Figure 1.1 Schematic diagram of a reversible redox reaction.

Electrochemistry is defined as the branch of chemistry that studies the phenomena that give rise to the interconversion of chemical and electrical energy. [1], [2] As a result, electrochemical measurements have been employed for various purposes, including obtaining thermodynamic data, generating unstable intermediates, analysing trace amounts of chemicals and investigating electrochemical properties of the system. Thus electrochemical techniques have been utilised in a number of applications such as chemical sensing (e.g., glucose sensor, pH sensor),[3], [4] technological application (e.g., electroplating of metals, large-scale

production of aluminium)[5] and energy storage devices (e.g., batteries, fuel cells).[6] Electrochemical processes occur at the heterogeneous electrode-solution interface rather than homogeneous bulk solution for many chemical reactions. As shown in Figure 1.1, a schematic diagram of the process is described. Therefore, it is necessary to understand the fundamental aspects of electrode reactions and electrode-solution interface.

The electrode dynamics are influenced by many parameters, which can control the rate of the charge transfer process. The factors include:

- The electrode potential;
- Transport of chemical species between the bulk solution and electrode;
- The reactivity of the redox reaction reactants;
- The nature of the electrode surface;
- Chemical reactions preceding or following the electron transfer;

In the following sections, the above indicated factors would be discussed.

1.2.1 Faradaic Process

In this section, the charge transport processes across the interface between an electrode and an electrolyte during redox reactions are described.

Consider a redox process of O (oxidized form) and R (reduced form) at the electrode surface:

$$O + ne^- \rightleftharpoons R \tag{1.1}$$

where n is the number of electrons transferred. A cathode is termed as the electrode at which the reduction occurs, while an anode is defined as the electrode at which the oxidation takes place. Thus reaction (1.1) is defined as a reduction half-cell reaction at the cathode.

Energy levels

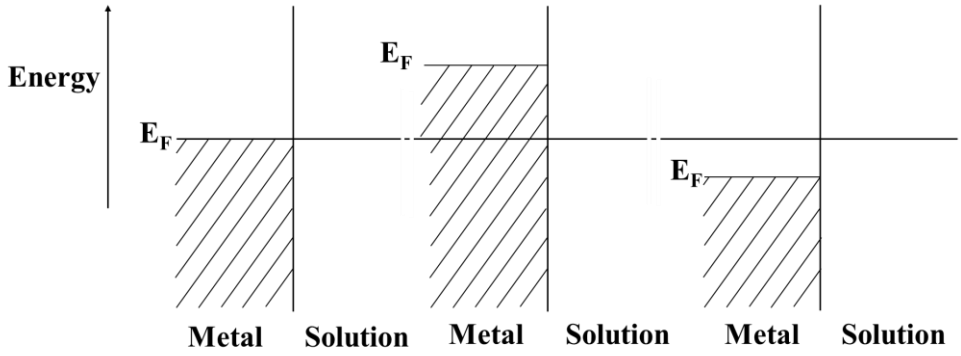

Figure 1.2 The influence of potential on the fermi level in a metal.

In this section, the concept of Fermi Level is explained and illustrated. Metals are composed of a lattice of closely packed atoms. The electrons in the metal can move freely due to the overlapping of atomic orbitals within the lattices. The electrons can occupy an effective continuum of energy states in the metal, where the maximum energy is termed as the Fermi Level. As shown in Figure 1.2, the energy of Fermi Level (E_F: Fermi energy) can be increased or decreased by applying an electrical potential to the metal.

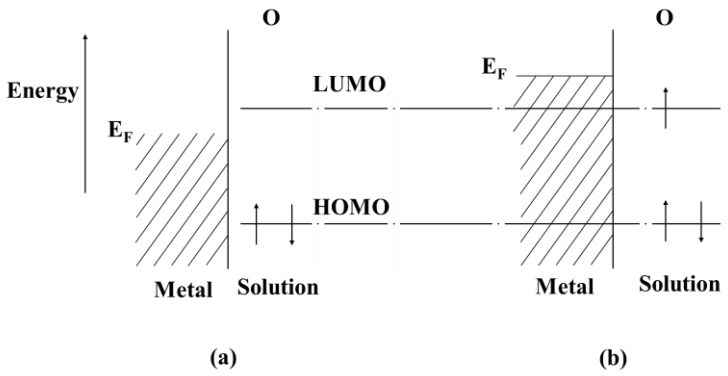

Figure 1.3 Electron transfer and energy levels. (a) Electrode potential is insufficient to drive the reduction of O; (b) The electrode process becomes thermodynamically favourable at a more reductive potential. [2]

After the introduction of a reactant molecule (O) that can undergo a charge transfer reaction. Figure 1.3 illustrates some of the energy states of O, which has a lowest unoccupied molecular orbital (LUMO) at an energy higher than that of the metal's Fermi Level. It is evident that the

process for electrons to leave the metal and occupy the LUMO is unfavourable. Nevertheless, the application of a negative potential can raise the energy in the metal to become higher than the LUMO, thus electron transfer becomes thermodynamically favourable.

For a reduction, the energy of the electrons in the electrode must be lower than the energy in the receptor orbital. While for an oxidation, the energy of the electrons in the orbital must be higher than the energy of the electrons in the electrode. Once this barrier energy is overcome and a thermodynamic equilibrium is established in the system, the relationship between electrode potential and concentrations of the electroactive species at the surface can be predicted using the Nernst equation

$$E = E^0 + \frac{RT}{nF} ln(\frac{\alpha_O}{\alpha_R}) \quad (1.2)$$

where

E^0: The standard potential of the redox couple (V);

R: The universal gas constant, 8.314 ($J \cdot K^{-1} \cdot mol^{-1}$);

T: Temperature in the absolute value (K);

F: The Faraday constant, 96487 ($C\ mol^{-1}$).

α_O, α_R: The activities of the oxidized and reduced forms of the redox couple in the bulk solution, respectively.

In the case of a negative standard potential, the oxidized form tends to get reduced, therefore the forward reduction reaction is more favourable. The current generated by this electron transfer reaction is defined as the Faradaic current, as it follows Faraday's Law. Faraday's Law stated that the reaction of 1 mol of substance involves a change of 96487 C. However, adsorption and desorption processes can also occur with changing applied potential or solution composition, which are known as the nonfaradic processes. During an electrochemical measurement, both faradic and nonfaradic processes would occur on electrode surface. It is the faradic process that is normally of primary interest in an electrode reaction, whilst the effects

of nonfaradaic processes must be considered. The summation of the faradaic current and the nonfaradaic charging background current account for the total current.[7] The rate of reaction can also be directly related to the faradaic current. In addition, a plot of current against potential can be drawn and is known as the voltammogram. Its shape and magnitude can be seen as an indication of the processes involved in the electrode reaction.

1.2.2 Essentials of Electrode Reactions

Electrode reactions can be regarded as heterogeneous electrochemical reactions between two species of a redox couple (electron transfer) at the electrode-electrolyte interface. Moreover, chemical heterogeneous processes such as dissolution or surface-bond reaction may also occur and are grouped as heterogeneous processes.

Again consider a redox process as described in equation (1.1). The magnitude of the generated current (i) from electrode reaction is given by

$$i = nFAJ \tag{1.3}$$

where A is the electrode area (cm^2) and J is the flux of the electroactive species reaching the electrode surface (mol s^{-1} cm^{-2}). The term J is envisaged as the rate of the electrochemical reaction. For a first order electrode reaction, J can be expressed as

$$J_f = k_f C_O(0,t) \tag{1.4}$$

$$J_b = k_b C_O(0,t) \tag{1.5}$$

where J_f and J_b are the forward (reductive) and backward (oxidative) fluxes, respectively, k_f and k_b are the heterogeneous rate constants, $C_O(0, t)$ and $C_R(0, t)$ are the surface concentration at time t for the reactants.

The overall current (i_{net}) is the difference between forward and backward current

$$i_{net} = i_f - i_b = nFA(J_f - J_b) = nFA[k_f C_O(0,t) - k_b C_O(0,t)] \tag{1.6}$$

The rate constants k_f and k_b can also be related to the standard rate constant (k^0, cm/s)

$$k_f = k^0 \exp[-\alpha F(E - E^0)/RT] \tag{1.7}$$

$$k_b = k^0 \exp[(1-\alpha) F(E - E^0)/RT] \tag{1.8}$$

Where α is the charge transfer coefficient, a measure of the symmetry of the energy barrier. Insertion of equation (1.7) and (1.8) into equation (1.6) yields the current-potential characteristic:

$$i = nFAk^0 \left[C_O(0,t) e^{-\frac{\alpha F(E-E^0)}{RT}} - C_R(0,t) e^{\frac{(1-\alpha)F(E-E^0)}{RT}} \right] \tag{1.9}$$

This relation and its derived forms are extremely useful for treating most problems related to heterogeneous kinetics. This equation can also be established based on standard exchange current (i_0) rather than k^0. The standard exchange current expresses the balanced faradaic activity when the net current is zero at equilibrium.

$$i_0 = FAk^0 C_O(\infty,t)^{(1-\alpha)} C_R(\infty,t)^{\alpha} \tag{1.10}$$

Where $C_O(\infty, t)$ and $C_R(\infty, t)$ are the bulk concentration at time t for the reactants. Then the current can be described in terms of the deviation from the equilibrium potential (overpotential, η), rather than the formal potential (E^0). The equation is known as the current-overpotential equation:

$$i = i_0 \left[\frac{C_O(0,t)}{C_O(\infty,t)} e^{-\frac{\alpha F \eta}{RT}} - \frac{C_R(0,t)}{C_R(\infty,t)} e^{-\frac{(1-\alpha)F\eta}{RT}} \right] \tag{1.11}$$

The equation (1.9) and some of its ramifications (e.g., equation (1.11)) are known as the Butler-Volmer equations of electrode kinetics. It predicts the variation of current as a function of the overpotential and transfer coefficient.

This Figure is not shown due to copyright issues

Figure 1.4 Effect of standard exchange current density on the overpotential to deliver the net current densities. (a) $j_0 = 10^{-3}$ A/cm^2, (b) $j_0 = 10^{-6}$ A/cm^2, (c) $j_0 = 10^{-9}$ A/cm^2.[1]

The surface and bulk concentrations of the reactants can be assumed identical if the solution is well mixed under stirring, then a simplified form of equation (1.11) can be obtained:

$$i = i_0 \left[e^{-\frac{\alpha F \eta}{RT}} - e^{-\frac{(1-\alpha) F \eta}{RT}} \right] \tag{1.12}$$

For a variation form of i shown in equation (1.12), two limiting cases can be considered (large or small values of i_0). In both situations, no current flows when $\eta = 0$. For a large i_0 (or a large exchange current density j_0), the system behave in a reversible way that no or little applied overpotential is needed to drive the reaction. As shown in Figure 1.4 (curve a and b), for the forward (reductive) reaction with large value of j_0, the cathodic component of the current becomes negligible with increasing overpotential, while the anodic current becomes dominant. In this case, the Butler-Volmer equation is simplified to

$$i = i_0 e^{-\frac{\alpha F \eta}{RT}} \tag{1.13}$$

In the second case of a small standard exchange current, a high overpotential is required to initiate the current flow, indicating an irreversible mechanism. When the overpotential reaches a value of driving the oxidative process, the corresponding reductive component becomes negligible. Then the equation becomes

$$i = i_0 e^{-\frac{(1-\alpha)F\eta}{RT}} \tag{1.14}$$

The two equations can be utilised to obtain the values of transfer coefficient α and standard exchange current i_0 through Tafel analysis.[8] Tafel analysis establishes the relationship between log(i) and η and is illustrated in Figure 1.5. The value of α and i_0 can be calculated from the slopes of the Tafel equation and the intersection point of the two extrapolated Tafel lines.

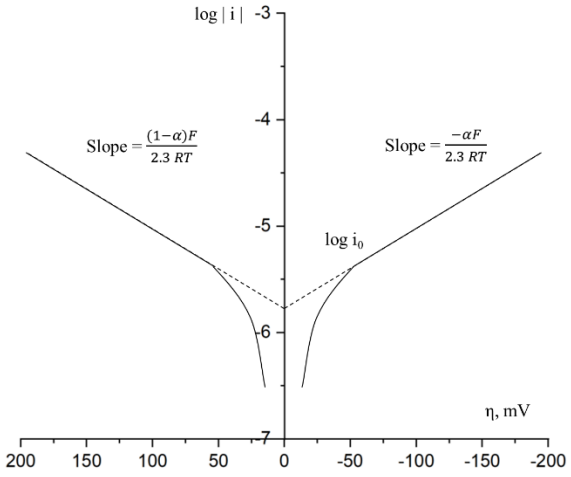

Figure 1.5 Tafel analysis for anodic and cathodic branches of the current-overpotential curve.

In this situation the voltage applied will not result in the generation of the concentrations at the electrode surface predicted by the Nernst equation. This happens because the kinetics of the reaction are 'slow' and thus the equilibria are not established rapidly (in comparison to the voltage scan rate).

The Electrical Double Layer

The electrode/electrolyte interface is then being considered as the phase boundary will interrupt the nature of the electrolyte solution. Several models have been developed to describe the nature of the processes at the solid/liquid interface.

The first and simple model was proposed by Helmholtz in 1853, which assumes no faradaic processes take place at the electrode. As is described by the model, the electrode possesses a charge density of q^m which arises from excess or deficiency of electrons at the electrode

surface. Thus an equal but opposite charge of q^s in solution must be matched to the charge on the electrode, which is necessary to maintain electrical neutrality in the interface.

$$q^m = -q^s \tag{1.15}$$

It is suggested that the charge in solution arises from the redistribution of electrolyte ions at the interface, which is driven by the electrostatic forces. Another reason can be attributed to the reorientation of dipoles in solvent molecules. As a result, a potential difference across the interface is created, generating an electric field gradient.

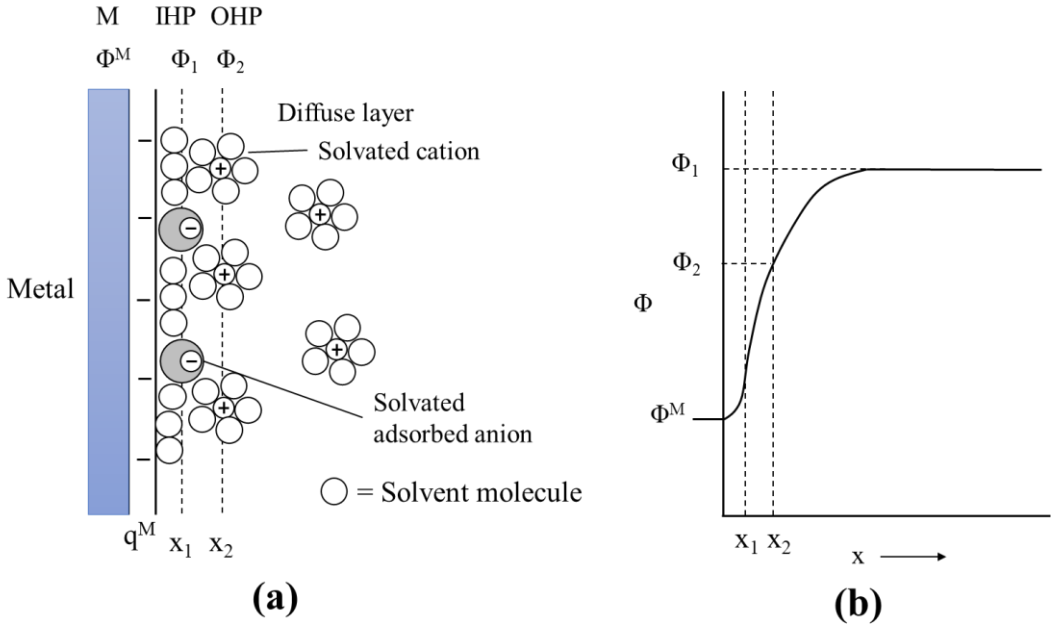

Figure 1.6 Schematic representations of (a) The proposed model of the double layer region, (b) Potential profile across the double layer region.

Figure 1.6 illustrates a proposed double layer model and the potential drop profile. It is suggested that the inner layer of the double layer closest to the electrode contains solvent molecules and some specifically adsorbed anion. The locus of the electrical centres of the adsorbed ions is named as the inner Helmholtz plane (IHP). The outer Helmholtz plane (OHP) as shown in the graph is defined as the centre of the solvated ions at a minimum distance of x_2 from the electrode surface. The interaction between the charged electrode and the solvated ions is independent of the chemical properties of the ions as their interaction involves only long-

range electrostatic forces. For this reason, these ions are termed as non-specifically adsorbed ions. Then the separated charges form a capacitor, generating the double layer capacitance. Another layer called the diffusion layer is the region from OHP to the bulk of the solution, where the non-specifically adsorbed ions distributed due to the thermal agitation in the solution. The thickness of the diffusion layer is heavily affected by the total ionic concentration of the solution. The potential drop across the double layer region is illustrated in Figure 1.6b.

1.2.3 Reaction Controlled by Mass Transport

For a mass transfer controlled process, the rates of heterogeneous electron transfer are very rapid compared to the mass transport processes. There exist three main types of transportation of reactants to the electrode surface during electrode reactions (As shown in Figure 1.7):

1. Diffusion. Movement of species by the influence of a concentration gradient.
2. Convection. Hydrodynamic transport by natural convention (density gradients) or forced convention.
3. Migration. Movement of charged particles under the influence of an electrical potential gradient.

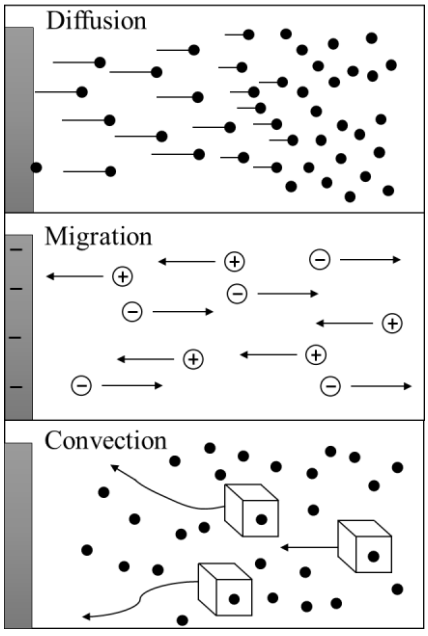

Figure 1.7 The three modes of mass transport.

Mass transport in an electrode reaction can be described by the Nernst-Planck equation, its one-dimensional form is written as:

$$J(x,t) = -D\frac{\partial C(x,t)}{\partial x} + C(x,t)V(x,t) - \frac{zFDC}{RT}\frac{\partial \phi(x,t)}{\partial x} \quad (1.16)$$

Diffusion Convection Migration

where

J: The flux of the substance at a distance of x to the electrode surface (mol s^{-1} cm^{-2});

D: The diffusion coefficient (cm^2 s^{-1});

$\partial C(x, t)/\partial x$: The concentration gradient at distance x;

$\partial \phi(x, t)/\partial x$: The potential gradient at distance x;

z and *C*: The charge and concentration of the substance;

v(x): The velocity of the substance.

The three terms on the right-hand side of the equation characterise the impacts of diffusion, migration, and convection, respectively.

Diffusion

For an electrode reaction, a concentration gradient close to the electrode surface would arise due to the consumption of reactants and generation of products. Diffusion then occurs to balance the concentration difference and establish a homogenization of the solution. The diffusion process would also create a depleted region that increases with time, denoted as the diffusion layer. The thickness of a diffusion layer can be estimated by a rule of thumb equation:[8]

$$\text{Thickness} = \sqrt{2Dt} \quad (1.17)$$

Where D is the diffusion coefficient, t is the time of the formed diffusion layer. For aqueous solutions, a typical value of D is $5 * 10^{-6}$ cm^2 s^{-1}. This indicates that a diffusion layer thickness of 10^{-4} cm can be grown in 1 ms.

Fick's laws of diffusion describe the relationship between the flux of a substance and its concentration as functions of position and time. For one-dimensional diffusion, the flux (J) is stated as proportional to the concentration gradient ($\partial C_O/\partial x$), given by the Fick's first law:

$$J = -D_O \frac{\partial Co}{\partial x} \tag{1.18}$$

Where D_O is the diffusion coefficient of substance O, C_O is the concentration of substance O, and x is the one-dimensional Cartesian coordinate. Here flux represents the number of moles of substance O that pass through a location per second per cm^2 of area normal to the axis of diffusion.[1]

Fick's second law defines the variation of substance concentration as a function of time (in one-dimension):

$$\frac{\partial C(x,t)}{\partial t} = D_O \frac{\partial^2 C(x,t)}{\partial x^2} \tag{1.19}$$

This equation is appropriate for electrode reactions take place at a planar electrode. However, in an electrochemical system when the electroactive species is present at a high concentration, solution properties (e.g., local viscosity) may change significantly during the measurement.[1] The equation is no longer appropriate as solution composition and diffusion coefficient may change dramatically. More complicated treatments are necessary to describe these systems.

Convection

The second mode of mass transfer is convection. Convection typically exist in two forms, natural and forced convections. Natural convection can take place in any solution, which is induced by thermal gradients or density gradients. Density gradients can build up at the electrode surface due to the difference in density between reactants and products. The influence of natural convection become significant when the diameter of working electrode reaches

millimetre. Longer experimental timescale would also lead to convective effects. This type of convection is undesirable as it is complicated to predict. It can be minimized by using shielded electrodes and placing the electrode horizontally. In addition, preventing stirring and vibrations in the electrochemical cell would also be beneficial.

Forced convection can be achieved by using external forces such as pumping, stirring and gas bubbling. This is normally conducted to reduce natural convection. In electrochemical experiments, this can be achieved by using microfluidic or a rocking disc electrode. Then this controlled forced convection can be predicted numerically to establish the concentration profiles

$$\frac{\partial Co}{\partial t} = -v_x \frac{\partial Co}{\partial x} \tag{1.20}$$

where v_x is the velocity of the solution.

Migration

The third mode of mass transfer is migration. Current flow in the solution can lead to a potential drop between solution and electrode interface, which induces an electric field. The ions in the electric field would be affected by the electrostatic force, and thus ion migration occurs. The migratory flux (J_m) is proportional to the ion concentration (C), the electric field ($\partial\phi/\partial x$) and the ionic mobility (u):

$$J_m = -uC \frac{\partial \phi}{\partial x} \tag{1.21}$$

The ionic mobility can also be affected by the solution viscosity, charge and magnitude of the ions. The direction of the electric field and the charge on the ions determines the direction of migration current. During electrode reactions, the migration phenomenon also take place, which together with diffusion would affect the faradaic current. As a result, it is ideal to minimise the magnitude of migration current. The most commonly adopted method is the utilisation of an inert supporting electrolyte. Normally it is introduced to the solution at a concentration much higher than that of the electroactive species (in excess of 0.1 M).

Having noted these above aspects in electrode dynamics, the next section will be focused on the classical and innovative voltammetry techniques for analysing electrochemical systems.

1.3 Voltammetry Techniques

Voltammetry is one of the most important technique used in electrochemistry studies, and has been adopted in various research areas such as electroanalysis and electrode material development. It can also be used to probe the kinetic, thermodynamic and mass transport mechanisms of redox reactions.[9] In general, the technique record the current response upon the application of a potential on an electrochemical cell. A three-electrode system is normally employed for voltammetric measurements, including working, reference and counter electrodes. The working electrode is of essential as electrode reaction occurs at this electrode. In order to apply potential, some standard or reference electrode whose potential is nearly constant is required. After that, the generated current response needs to be monitored across the working electrode and a third counter electrode.

Before describing these different voltammetric methods, it is needed to highlight the parameters employed in the electrochemical system and their importance. It is reported that a minimum of 10 parameters are required for explaining the simplest case of a redox process, either obtained from the measurement or estimated from theory versus experiment comparison.[10] In order to define the electrode kinetics of the electrode-solution interface, the reversible formal potential (E^0), heterogeneous charge transfer rate constant at potential E^0 (k^0) and the charge transfer coefficient (α, assuming Bulter-Volmer charge transfer kinetic model apply) are needed. In reactions with dissolved chemicals on a stationary electrode, the diffusional mass transport is often regarded as the controlling factor for the faradic current. As a result, Fick's law and the relevant parameters are necessary for the mathematical simulation of the system, including the diffusion coefficient (D) and concentration (C) of the chemicals, and electrode surface area (A). Another critical factor that contributes to the total current is the background current arising from the capacitance of the double layer (C_{dl}) or modified electrode surface. Additionally, Ohm's law stated that the voltammogram is strongly influenced by the uncompensated resistance (R_u), which exhibits the resistance of the solution phase between tips

of the working and reference electrodes. Furthermore, homogeneous rate constants are desirable for an electrochemical mechanism with chemical reaction step.[10]

1.3.1 Potential Step Voltammetry

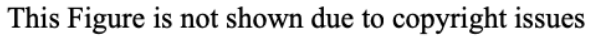

Figure 1.8 Experimental arrangement for controlled-potential experiments[1]

A basic experimental system for voltammetry measurement has been shown in Figure 1.8. Potentiostat is an instrument used to control the voltage between working electrode and reference electrode, and maintain their potential difference through a program defined function generator. Current response of the chemical system is recorded through working electrode and counter electrode. The current is unique since it is functionally related to the potential. This is due to the active electrochemical process need to be supported by the flow of electrons at a rate consistent with the potential.

Electrochemical test cells always have a solution resistance controlled by the cell geometry and the composition of the electrolyte. Current flow through this solution resistance can cause significant errors in the measured potential. A potentiostat with three-electrode setup is able to compensate some of the solution resistance through placement of a reference electrode. Because reference electrodes are not infinitely small and they cannot be placed infinitely close to the working electrode, this compensation is always incomplete. The portion of the total

solution resistance that is left uncompensated is called R_u (uncompensated resistance).

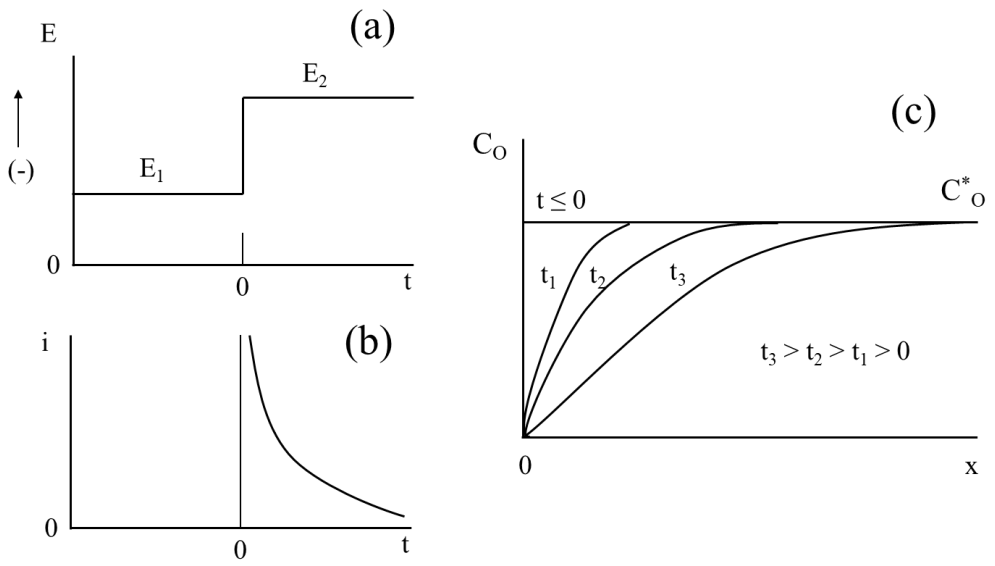

Figure 1.9 (a) Potential waveform for a step voltammetry (potential instantaneously jump from E_1 to E_2); (b) Concentration profiles for various time; (c) Current response *vs.* time.

A typical waveform applied in potential step voltammetry is shown in Figure 1.9a. The voltammetry starts at a potential range E_1 where no faradic activity occurs. It then instantaneously changes to another potential E_2 where the reaction enters the "mass transport limited" region.

Consider the reduction of O to R on the interface between a solid electrode and a stagnant solution. The reactant O is depleted on the electrode surface, which caused a concentration gradient that produces a flux of O from bulk solution to the electrode surface. The newly arrived reactant will continue to be reduced. Thus the flux of O and the current is proportional to the concentration gradient at the electrode surface. The thickness of the diffusion layer then expands with increasing time, leading to a decrease in the concentration gradient (the slope of the concentration profile declines with time). This effect is depicted in Figure 1.9b. As indicated in Figure 1.9c, the resulting current response also drops due to the

decreased concentration gradient. The Cottrell equation (1.22) describes the current is proportional to the square root of time.

$$|\mathrm{i}| = \frac{nFAC_O(b)\sqrt{D}}{\sqrt{\pi}\sqrt{t}} \tag{1.22}$$

1.3.2 Linear Sweep Voltammetry & Cyclic Voltammetry

Potential sweep voltammetry is another popular method used in the investigation of electrochemical systems. In this technique, the potential is applied at a certain scan rate. Linear sweep voltammetry (LSV) and cyclic voltammetry (CV) are the two common forms in this category.

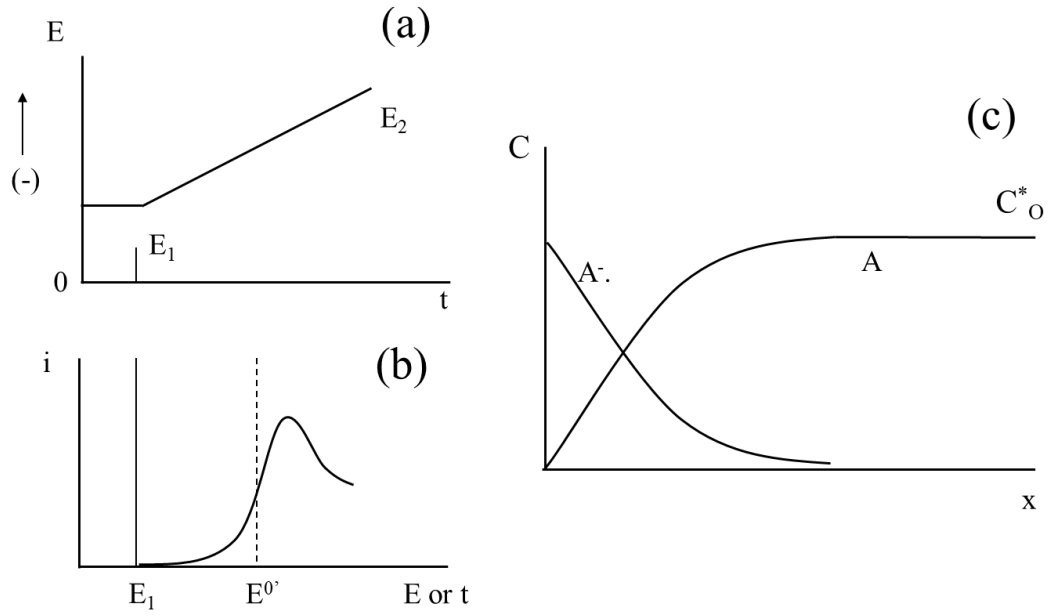

Figure 1.10 (a) Potential waveform for a linear potential sweep; (b) Current response *vs.* time; (c) Concentration profiles during the measurement.

Figure 1.10 illustrates a typical LSV potential waveform and measurement response for the reduction of O to R. The scan begins at a potential with no faradic current flows for a while,

then is swept to more reductive values, causing the reduction occurs and current flow. The surface concentration of O then drops as the potential is scanned further. The flux of the reactant O to the electrode surface then increases. When the potential scan passes peak potential, the surface concentration drops nearly to zero. The flux to the surface reaches the maximum rate and then decreases as the diffusion layer grows thicker above the electrode surface. The peak then occurs due to the flux is not fast enough to satisfy the Nernst equation (1.2). After the peak, the current starts to drop, following the same behaviour in Cottrell equation (1.22).

CV is a potential sweep voltammetry very similar to LSV with an extended potential scan from E_2 back to E_1 as shown in Figure 1.11a. The process can be described as the reduction reaction of O to R for the first half scan (identical as LSV), followed by the oxidation of R to O for reverse scan. It is a very popular technique for testing new electrochemical systems of a compound, an electrode surface or a biological material.[11] It has also been proven simple and useful in obtaining information for complex electrode reactions. For example, a simple examination of the cyclic voltammogram (Figure 1.11) can show that a redox active specie exists in solution can be oxidised to a stable product. The reversible potential of the redox couple ($E^{0'}$) can also be estimated from the average value of the oxidation and reduction peak potentials. $E^{0'}$ is a thermodynamic parameter that shows how difficult a specie can be oxidised (or reduced). Additionally, the kinetics of electron transfer (k^0) can be acquired from the comparison of the peak potential separation and theoretic predictions, given the evident of adequate departure from reversibility and negligible uncompensated resistance (R_u).[12] For a reversible reaction, the diffusion coefficients of the reduced reactant can also be calculated from the Randles-Sevick equation.[1] Thus, CV can provide many insights to a redox process and is seen as the most popular voltammetric method.

Nevertheless, there are inherent drawbacks associated with the CV technique. For an electrode process with slower rate constant, an increase of the peak-to-peak separation (ΔE_p) can be observed. Typically, the separation value is used to quantify the electrode kinetics in cyclic voltammogram.[12] Since ΔE_p is affected by R_u, the kinetics can only be solely derived from ΔE_p when R_u has a negligible effect on the system.

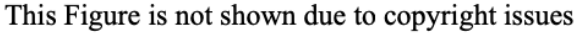

Figure 1.11 (a) Waveform for a cyclic voltammetry; (b) Resulting cyclic voltammogram;[1]

For a reversible reaction (rapid electron transfer kinetics) without coupled chemical reactions, some well-defined characteristics have been established.

- The reductive and oxidative peak current (I_p^c and I_p^a) has a ratio of 1.
- The difference in reductive and oxidative peak potentials is a good reference to the reversibility of a redox reaction. A value of 59/n mV is given under Nernstian condition at 25 ˚C. The difference is typically 70 – 100 mV in practical.[13]
- The position pf peak potential does not alter with changing scan rate.
- The peak current is proportional to the square root of scan rate as described in Randles-Sevcik equation.

$$|I_p| = 2.69 \times 10^5 n^{3/2} A D^{1/2} C v^{1/2} \quad (1.23)$$

In a reversible system, the peak current increases as the scan rate increases, shown in Figure 1.12a. This can be rationalised by relating the size of diffusion layer and the time required to complete the scan. It is obvious that slower scan rate would leads to longer measurement, which then causes a thicker diffusion layer to a fast scan rate. As a consequence, the flux of reactant to the electrode surface is more restricted at slower scan rate, resulting in a smaller current.

While for a quasi-reversible reaction (slow electron transfer kinetics), the cyclic voltammogram indicates significant different behaviours (Figure 1.12b). In this situation the overall form of the voltammogram recorded is similar to that above, but unlike the reversible

reaction now the position of the current maximum shifts depending upon the reduction rate constant (and also the voltage scan rate). This occurs because the current takes more time to respond to the applied voltage than the reversible case. It is often described that these reactions are diffusion controlled as opposed to the charge-transfer control in the reversible counterparts. The blue curve shows the case when the rate constants for reduction and oxidation are still fast. When the rate constant is decreased, the equilibrium at the surface cannot be established promptly, causing the peaks to more positive and negative positions for oxidation and reduction, respectively. Additionally, the difference in peak potential is not fixed, and relationship between peak current and scan rate no longer obey the Randles-Sevick equation. A new equation to estimate the current in this situation has been given by:

$$|I_p| = \frac{n^2F^2}{4RT} vA\Gamma_O^* \tag{1.24}$$

Where Γ_O^* is the concentration of absorbed O on the electrode surface.[1]

This Figure is not shown due to copyright issues

Figure 1.12 Cyclic voltammograms at (a) various scan rates and (b) rate constants.[14]

1.3.3 Square Wave Voltammetry

Square wave voltammetry (SWV), developed by Barker and Jenkins,[15] is a powerful electrochemical technique that has been extensively used in electro-kinetic measurements, analytical application and mechanistic study of electrode processes.[16] It unifies the merits of several pulse voltammetric methods, including the background suppression and sensitivity of differential pulse voltammetry (DPV), the diagnostic value of normal pulse voltammetry

(NPV), and the direct interrogation of products of reverse pulse voltammetry (RPV).[1] It also incorporates the advantages of cyclic voltammetry (insight into the electrode mechanism) and impedance techniques (kinetic information of fast electrode processes).[17] The ability to achieve a wider time scale than other pulse voltammetric methods also adds its popularity.[1] Currently SWV is regarded as one of the most advanced voltammetric techniques.

Figure 1.13 (a) Potential waveform for a square wave voltammetry; (b) One potential cycle; (c) Current response *vs.* potential, consists of forward (Ψ_f), backward (Ψ_b) and net (Ψ_{net}) component. (Reproduced from reference[17])

A typical potential modulation for SWV is shown in Figure 1.13a, a symmetric square wave potential is superimposed onto a staircase potential. Two potential pulses of same value but opposite direction is imposed at each step of the staircase, completing a single potential cycle in SWV (Figure 1.13b). In a single potential cycle, the electrode reaction is driven in both cathodic and anodic directions, therefore providing an insight into the electrode mechanism. The figure also illustrates the principle parameters used in SWV, including the amplitude (ΔE_{swv}), the pulse width (t_p), and the step height (ΔE_s). Thus the square wave frequency can be expressed as $f = 1/(2t_p)$ and the scan rate as $v = \Delta E_s/2t_p = f\,\Delta E$. The term frequency can be physically understood as a number of potential cycles in a unit of time. Commercially available

frequency range in a typical instrument is in the range of 5 to 2000 Hz (single pulse duration of 100 to 0.25 ms).[17] In each cycle period, t_p defines the measurement time scale, ΔE_s fixes the spacing of potential points, and their combination determine the required scan time.

Currents are sampled twice per cycle at the end of each pulse with the aim of discriminating against the charging current. The forward current (Ψ_f) is in the direction of the staircase scan, arising from the first pulse in each cycle. The backward current (Ψ_b), taken from the second pulse, is in the opposite direction. Consequently, a difference current Ψ_{net} can be calculated as $\Psi_f - \Psi_b$. Figure 1.13c indicates the three voltammograms (forward, backward, and net difference currents *vs.* potential) obtained in a single SWV scan. A bell-shaped curve would be observed for most electrode mechanisms, allowing precise determination of position and height. In addition, in the case of small amplitude, the charging current can be seen as identical at two neighbouring pulses since it depends on potentials with no change. As a result, the subtraction process in SWV helps to further cancel out the remaining charging current, which makes SWV an effective technique in the cancellation of capacitive current.

SWV has also been widely utilised in electrochemical studies. For instance, the technique was used to study the diffusion-controlled catalytic mechanism and surface catalytic mechanism.[18] In another study of the oxidation of epinephrine and norepinephrine on CNT-paste electrodes modified with 2-phenyl-hydrazine-carbo-thioamide, two well-defined square wave voltammetric peaks were resolved, which avoid the overlapping of the responses.[19] Furthermore, SWV was also utilised as the electrochemical probe of an alizarin-based carbon electrodes for monitoring pH due to its higher sensitivity to faradaic current.[20], [21]

1.3.4 Electrochemical Impedance Spectroscopy

Electrochemical impedance spectroscopy (EIS) is another approach that superimpose a periodic ac signal onto the dc waveform to elucidate the electrode mechanism more easily. It is a powerful method for characterising the electrical properties of the electrode and its interfaces.[22] Here a basic overview of the principles of the technique is provided.

The measurements can be performed using an oscillating sinusoidal potential waveform, *E(t)*.

$$E(t) = E_m \sin(2\pi ft) \tag{1.25}$$

Where f is the frequency, E_m is the maximum amplitude. The amplitude adopted in EIS is normally of small values such as 5 mV and 10 mV. A typical potential waveform of the technique is illustrated as curve E in Figure 1.14.

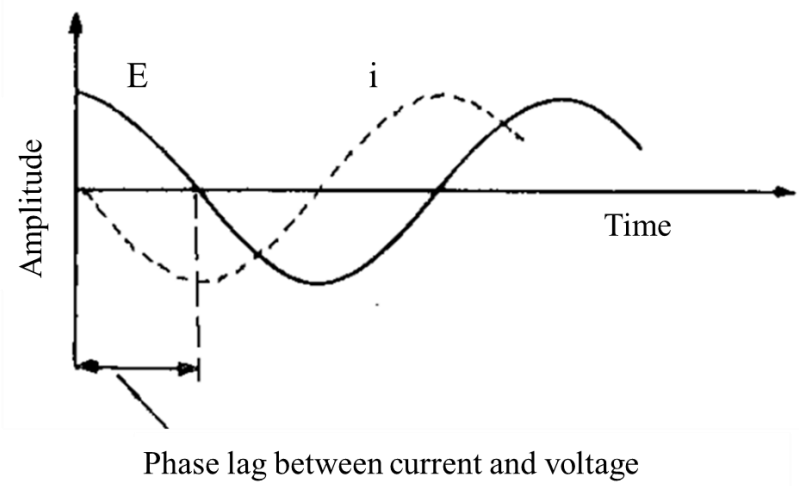

Figure 1.14 Sinusoidal current response with a phase difference of π/2.

Consider the waveform is applied to a simple capacitor. Then the generated current flow from the oscillating potential can be described as:

$$i(t) = i_m \sin(2\pi ft + \theta) \tag{1.26}$$

Where i_m is the maximum current amplitude and θ is the phase shift between the applied voltage and detected current. Therefore, the differential capacitance (C_d) can be related to the current as:

$$i = C_d\{2\pi f E_m \sin\left(\pi ft + \frac{\pi}{2}\right)\} \tag{1.27}$$

Another term of the impedance (Z) is commonly adopted to describe the response of electrical circuits to a.c. voltages:

$$Z(f) = \frac{E(t)}{i(t)} \tag{1.28}$$

The term Z can be used to understand the impeded passage of current caused by the circuit, which provides a measure of the resistance of the circuit. For the case of a single capacitor, the phase difference between current and voltage is $\pi/2$, while for a single resistor there is no phase difference with $\theta = 0$. The above situation can be explained that charge flows directly through a resistor, whereas the conduction in a capacitor is indirect that affected by the attraction or repulsion of electrons from the plates. In real and complex circuit, the phase difference can change with frequency and take on any value. Thus, the following equation is often utilised to describe impedance measurements:

$$Z(f) = Z_{Re} - jZ_{Im} \tag{1.29}$$

The expression for Z(f) is composed of a real part (Z_{Re}) and an imaginary part (Z_{Im}). Nyquist Plot can then be obtained by plotting the real part on the X-axis and the imaginary part on the Y-axis. At each frequency, the impedance Z is plotted as a point with coordinates (Z', $-Z''$). In experimental measurements, the impedance plot can be directly generated by using a frequency response analyser. A frequency range of 10^{-2} to 10^{5} Hz can be reached, which enables a huge range of time-scales to be probed.

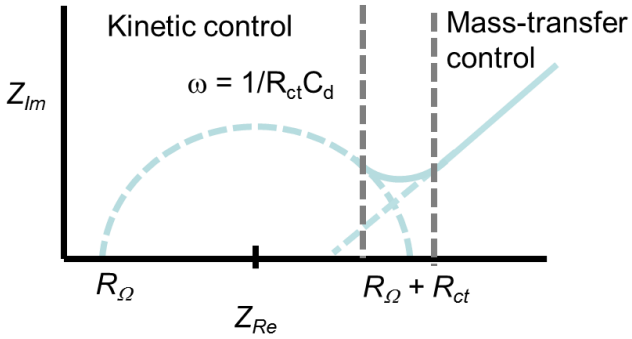

Figure 1.15 A typical Nyquist Plot with kinetic control and mass transfer control regions.

Figure 1.15 illustrates a typical Nyquist Plot with kinetic control region and mass transfer control region. This plot provides a sensitive diagnostic of the circuit for the investigated

electrochemical cells. These cells can be modelled as a network of passive electrical circuit elements, named as equivalent circuit. The basic circuit elements include resistor, capacitor, inductor and Warburg impedance. By fitting the circuit elements to form an equivalent circuit of the electrochemical cell, several important characteristics can then be obtained from the Nyquist Plot.

The EIS technique has been extensively adopted in a number of applications. Singh and cowokers utilised EIS to examine the oxygen reduction reaction in acidic media at a thin-film rotating disk electrode.[23] In another study, the technique was employed as a detection tool for sensing DNA and compared with other biosensors using similar platforms.[24] The result indicated the technique is more sensitive than other electrochemical measurements such as amperometric, voltammetric and potentiometric. Messaoud *et al.* also adopted this technique to assess the sensitivity of a MWCNT and gold nanoparticle modified electrochemical sensor for detecting bisphenol A.[25]

Traditionally, ac voltammetry and impedance spectroscopy are described in terms of small amplitude sinusoidal perturbations and used in mechanistic studies.[26] However, technique utilising small amplitude suffers from the low signal response, which is not suitable for analytical purpose. Thus ac voltammetry with large amplitude perturbation is used in analytical applications, which is believed to have exceptional faradaic to nonfaradaic current ratios.[9]

1.3.5 Fourier Transformed Large Amplitude Alternating Current Voltammetry

Direct current (dc) linear sweep and cyclic voltammetry have appeared as the most commonly used techniques to investigate electrode mechanisms.[27] In these techniques, the potential is scanned linearly over the range of interest at a known rate with or without scanning back to the initial point. As described in section 1.3.2, these dc techniques have some major drawbacks. Thus voltammetry employing ac is developed to overcome some of these weaknesses, and it is principally more powerful for evaluating mechanisms of electrode processes.[28] The first employment of ac voltammetry for the investigation of homogeneous chemical processes was proposed more than 40 years.[29], [30] In these experiments, a small amplitude sinusoidal potential (ΔE of 5-10 mV) is superimposed on a linear dc potential sweep in ac

measurement.[31] The reason behind using small amplitude is that there are limited theoretical solutions available to the ac technique at that time. By using a small amplitude, the theoretical analysis can be extensively facilitated.[32] This emphasis on linearization of the analysis limited the access to second and higher order harmonic Faradaic currents, and the responses for different transient waveforms are similar in frequency domain.[32], [33] Later on, this restriction in the linear and small amplitude regions for analysing data has been eliminated, owing to the accessibility of high-speed, low-cost and large-memory instrumentation as well as the significant developments in numerical methods.[26], [28] Larger amplitude is therefore employed to enhance harmonic strength over background current and increase sensitivity.[34] Routine usage of Fourier transformation (FT) is also possible, and there appears a growing interest in ac voltammetry.[26] Since then, this technique has been used and examined by several research groups on aspects such as mediated electrode processes,[35] analytical applications,[36] non-Faradaic processes on ac voltammetric responses[37], [38], and surface-confined substrates study[27], [39].

Figure 1.16 (a) Linear dc potential same as in LSV; (b) Periodic ac potential; (c) Total applied waveform in ac voltammetry by the addition of (a) and (b).[27]

Fourier transformed large amplitude alternating-current voltammetry (FTACV) adopts a large ac perturbation to generate larger contribution from nonlinear elements to the total current. The waveform of FTACV is made up of two components, E_{dc} (linear potential) and E_{ac} (alternating potential, $\Delta E \sin(\omega t)$). E_{ac} of known angular frequency (ω) and large amplitude (ΔE of 50-200 mV) is superimposed onto the E_{dc} waveform to form the potential input in FTACV.[28], [33] The input waveforms for the components and ac voltammetry shown in Figure 1.16 can be described as:

$$E_t = E_{dc} + \Delta E \sin(\omega t) \quad (1.30)$$

Then the ac response is measured as a function of both dc potential and angular frequency and used to extract the kinetic and thermodynamic information. As a consequence, extra data from the perturbation can be extracted, in addition to that available in dc voltammetric techniques. For instance, a sinewave with a frequency of f Hz superimposed on to the dc ramp would generate a series of higher order harmonics at 2f, 3f, 4f, and 5f Hz *etc* (Figure 1.17). The figure represents the data in both full format (black bulk) and envelope form (red curve), while for clarity reason, the envelope form is used in most cases.[10] It has been noted that better resolution of the kinetics can be obtained from slower frequencies. The adsorption effects is avoided by using a low frequency in fast reaction systems.[40] It is also suggested that the response is mainly dominated by capacitance effect in higher frequencies. One essential advantage of the technique is that the higher harmonics responses are extremely sensitive to fast heterogeneous electron transfer, while eliminating the catalytic and background charging currents.[41] The main attributes of dc technique is also preserved in FTACV as the 0 Hz component.

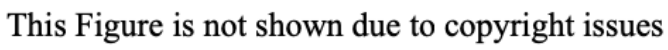

Figure 1.17 FTACV data processing *via* the FT – band selection and filtering – iFT sequence. Red curve as the envelope presentation of the periodic current.[10]

Another advantage of FTACV is its sensitivity of current magnitude to k^0 and R_u. The background current is typically not presented in the higher harmonics, though it appears in large value in the fundamental harmonic.[10] Double-layer charging component is mainly presented in dc and fundamental components. The behaviour of the purely faradic terms in the second and higher harmonic components can be obtained.[42], [43] Thus the need for baseline

subtraction can be eliminated, and this technique can be utilised to study coupled chemical reactions or charge transfer processes. Additionally, most inlaid macro disc electrodes (mm-sized) suffer from the non-planar diffusion effects caused by the edge diffusion.[44], [45] This edge current causing the semi-integral of a dc voltammogram to climb continuously instead of a true plateau, which makes the direct determination of D_R from the plateau height impossible.[46] However, this edge effect is negligible in FTACV, allowing simple utilisation of planar diffusion model. Other advantages includes noise extraction,[47] advanced windowing,[48] and variations of the periodic component.[33]

In terms of literature review, there is a growing interest in applying the technique to a variety of applications. For instance, in biological field, FTACV has been employed to probe biological redox chemistry. Protein film electrochemistry was one of the application initially being investigated by FTACV. An electron transfer protein of simple structure and contains mono-copper, azurin, studied by FTACV measurements demonstrated that the faradaic current can be separated from the background capacitive current.[27] Additionally, a further study pointed out that better isolation of Faradaic current from background current can be achieved in the higher harmonics.[49] The electron transfer rates can also be measured by the differing kinetic sensitivity of each harmonic. Furthermore, FTACV has also been applied to investigate a more complex biological redox protein, ferredoxin, which has two independent redox centres of similar redox potentials.[50] The result indicated that the Faradaic signals from the two centres can be resolved by FTACV. In another study, the FTACV technique has also been utilised to examine the two-electron redox reaction of the flavin adenine dinucleotide in glucose oxidase enzyme.[51] Possible two-electron transfer mechanisms can be effectively discriminated by the higher harmonics.

The FTACV technique has also been applied to study homogeneous and heterogeneous reactions. For instance, Song and coworkers demonstrated the utilisation of the technique to study the split wave phenomenon of the EC' mechanism of ferrocyanide carboxylic acid and L-cysteine.[43] As revealed by the technique, the behaviour of the split waves can be affected by the frequency of the input potential, the effective electrode surface area, and substrate concentration. Furthermore, Zhang *et al.* adopted the technique has been adopted to the electrocatalytic reduction of carbon dioxide (CO_2) to $HCOO^-$ and CO, attempting to provide

new mechanistic insights to the reaction.[41] Their study also suggested a possible mechanism of CO_2 reduction, including a reversible inner-sphere single electron reduction of CO_2 and a subsequent $CO_2^{\bullet-}$ protonation as the rate determining step.

FTACV also seems to be a promising technique in sensing applications. This is because the higher harmonic components are highly sensitive to electron transfer kinetics. For example, Zhang *et al.* used the technique to separate the overlapping process between the reversible $[Ru(NH_3)_6]^{3+}$ reduction and the irreversible oxygen reduction process.[52] In addition, the reduction of $[Ru(NH_3)_6]^{3+}$ can also be resolved from the non-reversible $[Fe(CN)_6]^{3-}$ reduction at a boron-doped diamond electrode.

However, FTACV has not been frequently utilised to characterise carbon-based materials. Therefore, it is appealing to utilise the technique for examining the sensing capability of CNT based electrode.

1.4 Coupled Homogeneous Kinetics

In section 1.2, purely electron transfer reaction has been studied without further coupled chemical reactions. Apart from electrode reactions, homogeneous reactions between species in bulk solution can also occur during an electrochemical measurement. This section describes the electrode reaction followed by subsequent homogeneous chemical reactions between electron transfer reaction products and other chemicals in the electrolyte. The electron transfer step is denoted as E, while preceding chemical reaction step is denoted as C. Three mechanisms have been introduced in this section, including EC, ECE and EC'.

1.4.1 EC Mechanism

In this case, considering the following reactions:

$$\text{E step: } R - e^- \overset{k_e}{\Leftrightarrow} O \tag{1.31}$$

$$\text{C step: } O + C \xrightarrow{k_{EC}} \text{S} \tag{1.32}$$

The product (O) of the electron transfer reaction form at the electrode surface, it then reacts with a non-electroactive species (C) in the solution phase to form anther non-electroactive product (S). The overall reaction process can be significantly affected by the rate constants of the two steps (k_e and k_{EC}). For a reaction system with a slow k_{EC} (compared to the voltage scan rate), the observed cyclic voltammogram is similar to a typical reversible voltammograms. This is due to the chemical reaction rate is relatively slow so that the species O is hardly consumed. In another situation of a fast k_{EC}, the product O would react immediately with C after it is formed on the electrode surface. As a consequence, the voltammogram for this case is different from that observed with solely electron transfer reaction. A comparison of the two cyclic voltammograms has been given in Figure 1.18. Therefore, the shape of the voltammogram and the height of backward peak are indicative of the kinetics of the chemical reaction step for an EC mechanism. Scan rate of the potential input is another factor that can influence the voltammetric response. For a slow scan rate case, the residence time for the product on the electrode surface is increased, resulting in a significantly reduced backward peak. This can be rationalised by the increased time for the chemical step to take place.

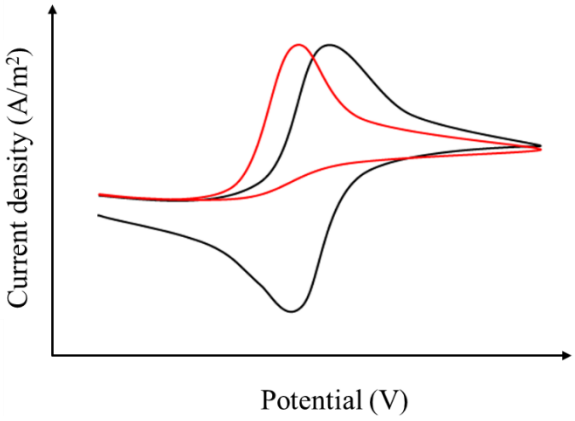

Figure 1.18 Cyclic voltammograms for EC mechanisms with fast (red) and slow (black) chemical reaction rates.

Figure 1.18 also indicates another phenomenon that the forward peak shifts slightly to more negative potential for reaction systems with fast k_{EC}. This causes the species R to be oxidised more readily, which can be justified by the Nernst equation (1.2). For a reversible electrode reaction, the Nernst equation associates the ratios of the electrode surface concentrations of oxidative and reductive species at a particular potential. The couple homogeneous reaction

eliminates the product O, which changes the equilibrium at the electrode surface. Therefore, the electron transfer is driven to the forward direction to re-establish the equilibrium, which produces more O to compensate those reacted in the chemical step. This then explains the negative shift of the voltammogram.[32]

1.4.2 ECE Mechanism

The second multistep reactions system is the ECE mechanism as shown below:

$$\text{E step: } R - e^- \overset{k_{e1}}{\Leftrightarrow} O \tag{1.33}$$

$$\text{C step: } O + C \xrightarrow{k_{\text{ECE}}} \text{S} \tag{1.34}$$

$$\text{E step: } S - e^- \overset{k_{e2}}{\Leftrightarrow} T \tag{1.35}$$

These equations describe the three steps for an ECE mechanism, with the initial two reactions identical to the EC mechanism. A third reaction following the EC reactions occurs as the product of the chemical step is also electroactive and can be oxidised. However this second electron transfer reaction normally takes place at a different potential to the initial electron transfer reaction.

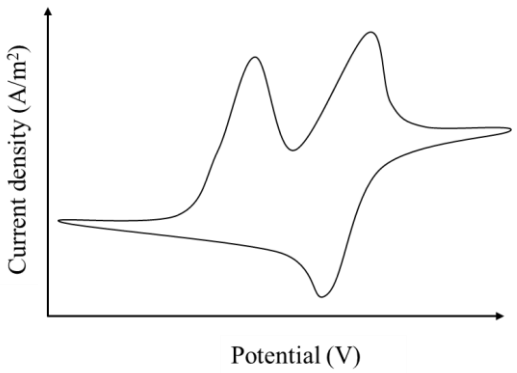

Figure 1.19 Cyclic voltammograms for an ECE mechanism.

Figure 1.19 illustrates the voltammogram for an ECE mechanism where the product of the chemical reaction step S is more difficult to reduce than the initial reactant R. The first peak in the graph denotes the oxidation of R to O. As the potential is scanned further to more positive

values, a new peak is spotted for the S/T redox couple. There is only a single peak for the reverse scan as no species O is existed for the reduction reaction. This is due to the irreversible and fast chemical reaction step, which removes approximately all the amount of O. Nevertheless, if the chemical step is reversible, then two separate peaks can be observed. Additionally, the second electron transfer step depends on the amount of the generated S from the chemical step. At a very fast scan rate, the chemical reaction and the second electron transfer reaction can be suppressed by the fast conversion of O to R.

1.4.3 EC' Mechanism

Another important mechanism is the EC', which can be regarded as a variant of the EC mechanism.

$$\text{E step: } R - e^- \overset{k_e}{\Leftrightarrow} O \tag{1.36}$$

$$\text{C}'\text{step: } O + C \xrightarrow{k_{\text{EC}'}} \text{R} + \text{S} \tag{1.37}$$

This Figure is not shown due to copyright issues

Figure 1.20 Cyclic voltammograms for EC' mechanisms with increasing concentration of C.[53]

In this case, the chemical step regenerates the initial reactant R. The C' represents a catalytic chemical reaction step, which increases the reaction rate of the electron transfer step. This then results in the increment of the peak current in the voltammogram compared with a system with pure electron transfer reaction. The corresponding cyclic voltammograms are shown in Figure 1.20 as the lowest curve. As the chemical C is introduced into the system, the current becomes

higher. This can be rationalised by considering the regeneration of R from the chemical step and thus react again at the electrode surface. The EC' mechanism is also regarded as the basis reaction used in glucose sensing by glucose oxidase.

1.5 Electrode Materials and Modified Surface

Working electrode is essential for the performance of electrochemical cells as all the important electrochemical processes occur at its surface.[2] Cells with different electrode materials or surface modification can lead to various characteristics. The selection of the materials depends heavily on the application being investigated. Commonly used electrode materials include metals and carbon based materials, and electrode surface can also be modified with metal oxides.

This Figure is not shown due to copyright issues

Figure 1.21 Volcano plot of the exchange current density against the DFT-calculated Gibbs free energy of adsorbed atomic hydrogen for various metals in hydrogen evolution reaction.[54]

Noble metals such as gold and platinum have been utilised as electrode materials. Their advantages include favourable electron rate kinetics and a large potential range. For instance, Figure 1.21 indicates the volcano plot of various metals utilised as catalysts in HER. Among these metals, Pt lies at the top of the curve which shows the highest HER activity. Nevertheless, the high cost of noble metal electrodes makes them unfavourable for use as disposable electrodes. This also hinders a wide application of the material in industrial processes.

Other elemental metals can be highly reactive, undergoing electrochemical processes, forming oxides which limit their electrical conductivity and results in the appearance of high background currents. The formed metal-oxide films would strongly affect the rate kinetics of the electrode reaction, resulting in irreproducible experimental data.

1.5.1 Carbon Based Materials

Common carbon materials include graphite, glassy carbon, and carbon nanotubes (CNTs). They have been extensively utilised in analytical and industrial electrochemistry for their wide potential window, long-term stability, low residual current, low cost, good electrical conductivity and easy modification of carbon morphology.[55] These materials have been utilised in various applications such as electrochemical sensing, organic synthesis, energy storage in batteries and supercapacitors and catalysis. The common carbon materials include carbon black, powdered graphite, glassy carbon (GC), highly ordered pyrolytic graphite (HOPG), CNTs, and graphene, each with different chemical and physical properties.

Figure 1.22 Crystallographic dimensions of sp^2 carbon. L_a, L_c, and d_{002} vary with carbon type. (Reprint from reference [55])

The essential structural factor that affects the assortment of these materials is the mean graphitic microcrystallite size along a-axis, L_a (shown in Figure 1.22). It is the average size of the hexagonal lattices that make up the macro structure, which may vary from 10 Å to about

10 μm or more.[56] As shown in Figure 1.23, the smallest L_a values can be found in amorphous carbon, GC and carbon black. Carbon fibres and powered graphite are in the intermediate range of 100 Å to 1000 Å. The largest graphite monocrystals of 1 – 10 μm can be found in HOPG. Therefore, L_a is a property to define a near continuum of materials with different properties. The figures also show the interplanar microcrystallite size, L_c, which is the distance along the axis perpendicular to the graphite plane (c-axis). Similar to L_a, different carbon materials are associated with different L_c value.

This Figure is not shown due to copyright issues

Figure 1.23 The approximate ranges of L_a and L_c for various sp^2 carbon materials. Two inset images show the microcrystalline characteristics of HOPG and GC. (Reprint from reference[56])

The properties of carbon based materials are also strongly affected by the degree of hybridisation. The electron configuration of carbon atoms at the ground state include $1s^2$, $2s^2$, $2p^2$ orbitals. The electron in s orbital can be promoted to unoccupied higher energy p orbital due to the small energy gap between 2s and 2p electron orbitals. Conditional on the bonding with adjacent atoms, the hybridisation of carbon can lead to electron configurations of sp, sp^2

or sp^3. Increased stability can be achieved by the covalent bonding with adjacent atoms, compensating for the higher energy state of the electron configuration. Additionally, the crystal structure of the carbon material can be modified by the hybridisation of the carbon atom. For sp^2 hybridisation, the carbon atom remains with one free electron in the 2p orbital. Then each sp^2 hybridised orbital combines together to form a series of planar hexagonal structures (Figure 1.24). The perpendicular orientated to the plane is the free delocalised orbital. As a consequence, the material is anisotropic since electrons can move freely from one side of the carbon atom layer to the other but not from one layer to another.

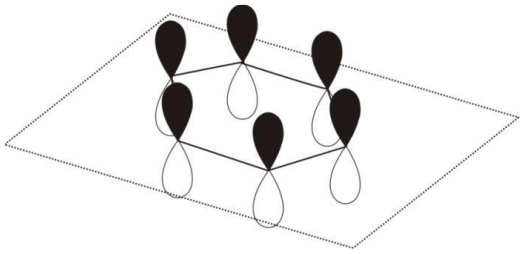

Figure 1.24 Schematic illustration of the sp^2 hybridised graphite.

The physical properties of these carbon based materials have been described in greater detail in Appendix A.

1.5.2 Electrochemical Properties of Carbon Based Materials

The electrochemical properties of several carbon-based materials are examined in this section. As discussed in the appendix, electrode kinetics at edge-plane pyrolytic graphite (EPPG) are faster than that at basal-plane pyrolytic graphite (BPPG). Figure 1.25 illustrates a schematic representation of the heterogeneous HOPG electrode surface with distinctive structural contributions of edge plane and basal plane sites. The two sites have been reported with different electrochemical activity and thus different values of Butler-Volmer terms (k^0 and α).[57] The band theory of solids can be accounted to explain the phenomenon. In a theoretical infinite graphite sheet, a series of closely spaced HOMOs and LUMOs overlap and form the valence and conduction bands. There also exist small energy gaps that discrete the bands to impart semi-metallic conductivity. It has been found that the conductivity along the basal plane is larger than the direction perpendicular to the basal plane. Nevertheless, graphite sheets are

finite in practice, and the basal planes will terminate at an edge plane site. Then the electron energy in the valence band rise dramatically due to the abrupt termination in the band structure. As a consequence, these sites become high energy and provide the place for electron transfer to occur. So the edge plane sites are more chemically reactive than the basal plane sites.

Figure 1.25 a) Schematic representation of an electrode reaction occurring on the same electrode surface with different Butler-Volmer characteristics, b) Top-down view of (a).[57]

A simple redox couple of $Fe(CN)_6^{3-}$/ $Fe(CN)_6^{4-}$ on working electrodes of BPPG, EPPG and CNTs-modified BPPG has been demonstrated in Figure 1.26.[58] There is a significant increase in the peak-to-peak separation for BPPG electrode (ca. 350 mV) over the CNTs-modified BPPG (58 mV) and EPPG (78 mV). This then suggests faster heterogeneous electrode kinetics have been observed for EPPG than that of BPPG.

Figure 1.26 Cyclic voltammograms of the reduction of 1 mM $Fe(CN)_6^{3-}$ at CNTs film-modified BPPG electrodes compared with an EPPG electrode and a bare BPPG electrode.[58]

The structure of GCE is less crystallographical with some amorphous characters. Its surface is regarded as a combination of basal and edge planes attributed to the intrinsic interwoven ribbons of graphitic crystallites. The surface chemistry of carbon materials is more complicated than that of metals. This is caused by both the variety of microstructures of different carbon and the formation of surface bonds and functional groups on the carbon surface. Thus the electrode surface is of fundamental importance in electrochemical studies as electron transfer processes take place at the interface. Consequently, a number of techniques have been developed to prepare carbon electrodes with increased selectivity or improved kinetics, including polishing, laser activation, electrochemical pre-treatment, and vacuum heat treatment. A list of the electrode kinetics for $Fe(CN)_6^{3-}$/ $Fe(CN)_6^{4-}$ with differently prepared electrodes is shown in Table 1.1.

Table 1.1 Electrode kinetics for $Fe(CN)_6^{3-}$/ $Fe(CN)_6^{4-}$ on different carbon electrodes. [a] (Reproduced from reference[55])

Electrode	**ΔE_p for $Fe^{3+/2+}$ (mV)**	**Atomic O/C ratio**
HOPG	1062	<< 0.01
HOPG, ECP [b]	162	NA
GC, polished in water-alumina	150	0.10 – 0.14
GC, polished in cyclohexane-alumina	352	0.04
GC, vacuum heat treatment	439	0.016
GC, polished + Ar^+ sputtered	908	< 0.01
GC, polished + Ar^+ +ECP	80	NA
GC, fractured	186	NA
GC, fractured + ECP	93	NA
GC, polished + anthraquinone	100	NA

a 0.2 M $HClO_4$, 200 mV/s. b ECP: Electrochemical pre-treatment by anodization.

For electrochemical properties of CNTs, two main aspects are necessary to be considered, which are impurities and defects. In many CNT fabrication techniques such as arc discharge and laser ablation, a certain amount of metallic impurities can exist in the CNTs in the form of encapsulated within graphite sheets or located outside the tubes.[59] Therefore, it is concluded that the presence of residual metallic nanoparticles could enormously enhance the electrochemical response of a particular redox system. For instance, research shows that the residual iron nanoparticles in MWCNTs are in charge of the electrocatalytic oxidation of hydrazine and reduction of hydrogen peroxide on MWCNTs modified electrodes.[60] The situation become more complex when there exist multi-component metallic impurities. It is shown that all metallic impurities of catalyst nanoparticles contribute to the electrochemical oxidation of hydrazine.[61] However, for the reduction of hydrogen peroxide occurs at acid-purified CNTs containing residual cobalt catalyst nanoparticles and iron-based impurities, only the latter is found to be responsible for the reaction.[62] As a consequence, the removal of metal impurities is preferred, while chemical treatments also impact the electrochemical response of the CNTs.

From the perspective of defects in CNTs, it is commonly realised that the edge-plane and defect sites are the main contributors for the electron transfer processes, while sidewall of the CNTs is mainly inactive.[63] The above reasoning can be seen as an analogy between MWCNTs and HOPG.[64] However, it is believed that SWCNTs own different properties than that of MWCNTs. Some researcher suggested that the sidewall on CVD grown SWCNTs may have higher electrochemical activity than previously thought.[65] One study conducted by Liu *et al.* shows that the oxidation of ferrocyanide was more facile at vertically aligned SWCNTs to randomly dispersed acid-purified SWCNTs on a gold surface.[66] In addition, the comparison between the roles of defects and sidewalls must be correlated with growth procedures, fabrication techniques and characterisation methods. The study of individual CVD grown SWCNTs with only sidewall exposed to solution for electrochemical application is one of the most convincing evidence of the activity of sidewall.[67] The result shows a steady voltammetric current proportional to the length of the exposed sidewall.

In addition, the surface chemistry of CNTs can be readily modified. A variety of techniques can be found in literature to chemically modify the structure of CNTs.[68] The most common methods being the covalent and noncovalent modifications, where the former creates a stable bond between CNTs and attached molecule, and the latter form physical adsorption of molecules onto CNTs surface.

This is followed in chapter 2 with an explanation of the characterization and fabrication techniques.

Chapter 2 Methodology and Materials

Abstract

This chapter demonstrates the experimental procedures utilised for the projects within the thesis, which involves the synthesis of materials, fabrication and assembly of devices, and characterisation techniques. The nanomaterial synthesis is achieved through a hydrothermal method, and CNT forest synthesis is conducted in a chemical vapour deposition process. Fabrication of electrochemical cells are accomplished by assembly of electrode (thermal evaporation of gold on substrates) and PDMS models. Several characterisations for examining the structural and chemical properties of the materials have also been described.

2.1 Introduction

The principal purpose of this chapter is to describe the fabrication techniques and the characterisation methods used in this thesis. The synthesis of metal oxide nanoparticles by hydrothermal method is first introduced. Then the preparation of carbon nanotube forest on gold electrode is discussed. Structural and chemical characterisations of the materials are then illustrated. In addition, the reagents and equipment used in the experiments have been listed.

2.2 Hydrothermal Synthesis

This section explains the synthesis method for preparing nanocatalysts in chapter 4.[1] The history of hydrothermal research can be traced back to 1845 when E.T. Schafthaul prepared fine quartz crystals from freshly precipitated silicic acid in Papin's digester.[69] Since then,

[1] The author gratefully acknowledges the support provided by the Campus for Research Excellence and Technological Enterprise (CREATE) program. The author would also like to acknowledge the Institute of Chemical and Engineering Sciences (ICES) for facilities to conduct H_2S reaction.

the method has been extensively developed and adopted to synthesise a wide range of materials. Hydrothermal synthesis can be regarded as a homogeneous or heterogeneous reaction in the presence of an aqueous solvent under elevated temperature and pressure in a closed system.[70] This method can be utilised to grow single crystals. The process generally involves the heating of the precursor solution in a sealed autoclave, resulting in a high pressure environment due to the evaporation of the solvent. In these conditions, the materials that would be insoluble under normal conditions can now be dissolved by water, enabling the crystallisation of the product phase. Water is the most common solvent used in hydrothermal method, which exhibits different properties under hydrothermal conditions than that of standard conditions. Water served as the solvent has several advantages. It is nontoxic, non-flammable, non-carcinogenic, non-mutagenic, and thermodynamically stable. Water is also an environmental friendly and low-cost material with ease change of the temperature and pressure. Furthermore, water can be easily separated from the product stream as it is volatile.

Hydrothermal synthesis possesses a number of advantages over conventional and non-conventional synthesis methods. Firstly, the cost for the instrumentation, energy and precursors is minimal compared to many advanced methods. In terms of environmental impacts, the hydrothermal methods are also inherently benign than other techniques. In addition, the method is capable of regulating the rate and uniformity of nucleation, growth and aging during the precipitation process. Thus the particle sizes and morphologies of the products can be well managed. It is argued that the cations in the solution and the pH of the solution are essential for controlling the product phases and structures.[71] More importantly, hydrothermal synthesis can be hybridized with other techniques such as microwave, electrochemistry, ultrasound and optical radiation. The combination of these techniques are able to achieve more benefits, including the enhancement of reaction kinetics and generation of new materials. Therefore, this facile hydrothermal method is a promising technique for growing large-scale and high-quality crystals.

2.3 Electrodes for Electrochemical Measurements

2.3.1 Gold Deposition by Thermal Evaporation

The thermal evaporation technique can be used to deposit a wide range of metals onto a substrate (e.g., glass, silicon). Thus the technique is adopted to fabricate gold electrode used in chapter 5. In a typical preparation procedure as shown in Figure 2.1, a thin film of Chromium (ca. 30 nm) with certain pattern is coated over the substrate by thermal evaporation (Auto 306 vacuum coating system), followed by another deposition of thin gold layer (ca. 100 nm). Chromium is a material providing high binding strength with oxygen. Thus the chromium layer is utilised as an adhesion layer to the substrate due to the poor adhesion of gold on substrate.

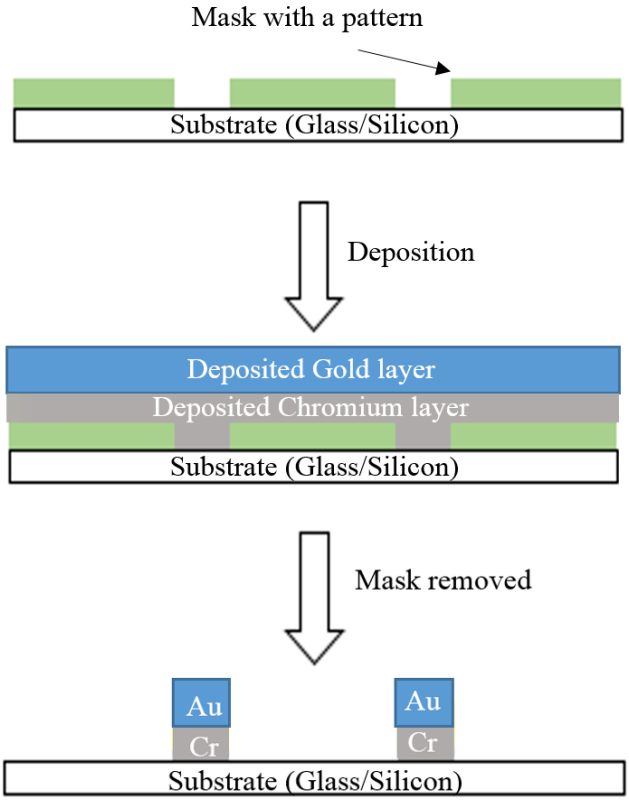

Figure 2.1 Gold deposition of gold and chromium onto substrate (glass/silicon) by thermal evaporation.

2.3.2 Synthesis of CNT Forests by Chemical Vapour Deposition

This Figure is not shown due to copyright issues

Figure 2.2 Collective model of catalyst evolution and CNT population dynamics, along with AFM image of catalyst nanoparticles and SEM images of 5 stages of CNT growth.[72]

Synthesis of CNT forests was conducted via a chemical vapour deposition (CVD) process by our collaborators.[2] Here a detailed description of the CVD process is given. Depending on the method to activate the carbon source during the formation of CNTs, CVD is classified as thermal CVD and plasma-enhanced CVD.[73] By combing the activated carbon source and a catalyst (typically first row transition metals) in a reactor, CNTs can be synthesised. The growth process, yield and growth rate of synthesising CNTs are determined by the type of catalysts.[74] Catalysts can be included in the floating of gas stream or deposited on the substrate surface during the process. In the former case, individual CNTs will be formed, and CNT forests or CNT mats will be formed for the latter case. CNT forests are vertically aligned and self-organising that can be synthesised directly on a substrate via CVD. It has been reported that vertical aligned CNTs are beneficial for specific applications such as enhanced diffusion in batteries[75] and transfer onto large area films for flexible electronics.[76] Different growth modes of CNT forest over the nano-, micro-, and macroscale can be achieved by controlling the pattern of catalyst. It is illustrated by Li *et al.* that large area alignment of CNTs can be

[2] The author gratefully acknowledges the support provided by NanoManufacturing Group, Institute of Manufacturing, University of Cambridge. The author would also like to acknowledge Chris Valentine for conducting the synthesis and characterisation of the CNT forest.

produced by the thermal decomposition of acetylene gas at high temperature (> 700) in the presence of Fe catalyst on a mesoporous silica substrate.[77]

A model to understand the mechanism of CNT forest growth has been established by Bedewy *et al.*[72] As shown in Figure 2.2, the growth dynamics of CNT forests formation have been studied by real-time height kinetics and X-Ray scattering. The following stages have been proposed to explain the growth of CNT forest:

1. Catalyst preparation: The iron film is reduced by heating the substrate in a reducing atmosphere. Then stable particles can be formed by the addition of a hydrocarbon gas.
2. Self-organisation: By the introduction of a hydrocarbon precursor source, the CNTs start to nucleate on the surface and form a mesh of tangle CNTs ('the crust'). It is believed to be the support for the subsequent aligned CNT forest synthesis.
3. Crowding: This process describes the formation of a high density CNTs region above the crust. Its kinetics are dependent on the composition of the hydrocarbon gas, carburisation of the surface and other parameters. The density of CNTs can reach to five-fold due to an increasing active catalyst population.
4. Steady growth: In this stage, the diameter of the CNTs is reduced and its structure become maximally orientated. Thus this region contains the straightest tubes.
5. Density decay: The CNTs undergo a further reduction of diameter, and its orientation starts to decrease as well. This then causing the reduction of CNTs density in the region.
6. Termination: The alignment of the CNTs loses rapidly in this stage and the diameter broadens out. The growth of CNTs terminates at this stage due to catalyst poisoning, carbon over-coating evaporation and diffusion into the alumina layer.

The growth of CNT forest can influenced by several parameters. One of the most significant factors is the catalyst, along with its variability. The material chosen as a catalyst is important, the common ones found in literature include iron, nickel, cobalt, metal oxides and alloys.[78] Additionally, the morphology of CNTs is affected by the oxidation state of the catalyst.[73] The thickness of the catalyst film can also strongly influence the diameter of CNTs.[78] Moreover, the growth rate of CNT forest can be largely affected by the under-layer below catalyst.[79] This is due to the de-wetting and coarsening of the catalyst on the under-layer that

might alter the particle size distribution of the catalyst. Another factor is the composition and flow rate of the gas stream, which affects the diameter and amount of walls within the MWCNT.[80]

In this work, the CNT forests are synthesised by the CVD process as described above directly on gold electrode (on a fused silica or silicon wafer). The gold layer under CNT catalyst acted as a retardant to the CNT synthesis. Thus some parameters were affected during the thermal CVD process. Preliminary study found that the height of CNT forest grow less for the case of synthesis on a gold electrode, compared to a forest grown from catalyst deposited on a silicon wafer. Therefore, the time of CVD process was increased to compensate this reduced forest height.

2.4 Characterization Methods

This section describes the techniques that were used for characterisation of physical and chemical properties of the prepared samples.

2.4.1 X-ray Diffraction

This Figure is not shown due to copyright issues

Figure 2.3 (a) Schematic of an X-ray diffractometer; (b) Bragg's diffraction.[81]

X-ray Diffraction (XRD) is a technique used to examine the chemical compositions and crystallographic structures of a material. This technique uses filtered monochromatic X-rays to direct towards the samples. Constructive interference and a diffracted ray will be produced by interaction of the incident rays with the sample when conditions (Figure 2.3b) satisfy Bragg's Equation.

$$n\,\lambda = 2\,d\,sin\theta \tag{2.1}$$

Where n is an integer, λ is the wavelength, d is the spacing between atom layers, and θ is the angle of incidence of the X-rays.

These diffracted X-rays are then detected, processed and counted. Owing to the random orientation of the materials, a range of 2θ angles will be scanned to attain all possible diffraction directions of the lattice. Finally, identification of the mineral can be completed by conversion of the diffraction peaks to d-spacing as each mineral has a set of unique d-spacing. This is achieved by comparing the obtained d-spacing with standard reference patterns.

2.4.2 Electron Microscopy

This Figure is not shown due to copyright issues

Figure 2.4 Schematic diagram of possible interactions of an electron beam with a specimen in electron microscopes.[82]

It is known that optical microscopes have a diffraction limited resolution of approximately hundreds of nanometres. Illumination source of smaller wavelength is required to obtain a higher resolution. Electron microscope adopts a beam of accelerated electrons to illuminate the specimen and acquire its structure and composition data. This method thus make sub-optical imaging possible. Several modes of electron microscopy have been developed, the two most extensively used are scanning electron microscopy (SEM) and transmission electron microscopy (TEM).

Scanning Electron Microscopy

In SEM, a small focused electron beam of spot size is scanned over the surface of a sample, either electron or photon emissions is collected by several detectors (Shown in Figure 2.4). The information is then gatherd to produce the topography and composition of the sample surface. Secondary electron imaging is perhaps the most common SEM techqniue that count low energy (< 50 eV) electron emissions. Sample topography can largely affect the emission of secondary electrons as their energy are relatively low. The electrons can exit the sample and be detected are those very near the surface (< 10 nm).[82] In consequence, SEM imaging is sensistive to the topography of the sample, but not the quantitative surface height information. Several factors accounts for the limitation of the SEM techqniue, including the size of focused beam and interaction volume. Thus the resolution of SEM can range from < 1 nm to macroscopic level depending on the instrument.

Transmission Electron Microscopy

TEM is a powerful techqniue to examine the morphology, size and lattice of nanomaterials by the transmission of electron beam through a thin specimen. The spatial variation between electrons and specimen is magnified and recorded by a fluorescent screen or a charge-couple device (CCD) camera. TEM and light microscope shares a similar mechanism except that high energy electrons are utilised to improve resolution in TEM. Its resolution can reach to 0.5 Å and is about an order of magnitude better than that of SEM.[83]

2.4.3 Energy Dispersive X-ray Spectroscopy

Energy Dispersive X-ray Spectroscopy (EDX) allows the inspection of the elemental composition of a sample on a micro-scale, which is mostly used in combination with the high resolution TEM (HRTEM). It utilises a high-energy beam of electrons to focus onto a sample, which ejects a core electron from an atom and leaves a hole. Then an outer electron with higher energy will drop down to fill the hole. This creates a difference in the strength of energies between the core electron and outer shell electron, which emits in the form of X-ray and detected. The energy of the X-ray can be used to distinguish the type of the atom, revealing the elemental composition of a sample.

2.4.4 Gas Chromatography & Mass Spectrometry

Gas Chromatography (GC) is a separation technique that capable of separating complex mixtures based principally upon differences of boiling point, vapour pressure and polarity. During the analysis, the injected sample will first be vaporised and transported to a column by a carrier gas (e.g., Helium) as the mobile phase.[84] The inner surface of the column includes a stationary phase such as polydimethylsiloxane. Depending on the partition of the compounds between the stationary phase and the mobile carrier gas, the compounds move through the column at differing rates and elute out of the GC column at various time. After that, the eluted compounds can be identified by comparing with external standards or mass spectrometry (MS). MS is an analytical technique for quantifying known materials, identifying unknown compounds and elucidating the structure and chemical properties of different molecules. The analytical process includes ionizing the chemical species and sorting the ions based on their mass-to-charge ratio.

2.4.5 X-ray Photoelectron Spectroscopy

X-ray Photoelectron Spectroscopy (XPS) is a widely used surface analysis technique for providing composition and chemical state information of elements within a material. The sample surface is excited by irradiating a beam of X-rays, causing photoelectrons to be emitted from the surface. The emitted electrons are then detected by an analyser, which have a certain

binding energy (E_b) and kinetic energy (E_{kin}). The continuously detected photoelectrons is then counted as a function of kinetic energy, producing the XPS spectrum for an element.[85]

$$E_b = hv - E_{kin} - \varphi \quad (2.2)$$

φ Work function of the spectrometer

h Planck's constant

v Frequency of excitation radiation

High vacuum environment is required in XPS measurement, and it is also a surface sensitive technique. In this work, all binding energies are referenced to C 1s (284.6 eV).

2.4.6 Nitrogen Adsorption-Desorption Analysis

Physical properties of samples such as surface area, pore size and pore volume are probed by nitrogen adsorption-desorption. This technique measures gas uptake (adsorption) for increasing partial pressure over a dry powder sample and the release of gas (desorption) at decreasing partial pressures. An isotherm is plotted as volume of adsorbed N_2 against relative pressure by the adsorption and desorption of N_2 at 77K. The specific surface area of the sample is calculated from the Brunauer-Emmett-Teller (BET) equation:

$$\frac{1}{v[\left(\frac{p_0}{p}\right) - 1]} = \frac{c-1}{v_m}\left(\frac{p_0}{p}\right) + \frac{1}{v_m c} \quad (2.3)$$

Where p and p_0 are the equilibrium and saturation pressure of N_2, v and v_m are the amount of adsorbed and monolayer adsorbed N_2, c is the BET constant.[86] The total pore volume and pore size distribution are determined by Barrett-Joyner-Halenda (BJH) method.

2.4.7 Raman Spectroscopy

Raman spectroscopy is a technique depends on the inelastic scattering of monochromatic light that interacting with a molecule. When energy is transferred between a photon and a molecule, the molecule is excited from ground state to a virtual state. The molecule returns to a different energy state rather than the ground state after the relaxation. A Raman shift then occurs due to the difference in the emitted photon energy. The resulting Raman bands can be assigned to the vibrations of different bonds in the molecule. The shortest bonds vibrate at the highest energy, resulting in high wave numbers for the Raman shift. Raman spectroscopy has often been applied for the purity evaluation in studying the quality of CNTs.

2.5 Reagents and Equipment

2.5.1 Reagents

The materials and chemicals used in experiments are detailed in Table 2.1. Also included are their abbreviation, suppliers and analytical grades.

Table 2.1 Reagent list

Reagents	**Abbreviation**	**Supplier**	**Grade**
Acetic acid	AA	Aldrich	≥99%
Acetone		Fisher Scientific	99.5%
Anthraquinone-1-diazonium chloride		Sigma	
Anthraquinone	AQ		
Boric acid		Sigma Aldrich	99.5%
Britton-Robinson	BR		
Chromium	Cr	Kuer J. Lesker	99.9%

1,2-Dihydroxybenzene (Catechol)		Aldrich	99%
Chitosan (Low Molecular Weight)		Aldrich	~ 85% degree of deacetylation
Cobalt(II) Acetate Tetrahydrate		Sigma	≥97%
D-glucosamine hydrochloride		Aldrich	99%
D-Glucose		Sigma	≥99.5%
Ferrocene carboxylic acid	FCA	Sigma-Aldrich	97%
Gold	Au	Advent Materials	99.99%
Hydrochloric acid	HCl	Sigma	32%
L-Cystiene		Sigma-Aldrich	≥98.5%
Monopotassium phosphate		Sigma-Aldrich	≥99%
Nickel(II) Acetate Tetrahydrate		Merck	≥99%
Phenyl-C61-butyric acid methyl ester	PCBM		
Phosphoric acid		Fisher Scientific	85%
Platinum on graphitized carbon	Pt/C	Sigma-Aldrich	20 wt% loading
Potassium chloride	KCl	Fisher Scientific	Analytical
Potassium ferrocyanide		Sigma	≥98.5%
Poly(Dimethylsiloxane)	PDMS	Premier Farnell	
Polyvinylidene fluoride	PVDF	Sigma	
Sodium Molybdate Dihydrate		Merck	≥99.5%
Sulfric acid	H_2SO_4	BDH	95%
Thioacetamide	TAA	Sigma	≥99.5%

- Chitosan solutions of 10 g/L were prepared by hydrating the polymer in 0.1 M Acetic Acid (reagent plus, >=99%, Aldrich). The solution was continuously stirred by a magnetic bar for 6 h. Concentrated D-glucosamine hydrochloride solutions (10 mM) were also prepared before the voltammetric measurements. The chitosan or D-glucosamine solution was then diluted to the desired concentration in the buffer solution with certain concentration of catechol.
- Buffer solutions for different pH values in Chapter 3 were prepared using several recipes: 0.05 M monopotassium phosphate/dipotassium phosphate for pH 7 and pH 8, 0.2 M sodium carbonate/bicarbonate for pH 9.2. All pH buffers were measured by using a pH meter (MeterLab PHM 220, Radiometer).
- Britton-Robinson buffer was prepared with 0.04 M boric, phosphoric and acetic acids, and it is adjusted by successive addition of KOH solutions to achieve pH values of 2 to 12.
- All solutions for measurement were made with 0.5 M KCl as the supporting electrolyte other than specified.
- All experiments were carried out in a solution volume of 50 mL and at ambient temperature of 293 ± 2 K.

2.5.2 Equipment

Equipment employed in the experiments are listed in Table 2.2, including the characterisation and fabrication apparatus.

Table 2.2 Equipment list

Apparatus	**Supplier**	**Model**
Alternating Current Voltammetric Potentiostat	Alan Bond Group in Monash University	Home-built
BET Surface Area Analyzers	Quantachrome	NOVA-3000 system
Energy-dispersive X-ray spectroscopy analyser	Oxford INCA	
Gas chromatography	Shimadzu	GC-2010

Glassy carbon macro-electrode	BAS Technical	Kel_F, 0.07 cm^2
Glassy carbon macro-electrode	ALS	PEEK, 0.07 cm^2
High-resolution transmission electron microscopy	JEOL	JEM 2100F
Packed bed flow reactor		
pH meter	Radiometer	MeterLab PHM 220
Potentiostat	Metrohm	PGSTAT 101
Powder X-ray Diffractometers	Bruker	Bruker D8 Advance
Rheometer	Bohlin Instruments	Bohlin C-VOR
Saturated calomel electrode	Radiometer	
Scanning electron microscopy	JEOL	JEOL-6700F
Silver/silver chloride electrode	BASi	
Silicon wafer	Mi-Net Technology	4”
Surface analysis spectrometer (XPS)	Kratos Analytical	AXIS-HSi
Thermal evaporator	Edward	E306 Belljar

Chapter 3 **Electrochemically Initiated Cross Linking of Chitosan**

Abstract

This chapter investigated the electrode mechanism of catechol oxidation and subsequent polymerisation through corsslinking with D-glucosamine or chitosan. It is discovered that a gel can be formed on the electrode surface during the process, which affects the solution viscosity and thus affects the mass transport processes. Several electrochemical techniques have been adopted to examine the electrode reactions, including CV and SWV. FTACV has also been attempted to extra more information from the system.

3.1 Introduction

Chitosan is a natural product and most important derivative of chitin. It is also a biocompatible and biodegradable polymer with enormous possibilities for chemical and mechanical modification to generate novel properties and functions. In recent decades, the popularity of research on functional biomaterials has led to the advancement in health science such as new drug delivery system and exceptional regenerative medicine.[87] Chitosan is known as a biomaterial for its biocompatibility, biodegradability and non-toxic properties. Thus it has been seen as a material with great potential for future development in various scientific areas. It is suggested that chitosan based materials exhibit excellent physical and chemical properties such as high surface area, tensile strength, porosity, conductivity and increased mechanical properties.[87] Modification of chitosan can be achieved through many methods.[88] The most common methods include physical modification (blending) and chemical modification (graft co-polymerization and curing). Blend is the simplest and easiest method to modify polymers that it mixes at least two polymers to generate a new material with different properties.

Nevertheless, in graft co-polymerization, one polymer is covalently bonded to another polymer chain. Enzymatic modification of chitosan is another attractive approach to researchers due to the specificity and low environmental impact. There are also different forms of chitosan based materials, including nanoparticles, microspheres, and hydrogels. Hydrogels are polymer networks that incorporate hydrophilic chains. The formation of hydrogel by chemical modification of chitosan is described in this work.

In this chapter, the electrochemical oxidation of catechol has been studied in the presence of D-glucosamine and chitosan using various electrochemical techniques such as CV, SWV and FTACV. The reaction is studied at various scan rates and different concentrations of D-glucosamine and chitosan. The results indicate that the reaction system between catechol and D-glucosamine follows an EC mechanism, with thin film product being produced on the electrode surface. Accordingly, the reaction of chitosan and catechol was studied to develop a means of crosslinking the chitosan to form polymer based gels.

3.2 Crosslinking and Hydrogel

The development of redox active, water permeable structures have wide applications in fuel cells,[89] sensors,[90], [91] and energy conversion.[92] Hydrogels containing redox active centres either trapped or bound within a polymer network are known as redox hydrogels.[93] In such systems the hydrogels once hydrated allows for the transport of chemicals and biochemicals, whilst the redox active centres allow the conduction of electrons by self-exchange of electrons or holes between rapidly reduced and rapidly oxidized redox functions.

The ideal redox centres, should allow fast electron transfer through the polymeric structure, providing fast heterogeneous kinetic as is evident by the redox couples chosen to date (quinoid functions,[94] ferrocene[95] and osmium$^{2+/3+}$[96]). These centres are usually chemically bound within the polymer network and often involve not only single redox active centres, but also polymeric based redox couples. These include, polyaniline,[97] polypyrrole[98] and polyhydroquinone[99] structures, each of which undergo two electron proton transfers per monomer base unit.

As shown in Figure 3.1a, chitosan is a linear polysaccharide composed of randomly distributed β-(1-4)-linked D-glucosamine and N-acetyl-D-glucosamine units. It can be produced by the exhaustive deacetylation of chitin (> 60%) commercially. Chitin (Figure 3.1b) is a structural element in the exoskeleton of crustaceans and insects, and it accounts for the second most abundant natural biopolymer after cellulose.[100], [101] Protective shells of crabs and shrimp are the most easily exploited sources of chitin. Under acidic conditions, the primary aliphatic amines of chitosan can be protonated (amine pKa of 6.3).[102]

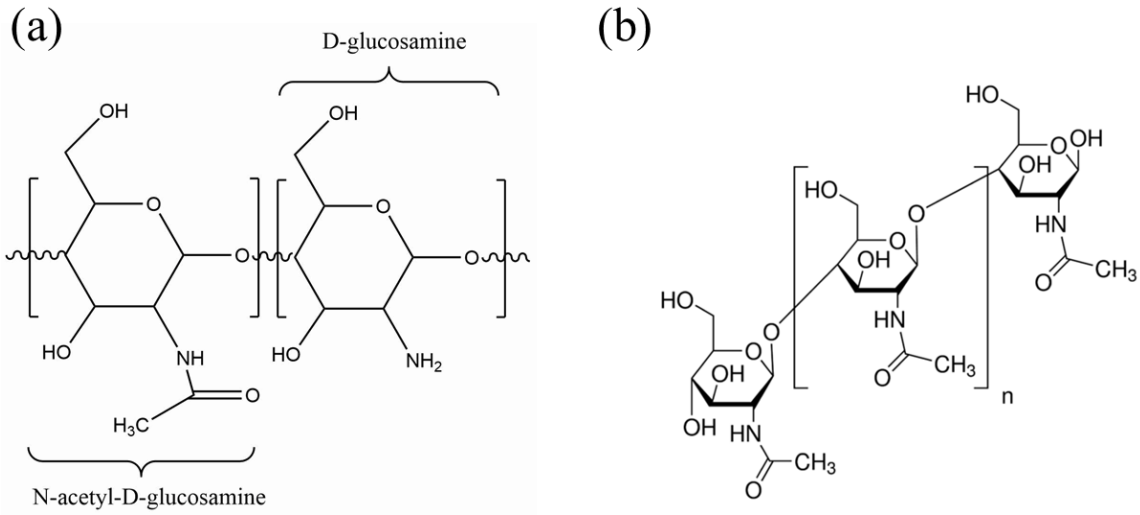

Figure 3.1 (a). Chemical structure of chitosan, with its monomers labelled. (b). Chemical structure of chitin.

The use of chitosan in gel systems is extremely attractive due to its biocompatibility and biodegradability. This has meant it has found numerous biomedical applications including gene delivery,[103], [104] tissue engineering,[105] drug delivery[106] and wound dressings.[107] There have been several papers published on developing chitosan based hydrogels using a variety of techniques such as physical crosslinking methods by reversible physical interactions in poly(N-isopropyl-acrylamide) or poly(ethylene oxide) grafted chitosan derivatives.[108], [109] Chemically crosslinked hydrogels have also been prepared by redox-initiated [110], [111] and photo-initiated crosslinking.[112], [113]

Chitosan has been used as template to develop redox hydrogels, through the acidic polymerization of polyhydroquinone (PHQ). As the PHQ undergoes polymerization it forms

hydrogen bonds within the chitosan structure, thus increasing the viscosity of the polymer structure and producing the hydrogel.[114] This has shown applicability for biomedical applications. Hydroquinone based systems have been shown when oxidized to the quinone species to undergo chemical reactions with amine moieties, this phenomena has been demonstrated through the electrochemical oxidation of catechol in the presence of chitosan. It was shown that oxidation of the catechol species on a gold electrode produced a hydrogel on the surface of the electrode when in the presence of chitosan.[115] Such covalently bound redox active centers could therefore have significant advantages over the purely hydrogen bonded interactions demonstrated previously. It has also been reported that attachment of catechol onto chitosan could form gels in acidic medium through the presence of coordinative crosslinkers (Fe^{3+} and Cu^{2+}) or oxidant (sodium periodate, $NaIO_4$).[116] In addition, the means of triggering and controlling the gelation process allows the resulting gels properties to be tailored to the application. Chitosan has been reported to remain in solution up to a pH of 6.2 and to form a hydrated gel-like precipitate above this value. This has some limitations on the crosslinking reaction, as for the Schiff-base reaction to occur, the amine group should be deprotonated, indeed when the reaction mixture was at pH 3, no crosslinking was observed, due to the protonation of the amine groups inhibiting the reaction.[117] As the pH of the solution was raised to pH 5, the crosslinking reaction was found to occur and gel formation observed.

In the following the electrochemical oxidation of catechol in the presence of the chitosan base unit glucosamine is first studied under various conditions to understand and optimise the reaction process after which the bulk electrolysis of catechol is in the presence of chitosan is demonstrated. Catechol has been found in varies natural molecules, and they serve many functions such as a reagent for photography, rubber and plastic production and in the pharmaceutical industry.[118] Catechol oxidation can be catalysed by heavy metals[119] and several enzymes such as the copper-containing fungal laccase and superoxide dismutase.[120] Catechol oxidation is pH dependant since electrons are removed from catechol which induce the loss of protons.[121] The likely transition state and redox mechanism for catechol oxidation have been established, which is known as the ‘scheme of squares’ model (Scheme 3.1).[121] Catechol oxidase (o-quinone) is likely to be attacked by hydroxide ions in relatively alkaline

solutions, which undergoes a 1,4-Michael addition reaction to form 1,2,4-trihydroxybenzene.[122]–[124]

Scheme 3.1 'Scheme of Squares' for Catechol Oxidation. (Reproduced from reference[121])

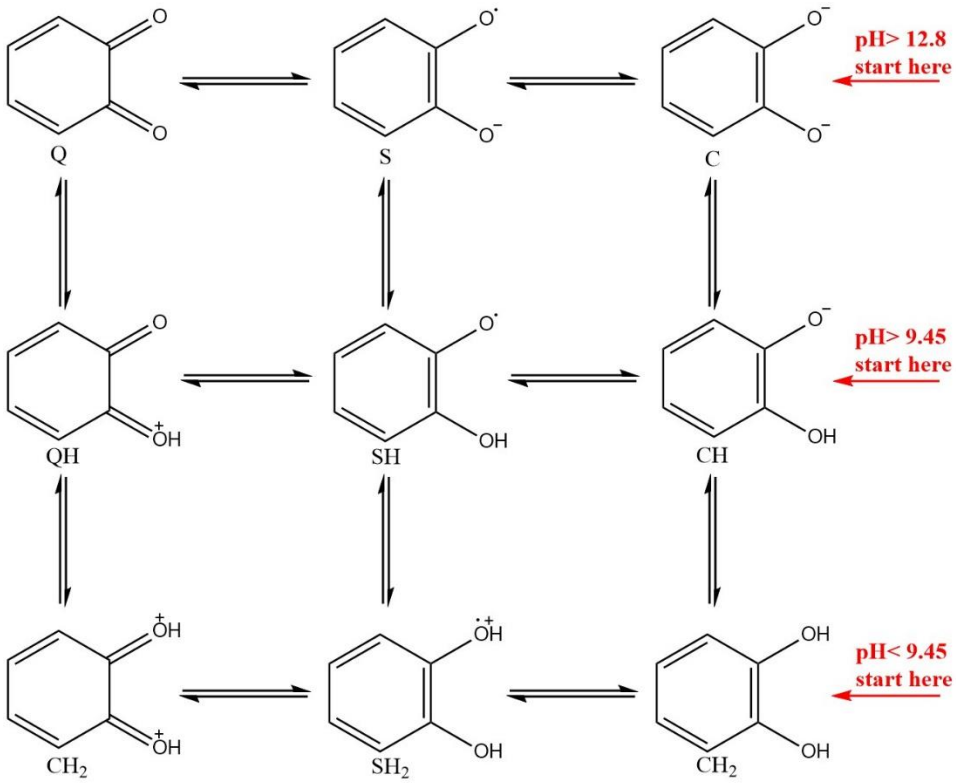

The determination of catechol has been extensively investigated by electrochemical detection on both metal and carbon electrode.[125]–[128] Typical electrode materials are required to be conductive and chemically inert, which provide stable interfaces for electron transfer. However, these electrodes are incapable to participate in complex reaction pathways such as Proton Coupled Electron Transfer (PCET) reactions. Drawbacks of these electrodes in PCET includes slow reaction, large over-voltages, and electrochemical irreversibility.[1], [129] Several activation processes have been developed for GCE, including plasma treatments in an oxygen environment, chemical or electrochemical oxidation, and addition of adsorbed catechol containing functionalities.[130], [131] Surface activation of the carbon electrode can impact the electrochemical oxidation of catechol; higher extent of surface activation enables cyclic voltammetry wave becoming more reversible.[132] It has been shown that the peak potential separation in the cyclic voltammogram can be significantly reduced by modifying GCE with

alumina slurries and graphene nano-platelets.[121], [133] Hypothesis suggests that alumina provides adsorption sites and graphene allows an alternative catechol oxidation pathway.[133] In addition, catechol oxidation is unchanged thermodynamically when studied at an alumina modified GCE.[121]

3.3 Experimental

3.3.1 Instruments

Cyclic and square wave voltammetric measurements were recorded using an Autolab Potentiostat PGSTAT 101 (Metrohm, The Netherlands) with a standard three electrode configuration. Fourier Transformed Large Amplitude ac Voltammetry (FTACV) characterisations were conducted using a homemade potentiastat. A glassy carbon macro-electrode (GCE, 0.07 cm^2, BAS Technicol, UK) was adopted as the working electrode. A platinum electrode was used as the counter electrode with a saturated calomel electrode (SCE, Radiometer) or a silver/silver chloride (Ag/AgCl, BASi, USA) provided the reference electrode. Before and between each voltammetric measurement, the GCE was polished by using alumina slurries of 1.0, 0.3 and 0.05 μm particle size and rinsed with deionised water (If not specifically stated). The method to polish the GCE was 60 repeated cycles of figure of eight. The approach to alter the concentration of chitosan or D-glucosamine is by addition of high concentrated solutions of corresponding chemicals into the catechol solution. The solution was mixed by a magnetic stirrer (300 rpm for 2 min) to ensure uniform chemical distribution after the addition.

For experiment data obtained from FTACV, Fourier transform (FT) technique was adopted to convert the time domain raw data into the frequency domain power spectrum. Then a series of current data was generated through the usage of an inverse FT algorithm as a function of time for the power spectrum. Although there are different expressions of the raw data, the current formats are chosen based on a previous research.[134]

Rheological measurements were performed in dynamic mode, on a Bohlin C-VOR rheometer (Bohlin Instruments) using a C14 concentric cylinder requiring 2 mL of solution. All oscillatory measurements were made within the linear viscoelastic region (LVER), so that G’

and G'' were independent of strain amplitude. The LVER was determined via an amplitude test, in which the amplitude was varied from 0.01 to 1. Measurements of G' and G'' were made with a constant-strain frequency test within a frequency-range 0.3-30 Hz. Measurements at 1 Hz were made as a function of time to assess the extent and rate of gelation. The error on a rheological measurement was estimated on a 0.5 wt% Low molecular weight chitosan preparation and yield 2.5 % and 5.6 % error for G' and G'' respectively.

3.3.2 Reaction Schemes

Scheme 3.2 a) Catechol oxidation; b) Catechol oxidise and d-glucosamine; c) Subsequent reaction.

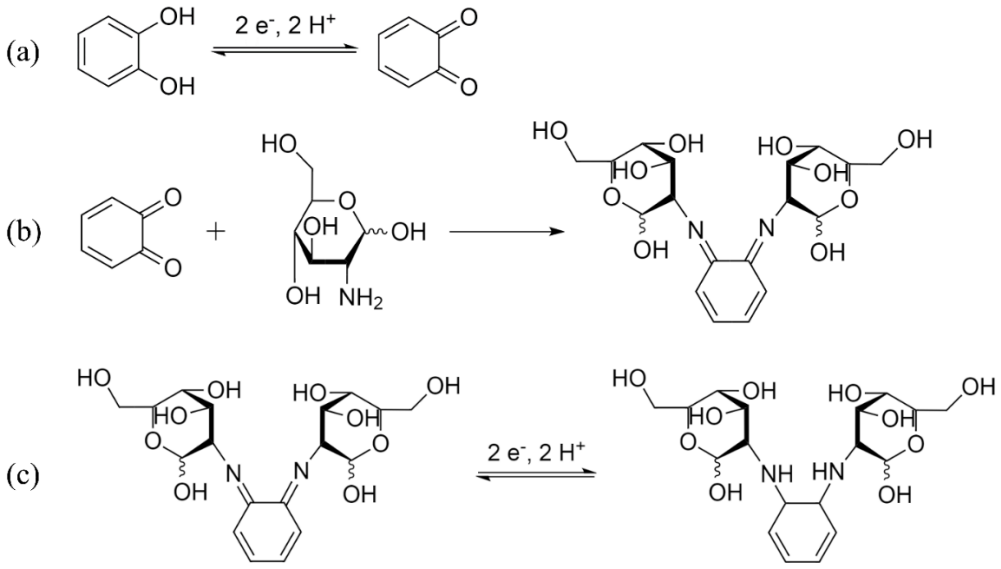

The electrode reaction mechanism of the catechol and D-glucosamine system is shown in Scheme 3.2. It is an EC Mechanism in which the product of the redox reaction turns into a final redox-inactive product by an irreversible chemical reaction.[135], [136] The subsequent reaction in Scheme 3.2(c) is proposed to explain a new reductive peak, which will be discussed in the result section. The catechol oxidation is a PCET with 2 electrons and 2 protons being transferred. The acidity dissociation constants (pKa) for catechol are $pK_a(1)$, 9.25 and $pK_a(2)$, 13.0.[137] In the case of for the catechol and chitosan system, it involves an electron transfer reaction (catechol oxidation) followed by an irreversible chemical reaction (Polymerisation).

Scheme 3.3 Two-proton, two-electron oxidation of catechol, and subsequent polymerisation between catechol oxidise and chitosan.

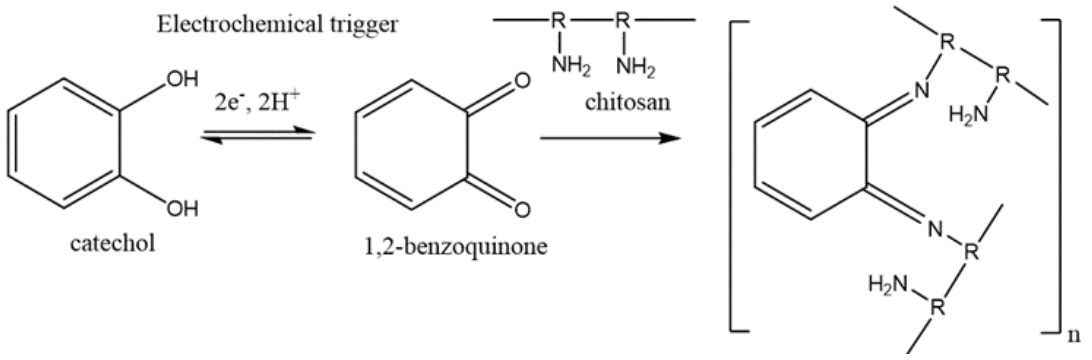

It has been demonstrated that surface activation of the carbon electrode can impact the electrochemical oxidation of catechol; increased activation enables faster electrode kinetics of the catechol redox couple.[132] In this study, alumina activated glassy carbon electrodes[133] is used as the working electrode to examines the EC mechanism of D-glucosamine and chitosan.

3.4 Results and Discussion

This section discusses the results of the experiments under various conditions. Catechol oxidation was first been investigated on glassy carbon electrode with and without alumina polishing by using cyclic voltammetry (CV). Then the catechol oxidation with subsequent reaction (D-glucosamine or chitosan) has been further studied to examine the mechanism of generating hydrogel. After that, other voltammetric methods such as Square Wave Voltammetry (SWV) and Fourier Transformed Large Amplitude ac Voltammetry (FTACV) have been conducted to analyse catechol crosslinking.

3.4.1 Catechol Oxidation

An initial investigation of the catechol oxidation has been studied by CV on glassy carbon electrode without alumina polishing. The aqueous solution (1 mM catechol, 0.5 M KCl, pH4 buffer solution) was prepared as the electrolyte, and it was characterised with a 3mm diameter glassy carbon electrode at different scan rate (0.01 V/s to 0.1 V/s). Figure 3.2a shows the

resulting voltammogram of the system. The redox peak potentials remain unchanged as the scan rate varies. A value of 0.456 V (*vs.* SCE) has been found for the oxidative peak potential, and 0.135 V (*vs.* SCE) for the reductive peak potential. Then the difference in the two values calculated as a significantly large peak potential gap (ΔE_p = 0.321 V) for the system. In addition, both oxidative and reductive peak currents have been plotted as a function of the square root of the scan rate. Two well linear fitted curves have been found. These findings indicate that catechol oxidation under these conditions shows a quasi-reversible process.

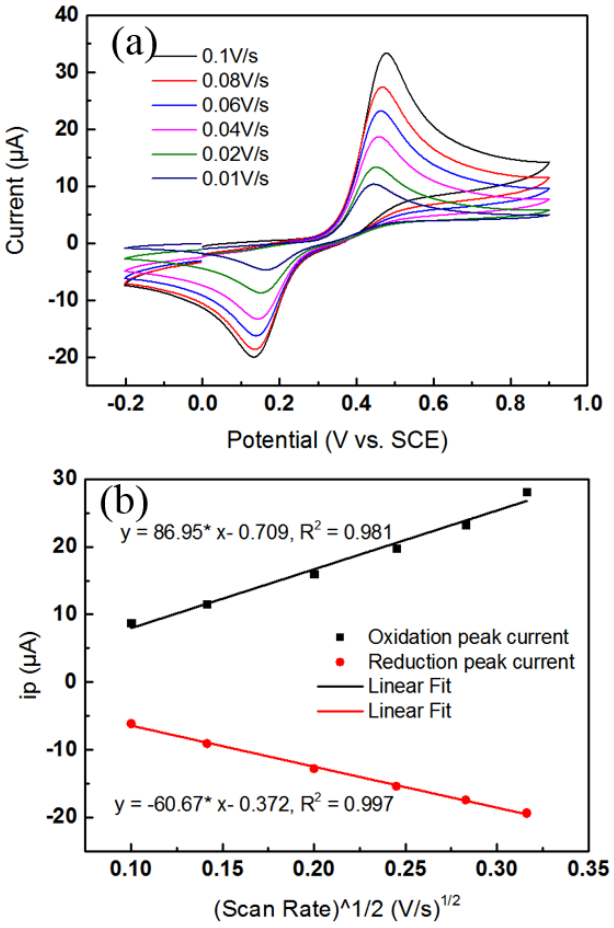

Figure 3.2 Cyclic voltammograms of 1 mM catechol and 0.5 M KCl in pH 4 buffer solutions recorded on a GCE without alumina polishing at scan rate range of 0.01 V/s to 0.1 V/s.

Next, in the light of literature observations and suggestions of possible 'catalysis',[138], [139] the effect of surface modification with alumina onto the glassy carbon was inspected. The method of obtaining an alumina modified surface has been described in the experimental

section. Figure 3.3 shows the cyclic voltammetry of 1 mM catechol in pH 4.0 solution recorded on an unpolished GCE (black) in comparison with that on a polished GCE (red) at a scan rate of 0.05 V/s. The two curves show that ΔE_p is reduced from ca. 0.32 V *vs.* SCE to ca. 0.13 V *vs.* SCE, and the E_{mid} remains at ca. 0.3 V *vs.* SCE. Consequently, it can be concluded that the reaction mechanism has been altered significantly. A possible reason of the catalysis phenomenon of the catechol oxidation has been proposed by a literature discussion.[121] In principle, proton accepting oxide groups may presented on the surface alumina, which allow the process to progress rapidly without the formation of a semiquinone species. The electrons and protons may be transferred to and from the catechol adsorbed on the alumina rather than the electrode surface. A triple boundary among the electrode surface, the solution and the alumina particle is required for this process to occur.

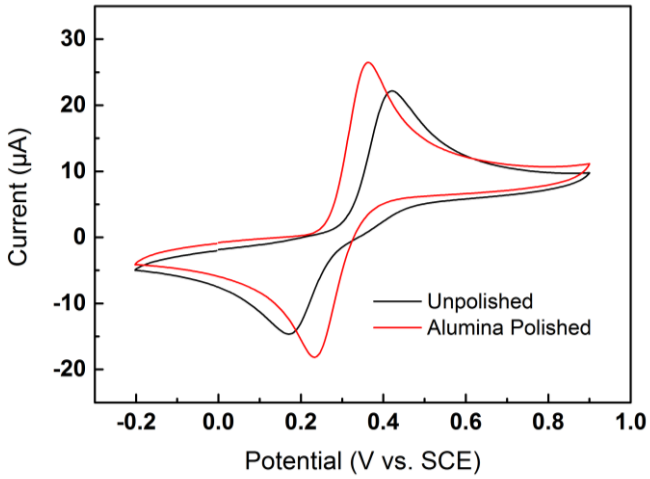

Figure 3.3 Comparison of cyclic voltammograms measured on an unpolished (black) and alumina polished (red) glassy carbon electrode, of 1 mM catechol and 0.5 M KCl in pH 4.0 buffered solution. Scan rate = 0.05 V/s.

Scheme 3.4 Schematic drawing of the three-phase boundary formed between the glassy carbon electrode, alumina particles, and the solution.[121]

This Figure is not shown due to copyright issues

As a consequence, glassy carbon electrodes used in later sections have all been modified with alumina to decrease the peak potential separation.

3.4.2 Catechol and D-glucosamine

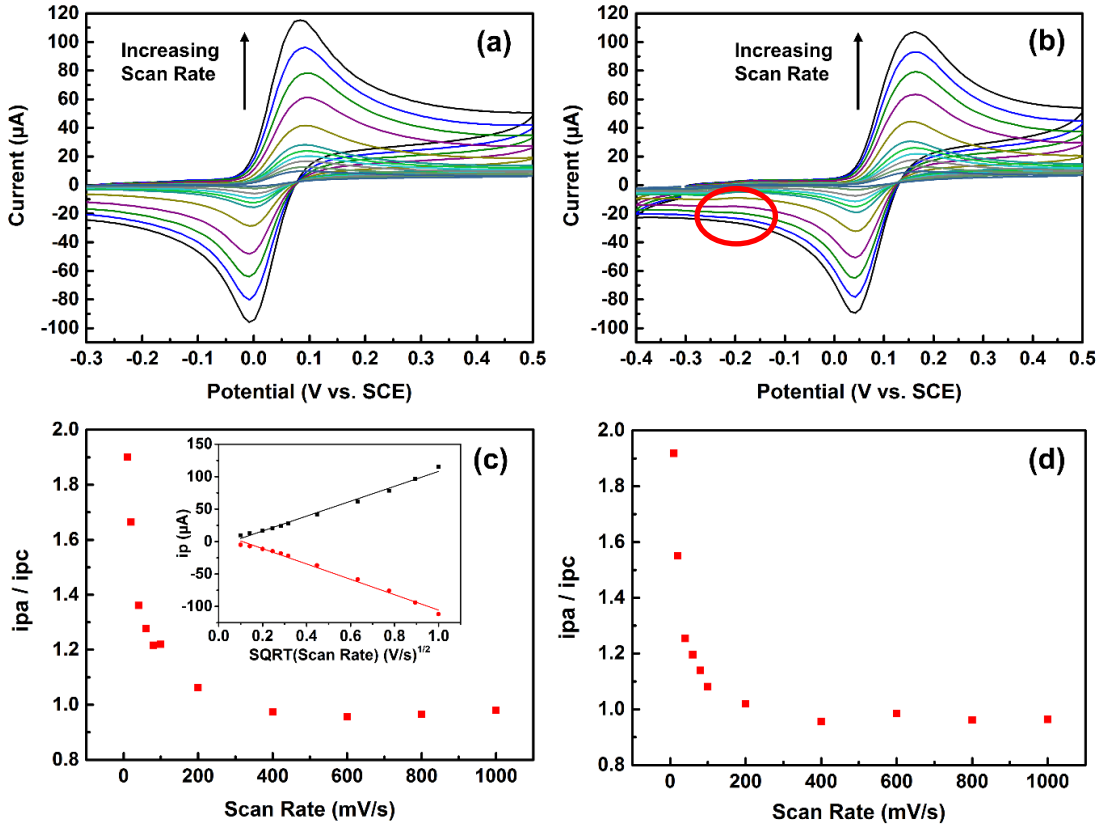

Figure 3.4 Cyclic voltammograms of 1 mM catechol and 0.5 M KCl in 0.2 M Na_2CO_3/$NaHCO_3$ pH 9.2 buffer solutions recorded on a GCE at scan rate range of 0.01 V/s to 1 V/s. a) in the absence; b) in the presence of 10 mM D-glucosamine; c), d) Variation of peak current ratio (i_{pa} /i_{pc}) versus *v* for (a), (b), respectively. Inset in (c): Peak current *vs.* SQRT(Scan Rate) for (a).

The characterization of the electrochemical response of catechol was carried out in pH 9.2, 0.2 M Na_2CO_3/$NaHCO_3$ buffer. This pH was chosen based on initial experiment under different pH values and previous research on catechol oxidation at different pH values on GCE.[121], [140] Figure 3.4 indicates the cyclic voltammetric response at varying scan rates (0.01 V/s – 1 V/s) at a GCE in a solution consisting of 1mM catechol, 0.5 M KCl and pH 9 buffer in the absence (Figure 3.4a) and presence (Figure 3.4b) of 10 mM D-glucosamine. In each case well defined quasi reversible redox processes were observed. In the absence of D-glucosamine an oxidation peak at ca. + 0.09 V *vs.* SCE followed by a reduction peak at ca. -0.08 V *vs.* SCE was recorded, consistent with the two electrons and two protons oxidation/reduction of the catechol/o-quinone redox couple.[140] Figure 3.4c, shows at high scan rates, the peak current ratio (I_P^C/I_P^A) is nearly unity, lowering the scan rate lowers the ratio from unity, indicating the reversibility increases as scan rate increases, consistent with previous reports.[140] At lower scan rates, as the peak current ratio (I_P^C/I_P^A) decreases these changes can be related to the coupling of the anodic or dianionic forms of catechol with *o*-quinone (dimerization reaction).[141] It has also been reported that increasing pH values will also contribute to the occurrence of dimerization reaction.[140], [142] Literature also shows that the reductive peak of catechol oxidation at a GCE is gradually reduced as the pH increases from 1 to 14.[121], [140] This is due to be the result of nucleophilic attack of 1,2- benzoquinone by the hydroxide ions via a 1,4-Michael addition reaction in alkaline solutions.[122]–[124], [143]

To verify a diffusion controlled reaction it was found that the catechol oxidation current increased linearly with the square root of scan rate over the 0.01- 1 V/s range (regression data for inset in Figure 3.4c: oxidative current (μA) = 108.46 (square root scan rate ($V^{1/2}$ $s^{-1/2}$)) – 4.83, $R^2 = 0.993$).

Figure 3.4b details the electrochemical response of 1 mM catechol and 10 mM D-glucosamine at various scan rates. When comparing the data in Figure 3.4a and Figure 3.4b, it shows the voltammograms in Figure 3.4b shift to more positive values, oxidative wave at ca. 0.163V *vs.* SCE and reductive wave at ca. 0.042 V *vs.* SCE. Furthermore, the ratio of I_P^C/I_P^A is lower in the presence of glucosamine at lower scan rates (<0.4 Vs^{-1}) compared to the absence at each of the scan rates studied (Figure 3.4d). The shift in redox potential suggests a new product has been formed, which might be due to the pre-equilibrium. Additionally, a new reduction wave

is observed in Figure 3.4b at -0.26V *vs.* SCE consistent with further follow up reactions of glucosamine with the glucosamine catechol species as shown in Scheme 3.2. [1]

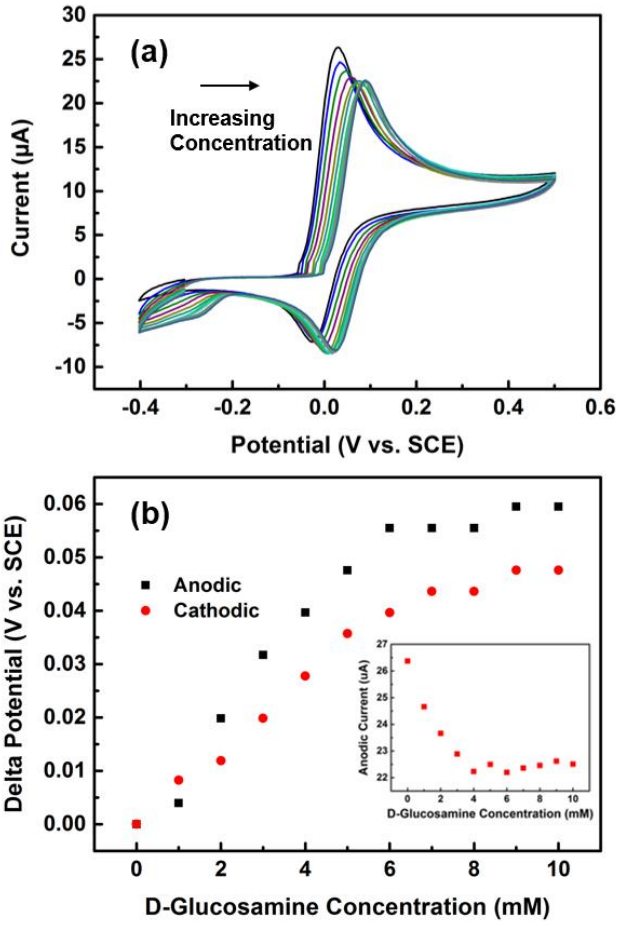

Figure 3.5 a) Cyclic voltammograms of 0 mM to 10 mM D-glucosamine in 1 mM catechol and 0.5 M KCl recorded on a GCE at at a scan rate of 50 mV s^{-1} and potential range of -0.4 to +0.5 V *vs.* SCE, in 0.2 M Na_2CO_3/$NaHCO_3$ pH 9.2 buffer solutions; b) Change of peak potential against D-glucosamine concentration in (a).

To validate the mechanism shown in Scheme 3.1, experiments involving stepwise additions of glucosamine to a catechol solution were conducted. Figure 3.5a details the electrochemical response of 1 mM catechol over 0 mM – 10 mM D-glucosamine at pH 9.2 buffer was recorded by utilising a GCE. The GCE was polished by using alumina slurries before each voltammetric scans to ensure no electrode fouling occurred. In the absence D-glucosamine voltammogram, one anodic peak is observed at 0.03 V *vs.* SCE. On the reverse scan, a cathodic peak appeared

at -0.03 V *vs.* SCE. The slight differences in the redox potential observed between Figure 3.4 and Figure 3.5 are consistent with difference in the modification of the electrode surface with alumina, however they do not impact the chemical reaction of glucosamine with oxidised catechol. As glucosamine is introduced to the solution, the oxidative wave decreases and shifts to higher potentials, whilst the reductive wave increases and shifts to higher potentials, at higher concentrations the oxidative peak current increases. Figure 3.5b details the variation of redox potential with glucosamine concentration, as the concentration increases the redox potential plateaus to a constant value. In addition, a new reductive wave emerges at -0.26V *vs.* SCE consistent with the data presented in Figure 3.4. The newly emerged reductive peak also increases as the D-glucosamine concentration increases, which indicates more product has been formed from the chemical step as proposed in Scheme 3.2c.

The addition of D-glucosamine concentration increases the rate of reduction and causes peak potential moves to a more positive value, which can be attributed to the formation of the catechol glucosamine adduct. This phenomenon is consistent with the theory as described below:

For an E_rC_i reaction case (a reversible electrode reaction followed by an irreversible chemical reaction), the electrode potential is given by the Nernst equation:

$$\mathrm{E} = E^0 + \frac{RT}{nF} ln \frac{C_O(x=0)}{C_R(x=0)} \tag{3.1}$$

Where $C_O(x=0)/\ C_R(x=0)$ is the concentration ratio between oxidant and reductant at the electrode surface and is determined by the experimental conditions. The chemical reaction will decrease $C_R(x=0)$, which then increases $C_O(x=0)/\ C_R(x=0)$. As a consequence, the electrode potential will become more positive than in the absence of the chemical reaction at any current level. The voltammetric wave will also shift toward more positive potentials.

Finally, the electrochemical responses of catechol and D-glucosamine reaction under different pH values was then examined. This was carried out using cyclic voltammetry in a solution consisting of 1 mM catechol, with or without 10 mM D-glucosamine. As can be seen from Figure 3.6a, b, c, as the pH is increased the voltammograms shift to more positive values for

the 10 mM D-glucosamine curve, compared to the 0 mM curve. Furthermore, the new redox wave observed at low redox potentials (ca. -0.192 V *vs.* SCE at pH 7) shifts to negative potentials as the pH is increased. Table 3.1 details the trend with pH for the first (cathodic 1) and second (cathodic 2). It can clearly see as the pH is increased the species undergoes a pKa change as noted by the change in slope. In addition, it appears the newly formed adduct at lower potentials has a higher number of protons transferred per electron compared to the product outlined in Scheme 3.2.

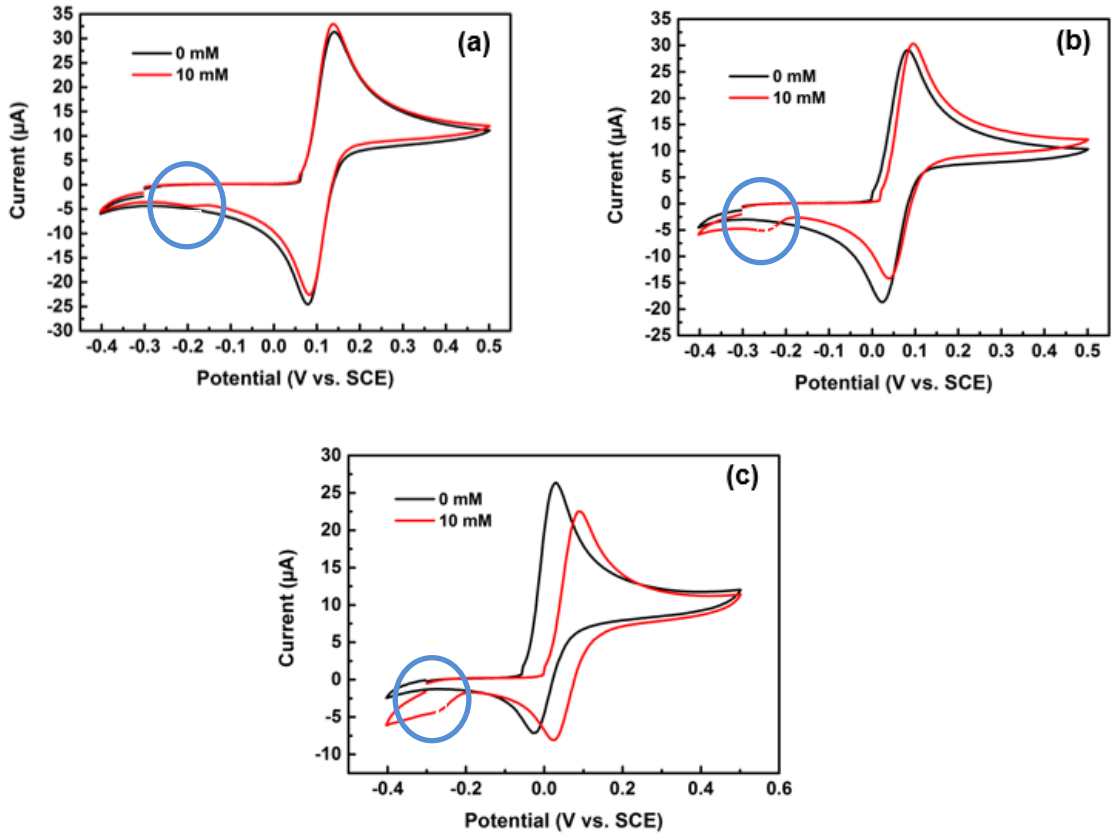

Figure 3.6 Cyclic voltammograms of 0 mM to 10 mM D-glucosamine in 1 mM catechol and 0.5 M KCl recorded on a GCE at a scan rate of 50 mV s^{-1}, in pH buffered solutions of a) KH_2PO_4/K_2HPO_4 pH 7 buffer; b) KH_2PO_4/K_2HPO_4 pH 8 buffer and c) $Na_2CO_3/NaHCO_3$ pH 9.2 buffer, with voltammogram at each D-glucosamine concentration labelled.

The results show that under various alkaline pH values the oxidation of catechol promotes the substitution reaction with glucosamine and with loss of water. As the pH increased the generation of a new redox active couple is observed at higher potential values, as detailed in

Scheme 3.2. In the following we understand the voltammetric response of catechol in the presence of chitosan and demonstrate through monitoring of the associated redox waves the polymerisation process can be monitored.

Table 3.1 Peal potential changes of 10 mM D-glucosamine addition in 1 mM catechol and 0.5 M KCL.

Peak potential change	pH7 to pH8	pH8 to pH9
Cathodic peak potential 1	39.7 mV	19.8 mV
Cathodic peak potential 2 (New Wave)	60 mV	40 mV

3.4.3 Catechol and Chitosan

Figure 3.7 indicates the cyclic voltammetric response in a 1 mM solution of catechol with increasing concentrations of chitosan measured at a scan rate of 50 mV s^{-1} using a GCE in pH 8 (Figure 3.7a) and pH 9.2 (Figure 3.7b) buffers. In the absence of chitosan, a redox process was observed, which is the two-electron and two-proton oxidation reduction of the catechol/o-quinone redox couple. Upon increasing additions of chitosan to the solution, the cyclic voltammogram shifts to positive potentials. From the analysis of anodic peak potential against chitosan concentration, it was shown that the peak potential shifts ca. 0.004 V *vs.* SCE per addition of 0.01 wt% of chitosan over the range 0 to 0.08% chitosan, above which a plateau is observed indicating the reaction has gone to completion.

Figure 3.7b illustrates the response at pH 9.2, the data obtained is consistent with those shown in Figure 3.5 for glucosamine, where the anodic peak current decreases as the chitosan concentration increases and gradually diminished as the chitosan concentration reaches ca. 0.04 wt%. The decreasing of the anodic peak current is likely to be caused by increased solution viscosity as the chitosan is crosslinked. As the chitosan concentration reaches 0.035 wt%, a second anodic current peak appears, which increases as the chitosan concentration continues

to raise. This new oxidation wave is likely to be related to the oxidation between o-quinone and amine functional group in chitosan, indicating the reaction has gone to completion. Figure 3.7c details the variation in potential for the catechol oxidation wave as a function of chitosan concentration. It can be clearly seen that at higher pH values the change in oxidation potential is larger than at the lower pH value, indicating that the reaction is faster at higher pH values.

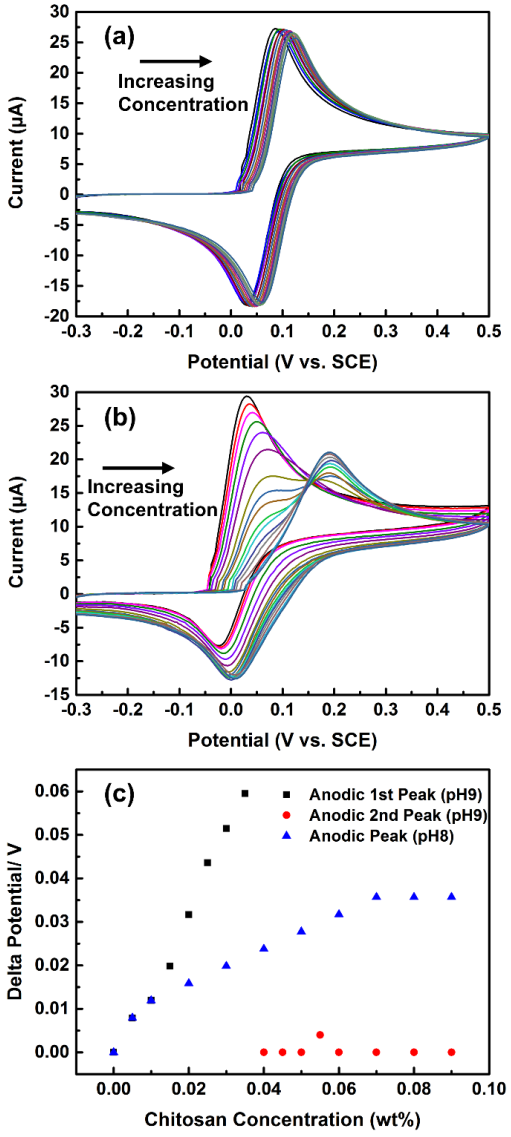

Figure 3.7 Cyclic voltammograms of 0 wt% to 0.09 wt% chitosan in 1 mM catechol and 0.5 M KCl recorded on a GCE at a scan rate of 50 mV s^{-1} and potential range of -0.3 to +0.5 V *vs.* SCE, in pH buffered solutions of (a) KH_2PO_4/K_2HPO_4 pH 8 buffer and (b) $Na_2CO_3/NaHCO_3$ pH 9.2 buffer; (c) Anodic peak potential against chitosan concentration at pH8 and pH9.2 buffer solutions.

Bulk electrolysis of the solution (catechol and chitosan) has been conducted and its rheological characteristic has also been studied to confirm the gel formation. An oxidative current of 20 mA was applied to all the solutions for 1 hour to obtain the gelling solutions. These solutions were left undisturbed at room temperature, for 48 h, before the oscillatory measurements were carried out. Table 3.2 indicates the values of G'/G" for solutions with varying chitosan concentration. The results show that all the solutions reveal rheological data in terms of the G'/G" values. This therefore confirms the generation of gel upon the crosslinking mechanism between catechol and chitosan. The ratio of G'/G" at 0.5 wt% chitosan is around 3.07, and found to be the maximum among other concentrations.

Table 3.2 Influence of the chitosan concentration on the ratio of G' to G'' for gelling solutions (0.2 M catechol).

Chitosan concentration (wt%)	**0.2**	**0.3**	**0.4**	**0.5**	**0.6**
***G'/G''* for CHI**	0.35 ± 0.03	2.23 ± 0.18	1.51 ± 0.12	**3.07 ± 0.25**	2.40 ± 0.19

3.4.4 Square Wave Voltammetry of Catechol and Chitosan

The electrochemical initiated crosslinking of catechol and chitosan is then further studied by SWV under different conditions. Catechol oxidation is first being examined without the addition of chitosan. Figure 3.8 shows the square wave voltammograms of 1 mM catechol and 0 wt% chitosan on GCE under various pH values and frequencies. Typical bell-shaped curves have been obtained for all conditions. In each pH values, the peak current increases as the frequency increases from 25 Hz to 75 Hz, while the peak potential stays at the same value. It can also be found that the peak potential shifts to more negative values as the solution pH increased from 4 to 13. This phenomenon is also shown in Figure 3.9a. Then a correlation between peak potential and pH is established, and a linear fitting is applied (Regression data in Figure 3.9b: Peak Potential (V) = -0.058 * pH – 4.83, R^2 = 0.993). A slope of 58mV per pH

unit has been found, which is close to the theoretical value of 59.2 mV per pH unit at 25 ˚C (according to the Nernst equation).

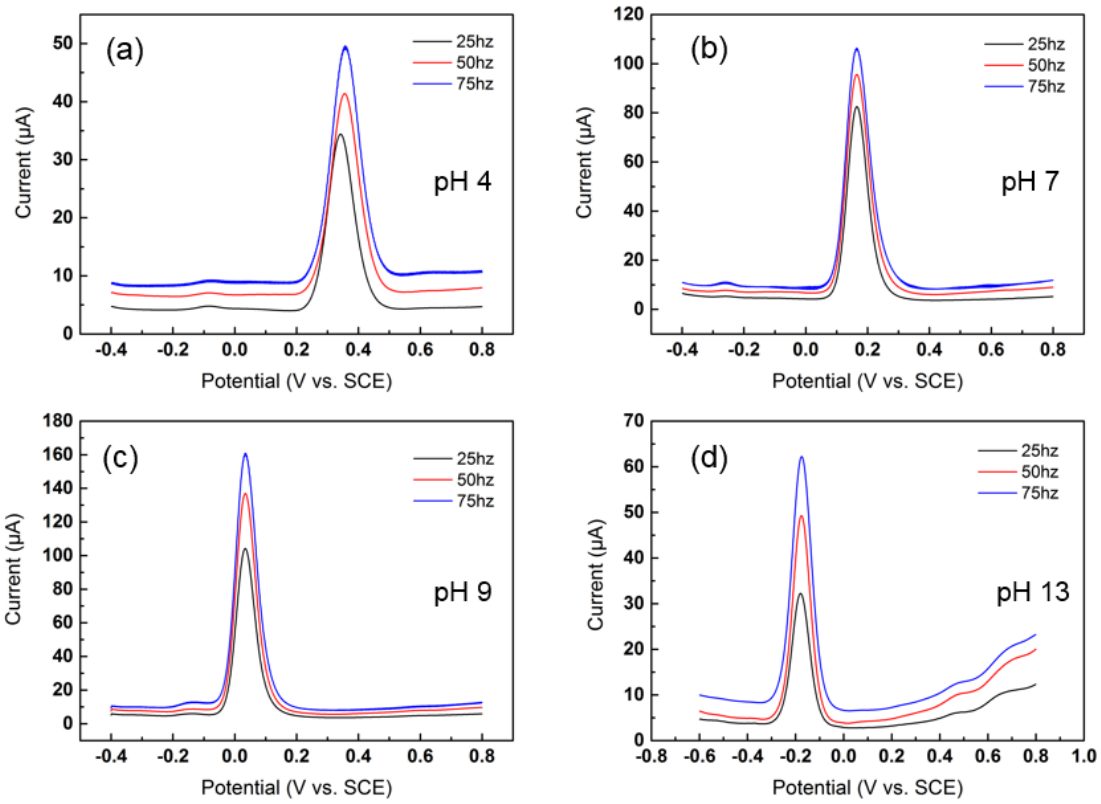

Figure 3.8 Square wave voltammograms of 1 mM catechol and 0 wt% chitosan in 0.5 M KCl recorded on a GCE in pH 4, pH 7, pH 9.2 and pH 13 buffer solutions with varying frequencies of 25 Hz, 50 Hz, 75 Hz.

Subsequently, 0.1 wt% chitosan is added into the electrolyte to examine the effect of chitosan onto catechol oxidation. Figure 3.10 illustrates the square wave voltammogram of catechol oxidation with and without 0.1 wt% chitosan in different pH values. In all pH values, the peak current decreased as the chitosan is added into the system. This can be rationalised by the change of viscosity of the solution. As have been discussed earlier, the polymerisation between catechol oxidise and chitosan leads to a crosslinking process. Hydrogel is formed during the process, which causes the solution viscosity increased. This then affects the diffusion of redox species to the electrode surface. Additionally, voltammogram at pH 9.2 (Figure 3.9c) exhibits an interesting phenomenon as the peak potential also shifts to a more positive position for the

0.1 wt% chitosan case. However, in other pHs, the peak potential position remains at a similar value. This shift can be related to the previous discussion on the formation of a new oxidative peak in the cyclic voltammogram.

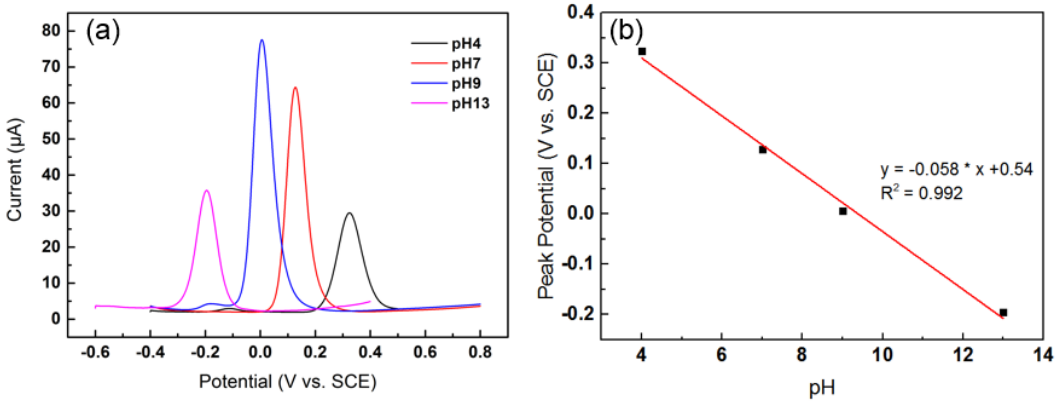

Figure 3.9 Square wave voltammograms of 1 mM catechol and 0 wt% chitosan in 0.5 M KCl recorded on a GCE with a frequency of 25 Hz in pH 4, pH 7, pH 9.2 and pH 13 buffered solutions.

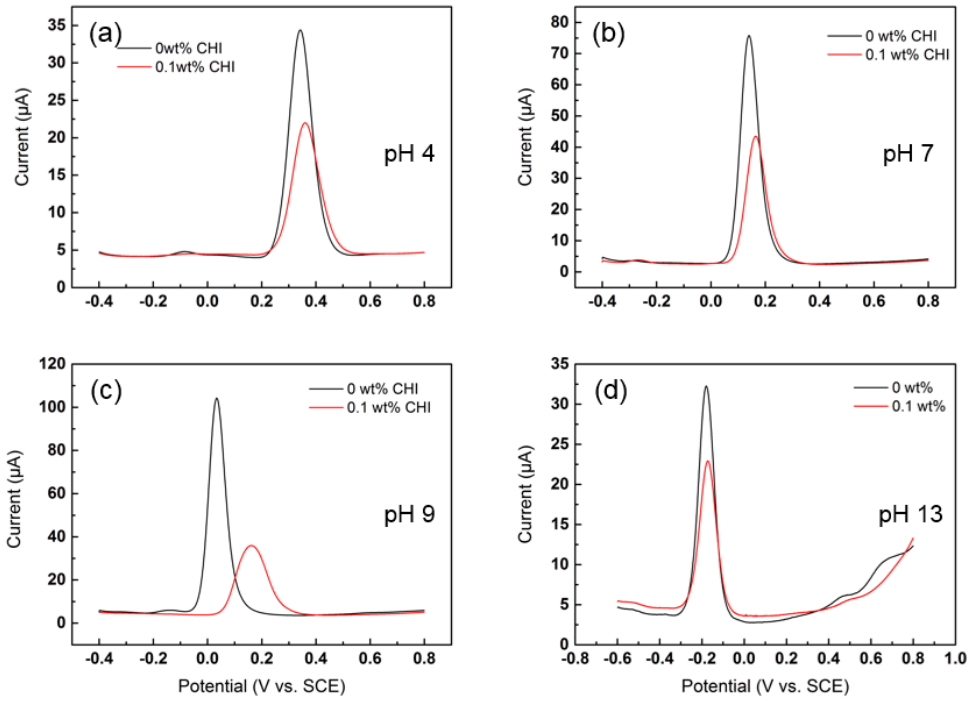

Figure 3.10 Square wave voltammograms of 1 mM catechol and 0 & 0.1 wt% chitosan in 0.5 M KCl recorded on a GCE with a frequency of 25 Hz in pH 4, pH 7, pH 9.2 and pH 13 buffered solutions.

In order to study the change of the new oxidative in SWV, chitosan concentration is varied between 0 wt% and 0.1 wt% with an increment of 0.01%. Figure 3.11 exhibits the square wave voltammogram of 1 mM catechol with varying chitosan concentration on a GCE in pH9.2 buffered solution. It is obvious that peak current also decreases as chitosan concentration arise, which is consistent with previous findings. Following a similar trend as in Figure 3.7b, the peak potential moves towards positive values as the chitosan concentration increases from 0.01 wt% to 0.06 wt%. As is shown in Figure 3.11b, after this value, the peak potential remains in the same position, which can be seen as a signal indicating the completion of the new oxidation wave between o-quinone and amine functional group in chitosan. As a consequence, the SWV response confirms the discussion on the CV results, proving this mechanism between catechol and chitosan can be used as an effective indicator of hydrogel forming process.

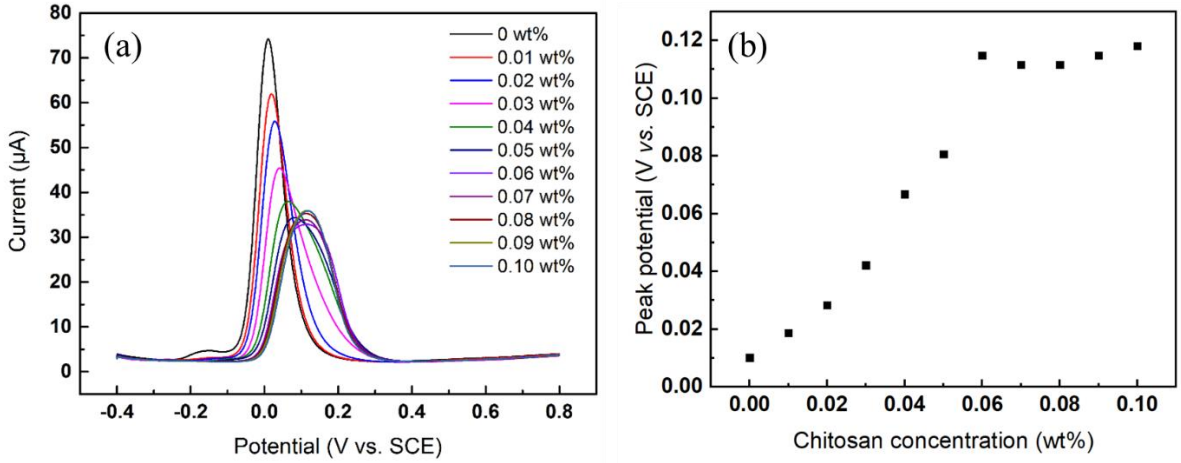

Figure 3.11 (a) Square wave voltammograms of 0 wt% to 0.1 wt% chitosan in 1 mM catechol and 0.5 M KCl in Na_2CO_3/$NaHCO_3$ pH 9.2 buffer solution recorded on a GCE. (b) Change of peak potential against chitosan concentration in (a).

3.4.5 Fourier Transformed Large Amplitude ac Voltammetry of Catechol and Chitosan

In this section, FTACV was utilised to further examine the catechol and chitosan system. To the best of our knowledge, this technique has not been applied in a chemical system with viscosity change, and this is the first FTACV study in this area. Under the condition of pH 9.2

buffer solution, the SWV results from last section indicates a similar phenomenon with the CV responses. Thus preliminary FTACV measurements were carried out at a GCE in pH 9.2 buffer solution with the following conditions: potential range of -0.3 to 0.5 V (*vs.* Ag/AgCl reference electrode), scan rate of 15 mV/s, frequency of 1 Hz and ac superimposition of ΔE=100 mV.

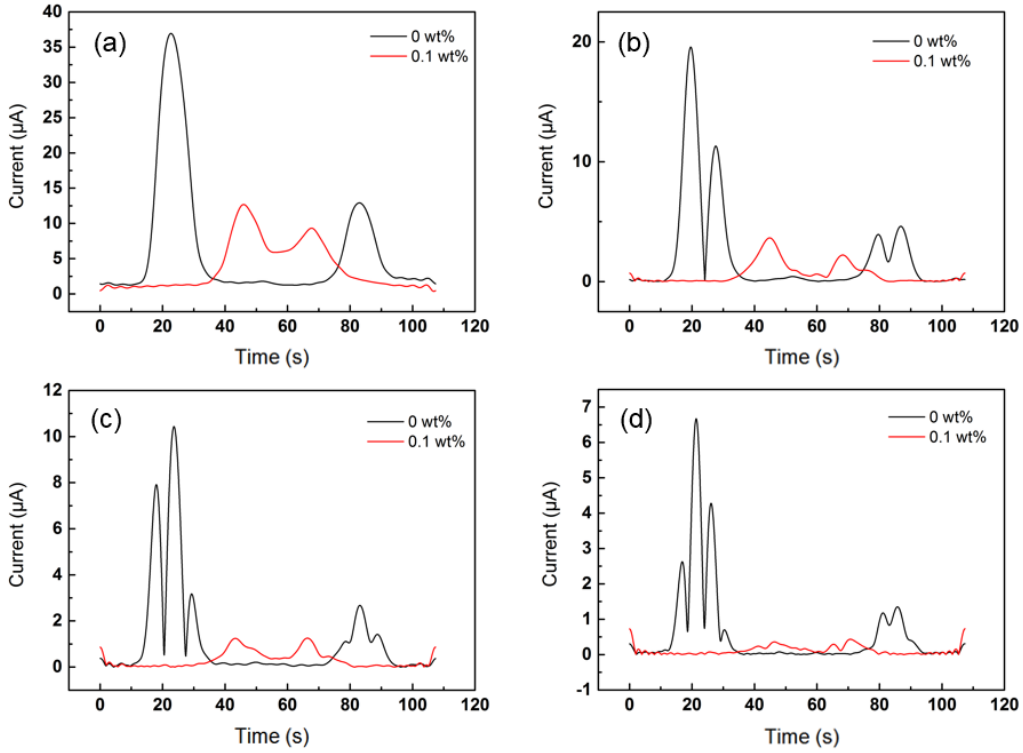

Figure 3.12 Large amplitude ac voltammograms of 1 mM catechol supported with 0.5 M KCl recorded on a GCE at chitosan concentration of 0 wt% (black) and 0.1 wt% (red) at a scan rate of 15 mV s^{-1}, amplitude of 100 mV and frequency of 1 Hz in Na_2CO_3/$NaHCO_3$ pH 9.2 buffer solutions. (a) Fundamental harmonic; (b) Second harmonic; (c) Third harmonic; and (d) Fourth harmonic.

Figure 3.12 shows the fundamental to fourth ac harmonic components for 1 mM catechol oxidation with and without 0.1 wt% chitosan in Na_2CO_3/$NaHCO_3$ pH 9.2 buffer solution on a GCE. In the absence of chitosan (black curves), classical FTACV harmonics have been obtained. For the fundamental harmonic shown in Figure 3.12a, two clear peaks have been recorded for the oxidation and reduction reactions. The magnitude of oxidative peak is much larger than its reductive counterpart, which is consistent with the cyclic voltammogram in Figure 3.6c. This unequal heights of the two peaks also reveal the quasi-reversible response of

catechol oxidation at the sweep rate. Similar unequal responses have been observed for the second, third and fourth harmonics.

After the FTACV response of catechol oxidation was studied, the presence of 0.1 wt% chitosan in the redox system was carried out and measured. Same FTACV parameters have been applied in this new chemical system, and the responses are shown in Figure 3.12 as the red curves. The oxidative peak in the fundamental harmonic shifts to positive potentials, and reductive peak moves towards negative values. Comparing with pure catechol oxidation, the magnitudes of peak currents also decrease for both oxidative and reductive processes. This finding is in line with aforementioned CV and SWV results. In higher harmonics, the peaks are also smaller than that in the absence of chitosan and shifts also occur. The shape of these peaks have gradually lost typical harmonic characteristics for third and fourth harmonics. Additionally, nearly zero background current was observed in the higher harmonics, which indicates most capacitive current has been eliminated.

Next, FTACV characteristics of catechol oxidation with varying chitosan concentration were evaluated. Figure 3.13a shows the fundamental harmonics for FTACV measurements on 1 mM catechol solutions containing various chitosan concentrations (0–0.09 wt%). It should be noted that the oxidative peak potential shifts to right positions as chitosan concentration increase from 0 wt% to 0.05 wt%, and reductive peak potential move towards left positions. After this concentration, the oxidative peak potential stays at the same position, while reductive potential continues to shift. In terms of the current magnitude, a dramatic drop has been observed for the oxidative current at 0 wt% to 0.01 wt%. As the chitosan concentration further increases to 0.05 wt%, current continues to decrease. After this point, however, the current starts to rise for both oxidative and reductive processes. These phenomenon are consistent with the CV responses. Nevertheless, the transformation of single peak to two peaks and back to single peak (Figure 3.7b) has not been discovered in the first harmonics. Only broad peaks have been seen in the chitosan concentration of 0.01 wt% and 0.03 wt%.

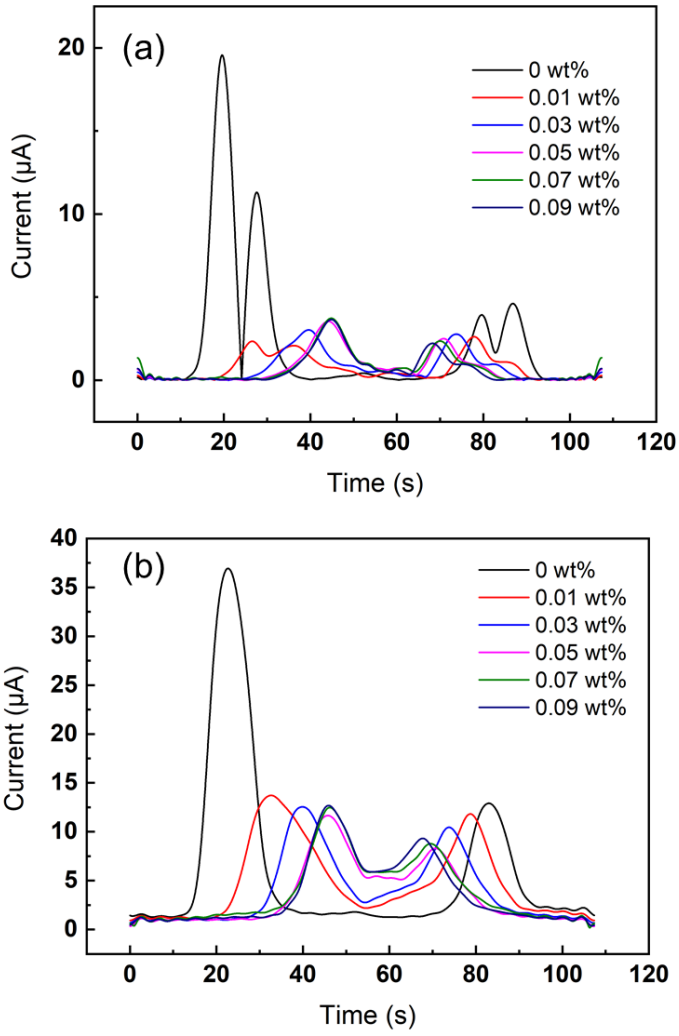

Figure 3.13 Fundamental (a) and Second (b) harmonics in large amplitude ac voltammograms of 0wt% to 0.09wt% chitosan, 1 mM catechol and 0.5 M KCl in Na_2CO_3/$NaHCO_3$ pH 9.2 buffer solutions recorded on a GCE at a scan rate of 15 mV s^{-1}, amplitude of 100 mV and frequency of 1 Hz.

The second harmonic data of the catechol and chitosan system with same parameters is shown in Figure 3.13b. In the absence of chitosan, two typical peaks are observed with the oxidative peaks much higher than the reductive counterparts. While in the 0.01 wt% and 0.03 wt% cases, three peaks occur in their oxidative reactions. The left peak shifts to positive potentials and gradually diminished as the chitosan concentration increased further. The other two peaks also shift positively, and then remain constant when they reached the concentration of 0.05 wt%. This again can be seen as the completion of the crosslinking reaction. The mechanism is

suggested to be related to the formation of new catechol glucosamine adduct during the pre-equilibrium process.

3.5 Conclusion

This chapter describes the mechanistic studies of catechol oxidation with subsequent homogeneous chemical reaction with chitosan. The process involves the viscosity change, which could inhibit the transport of reactants and products. Various voltammetric methods have been adopted to investigate the chemical systems, including CV, SWV and FTACV. Parameters such as scan rate, chemical species and reactant concentration have been altered during the measurements.

The electrochemical responses of catechol in the presence of glucosamine at a GCE revealed an EC reaction process. According to our results, the cyclic voltammograms of catechol and D-glucosamine move towards more positive potentials as the D-glucosamine concentration increases, which can be attributed to the formation of the catechol glucosamine adduct. This understanding of the pre-equilibrium and catechol glucosamine adduct then allowed the monitoring of the reaction of crosslinking reaction between catechol and chitosan. In the presence of chitosan the voltammetric response of the catechol was perturbed in an analogous manner, as the concentration of chitosan was increased the voltammetric response was stabilised indicating the reaction had gone to completion. This voltammetric profiling therefore provides a means of understanding the degree of crosslinking through polymeric structures. Additionally, SWV and FTACV were also utilized to analyse the chemical system of catechol and chitosan. Their results reveal a similar phenomenon as the CV responses. However, the peak transformation is not observed in the first harmonics in FTACV, while it occurs in the second harmonics.

Chapter 4 Molybdenum Disulfide Nanocatalysts for Catalytic Hydrogen Production

Abstract

This chapter reports the synthesis of mesoporous carbon microsphere supported molybdenum disulphide via a hydrothermal method. Doping of cobalt or nickel into the particles has also been attempted. The material has been served as an electrocatalyst for HER in acidic condition. Then the performances of the catalysts have been examined by traditional LSV and advanced FTACV techniques. In order to obtain more mechanistic insight of the HER processes, FTACV technique has been utilised onto the process for the first time. Moreover, the synthesised particles have also been utilised for catalytic decomposition of hydrogen sulfide at elevated temperatures, which exhibits an advanced conversion rate over conventional catalysts.

4.1 Introduction

The previous chapter studies the complex electrochemical mechanism in the solution phase. The result shows the formation of hydrogel on the electrode surface can be initiated by an electrochemical method and the progress also be monitored. This chapter looks at the modification of electrode surface by deposition of nanocatalytsts, and the electrode examined for hydrogen evolution reaction (HER). Traditionally the performance of the catalyst for HER processes can be evaluated by the linear sweep voltammetry (LSV). In this technique, a polarisation curve can be obtained, which can be further analysed to give several parameters for measuring the performance of the catalyst and exhibit potential reaction pathway, including overpotential, exchanged current density and Tafel slope. However, this technique is hardly to detect and quantify the redox transformations involved in the HER processes. The utilisation of large amplitude Fourier transformed alternating-current voltammetry (FTACV) is believed

to provide extra information than the dc LSV. The technique offers a few advantages over other voltammetric techniques such as the ability to measure catalytic chemical redox reactions and reversible electron transfer processes in a single experiment.[10], [45] It has been well noted that the fast and reversible redox reactions are responsible for the higher harmonic components in FTACV, while no contributions from the catalysis and baseline.[26], [27] In addition, the dc component (f = 0) provides the same catalytic information as the dc CV responses. The non-linear high order harmonic components are also highly sensitive to kinetic data, while insensitive to homogeneous catalysis and can reject background charging current.[144] Currently, the technique is rarely used in the field of water splitting studies. Bonke et. al reported the utilisation of FTACV onto the study of water electrooxidation catalysed by metal oxides.[145] They argued that this technique can potentially improve the sensitivity to quantify the kinetic studies of the water electrooxidation. In addition, FTACV can also benefit the understanding of the mechanism of water electrooxidation. Thus, as analogues to oxygen evolution reaction, it is supposed that the adoption of FTACV is highly possible to extract useful information on the mechanism of the HER process.

In this chapter, the carbon microsphere supported molybdenum disulfide nanocatalysts have been synthesised and utilised for the catalytic production of hydrogen. The morphology and properties of the samples have first been characterised by a series of techniques as described in Chapter 2. The materials were then utilised as an electrocatalyst for HER and examined by traditional potential sweep technique and FTACV. The particles were also used as a heterogeneous catalyst for thermal decomposition of hydrogen sulfide. The performance of the samples for the two applications is tested and compared with literature.

4.2 Production of Hydrogen

There is a growing need of renewable energy sources due to the increasing concern about the energy crisis and environmental damage associated with the current excessive use of fossil fuels.[146] Also, fossil fuels have been considered to be diminishing, thus renewable energy can be utilised as alternative energy sources. Hydrogen is an abundant, renewable and clean

fuel with characteristics of high energy density and environmental friendly. Therefore, hydrogen is one of the most promising energy carrier to fulfil future energy demands. As described in Chapter 1, hydrogen can be produced through several industrial processes, including thermochemical processes, splitting of water and biological methods. Thermochemical processes utilise heat and chemical reactions to generate hydrogen from organic materials. The processes include steam methane reforming, coal and biomass gasification and biomass-derived liquid reforming. Hydrogen can also be produced by biological processes in microorganisms such as bacteria and algae. This biological method is under early stage of research at present, while it has a potential to achieve sustainable and low-carbon hydrogen production in the long term. Water splitting using electrolysis or solar energy is another technique to generate hydrogen. The overall process includes two half-cell reactions, cathodic hydrogen evolution and anodic oxygen evolution.[147] Among these, HER is one of the most studied electrochemical processes. This section describes the hydrogen production by HER and an alternative method by hydrogen sulfide decomposition.

4.3 Hydrogen Production Processes

Fossil fuels are regarded as depleting and environmental unfriendly energy sources, while constituting 80% of the present world energy demand.[148] Thus the need for clean energy is necessary. Hydrogen gas (H_2) is considered to be the most promising energy carrier as it is abundant in the universe and burns without producing any environmental pollutants. The energy content per unit of weight of H_2 (120.7 kJ/g) is highest among all the known fuels.[149] Consequently, a number of techniques have been proposed to develop hydrogen generation systems. The four broad categories of the hydrogen production technologies are: thermochemical, electrochemical, photobiological and photoelectrochemical.[149]

Thermochemical Processes

Steam reforming of raw materials such as natural gas and light oil fraction at high temperatures is the most extensively used thermochemical process to release H_2. A general reforming process for hydrogen production has been illustrated in Figure 4.1. This technology represents approximately 90% of the H_2 production currently.[148] Among these, steam reforming of

natural gas is the most cost-effective process for large scale production of H_2, which represents 50% of the world feedstock.[150] Nevertheless, production of H_2 from natural gas is associated with large amounts of carbon dioxide as by-product. In addition, compared with current hybrid vehicles, it only achieves a modest reduction in vehicle emissions. Some researchers have been focused on the steam reforming of ethanol, which is an environmental friendly renewable resource. Other thermochemical process such as gasification and pyrolysis can be utilised when the feedstocks are solids or semisolids.[151]

This Figure is not shown due to copyright issues

Electrochemical Technology

Electrocatalytic water decomposition is one crucial and mature technology for generating molecular hydrogen.[153] Compared with thermochemical processes, H_2 can be produced cleaner, easier and with higher purity by water electrolysis. However, this method only constitutes 4% of the global production.[154] This is due to the relatively low cost of natural gas for steam reforming and the high cost of electrical energy consumption during electrolysis.[155] It is reported that H_2 production by the current electrolysis system requires an energy input of 53.4 to 70.1 kWh per kg of H_2.[156] A high electrical potential is necessary

to efficiently and successfully split the stable water molecules into hydrogen and oxygen. The extra potential required beyond the thermodynamics is named the overpotential, which is the crucial reason for the high cost of the technology. Consequently, current researches mostly focus on several aspects that could potentially decrease the overpotential for water electrolysis, such as developing new electrodes,[157] improving electrolyte,[158] and understanding the electrode kinetics for the reaction.[159] Platinum supported on carbon (Pt/C) has been proved to serve as an exceptional electrocatalyst for the hydrogen evolution reaction (HER) in water electrolysis.[154] Nevertheless, the high cost of platinum prohibited its utilisation as an industrial electrocatalyst. Thus, tremendous amount of research has been carried out to develop an alternative inexpensive material with a similar catalytic activity to platinum. A detailed description of the HER process and literature review is given in Chapter 5.

Figure 4.2 Direct photolysis process. (Reproduced from reference [152])

Photobiological Technology

In photobiological systems, the natural photosynthetic processes of bacteria and algae are utilised to generate hydrogen. A wide range of methods have been developed based on this technology, including photo-fermentation, dark-fermentation, microbial electrolysis cells, direct and indirect biophotolysis.[149], [152] Figure 4.2 shows a direct biophotolysis of water using the photosynthesis capabilities of green algae. The process incorporates two photosystems that located on the thylakoid membrane.[152] However, the major limitation associated with this technology is the relatively slow conversion rate. It has been reported that

the rates of photobiological H_2 production varies in the range from 0.07 mmol H_2 L^{-1} h^{-1} in direct biophotolysis to 96 mmol H_2 L^{-1} h^{-1}in photoheterotrophic water gas shift (WGS).[160] The biological WGS reactors are challenged with slow mass transfer and kinetics, and thus cannot replace catalytic WGS reactors at the present.[161] Additionally, the practical applicability of technology is uncertain as it is currently in the early stage of development.

This Figure is not shown due to copyright issues

Figure 4.3 Energetic diagram of n-type semiconductor photoelectrochemical cells. (Reproduced from reference[152])

Photoelectrochemical Technology

Photoelectrolysis utilises the illumination of sunlight onto a water-immersed semiconductor to directly decompose water into hydrogen and oxygen. A short description of a photoanode-based process is illustrated in Figure 4.3. A photon with energy higher than the bandgap hits the anode surface, establishing an electron-hole pair. Then the decomposition of water occurs on the anode surface by the hole, generating hydrogen ions and gaseous oxygen. Next, the hydrogen ions transport to the cathode and accept electrons to form hydrogen gas.[162] Finally, the hydrogen and oxygen gases can be separated using a semi-permeable membrane. However, the technology is immature and currently in experimental stage. A few difficulties have been encountered for developing a durable and high-efficiency photoelectrochemical system. The first being the poor matching of the solar spectra with the semiconductor bandgap. Another

barrier is the difference between the semiconductor band edges and the electrochemical reactions. Moreover, most semiconductor materials are instable in aqueous phases.

In conclusion, the current most developed and utilised technique for producing hydrogen is the reforming of hydrocarbon fuels. The technique depends heavily on fossil fuels, thus other hydrogen production technologies from renewable sources such as water and biomass is desired to minimise environmental impact. In order to compete with the large scale reforming technologies, these alternative hydrogen production systems require more technical breakthroughs and cost reductions. While for small scale hydrogen generation at distributed facilities, electrolysis may be cost competitive. Furthermore, a wide range of raw materials can be adopted to produce hydrogen, resulting in the development of many sustainable processes.

4.3.1 Hydrogen Evolution Reaction

Water is the most desirable source for hydrogen production as it is abundant on earth and contains no carbon. Water electrolysis is achieved through the passage of electrical currents between electrodes in the presence of an electrolyte, producing hydrogen and oxygen at the electrode surfaces. The overall reaction is described below:

$$H_2O \rightleftharpoons H_2 + \frac{1}{2}O_2 \tag{4.1}$$

The reaction is composed of two half-cell reactions, hydrogen evolution reaction (HER) and oxygen evolution reaction (OER). In HER, hydrogen is formed at the cathode, and for OER, oxygen is formed at the anode. Depending on the pH value of the solution, the reactions exhibit different mechanisms due to the nature of the active ions in the reaction. In acidic solutions, the active ion is proton, while in alkaline solutions the active ion is hydroxide ion. For water electrolysis performed in acidic solutions, water molecule is the source for hydroxide ion, and the following reactions occur:[163]

$$\text{Cathodic (HER): } 4\,H^+ + 4\,e^- \rightleftharpoons 2\,H_2 \tag{4.2}$$

$$\text{Anodic (OER): } 2\,H_2O \rightleftharpoons O_2 + 4\,H^+ + 4\,e^- \tag{4.3}$$

In alkaline solutions, the proton is from water, and these reactions become:[164]

$$\text{Cathodic (HER): } 4\,H_2O + 4\,e^- \rightleftharpoons 2\,H_2 + 4\,OH^- \quad (4.4)$$

$$\text{Anodic (OER): } 4\,OH^- \rightleftharpoons 2\,H_2O + O_2 + 4\,e^- \quad (4.5)$$

The cathodic half reaction of water splitting, HER, has gained increasingly attention. The processes have been illustrated in the above equations of (4.2) and (4.3), which shows the reduction of protons or water molecules followed by the subsequent evolution of gaseous hydrogen. The standard reduction potential of HER is defined as $E_{H+/H2O}{}^0$ = 0 V *vs.* a normal hydrogen electrode at pH = 0. However, a certain amount of activation energy barrier can occur during the process, known as the overpotential (Figure 4.4a). This is one of the most important parameters to evaluate the electrochemical performance of a catalyst. Also smaller overpotential can generally increase the energy efficiency. As a consequence, electrocatalysts are usually utilised to lower the overpotential and thus promote reaction rate. They can be divided into two main categories, homogeneous and heterogeneous, depending on whether the catalyst is in the same phase as the reactants. Homogeneous HER electrocatalysts are normally water-soluble molecule such as hydrogenase.[165] For heterogeneous electrocatalysts, they are mostly water-insoluble solids that directly attached onto the working electrode. The most efficient electrocatalysts for HER have been proven to be platinum and platinum group metals that can reach extremely low overpotential. The most significant drawback of the materials is the high cost, which prohibits their large scale industrial applications. Thus current purpose of research has shifted towards low-coast alternatives with appropriate catalytic efficiencies.

This Figure is not shown due to copyright issues

Figure 4.4 (a) Schematic representation of the HER energetics. (b) Typical HER polarisation curves of two different electrocatalysts (I and II). (c) Tafel plots of two different electrocatalysts (I and II).[166]

Next, the fundamentals of HER process are discussed. Figure 4.4a shows the activation energy curve in HER with overpotential highlighted. The nature of the electrode/electrolyte interface would largely affect the size of the energy barrier. Therefore, electrochemical reactions usually require extra electric potential than thermodynamics, and the potential to drive HER reactions can be expressed as:

$$E_i = E_{HER} + iR + \eta \tag{4.6}$$

Where *iR* is the ohmic potential drop across the electrolyte by the flow of current.

Ideal electrocatalysts for HER are supposed to have small overpotentials, low Tafel slopes and large exchange current densities. Unfortunately, these parameters are not completely independent of each other. As shown in Figure 4.4b, c, HER electrocatalyst with a lower Tafel slope often reveals a smaller exchange current density. As a result, a catalyst with smaller overpotential at the targeted current density is regarded as better catalytic ability. It has been proposed that the potential to achieve an exchange current density of 10 mA cm^{-2} can be used to quantify the electrocatalytic activity.[167]

In order to better understand the HER kinetics, the mechanisms of the half-reaction pathways are considered. The pathway is believed to be both catalyst-dependent and potential-dependent. Here the mechanism of HER half-reaction is described with the following three steps in acidic media.[168]

$$\text{Volmer reaction: } H^+ + e^- \rightleftharpoons H_{ads} \tag{4.7}$$

$$\text{Heyrovsky reaction: } H^+ + H_{ads} + e^- \rightleftharpoons H_2 \tag{4.8}$$

$$\text{Tafel reaction: } 2\,H_{ads} \rightleftharpoons H_2 \tag{4.9}$$

From the above reactions, several pathways for hydrogen evolution have been proposed. Owing to the existence of different surface crystalline facets, more than one pathway can be simultaneously operative on one electrocatalyst. It has been generally accepted that HER in acidic solutions consists of two primary steps.[169] The first step is known as the Volmer reaction or the discharge reaction (equation (4.7)), which describes the formation of an intermediate adsorbed hydrogen atom from a proton-coupled electron transfer at the catalyst

surface. After this first step, hydrogen desorption can proceed through two pathways, which are Heyrovsky reaction (4.8) or Tafel reaction (4.9). For the first case, the adsorbed hydrogen atom can initiate another electron transfer with another proton from the solution to form molecular hydrogen. Thus the Heyrovsky reaction is also known as the electrochemical desorption reaction. The second pathway is the Tafel reaction or recombination reaction that formation of molecular hydrogen is achieved through the combination of two adsorbed hydrogen atoms. A three step pathway has also been proposed that consists of all three reactions simultaneously.[159] It is argued that different HER electrocatalysts would not have the same reaction pathway and the mechanisms are challenging to be elucidated. Nevertheless, the Tafel slope is believed to be an indication of the rate limiting step, and some insight into possible reaction pathways might be obtained.[1], [167] The theoretical values of Tafel slope calculated from Bulter-Volmer kinetics are 118 mV per decade, 39 mV per decade or 29.5 mV per decade when the rate-determining reaction is Volmer reaction, Heyrovsky reaction or Tafel reaction, respectively. It is shown that platinum used as an HER electrocatalyst in acidic solutions follows the Volmer-Tafel reaction pathway. At low overpotentials, the Tafel reaction is the rate-determining step, while the initial discharge step is relatively fast.[167]

A wide variety of HER electrocatalysts have been developed, which can be categorized into four groups, precious metals, non-precious metals and alloys, transition metals and metal free catalysts. As mentioned before, platinum group metals have the best known HER catalytic activities, thus Pt is normally used as a benchmark to assess the activity of other HER electrocatalysts. However, their high cost and low abundance prohibit the extensive application of the material. In general, two strategies can be attempted to solve the problem. The first being the increment of catalyst loading by the utilisation of micro-structured or nano-structured electrocatalysts with large surface to volume ratio. It has also been proven that the Electrocatalytic performance of Pt nanostructures can be benefited with engineered porosity due to the accelerated mass transport of reactants.[170], [171] The second strategy is the increment of site-specific activity by alloying Pt with other metals, which allows lower catalyst loading.[172] Computational work based on density functional theory shows that binary surface alloy formed between Pt and Bi is the most promising candidate.[172]

Non-precious metals such as Ni are frequently utilised as cathodes for producing hydrogen in industrial alkaline electrolysers for their low cost and resistance to corrosion at high pH.[173] The major drawback of Ni based electrodes is the progressive deactivation of the catalysts due to the formation of nickel hydride species during continuous alkaline electrolysis.[174] Thus Ni-based alloys such as Raney®-Nickel, Ni-Mo and Ni-Co have been developed for improved activity and durability.[175]

Transition metals based HER catalysts have also been developed. For transition metal chalcogenides, MoS_2 is the most renowned candidate, which has a layered structure with weak van der Waals interactions. DFT calculations on the free energy of hydrogen bonding in MoS_2 exhibit that the basal plane of MoS_2 was catalytically inert, while the edge planes were responsible for the efficient HER activity, close to those of Pt, nitrogenase and hydrogenase.[176] Another study by Chorkendorff *et al.* shows that the edge length of MoS_2 nanoparticles has a linear effect on the HER exchange current density, confirming the edge planes are HER active sites.[177] Different methodologies have been investigated to improve the HER activity of MoS_2 particles. Structural engineering of the MoS_2 materials is one of the approaches to expose edge site. Stabilisation of the MoS_2 particles formation can also be achieved by utilising appropriate functional substrates, with nanoscale dimensions and abundant edges. The crystal structure of MoS_2 would also significantly affects HER activity, with tetragonal 1T-MoS_2 suggested more active than the hexagonal 2H-MoS_2.[178] In addition, some achievement have also been made for HER with amorphous MoS_x materials. Another strategy to enhance the HER activity of MoS_2 can be attained by combining with other metal cations such as Co or Ni.

Apart from transition metal chalcogenides, transition metal carbides (particularly molybdenum or tungsten carbides) have attracted extensive interest as low-cost HER electrocatalysts.[179] This type of material exhibits a Pt-like electrocatalytic activity for HER process with certain robustness to poisoning and deactivation. For molybdenum carbides, many stoichiometries and phases can be found, with a focus on the hexagonal β-Mo_2C as a result of its high HER catalytic response.[180] Furthermore, conductive carbon supports for growing carbide nanomaterials have also been proven to be a promising approach. This method allows the increment of the dispersion and electric conductivity of the electrocatalysts, thus improving the electrocatalytic

ability. Other transition metal based HER electrocatalysts include transition metal nitrides, borides, and phosphides.

Carbon-based metal free catalyst is another research focus. Nevertheless, pristine carbon materials such as glassy carbon are normally used as current collector in electrochemical measurements due to their inert electrochemical behaviour. Thus, in order to improve the electrocatalytic activity of these materials, chemical modification of the surface by heteroatom doping to form heteroatom functionalities is often necessary.[181]

In this study, as-synthesised MoS_2 were utilised as the heterogeneous electrocatalysts for HER reaction. The reaction were tested in both traditional technique of dc voltammetry and modern ac voltammetry.

4.3.2 Hydrogen Sulfide Decomposition

An alternative source for hydrogen production is hydrogen sulfide (H_2S). The hazards of the gas have been widely reported. It is a highly toxic gas that can lead to personal distress even at low concentrations and cause loss of consciousness, permanent brain damage or death at a high concentration[182]. Large amounts of hydrogen sulfide are produced worldwide, which can be found in many industrial processes such as oil and natural gas industry, landfills, sewers and waste treatment plants. Naturally, it is produced primarily by decomposition of organic materials, while it is also a component of natural gas, sulfur deposits and volcanic gases[183], [184]. The Black Sea is a unique basin because 90% of sea water is anaerobic and contains hydrogen sulfide produced by sulfur reducing bacteria. The total amount of H_2S in Black Sea is estimated to be 4.6 billion tons, which may potentially be recovered into 270 million tons of hydrogen.[185] The Claus process is a well-established method that converts H_2S into sulfur and water, while hydrogen is lost during the process. The hydrogen is loosely bound in H_2S (standard enthalpy of formation, $\Delta_f H_{298}^o$ = -4.82 kcal/mol), compared to other simple compounds such as water (H_2O, $\Delta_f H_{298}^o$ = -57.80 kcal/mol) and methane (CH_4, $\Delta_f H_{298}^o$ = -17.89 kcal/mol) [185], [186]. Thus, different approaches have been researched to obtain hydrogen from H_2S, while eliminating H_2S[187]. These include thermal, thermochemical, electrochemical, photochemical and plasmochemical methods. One promising method is the

thermal decomposition of H_2S into hydrogen and sulfur. Consequently, simultaneous generation of hydrogen and elimination of H_2S is a highly appealing process, which could fulfil both energy and environmental requirements.

Low thermal decomposition rate of H_2S is found at high temperature, due to both unfavourable thermodynamic and kinetic constraints. At atmospheric pressure, the conversion is as low as 7 % at 1073 K[188]. It is stated that the dissociation fraction of H_2S can be benefited at low pressure and high temperature [188], [189]. It has been observed that enhanced yields of hydrogen can be achieved in non-equilibrium flow systems, where the product can be removed from the reaction zone [190]. This has prompted many researches to shift the equilibrium by removing reaction products, using membranes, sulfur condensation or thermal diffusion [187]. It has been shown by Fukuda that 95% of H_2S can be converted to hydrogen and sulfur by using MoS_2 as a catalyst in a closed circulating system, with continuous removal of sulfur and separation of hydrogen at 1073K and sub-atmospheric pressure (5-20 kPa) [191]. However, the product removal scheme cannot be scaled up due to the large heating and cooling load.

It has been reported that the reaction is entirely thermal when H_2S splitting at temperatures higher than 1073 K, in which catalysts will play a low significant role [192]. Nevertheless, by using a catalyst, material resistance and residence time will benefit, thus, it is desirable to find a catalyst to optimise H_2S decomposition. In general, transition metal sulfides are adopted as catalysts, for example, molybdenum, vanadium, iron, cobalt, nickel and copper sulphides [189]. Research has been conducted to compare three catalysts of silica beads, cobalt molybdate and 1% pre-sulfided platinum for the decomposition reaction [187], [193]. The cobalt molybdate was found to be the most active catalyst. Another study by Kaloidas, *et al.* used powdered MoS_2 as a catalyst for the decomposition of H_2S in an alumina tube. The stabilised catalytic activity was 65% of the initial value after 15-25 h of reaction [187], [194]. The cracking of hydrogen-sulfur bonds in the H_2S molecule adsorbed on the active site was suggested as the rate determining step by using a Hougen-Watson type model. Among the catalysts, research on MoS_2 are most popular, while scarce information is obtained on the improvement of the catalyst by additional modifications [187]. Therefore, preparation of porous material supported nanocrystalline MoS_2 with doped transition metals is a promising approach.

For synthesizing nanocatalysts for heterogeneous catalysis, a homogeneous dispersion of catalytic active phases within porous solid media or permeable shells is desirable. Then these active phases such as metal or metal oxide nanoparticles can be isolated, preventing the agglomeration during reaction [195], [196]. Carbon as the porous support for metal and metal oxide catalysts has been well researched recently and various synthesis techniques have been proposed such as chemical vapour deposition [197], metal impregnation [198]–[200], cocarbonization of carbon and metal precursors [201], and hydrothermal synthesis [202], [203]. Among these, the hydrothermal method is one of the favourable techniques to synthesize MoS_2 nanocrystal with porous carbon support. It has been reported that the synthesis temperature has a huge effect on the morphology and crystallinity of MoS_2. Only amorphous MoS_2 nanospheres can be produced at a low temperature range between 120 °C and 150 °C [204], [205]. Higher temperatures are required to increase the crystalline size. The introduction of doping metals like cobalt (Co) or nickel (Ni) will also affect the morphologies of the particles. It is known that the degree of promotion of MoS_2 by adjacent Co and Ni sulphides contributes significantly on the hydrodesulfurization performance [206]. For H_2S decomposition, engineered surface structures and electronically modified by Co or Ni doped MoS_2 have an opportunity to improve conversion.

4.4 Experimental

4.4.1 Materials Preparation

Mesoporous carbon supported molybdenum oxide (MoO_2@C), with or without doping metal, were first synthesized via a similar hydrothermal method by the following literature procedures[202]. In a typical experiment, 100 mg of $Na_2MoO_4 \cdot 2H_2O$ solid was dissolved in 12 mL of HCl (0.5 M) solution, following an addition of 1.08 g of glucose ($C_6H_{12}O_6$) solid. The solution was then well stirred for 10 min at room temperature and then transferred to a Teflon-lined stainless steel autoclave (50 mL in volume). It was then hydrothermally treated in an electric oven at 180 °C for 6 h. Afterwards, the product, black solid residue (nonporous MoO_2@C), was separated by centrifugation and washed with deionized water and ethanol and dried in an electric oven. It was then moved to a tube furnace, heated in a nitrogen stream (40

mL/min) under 700 °C for 4 h (heating rate: 4 °C/min) to form mesoporous MoO_2@C (Figure 4.5). The product was then used as a feedstock in the hydrothermal synthesis of Molybdenum sulfide.

This Figure is not shown due to copyright issues

Figure 4.5 A schematic drawing of transforming as-synthesised non-porous MoO_2@C to mesoporous MoO_2@C by thermal treatment in nitrogen. (Reproduced from reference[202])

In a typical synthesis, 100 mg of previously synthesized mesoporous MoO_2@C and 150 mg of Thioacetamide (TAA) were used as precursor, and were dissolved in 40 mL deionized water. The synthesis reaction occurred at 200 °C for 24 h. Synthesis with doping metals (cobalt or nickel) were also conducted by adding cobalt acetate tetrahydrate or nickel acetate tetrahydrate in the precursors. Catalysts prepared at different conditions were denoted as material-weight percent of doped metal, e.g., MoS_2-3%Co@C stands for molybdenum disulfide with doped 3 wt% cobalt supported with mesoporous carbon microspheres.

4.4.2 Materials Characterization

The crystallographic structure of the solid samples was investigated using powder X-ray diffraction (XRD, Bruker D8 Advance, Cu Kα radiation, $\lambda = 1.5406$ Å) at a scan rate of 1°/min. The microscopic features of the samples were characterized by scanning electron microscopy (SEM, JEOL-6700F) equipped with an energy-dispersive X-ray spectroscopy analyser (EDX, Oxford INCA), field-emission SEM (FESEM, JSM-5600LV), transmission electron microscopy (TEM, JEM2010, 200 kV), and high-resolution TEM (HRTEM/EDX, JEM2100F, 200 kV). Inductively coupled plasma – optical emission spectrometry (ICP-OES) (Dual-view Optima 5300 DV ICP-OES) was also conducted to determine the elemental compositions of the samples. Surface and texture properties of the samples were studied by nitrogen adsorption−desorption isotherms (Quantachrome NOVA-3000 system) at 77 K. Prior to

measurements, the samples were degassed at 150 °C overnight. The specific surface areas of the catalysts were determined using the Brunauer−Emmett−Teller (BET) method with linear region in the P/P_0 range of 0.10 – 0.30. X-ray photoelectron spectroscopy (XPS, AXIS-HSi, Kratos Analytical) analysis was conducted using a monochromatized Al Kα exciting radiation (hν = 1286.71 eV) with a constant analyser-pass-energy of 40.0 eV. All binding energies (BEs) were referenced to C 1s peak (BE set at 284.5 eV) from C−C bonds.

4.4.3 Catalytic Hydrogen Evolution Reaction

HER measurements were carried out using a three-electrode cell with a 0.5 M sulfuric acid (H_2SO_4) electrolyte solution. The catalyst ink was prepared by dispersing 5 mg catalyst and 2 mg carbon black powder in 1.0 mL solution which consists of 0.50 mL deionized water, 0.47 mL ethanol and 30 µL 5%Nafion solution by ultrasonication for 30 min. Then 5 µL of the ink was drop-casted on a polished glassy carbon electrode (GCE, ALS, 3 mm diameter) and dried at room temperature overnight. Ag/AgCl and Platinum electrodes have been used as reference and counter electrodes, respectively. The reference electrode was calibrated with respect to reversible hydrogen electrode (RHE) according to the general conversion equation:

$$E_{RHE} = E_{Ag/AgCl} + 0.059 * pH + E^{o}_{Ag/AgCl} \quad (4.10)$$

The value of $E^{o}_{Ag/AgCl}$ is 0.1976 V at 25 °C, and the pH of 0.5 M H_2SO_4 solution is close to 0, thus the overall equation become $E_{RHE} = E_{Ag/AgCl} + 0.1976$ V. For the dc measurement, potential sweeps were taken with a 5 mV/s scan rate using a potentialstat PGSTAT 101 (Metrohm, The Netherlands). FTACV measurements were performed at a home-built instrument.[26] As described in section 1.3.5, a large-amplitude sine wave of frequency *f* is superimposed onto a linear CV potential sweep, which generates a current-time response. This response in time domain is then converted to frequency domain by Fourier transform, giving a power spectrum of harmonic contributions at frequencies *f*, 2*f*, 3*f*, 4*f*, etc. The data is then reverted to time domain by inverse FT after the band selection of the individual harmonics to generate the required dc or ac harmonic components.

4.4.4 Catalytic Decomposition of H_2S

The catalytic decomposition of gaseous H_2S were tested in a 1/8" quartz tubular reactor inside a tubular furnace under atmospheric pressure. An illustration of the experimental rig utilised for the decomposition reaction is shown in Figure 4.6. Hydrogen sulfide employed in this study was supplied from a 2500 ppm H_2S (balance N_2) high pressure gas cylinder. The gas stream was fed through a mass flow controller, operated at a total gas flow rate of 40 mL/min. In a typical experimental run, 50 mg of catalyst powder was loaded in the middle of a quartz tube, supported by quartz wool in both sides to prevent leakage. The quartz tube was put inside a furnace for temperature adjustment. A temperature range of 500 °C to 800 °C with 2 h of runtime at each 100 °C interval was studied for the catalytic decomposition test in atmospheric pressure. Overnight tests were also conducted to analyse the stability of the catalysts. Solid elemental sulfur was accumulated and collected at the end of the quartz tube under room temperature. The product gas stream was bubbled through a saturated aqueous Cu(II) acetate solution to remove unreacted H_2S. The generated hydrogen concentration in the gas stream was analysed via a Gas Chromatography (GC, Shimadzu GC-2010) device equipped with a GS-GASPRO column (60 m, 0.32 mm) and a thermal conductivity detector (TCD). The conversion of hydrogen sulfide was determined by comparison of H_2 concentration in the product stream to the H_2S concentration in supply stream in every 7 min using N_2 as an internal standard.

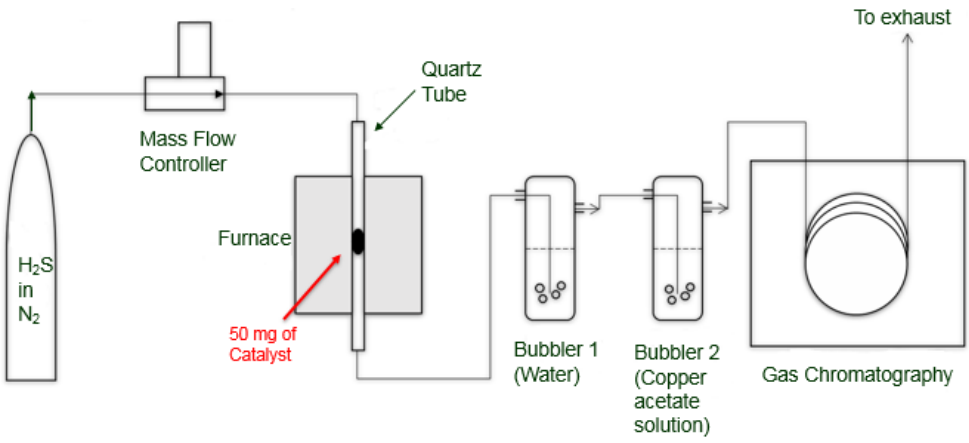

Figure 4.6 Process flow diagram of the experimental rig for catalytic H_2S decomposition.

4.5 Results and Discussion

This section describes the results of the synthesised MoS_2 catalysts with and without doping metals. A series of characterisation of the samples have been conducted, including SEM, TEM, XRD, XPS and adsorption isotherms. Then the performance of the samples for HER were examined in an acidic environment via electrochemical techniques of LSV and FTACV. LSV is the most common technique for measuring essential parameters (e.g., overpotential, tafel slope and exchange current density) of a catalyst used in HER. Nevertheless, FTACV is a state-of-the-art technique that has rarely been applied in the investigation of HER. The utilisation of the technique could potentially bring some insights into the HER mechanisms. After that, MoS_2@C samples were also utilised as heterogeneous catalyst for the thermal decomposition of H_2S.

4.5.1 Characterisation of MoO_2@C and MoS_2@C

Molybdenum oxide embedded carbon spheres have been prepared via a hydrothermal synthesis method using low-cost chemicals of sodium molybdate and glucose as precursors. The morphology of as-synthesised nonporous MoO_2@C prepared at 180 °C for 4 h under hydrothermal conditions is shown in Figure 4.7a, b. The SEM images indicate that the size distribution of the discrete carbonaceous spheres is in the range of 2 to 8 μm. The material was subsequently calcined in nitrogen at 700 °C for 4 h to form mesoporous MoO_2@C (Figure 4.7c, d). After this carbonisation process, the spherical morphology remains nearly unchanged, however their size reduces to less than 5 μm. The reason behind this phenomenon can be attributed to the gasification of carbon at high temperature. Along with the carbon microsphere, some tiny particles emerge in small quantity after the process, which are also carbon-enwrapped molybdenum oxides (Figure 4.7f). This occurs because of the increase in degree of supersaturation during the cooling of hydrothermal synthesis, which leads to the formation of the small particles.[202] The microstructure of the samples was further characterised by TEM. The lattice spacing of 0.24 nm found in Figure 4.7e can be assigned to the (200) plane of MoO_2 phase. This indicates that molybdenum oxide was readily formed during the hydrothermal step that even prior to carbonization. This is further confirmed by the XRD analysis in Figure 4.12.

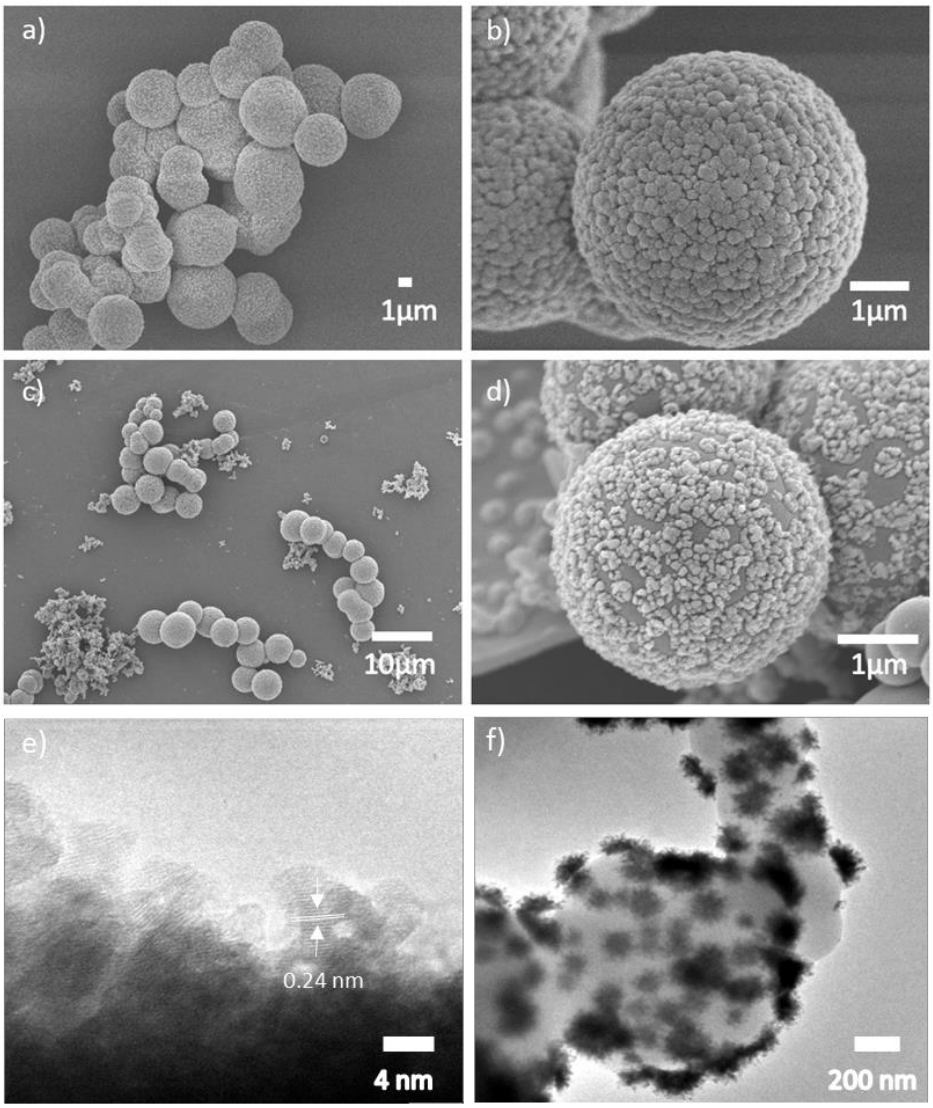

Figure 4.7 FESEM images of (a, b) nonporous MoO_2@C; (c, d) mesoporous MoO_2@C. TEM images of (e) nonporous MoO_2@C; (f) mesoporous MoO_2@C.

The above sample of MoO_2@C was then mixed with TAA, and the mixture used as a precursor for hydrothermal synthesis to produce MoS_2@C. The introduction of Co or Ni in the synthesis procedure were also attempted. Figure 4.8 shows the surface morphologies of MoS_2@C and doped catalysts by FESEM. The size distribution of the carbon spheres is in the range of 2 to 5 µm in all samples. The tiny particles observed in Figure 4.7c also appears in the MoS_2@C samples with a larger quantity, which are carbon-enwrapped MoS_2. The cause for a larger ratio of the small particles might be that MoS_2 occupying more space in the particle than MoO_2. They may also be formed due to the increase in degree of supersaturation as discussed earlier.

Less cleaved particles were observed for the doped samples, indicating the doping metals were beneficial to the stability of the carbon spheres.

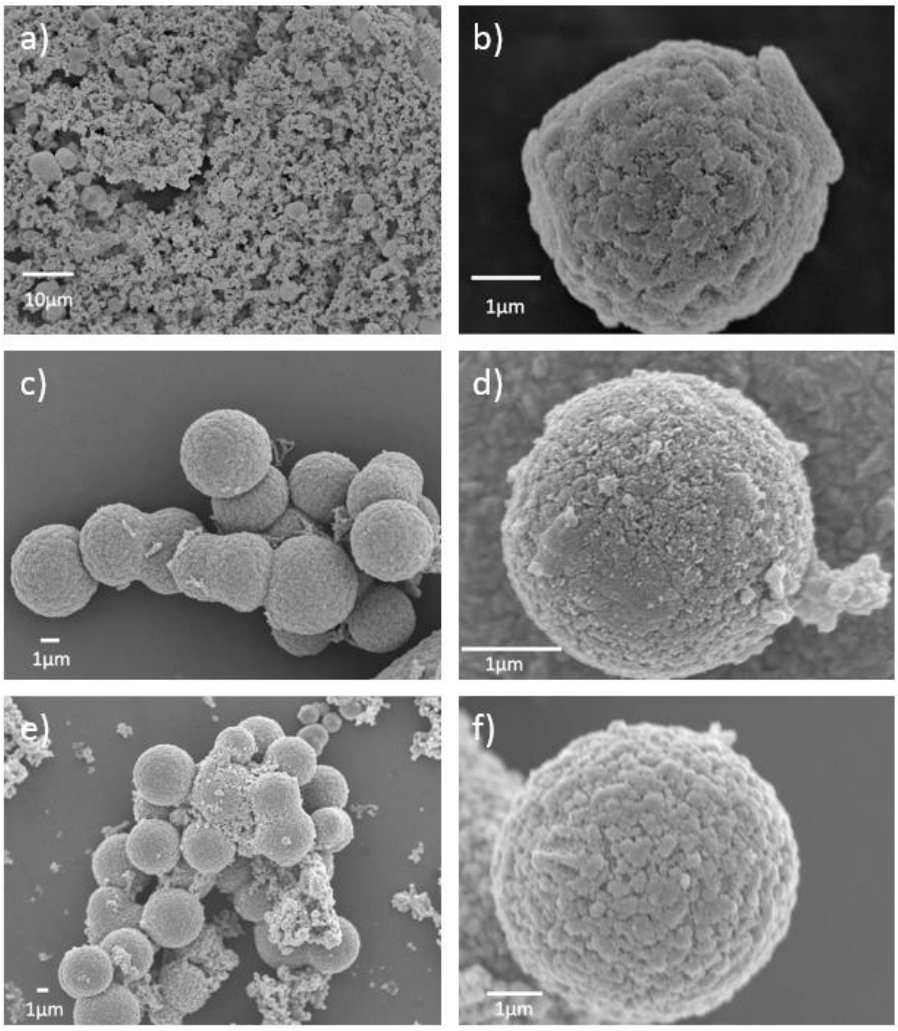

Figure 4.8 FESEM images of (a, b) MoS_2@C; (c, d) MoS_2-3%Co@C; (e, f) MoS_2-3%Ni@C.

The samples were further characterized by HRTEM to investigate the crystal structures. In Figure 4.9, the crystalline structure on the surface of the microspheres was examined. A lattice spacing of 0.65 nm is found in all samples and can be assigned to the (002) plane of MoS_2 phase, which will be further confirmed by XRD analysis in Figure 4.12. The MoS_2 nanosheets was mainly composed of 4 to 6 crystal layers. In Figure 4.9c, EDX elemental mapping confirms the chemical composition of MoS_2. A high dispersion of Mo and S elements was observed, while a small amount of O still existed in the particle. This implies the existence of

molybdenum oxide, which is likely to be in the form of MoO_3. For the Co-doped sample, besides the MoS_2 crystal planes, another crystalline structure with much less lattice spacing of 0.25nm was observed (white circles in Figure 4.9d, e), which is likely belong to CoMoS. This is consistent with the XRD results in Figure 4.12. The EDX result was obtained from the smaller particles, indicating minimal O existing in the material. Another crystalline structure (Figure 4.9h, white circled, interlayer spacing of 0.23nm) has also been observed for the Ni-doped sample, which might belongs to NiS_2. EDX confirming the existence of Ni inside the material with good dispersion.

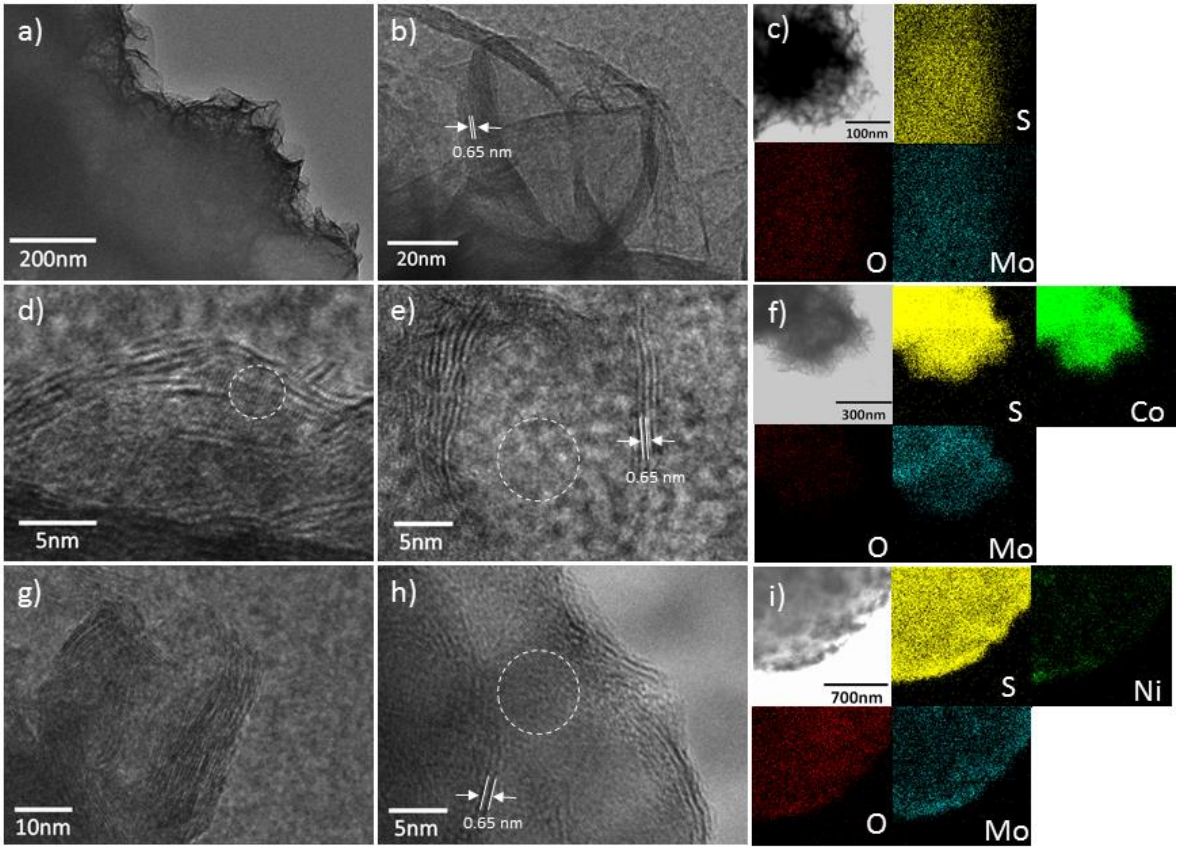

Figure 4.9 HRTEM images and EDX elemental mapping of (a, b, c) MoS_2@C; (d, e, f) MoS_2-3%Co@C; (g, h, i) MoS_2-3%Ni@C.

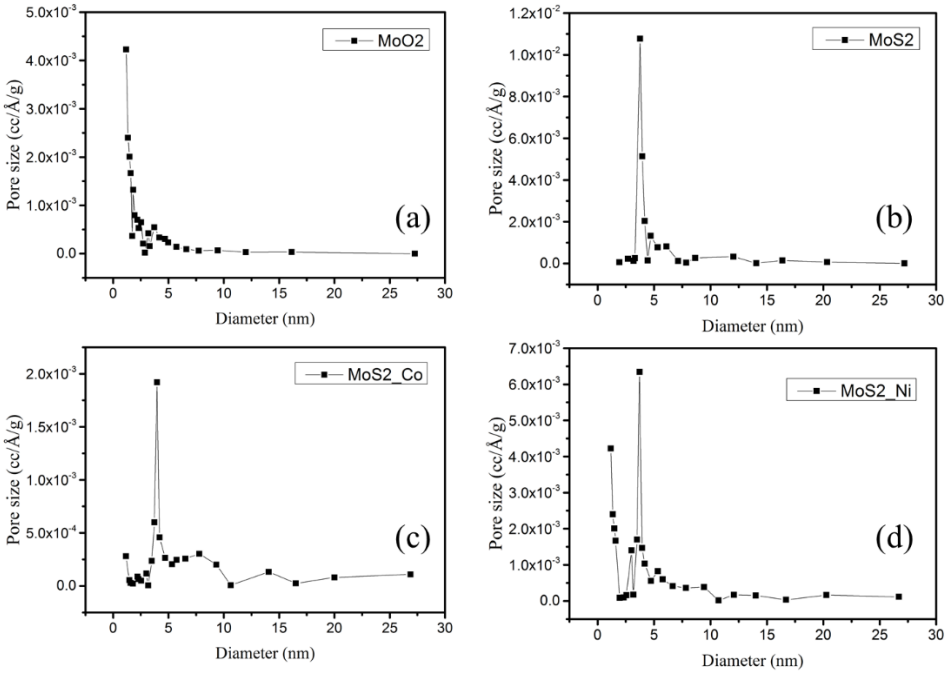

Figure 4.10 Pore size distribution of synthesized catalysts. (a) MoO_2@C, (b) MoS_2@C, (c) MoS_2-3%Co@C, (d) MoS_2-3%Ni@C.

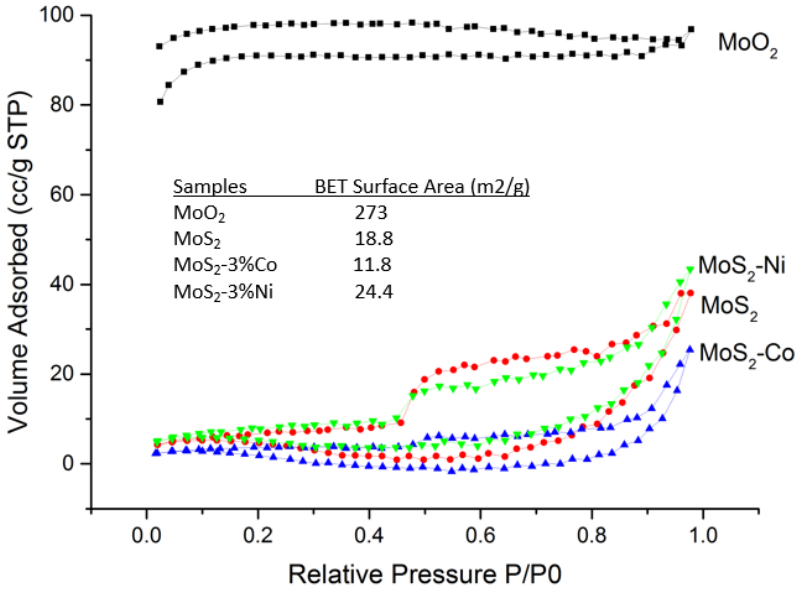

Figure 4.11 Nitrogen adsorption-desorption isotherms at 77 K of (Black) mesoporous MoO_2@C, (Red) MoS_2@C, (Blue) MoS_2-3%Co@C, (Green) MoS_2-3%Ni@C. Insert: Specific surface area of the catalysts calculated by BET method.

The distribution of pore size in the catalysts is shown in Figure 4.10. The Barrett-Joyner-Halenda (BJH) method was employed to quantitatively investigate the porosity of the samples using nitrogen adsorption-desorption isotherms. A distinct pore sizes under 20 Å was observed for the Molybdenum Oxide precursor in Figure 4.10a. This indicates micro pores are dominating in the Molybdenum Oxide sample, with only a small amount of mesopores existing. After sulfur is introduced to the particle to form MoS_2, the main pore size generated are centred at a range between 40 to 60 Å. These larger pores are supposed to be formed during the synthesis of MoS_2. The hysteresis loops in the isotherms also exhibit the mesoporosity of these samples (Figure 4.11). These loops can be regarded as type IV, which is normally caused by mesoporous structures. The calculated specific surface area for the Molybdenum Oxide sample is 273 m^2/g, while the values for MoS_2, Co or Ni doped MoS_2 decreased to 18.8, 11.8 and 24.4 m^2/g. The reason behind this phenomenon can be attributed to the increase in pore sizes and collapse of some pores during hydrothermal treatment.

The XRD spectra was performed on catalyst samples to investigate their crystallinity. The major peaks such as (-111), (-211), (200), (-222) and (031) of Molybdenum Oxide (JCPDS card no. 32-0671, space group: $P2_1/n$, a_0 = 5.607 Å, b_0 = 4.859 Å, c_0 = 5.537 Å) can be observed in Figure 4.12a, which confirms a good crystallinity of synthesized Molybdenum dioxide. The poorly crystalline phase in Figure 4.12b was assigned to MoS_2. Apart from the characteristic diffraction peaks assigned to (100) of hexagonal MoS_2, the shifted peak ($2\theta = 12.7°$) associated with the expanded (002) d spacing is observed. This (002) peak also reveals a typical layered structure. A small peak at $2\theta = 56.2°$ is noted and assigned as a shifted (110) lattice facets. This spectra indicate a more amorphous-like MoS_2 structure. Together with the TEM results, it can be concluded that the well-defined crystalline structure of MoS_2 mainly exists on the surface of microspheres, while amorphous MoS_2 inside the particle. Similar expanded (002) d spacing has also been found for the Co or Ni doped samples. For the MoS_2-3%Co sample, the peaks at 20.2° and 39.6° (Figure 4.12c) can be assigned to cobalt molybdenum sulfide. In Figure 4.12d, peaks of (200), (0-12), (-202) and (-1-13) corresponds to NiS_2 phase (JCPDS card no. 73-0574, space group: P1, a_0 = 5.685 Å, b_0 = 5.685 Å, c_0 = 5.685 Å). These observed peaks in XRD and the lattice in TEM confirm the existence of these compounds.

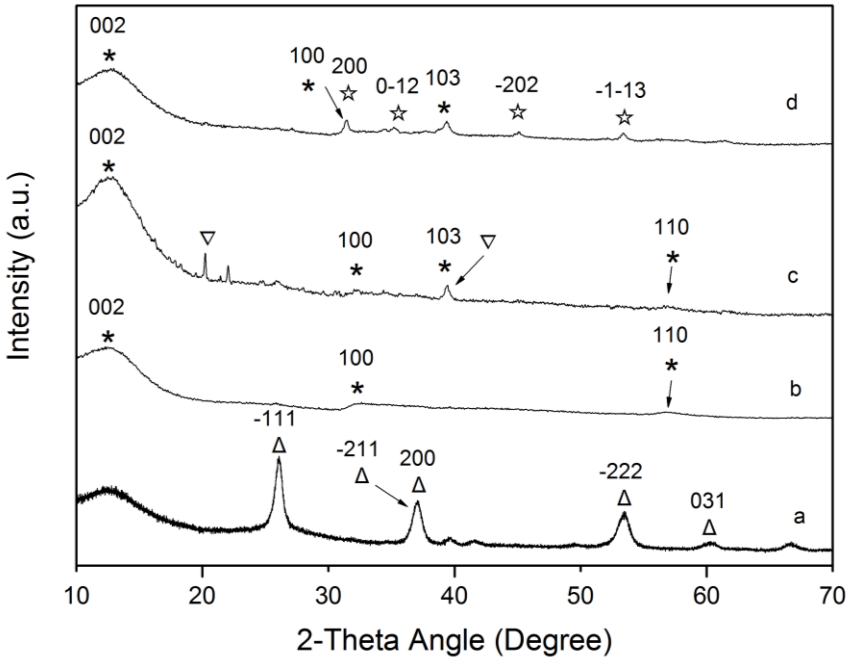

Figure 4.12 XRD spectra of synthesized catalysts. (a) MoO_2@C, (b) MoS_2@C, (c) MoS_2-3%Co@C, (d) MoS_2-3%Ni@C. Peaks marked with symbols ∆, ★, ∇, and ☆ correspond to monoclinic Molybdenum Oxide, hexagonal MoS_2, CoMoS and NiS_2 phases, respectively. Note that XRD peak heights are not scaled according to metal content.

XPS measurements were subsequently conducted to further investigate the chemical composition and valence states of the samples, shown in Figure 4.13. For the Mo 3d spectra in all synthesized samples, two major peaks at 228.9 eV and 232 eV are consistent with Mo $3d_{5/2}$ and Mo $3d_{3/2}$, which can be assigned to the Mo^{4+} ions [207], [208]. These ions mainly exist in the form of MoS_2, which will be further confirmed with S 2p spectra below. Separation of 3.1eV between $3d_{5/2}$ and $3d_{3/2}$ is due to d-d spin orbital splitting, the peak at 229.7eV is for Mo^{5+} separately[209]. The higher BEs between 235.7 to 236.2 eV correspond to Mo^{6+} ions [210], [211]. For the S 2p spectra, the doublets located at 161.8 eV (S $2p_{3/2}$) and 163 eV (S $2p_{1/2}$) can be assigned to S^{2-} ions. It likely exists in the form of MoS_2, and CoMoS or NiMoS in the Co or Ni doped samples, respectively. The small peaks at 164.2 eV to 164.35 eV can be assigned to S_2^{2-} $2p_{1/2}$ [208]. It has been found that the Ni doped sample has a larger peak of the S_2^{2-} phase, which confirms the existence of NiS_2 as described in XRD spectra (Figure 4.12d). To decompose the Co 2p spectra in the Co doped sample (Figure 4.13b), the peaks at 779.5 eV

(Co $2p_{3/2}$) and 794.4 eV (Co $2p_{1/2}$) corresponds to the CoMoS phase. The second doublets at 781.4 eV (Co $2p_{3/2}$) and 797.9 eV (Co $2p_{1/2}$) arise from the Co^{2+} [211]–[213]. A value of 550.6 eV was found after the examination of the difference in BEs between Co $2p_{3/2}$ and Mo $3d_{5/2}$. This is close to a reported literature value of 550.0 eV for the cobalt atoms located in a MoS_2 phase [211], [213]. This also supports the formation of CoMoS phase in the Co doped sample. For Ni 2p spectra in the Ni doped sample (Figure 4.13c), the peak at 854.7 eV (Ni $2p_{3/2}$) can be assigned to the NiMoS phase, and 857 eV (Ni $2p_{1/2}$) from Ni^{2+} phase [214], [215].

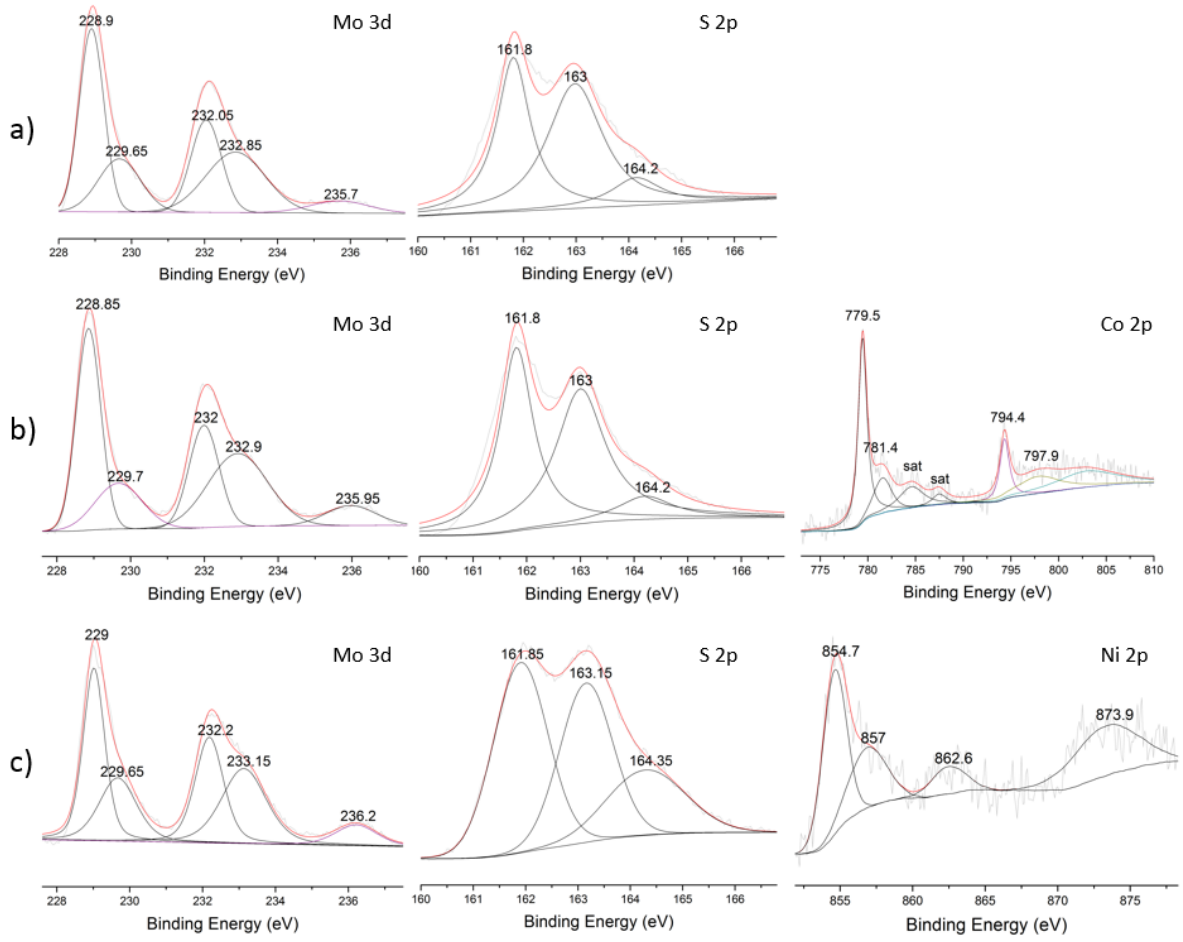

Figure 4.13 XPS spectra of Mo 3d, S 2p, Co 2p and Ni 2p for (a) MoS_2@C, (b) MoS_2-3%Co@C, (b) MoS_2-3%Ni@C.

Table 4.1 ICP and SEM EDX mapping of synthesized catalysts

	ICP (wt%)		SEM EDX mapping (wt%)	
Samples	**Mo**	**Doping metal (Co/ Ni)**	**Mo**	**Doping metal (Co/ Ni)**
MoS_2	15.9%	-	14.1%	-
MoS_2-3%Co	13.7%	3.1%	10.0%	2.6%
MoS_2-6%Co	13.1%	6.5%	11.7%	5.5%
MoS_2-9%Co	12.2%	8.5%	11.2%	6.6%
MoS_2-3%Ni	14.7%	2.9%	10.3%	2.7%

The effect of cobalt doping weight on the properties of the catalysts was also examined. Table 4.1 lists the weight percent of Mo and doping metals in the samples, determined by both ICP and SEM EDX mapping. In general, ICP results are more accurate, but the SEM EDX mapping roughly confirms the ICP results. The Mo loading in the MoS_2 sample was 15.86 wt%, which is slightly larger than that of MoS_2-3%Co (13.71 wt%) and MoS_2-3%Ni (14.71 wt%). For the doping metal loadings, both Co and Ni occupied around 3 wt% in Co or Ni doped samples. However, as Co loading was increased in the samples, the Mo loading decreased. This is likely to be caused by some ion exchange of Co with Mo, causing the formation of CoS_2.[216]

In the case of MoS_2-9%Co, FESEM images (Figure 4.14a, b) reveal that the particle remains spherical and has similar size (2 – 8 μm) as of the lower Co loading samples. However, the surface morphologies changes significantly with increased Co loading. In the XPS spectra (Figure 4.14c-e), Mo^{4+} ions are illustrated by the two major peaks at 228.95 eV and 232.1 eV. [207], [208] Two peaks at 229.4 eV and 232.95 eV indicate the appearance of Mo^{5+} ions. In addition, no Mo^{6+} phase is found in the spectra. Both S^{2-} and S_2^{2-} ions are identified from the peaks at 161.75 eV (S $2p_{3/2}$), 163 eV (S $2p_{1/2}$) and 164.3 eV (S $2p_{1/2}$). The S_2^{2-} phase is most likely existed in the form of CoS_2. Our XPS analysis of Co 2p spectrum gives two major BE peaks of Co $2p_{3/2}$ (779.6 eV) and Co $2p_{1/2}$ (794.5 eV), which belong to the CoMoS phase. The second doublets at 781.4 eV (Co $2p_{3/2}$) and 797.9 eV (Co $2p_{1/2}$) are a typical characteristic of the Co^{2+} ions.[211]–[213] This further confirms the existence of the CoS_2 phase. The XRD pattern of MoS_2-9%Co (Figure 4.14 f) indicates the shifted peaks (002, 110) and characteristic

peak (100) of hexagonal MoS_2. The diffraction peaks at (111), (200), (210), (220), (211) and (311) correspond to CoS_2 phase (JCPDS card no. 70-2865, space group: Pa-3, a_0 = 5.528 Å, b_0 = 5.528 Å, c_0 = 5.528 Å). Small peaks at 25.8° and 30.9° are assigned to the CoMoS phase. This indicates that CoS_2 is the dominant phase in the MoS_2-9%Co sample, as also confirmed by the XPS spectra (Figure 4.14d, e) and Mo wt% change (Table 4.1).

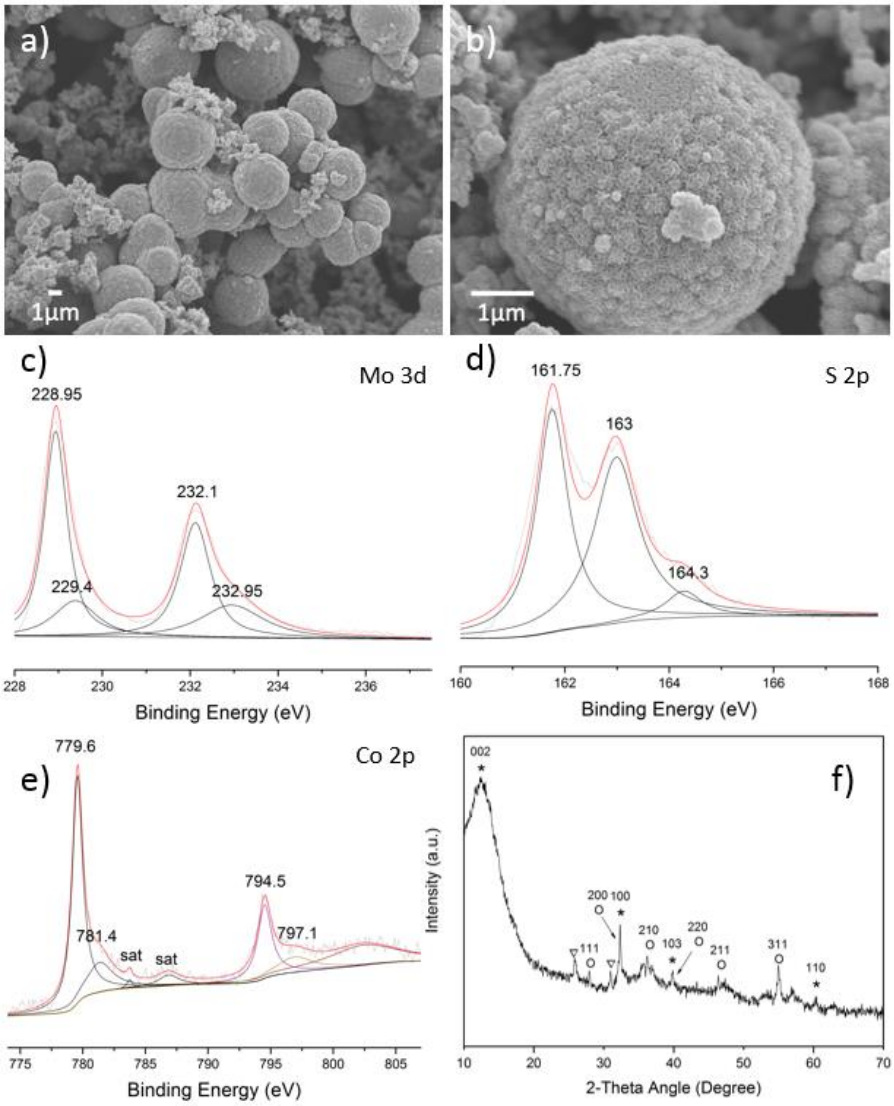

Figure 4.14 (a, b) FESEM image, (c-e) XPS spectra, (f) XRD pattern of MoS_2-9%Co@C. Peaks marked with symbols O, ★, and ∇ correspond to CoS_2, hexagonal MoS_2 and CoMoS phases, respectively.

4.5.2 Catalytic Hydrogen Evolution Reaction

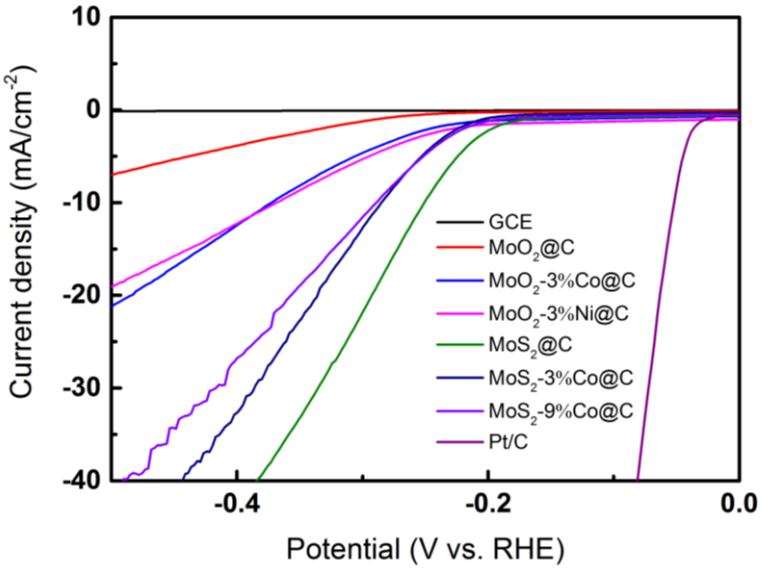

Figure 4.15 Polarization curves of prepared catalysts.

HER measurements with the prepared nanocatalysts drop-casted on glassy carbon electrodes were conducted using a conventional three-electrode setup with 0.5 M sulfuric acid as the electrolyte. All potentials are referenced to the reversible hydrogen electrode (RHE) based on Equation (4.10). Figure 4.15 shows the polarization curves for the prepared catalysts in comparison to a pure GCE and a commercial Pt/C electrocatalyst. The featureless polarization curve indicates that GCE provides almost negligible HER activity. The electrode coated with Pt/C exhibits an extremely small HER onset overpotential and delivered a current density of 10 mA cm^{-2} at an overpotential (η) of ca. 50 mV. Nevertheless, the Pt/C catalyst peeled off from the electrode surface due to the generated H_2 bubbles, leading to the maximum current density merely reached 100 mA cm^{-2}. The onset potential for MoO_2@C is approximately -300 mV, whereas the MoS_2@C indicates a value of -190 mV in acidic solutions. Figure 4.15 shows that MoO_2-3%Co@C, MoO_2-3%Ni@C, MoS_2@C, MoS_2-3%Co@C and MoS_2-9%Co@C can achieve a catalytic current density of 10 mA cm^{-2} at η of 372, 370, 250, 284, and 290mV (*vs.* RHE), respectively. The MoO_2@C indicates an extremely slow HER activity as its current density does not reach 10 mA cm^{-2} even at -500 mV. For the effects of doping on HER, doping metals in MoO_2@C promotes the catalytic HER activity, while doped MoS_2@C samples

exhibit slower current density. The slower activities can be attributed to the lower Mo loading in the doped samples (Table 4.1). Thus, this phenomenon concludes that the doping metal is beneficial to HER processes. In addition, all the catalysts suffer from the H_2 bubbling problem, which limits their maximum current density.

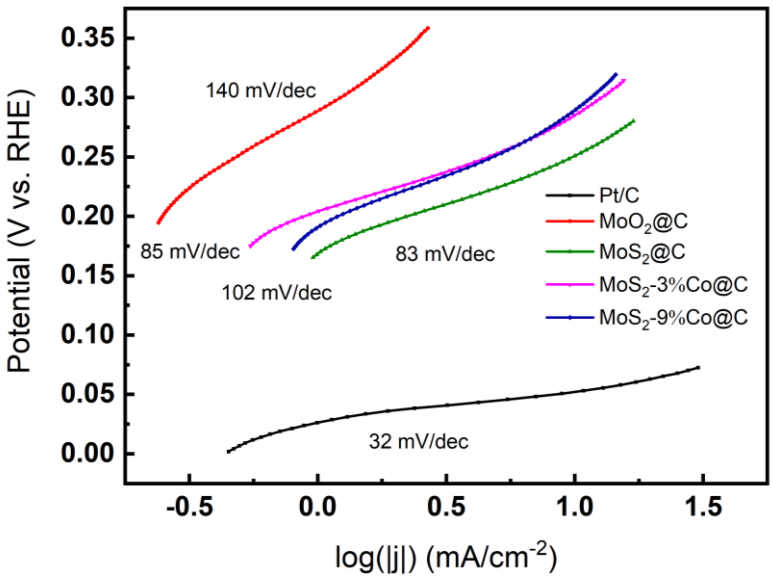

Figure 4.16 Tafel plots for the various samples.

Tafel plots of the corresponding polarization curves are displayed in Figure 4.16, providing profound insights into the fundamental HER kinetic mechanism. The HER on a Pt surface is known to proceed via the Volmer-Tafel pathway.[217] The kinetic rate-determining step is the Tafel process due to the low energy barrier (0.44 eV on Pt) of the Volmer step.[146] The Tafel slope is 30 mV per decade in theory, here the measured Tafel slope for a commercial Pt/C catalyst is determined as 32 mV per decade.[218] The Tafel slope of the MoS_2@C electrocatalyst is 83 mV per decade, and the value for the doped 3 wt% Co and 9 wt% Co is 85 and 102 mV per decade, respectively. These results suggest MoS_2@C and its doped catalysts catalyse hydrogen evolution occurs through various reaction pathways proceed via a Volmer-Heyrovsky mechanism.[219]

FTACV Investigation of the Catalysts

It has been a subject of debate for interpreting how nanocatalysts contribute to HER process using dc technologies.[220], [221] However, to the best of my knowledge, FTACV has not

been applied to HER processes. Some studies utilising FTACV for oxygen evolution reaction can be found in literature.[222] Thus, the investigation of HER by using FTACV technique is reported for the first time. The results of the more comprehensive FTACV can resolve some ambiguities in the electron transfer processes and provide some qualitative mechanistic insights.

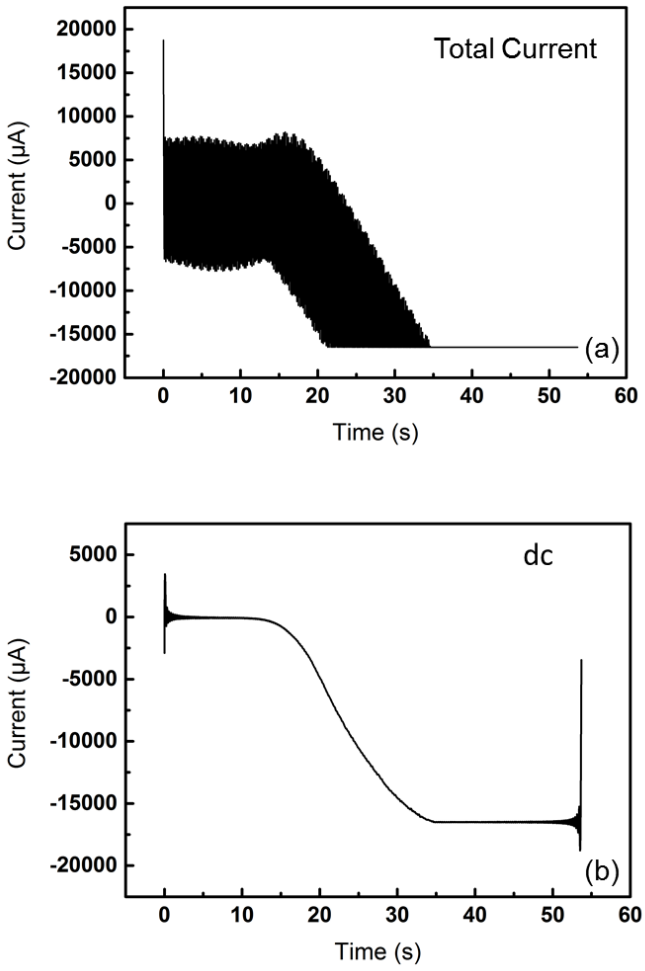

Figure 4.17 The total current (a) and dc component (b) in large amplitude ac voltammograms of HER process for the **Pt/C** electrocatalyst. FTACV parameters: Frequency = 5 Hz, Amplitude = 100 mV, Scan rate = 14.9 mV/s. Potential scanned from +0.196 to -0.604 V *vs.* RHE.

Preliminary characterisation of Pt/C catalyst for HER process in 0.5 M H_2SO_4 has been conducted by FTACV using an amplitude of 100 mV and a scan rate of 14.9 mV/s in a linear sweep range from 0 to -0.8 V *vs.* Ag/AgCl (+0.196 to -0.604 V *vs.* RHE), as shown in Figure 4.17. Due to the limitation of the instrument, current signal larger than 16.5 mV cannot be detected. Valuable information can be extracted from the total current (Figure 4.17a) using the

FT-band selection-iFT process.[10] The extracted aperiodic component from the total current is governed by the featureless water reduction current and can be analogous to a dc voltammogram (Figure 4.17b). Nevertheless, catalytic water reduction has a negligible contribution to the ac harmonics, thus the underlying redox processes become directly accessible.

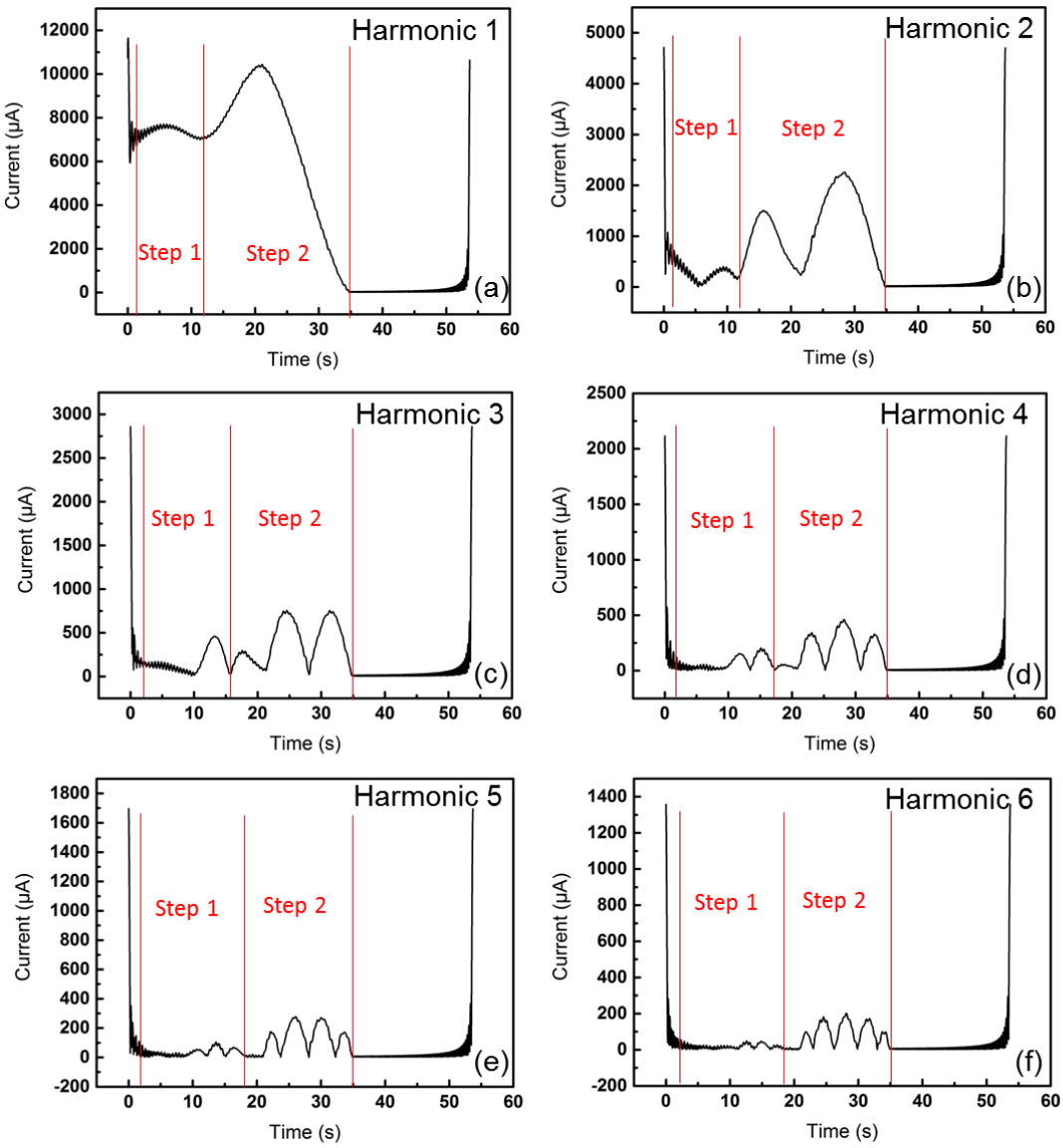

Figure 4.18 Fundamental to sixth harmonics (a-f) in large amplitude ac voltammograms of HER process for the **Pt/C** electrocatalyst. FTACV parameters: Frequency = 5 Hz, Amplitude = 100 mV, Scan rate = 14.9 mV/s. Potential scanned from +0.196 to -0.604 V *vs.* RHE.

Figure 4.18a-f show the fundamental to sixth harmonics data for the Pt/C catalyst. For the first harmonic, two peaks can be discovered at potential of ca. 0.112 V and – 0.119 V (*vs.* RHE). However, the first peak is only observable in the harmonic data, while the dc signal shows no signal in the corresponding potential range. The first peak (step 1) is designated as the hydrogen adsorption process (Volmer step, equation (4.7)). The second peak (step 2) is assigned to the electrochemical desorption process (Heyrovsky step, equation (4.8)). The onset potential for the two steps can also be identified. For second and higher harmonics, step 2 had typical harmonic peaks, while some peaks disappeared in the step 1. When comparing the harmonic data, it is found that the onset potential of step 2 shifts to more negative values for higher harmonic data.

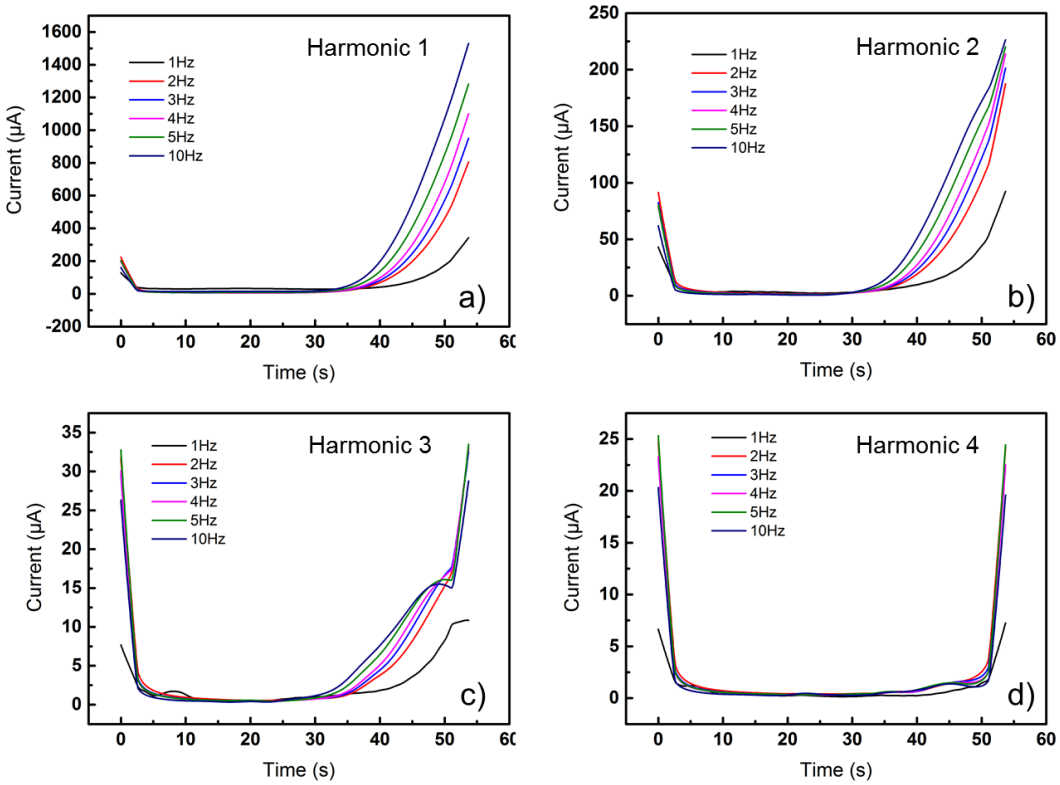

Figure 4.19 Fundamental to fourth harmonics in large amplitude ac voltammograms of HER process for the **MoO_2@C** electrocatalyst. FTACV parameters: Frequency = 1-10 Hz, Amplitude = 100 mV, Scan rate = 14.9 mV/s, Potential scanned from +0.196 to -0.604 V *vs.* RHE.

Considering the harmonic data for Pt/C as the reference signal, it is possible to elucidate the performance and mechanism of the as-synthesised catalysts via the FTACV responses. Figure

4.19 indicates the FTACV response of MoO_2@C HER electrocatalyst in 0.5 M H_2SO_4 solution with varying frequencies. There are no peaks existed in the harmonic 1 data before the potential of -0.8 V (*vs.* Ag/AgCl). Similar poor peak observation can also be found for the higher harmonics. It can be argued that these results imply the bad performance of the catalyst, which is confirmed in the dc LSV polarisation curve. In addition, this result then indicates that for an electrocatalyst with poor catalytic performance, the redox reaction is also affected and can hardly be detected by the FTACV higher harmonics.

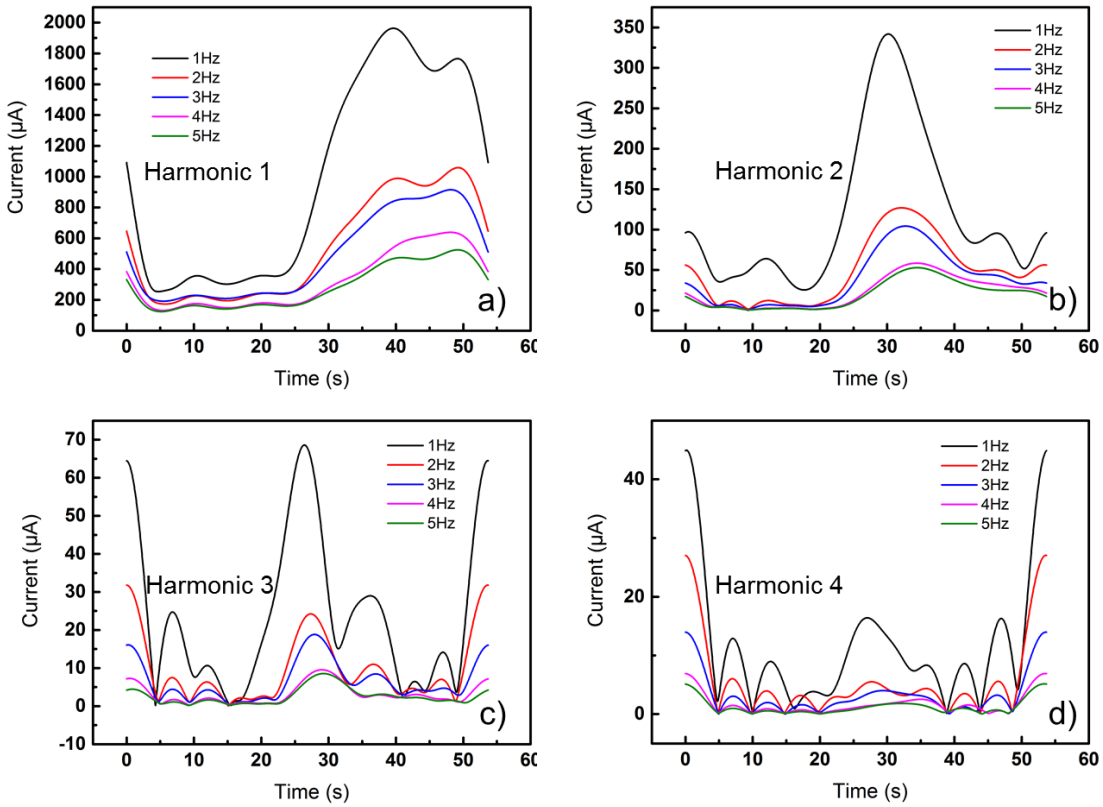

Figure 4.20 Fundamental to fourth harmonics in large amplitude ac voltammograms of HER process for the **MoS_2@C** electrocatalyst. FTACV parameters: Frequency = 1-5 Hz, Amplitude = 100 mV, Scan rate = 14.9 mV/s. Potential scanned from +0.196 to -0.604 V *vs.* RHE

Next the FTACV characterisation of MoS_2@C and MoS_2-9%Co@C nanocatalysts for HER process in 0.5 M H_2SO_4 were also performed, as shown in Figure 4.20 and Figure 4.21. For MoS_2@C catalyst, noisy responses have beeen detected along with peak signal in the first harmonics with varying frequencies. Thus, it is difficult to identify step 1 and step 2 processes

in the first harmonics. In higher harmonic responses, the FTACV harmonic characteristics become more noticeable. For instance, the two left peaks in harmonic 2 data (1 Hz) can be assigned to the step 1 process, and the two peaks on the right hand side can be designated to step 2 process. For the MoS_2-9%Co@C sample, similar FTACV characteristics have been found for the fundamental to fourth harmonics when compared to the MoS_2 catalyst. Nevertheless, they differ in terms of the magnitude of the current. This can be explained that higher current responses would lead to more redox reactions, and thus producing more hydrogen. The polarisation curves for the two catalysts also confirm this argument. In addition, by comparing the signals of the step 1 process for the two catalysts, it can be concluded that the MoS_2@C sample has a more drastic step 1 process.

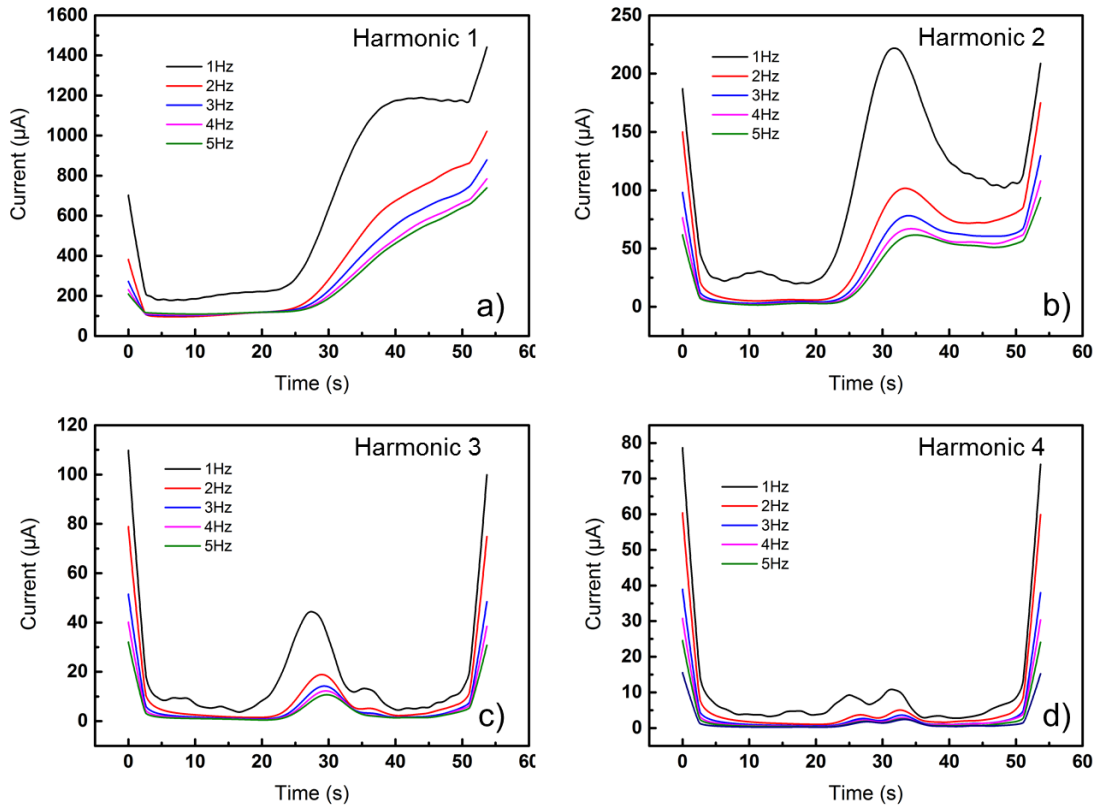

Figure 4.21 Fundamental to fourth harmonics in large amplitude ac voltammograms of HER process for the **MoS_2-9%Co@C** electrocatalyst. FTACV parameters: Frequency = 1-5 Hz, Amplitude = 100 mV, Scan rate = 14.9 mV/s. Potential scanned from +0.196 to -0.604 V *vs.* RHE

Next, a further analysis of the harmonic data for different electrocatalyst can be conducted. Figure 4.22 shows the comparison of the harmonic 2 responses for the three catalysts, MoS_2@C, MoS_2-3%Co@C, and MoS_2-9%Co@C. Both step 1 and step 2 processes can be identified from all three catalysts, while they differ in terms of the shape and magnitude. For the largest peak in step 2, a similar trend can be seen when comparing the magnitude of the peaks with the polarisation curve in LSV. Consequently, this response provides a means of method to evaluate the performance of a catalyst. However, for FTACV to be more accepted in the general research community, a comprehensive simulation of the process is necessary. An experiment-simulation comparison would then be more convincing to show the performance and unveil the underlying mechanisms.

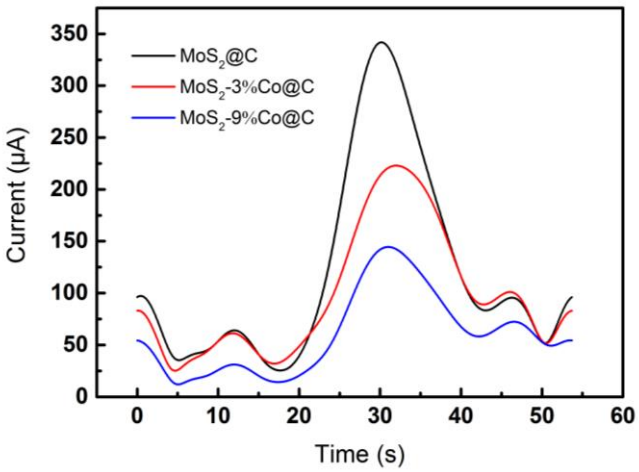

Figure 4.22 Second harmonic responses in large amplitude ac voltammograms of HER process for the **MoS_2@C (black)**, **MoS_2-3%Co@C (red),** and **MoS_2-9%Co@C (blue)** electrocatalysts. FTACV parameters: Frequency = 1 Hz, Amplitude = 100 mV, Scan rate = 14.9 mV/s.

4.5.3 Catalytic Thermal Decomposition of Hydrogen Sulfide

The synthesised molybdenum disulfide samples were then served as a heterogeneous catalyst for the thermal decomposition of hydrogen sulfide (H_2S). The catalytic performance of prepared MoS_2 Catalysts were evaluated by thermal decomposition tests on H_2S. Figure 4.23 illustrates the conversion of H_2S into H_2 for different temperature runs. The test was performed under 1 atmospheric pressure at each temperature (500 °C, 600 °C and 700 °C) for 2 h with no

interrupt, followed by a 6-hour run at 800 °C. The conversion of H_2S to H_2 was determined every 7 minutes. As is shown in Figure 4.23 (a, b, c), conversion of H_2S increases as temperature increases, which is consistent with theory and literature [223]. When the reaction temperature increases, the nanocrystal MoS_2 transferred to higher crystalline structures. A value of 88% H_2S conversion was soon achieved with MoS_2 catalyst at 800°C (Figure 4.23a). In comparison, the MoS_2-3%Co and MoS_2-3%Ni catalysts gave maximum 80.14% and 86.1% at the same condition. However, it has been reported that Co and Ni can act as a promoter for H_2S decomposition and hydrotreating process [224], [225]. The cause for the decrease in conversion can be explained by the lower Mo loading in the doped samples as Mo is supposed to be the active component for the decomposition. Stability test shows that 63% conversion was still attained after 6 h of operation for MoS_2 catalyst. Both 3% Co or Ni doped sample has a stable conversion of 60%.

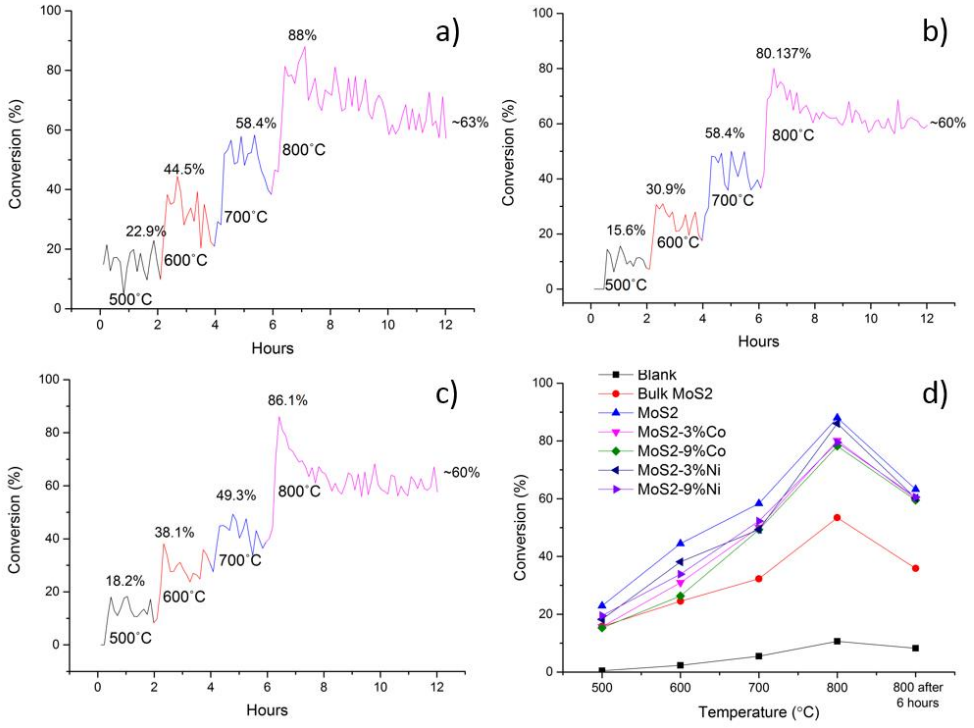

Figure 4.23 Conversion rates of the catalytic H_2S decomposition reaction. (a) MoS_2@C, (b) MoS_2-3%Co@C, (c) MoS_2-3%Ni@C. (d) Conversion vs. Temperature for all tested catalysts.

The blank non-catalytic run and commercial bulk MoS_2 catalytic run have been used as references for activity comparison, as shown in Figure 4.23d. Catalysts with higher doping metal weight have also been tested and used for evaluation. For the reaction without catalyst,

extremely low conversion of ca. 10% was obtained at 800 °C in our setup. In the test of bulk MoS_2 catalyst, 53.5% H_2S conversion is found at 800 °C and stabilised at 35.9% after 6 h. All of our synthesised catalysts show extraordinary activities to the bulk MoS_2 one. This could be attributed to the nano-structures created in the catalysts with high dispersion of active site. When comparing the H_2S conversions for increasing Co doped samples, the conversion drops slightly owing to the decreasing in Mo wt%. This further confirms the above statement of Mo being the active component. However, in the case of MoS_2-3%Ni, it attained 86.1% conversion at 800 °C with lower Mo loading (14.71 wt%, ICP data in Table 4.1). Also, literature shows that the adsorption of H_2S onto nickel metal surface is strong and dissociative [226]. This implies that Ni has a better promoter effect compared to Co.

4.6 Conclusions

In summary, a series of molybdenum sulfide embedded mesoporous carbon microspheres have been synthesized via a hydrothermal method. The prepared MoS_2 nanocrystals are evenly distributed in the mesoporous carbon microspheres. These microspheres are in the size of 2 – 8 μm. Transition metals of cobalt and nickel have been added into the synthesis route, and were successfully loaded into the samples with high dispersion. XRD and XPS shows CoMoS and CoS_2 phases have been formed for the Co doped sample, NiS_2 phases for Ni doped sample. Catalysts with higher doping metal loadings were also synthesised, with different surface morphologies observed.

The synthesised particles were then examined as the HER electrocatalysts via traditional LSV and advanced FTACV techniques. From the polarisation curves, the performances of the electrocatalysts cannot compete with the ideal candidate, while this study provides a means of innovative electrochemical technique to qualitatively study the mechanisms involved in the HER processes.

The prepared samples were then also evaluated as the catalysts for thermal decomposition of hydrogen sulfide. The results show excellent activity and stability compared to the commercial bulk MoS_2 catalyst, owing to the structures of the nanocatalysts. The synthesised Co or Ni doped samples have slightly lower conversions, which is caused by the lower Mo loading in the catalysts.

Chapter 5 Carbon Nanotube Forest on Gold Electrode for pH Sensing

Abstract

This chapter demonstrates the preparation of an electrochemical pH sensor constructed by functionalised CNT forest electrode. Growth of vertically aligned CNT forests on a gold electrode was achieved via a chemical vapour deposition process. Voltammetric techniques such as CV and SWV have been adopted to examine the electrochemical response of the fabricated electrode. In addition, anthraquinone has been covalently immobilised onto CNT forest structure to be utilised a pH sensor. The voltammetric results indicate well correlated pH-potential relationships in the pH range of 2 to 12 for both CV and SWV. The electrochemical properties of the sensor have also been assessed by the FTACV technique.

5.1 Introduction

In chapter 4, the modification of the glassy carbon electrode by the carbon sphere supported molybdenum disulfide has been described, and its application in hydrogen evolution reaction examined. This chapter describes the modification of a gold electrode surface by carbon nanotubes (CNTs). The most common method to combine CNTs onto the electrode surface is the drop casting of CNTs-dispersed solvent onto an electrode. However, the CNTs structure is normally unorganised and deposited as a bulk material or a thin film. In this work, an innovative procedure to produce CNTs directly on gold electrode has been developed. CNT forest, an organised structure, was directly synthesised onto the gold surface via a CVD process.

Additionally, the electrochemical properties of the prepared CNT forest electrode was studied by a well-defined redox couple via electrochemical techniques of CV and FTACV. Its application as an electrochemical sensor has also been studied by depositing anthraquinone

onto the CNT forest structure. Then the performance of the CNT forest sensor was tested and compared to literature.

5.2 Carbon Nanotube Electrode

Carbon nanotubes (CNTs) have been a popular research topic since their discovery by Iijima in 1991.[227] After more than two decades of development, the material is now utilised in many applications such as polymer composites, electrochemical energy storage, conductive additives, air filtration, superstrong fibres.[228] Currently, an annual global production of thousands of tons of CNTs has been achieved. In particular, CNTs are extremely attractive material for electrochemical sensing due to their unique mechanical, chemical and electronic properties.[229] One of which is the fast electron transfer kinetics that results from the edge plane graphite sites within the walls and at the ends of CNTs.[230] It has been reported that the edge plane / basal plane ratio in CNTs is large.[231] These remarkable electrochemical features make CNTs great candidates for use in Faradaic processes. Moreover, CNTs are able to accept or withdraw charges from or to molecules in the nearest chemical environment, attributed to the electron clouds surrounding the walls. It has also been demonstrated that CNTs exhibit great electrocatalytic activity for a number of compounds, including neurotransmitters,[232] hydrogen peroxide,[233] ascorbic and uric acid,[234] hydrogen sulfide,[235] amino acids[236] and DNA.[237] As a consequence, CNTs have been incorporated into electrochemical sensors, which hold many benefits such as high sensitivity, low limits of detection, and fast electron transfer kinetics.[231] The performance of the CNTs based electrode is governed by the synthesis method of the nanotubes, method of electrode attachment, surface modification of CNTs, and the addition of electron mediators.

Synthesis Method

Among these criteria, the synthesis techniques for CNTs have been discussed in chapter 1. In short, three primary techniques are used for synthesising CNTs, which are arc discharge, laser ablation and chemical vapour deposition (CVD). CVD is the most dominant synthesis method for producing high-volume CNTs. A detailed description of CVD process for synthesising CNTs has also been given in chapter 2.

CNTs Attachment

The next criterion is the electrode attachment of CNTs. Physical adsorption of CNTs onto electrode surface (e.g., glassy carbon) is the most common method to prepare CNTs based electrodes for electroanalytical purposes.[238] Typically CNT powders are dispersed in polymer matrices or deposited as thin films. A summarisation of the different deposition methods of CNTs onto an electrode surface is illustrated in Figure 5.1. The first technique in the top left corner is drop casting, which is the simplest technique accomplished by the dropping of low-carboxylated CNTs dispersed solvent (e.g., DMF) onto the surface. Next is the spraying of an aqueous solution (non-carboxylated CNTs dissolved with surfactants) by using aerosols. Electrophoretic deposition uses DC field to deposit CNTs onto a metallic surface. The last method of Teflon-CNT composite is prepared from the tight press of the homogenized mixture (50 w/w %) by using a stainless-steel screw.

Figure 5.1 Several deposition techniques for CNTs on the surface of electrodes. (a) Drop casting; (b) Spraying; (c) Electrophoretic deposition; (d) Teflon-CNT composite.[239]

In general, CNTs can be divided into three types based on morphology differences: agglomerated CNTs, vertically aligned CNT (VACNT) arrays, and horizontally aligned CNT (HACNT) arrays. The CNTs described above belong to the agglomerated category, which are usually unorganised architectures with limiting properties. Partially aligned or organised CNT structures are more promising to expand the properties of individual CNTs and achieve new functionalities. As shown in Figure 5.2, bulk mixing of CNT powders to form random dispersion and large-scale film CNT structure is the dominant application at present. For CNTs application in the future, more organised structures such as CNT forest and yarn or even single and multiple CNTs are preferable in both macroscale and nanoscale devices. Nevertheless, the mechanical, thermal and electrical properties of current CNT macrostructures remain considerably lower than that of individual CNTs.

Figure 5.2 Emerging CNT applications, from large-scale dispersions and films that are presently commercialized, to ordered macrostructures and nanoscale devices in the future.[228]

Surface Modification and Functionalisation of CNTs

There are mainly two functions of CNTs when utilised in electrochemical devices, either they are used as an active material or a scaffold of other active materials. In the first case, the electrochemical sensor can achieve a higher surface area with good electrical conductivity.

This in theory will increase the sensitivity of the sensor, while also reduce the selectivity of device. Hiura *et al.* reported that a mixture of HNO_3, H_2SO_4 and potassium permanganate applied for more than 5 h to MWCNTs can successfully purify and oxidize the nanotubes, while CNT fragmentation also occurs during the process.[240]

From the perspective of CNTs being used as a scaffold, the improvements on surface area and electrical conductivity are preserved, and the selectivity will also be promised in consequence of the coating of active material. Hence, the researches focused on CNTs have trended to use them as the scaffold for other active materials in recent literature. The CNTs themselves used as the active substances for the direct interaction with the analyte are less concerned.

Alignments of CNTs

The arrangement of CNTs on electrode is then reviewed, as shown in Figure 5.6. Three categories have been proposed based on the control of the CNTs arrangements, which are unorganised network, partial alignment and organised structure.

Figure 5.3 Increasing control over CNT structures, from (a) unorganised network,[241] to (b) partial alignment,[242] to (c) organised structure.[243]

The first application of CNTs for electrochemical sensing was reported by Britto *et al.* that the oxidation of dopamine was examined by a randomly distributed network of CNTs on a glass rod.[244] Their result illustrates an ideal reversibility of the reaction under CV, which differs from traditional carbon electrodes (e.g., CPE, GC).[244] It is argued that the enhanced

reversibility is resulted from the defect sites and edge planes inside the CNTs.[245] After the publication of these results, the application of CNTs in electrochemical processes received tremendous attention. One important application of CNTs is the study of neurotransmitters (e.g., dopamine, uric acid and ascorbic acid). For instance, Hocevar *et al.* reported that enhanced voltammetric performance for the detection of dopamine has been obtained by using a carbon fibre microelectrode modified with MWCNT and Nafion.[246] Electrochemical biosensors incorporated with unorganised CNT structure have also been developed to detect glucose.[247]–[249] In these studies, glucose oxidase was fixed onto the CNT network to achieve the selective detection of glucose. This type of CNT arrangement has also been applied for other biological applications such as identification of cancer and disease biomarkers,[250], [251] detection of antigens,[252] and proteins associated with pregnancy.[253] In addition to these biological applications, heavy metal ions and other water contaminants can also be identified by CNT based electrochemical sensors. Profumo *et al.* reported the detection of arsenic (III) and bismuth (III) ions in natural and high-salinity waters by a gold electrode modified with thiol ended CNTs.[254] The unaligned CNTs can also be used to form a conductive polymer composite, which offers the material flexibility and thus can function as a stretchable electrochemical sensors. The CNTs in above described applications are normally of random distribution with no control of the alignment or orientation.

Next the partial controlled and aligned CNT arrangements are reviewed. Partial alignment of CNT structure can be achieved through two methods, which are the usage of CNT forest arrays or the self-assembly mechanism. For the array approach, the electrochemical properties of electrodes incorporated with arrays of VACNT have been examined by Li *et al*., which illustrates a three dimensional interaction with the redox species.[255] Significant improved faradaic responses have been obtained for the CNT electrode. Moreover, CNT forest arrays coated with glucose oxidase at their ends have been utilised as an electrochemical glucose sensor.[256] Functionalisation of the CNT forest arrays by immobilising carboxyl group onto the CNT surface has also been attempt to sense DNA strands.[257] check. In addition, antibodies have been grafted onto the ends of carboxylated VACNTs, allowing high selective sensing of specific biomarkers.[258], [259] As for the second approach of self-assembly, Gooding *et al.* first reported that CNTs can be stacked vertically onto a cysteamine modified

gold electrode.[260] The approach was also attempted to control the assembly of CNTs on a gold electrode by using thiol groups, and a further attachment of glucose oxidase on the ends of the CNTs allows the selective sensing of glucose.[242] However, both of the approaches cannot guarantee a well-defined organisation of the CNTs on the electrode surface. This can be rationalised by considering the mechanism behind the two methods. A large portion of CNTs would stack vertically end to end on electrode surface. This is due to functional groups prefer to combine at the edge or defect sites, which mostly appear at the end of the CNTs. Consequently, a part of the CNTs assemble in a parallel manner, which destroy the vertical alignment and result in a partial alignment.

A more organised CNT based electrode beyond the partial alignment is also appealing. These can be achieved by further developing the previous approach. Nguyen *et al.* reported that spun on glass can be used to support the CNT forest array on electrode surface.[261] This approach has since been modified and continued for several applications, including glucose sensor,[246] DNA sensor,[262] heavy metal ion detector,[263] and identification of specific proteins.[264] A different approach to Nguyen has also been proposed by Taurino *et al.* that the CNT forest array was uncovered to ensure the diffusion of chemical species throughout the whole structure, while the parameters of the CVD procedure was altered.[265] Results show that vertically aligned CNT forests can be formed, different morphologies such as kinked, horizontal or grouped could also be attained.

Vertically Aligned CNT Forests

Figure 5.4 summarises the major research trends of electrochemical sensing device made of CNTs. The two main streams are the development of more complex functionalisation and the more organised and aligned CNT structure. The bottom right corner on the graph, an organised and functionalised device, is the goal of many research work to achieve an ideal electrochemical sensor with superior performance. A third alternative approach to improve the sensing performance might be the control of CNT porosity and thus the diffusion of redox species along the structures.

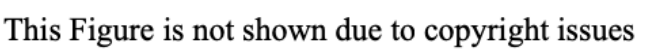

Figure 5.4 Literature trends of CNT researches as electrochemical sensor towards more organised and functionalised electrode structure. (a),[266] (b),[267] (c),[241] (d),[256] (e),[260] (f),[242] (g),[261] (h).[243]

It has been demonstrated by Gokoglan *et al.* that a flexible glucose sensor can be produced by utilising vertically aligned CNT forests. The reported improved electrochemical sensing ability of VACNT forests can be explained by considering the structure of the material. It is suggested that the observed fast electrode kinetics are arising from the defect sites within the hexagonal lattice and the edge planes inside the CNT structure.[64]

In addition, it has been argued that the orientation of the CNTs, number and type of defects and processing technique are crucial to the electrochemical activity of the CNTs.[268] Therefore, enhanced sensing performance can be attained by orientating the CNTs vertically regards to the electrode surface. This orientation of the CNT structure would thus causing the exposure

of the ends of the CNTs to the electrolyte and analytes. The forest structure would also enable the redox species reaching the sidewalls of CNTs, resulting in a higher active surface area.

5.3 Electrochemical pH Sensing

Chemical sensors are devices that can provide a certain type of response correlated to the quantity of a specific chemical species. They can be categorised into electrical, optical, mass, thermal and electrochemical sensors. Among these, electrochemical sensors are of particularly appealing due to their excellent detectability, experimental simplicity and low cost.[269] The sensors normally include a receptor to transform the chemical information into a form of energy via electrochemical techniques, and a transducer to transfer the energy information into a detectable signal.[13] Electrochemical sensors have been utilised in a vast range of applications in the fields of environmental, agricultural, pharmaceutical and clinic analysis. Among these, the detection and control of the pH is of great importance in many biomedical and chemical processes. For instance, pH measurement of water is essential to manage water resources and protect them from contamination as pH is one of the significant parameters in water quality.[270] In addition, monitoring the pH changes in food and beverages industry is also important as it is an indicator of freshness or deterioration.[271] Furthermore, pH changes may affect and monitor potential physiological processes such as tumor metastasis, [272] wound healing[273] or microbial infection.[274]

There are mainly three types of electrochemical sensors: potentiometric, amperometric and voltammetric. Potentiometric sensors measure the potential across an electrode/electrolyte interface to quantify the concentration of the analyte.[275] They are normally operated in zero-current conditions to achieve thermodynamic equilibrium conditions. Consequently, the half-cell potential at the electrode can be related to the concentration of the desired analyte by the Nernst equation. The three basic types of potentiometric devices are ion-selective electrodes (IES), coated wire electrodes (CWES) and field effect transistors (FET). IES constitutes the largest group in potentiometric sensors, and the most widely utilised ion-selective electrodes are the glass pH sensors.[276] The first commercialised glass pH electrode adopted the Corning 015, which is a glass made of ca. 22% Na_2O, 6% CaO and 72% SiO_2.[277] In CWES, a sensing

system is constructed by directly coating an appropriate ion-selective polymer membrane onto a conductor. This type of device eliminates the requirement for an internal reference electrode, which is valuable for *in vivo* monitoring.[278] The third type, FET, is often combined with an ion-sensing membrane to construct ion-sensitive field-effect transistors (ISFET). The FET is a solid-state device capable of detecting the buildup of charge on the ion-sensing membrane due to their high-input impedance and low-output impedance.[269] For instance, Akiyama *et al.* reported the fabrication of ISFET by using silicon films on sapphire substrates.[279] By using the structure, the Ta_2O_5 film has been discovered to have the highest pH sensitivity (56 mV/pH), compared to SiO_2 and ZrO_2 films. In addition, it is reported that an electrolyte-gated graphene FET exhibited a linear relationship between its conductance and electrolyte pH, implying a potential application as pH sensor.[280]

For amperometric and voltammetric sensors, a current-potential relationship is established through the oxidation or reduction of an electroactive species. In amperometric method, a fixed potential is applied, and the resulting current is measured against time. While in voltammetric sensors, the potential is varied during the measurement, including different potential patterns such as CV, LSV and SWV. The performance of these sensors is strongly affected by the working electrode materials. Solid electrodes such as carbon, platinum and gold have been extensively utilised as working electrode materials. These materials exhibit several advantages such as versatile potential window, low background current, low cost, and chemical inertness. Chemically modified electrodes have received considerable attention in electrochemistry. In these electrodes, a modifier agent is deliberately immobilised onto the electrode surface via chemical reactions, chemisorption, composite formation or polymer coating.[269] For example, Wildgoose and co-workers have shown the covalent chemical derivatisation of anthraquinone on carbon powder to produce a simple pH probe.[281] Another demand for amperometric sensors is the small dimension of working electrode, which promotes the development of microelectrode systems. A number of attractive characteristics are associated with the microelectrodes, including the exploration of microscopic domains, detection in microflow system, time-resolved probing of processes in cells, and small analyte volume.[282] For example, Makos and co-workers developed a carbon-fibre microelectrode modified with a diazonium salt to measure physiological pH changes in biological media.[283] Screen printed

electrode constitutes another large section of pH sensors due to its simplicity and portability. This enables them to be adopted in clinical, environmental or industrial analysis outside a centralised laboratory.[284] Dai *et al.* fabricated an alizarin based carbon electrodes by screen printing technology, which was utilised as a voltammetric sensor to monitor pH in unbuffered media.[20] Another study by Koncki *et al.* prepared a plastic and screen-printed disposable pH sensors based on ruthenium dioxide for pH measurements.[285]

Apart from the above electrodes and materials, CNTs have also been utilised for pH sensing applications. Since the discovery of CNTs, the material has been extensively researched and applied in different fields for various applications. Sensor development is one of the most widely investigated topics for CNTs-based-devices. These sensing devices are benefited from the physical and catalytic properties of CNTs, including high electrical conductivity, chemical stability, high surface area and mechanical strength. In particular, there have been huge effort to utilise CNTs as pH sensors. The effect of hydrogen or hydroxyl ions on the electrical properties of CNTs have been extensively investigated. For instance, Lee *et al.* discovered that the electrical conductivity of MWCNTs can be altered by different pH values of the surrounding environment.[286] This pH dependent property of the MWCNTs was then utilised to prepare a pH sensor. Another study by Wang *et al.* illustrated the temperature and pH-responsive properties of SWCNTs when the material is dispersed in poly(N-isopropylacrylamide) and poly-L-lysine solutions.[287] Furthermore, it is reported that MWCNT sheets decorated with Ni particles can also be served as pH sensors.[288] The size of the Ni particles was determined to significantly affect the pH-sensing properties of the material.

Various functionalisations on CNTs have also been developed for a wide range of applications, including pH sensors.[289] For example, in biological field, CNTs offer the advantages of effectively crossing biological barriers. It has been indicated by a ground-breaking study that various functionalised SWCNTs or MWCNTs show the capacity to be taken up by a number of cells.[290] Thus, the material can be potentially adopted in many biological systems. It has been reported that a pH-dependent optical device for cell sorting and imaging can be produced by noncovalently binding CNTs with polyethylene gylated fluorescein. [291] However, the study points out that the physically adsorbed dyes may drop from the surface of CNTs due to

a weak interaction.[291] As a result, the sensor reliability will be decreased, and the dropped dye may be toxic to the environment. Therefore, a firm binding of the dyes onto the CNT structure is essential to fabricate a robust and effective pH sensor. Zhao *et al.* functionalised CNTs with a pH responsive dye of 6,8-dihydroxy-1,3-pyrenedisulfonic acid disodium salt to monitor pH values over the range of pH 5.6–8.3.[292] In another study, functionalised and dielectrophoresis aligned SWCNTs have been developed to give a linear response in the pH range of 5-9.[293]

In this work, the directly synthesised vertically aligned CNT forest on gold surface was first studied by electrochemical voltammetric techniques such as CV and FTACV. A further functionalisation of the CNT structure was also attempted by covalently immobilising anthraquinone onto the CNT structure, and the electrode was utilised as a pH sensor.

5.4 Experimental

5.4.1 Electrode Fabrication and Device Assembly

Three types of gold electrode with different substrates have been fabricated using the method described in chapter 2. The substrates utilised include glass, fused silica and silicon. However, the preparation of CNT forest onto the gold electrodes were different. Initially, for gold electrode on glass substrate, it was suggested that a liquid mixture of PVDF, PCBM and CNT was prepared and used as a conducting and adhesive film on gold electrode to support CNT forest. Self-synthesised CNT forest on a separate substrate was then transported onto the film by using a mask and aligned to the right position. This electrode is denoted as CNT-Au-glass. In terms of the gold electrodes with fused silica or silicon substrates, CNT forest was directly grown onto the gold electrode, denoted as CNT-Au-FSi and CNT-Au-Si. Anthraquinone has also been immobilised onto the CNT-Au-Si electrode by using a method described in literature,[281] and denoted as AQ-CNT-Au. As shown in Scheme 5.1, an acid treatment of the anthraquinone-1-diazonium chloride on SWCNT by hypohosphorous acid can form 1-anthraquinoyl radical, which then bond to the edge-plane site on the CNT forest structure.

Scheme 5.1 Schematical illustration of (a) the derivatization by the reduction of anthraquinone-1-diazonium chloride using hypohosphorous acid, with (b) subsequent attack of the 1-anthraquinonyl radical onto the edge-plane sites on a vertically aligned SWCNT.

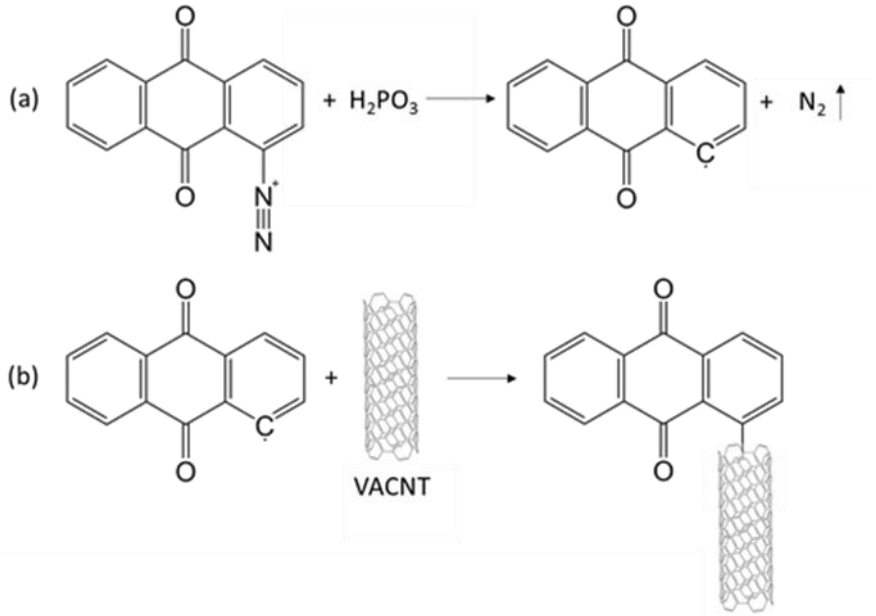

The set-up for electrochemical measurements is shown in Figure 5.5. After the electrode is fabricated, a PDMS cell with a hole of 3 mm diameter in its bottom centre was made to cover the electrode surface, providing a defined working area. Then the three-electrode configuration was completed by combing a reference electrode and a counter electrode.

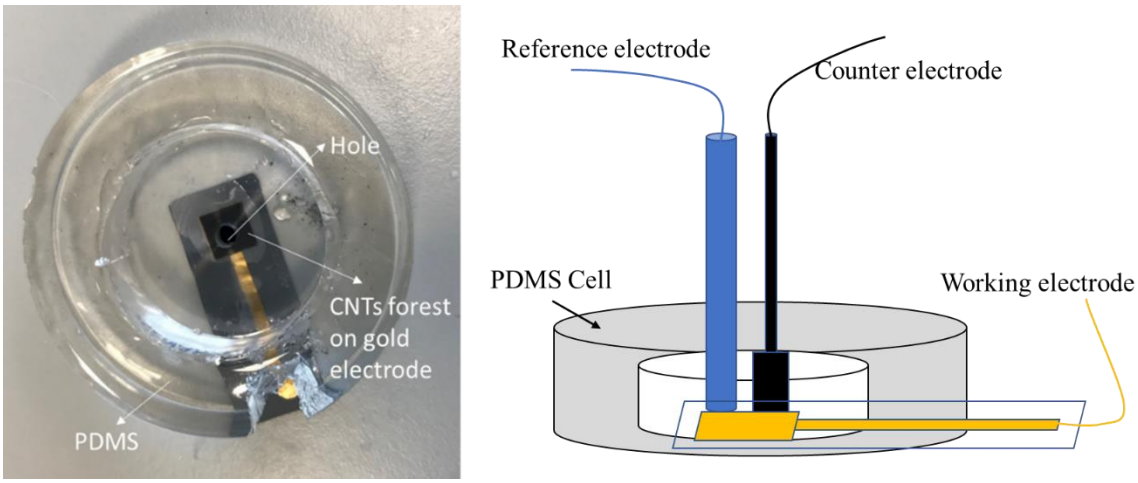

Figure 5.5 Image showing the electrochemical cell used for measurement, including a self-made PDMS cell attached onto the working electrode.

5.4.2 Materials Characterization

All cyclic voltammetric measurements were recorded using an Autolab Potentiostat PGSTAT 100 (Metrohm, The Netherlands) with a standard three electrode configuration. A gold electrode on silicon wafer with CNT forests was adopted as the working electrode. A platinum electrode was used as the counter electrode with a silver/silver chloride (Ag/AgCl) provided the reference electrode. The approach to alter the concentration of ferrocyanide was by addition of high concentrated solutions of corresponding chemicals into the solution. The solution was then mixed by a plastic pipette and stood for a while to ensure uniform chemical distribution. FTACV measurements were conducted using a homemade potentiastat. The data handling and analysis procedure is the same as described in section 3.3.1.

5.5 Results and Discussion

This section describes the results of the fabricated CNT forest on gold electrode and its applications in electrochemical measurements. The characterisation of the CNT forest is first being examined by several techniques such as SEM and Raman Spectroscopy. Then the performance of the CNT forest on different types of substrate have been studied and compared by the redox reaction of Ferrocyanide using CV. After that, CNT forest directly grown on gold electrode was utilised for cyclic voltammetric measurements of Ferrocyanide with varying concentration. Furthermore, anthraquinone was deposited onto the CNT forest and employed as a pH sensor. The performance of the sensor has been studied and compared with literature.

5.5.1 Gold Electrode and CNT Forest

The production of CNT forest on gold electrode was initially conducted by the approach outlined by Ahmad *et al.* that the CNT forest was synthesised on a separate substrate and transferred onto the gold electrodes by using an adhesive polymer film.[76] A graph shows the structure of the fabricated CNT forest on gold electrode has been shown in Figure 5.6a. Nevertheless, a number of issues have been found for this procedure. The first problem is the alignment of the CNT forest onto the underlying gold electrode can be relatively difficult. Reproducibility of the CNT forest electrode can also not be guaranteed due to the transfer procedure. Next is the polymer film also contributes to the electrochemical responses of the

electrode. Therefore, the direct synthesis of CNT forest on gold electrode has been attempted for fused silica and silicon substrates (as shown in Figure 5.6b, c).

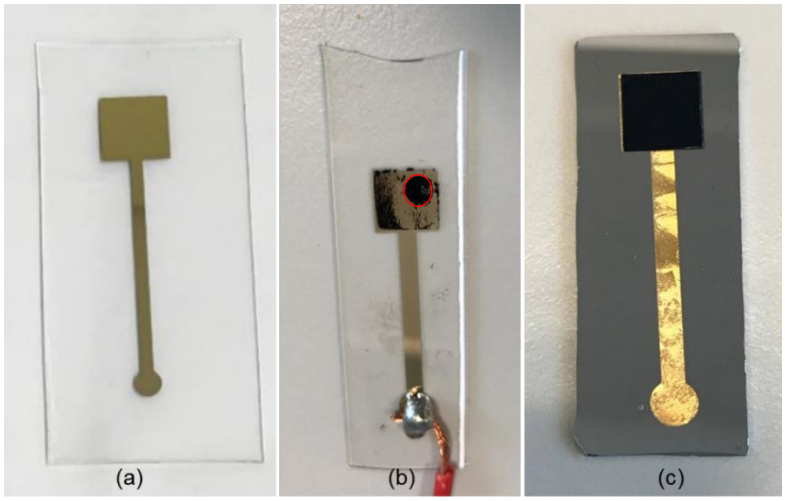

Figure 5.6 Images illustrating the gold electrode structure on glass substrate (a) and CNTs forest grown directly onto the gold electrode on fused silica (b, after PDMS cell removed, red circle shows the working area) and silicon substrate (c).

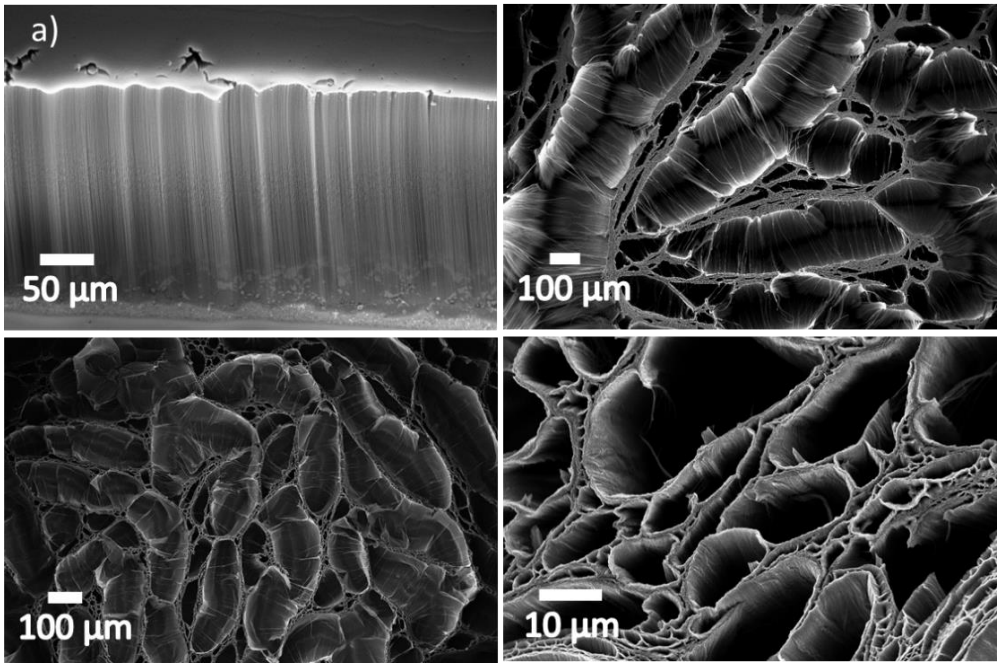

Figure 5.7 SEM images of the prepared CNT-Au-Si electrode. (a), (b) Before measurements; (c), (d) Densified and after measurements. *Characterisation done by our collaborator Chris Valentine.

Figure 5.7 show the surface morphologies of CNT forest before and after measurements by SEM. As shown in Figure 5.7a, vertically aligned CNT forest with a height of ca. 200 µm has been successfully synthesised on gold surface. It can be seen that some CNT structures have been aggregated into a single large cluster. A closer examination at the top of the CNT forest is given in Figure 5.7b. After the measurements, an increased amount of aggregation of the CNT forest can be observed. Additionally, the vertically aligned structure of CNT forest become inclined towards a centred aggregate.

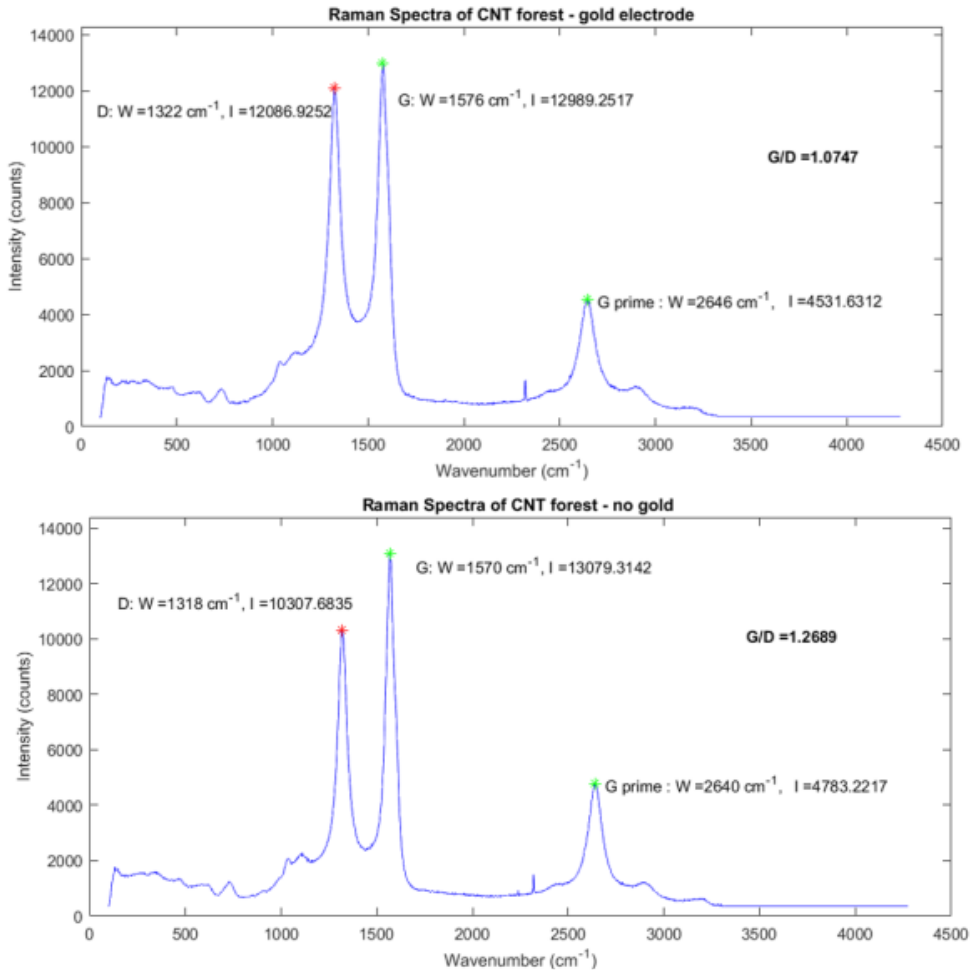

Figure 5.8 The Raman spectra for CNT forests synthesised in the presence (upper) and absence (lower) of gold under-layer. *Characterisation done by our collaborator Chris Valentine.

The quality of CNT forest synthesised on gold (on a silicon wafer) has also been examined by Raman spectroscopy, compared with those synthesised on silicon. Figure 5.8 shows the Raman

characterisations of the two synthesised CNT forests. The ratio of the G-band (ca. 1593 cm^{-1}) and D-band (ca. 1350 cm^{-1}) peak heights can be used to assess the quality of the CNTs.[294] The G/D ratio of the CNTs synthesised without gold under-layer has been calculated as 1.27, and 1.08 for its counterpart. The gentle decrease in the G/D ratio and an increase in the D peak intensity reveal a quality reduction of the CNT forest synthesised with gold under-layer. Nevertheless, the decrease is minimal, and the direct synthesis of CNT forest on gold electrodes overcomes some of the difficulties faced with the transfer method. Thus this procedure was utilised to fabricate the electrodes and their electrochemical properties examined in later sections.

5.5.2 Electrochemical Characterisation of Different Substrates

In order to investigate the electrochemical performance of the CNT forest gold electrodes, they were subjected to cyclic voltammetric analysis using ferrocyanide oxidation in the voltage range of -0.2 – 0.7 V *vs*. Ag/AgCl. Figure 5.9 shows the cyclic voltammetric response at varying scan rates at a CNT-Au-glass electrode in a solution consisting of 0.5 M KCl in the absence (a) and presence (b) of 2 mM ferrocyanide. A typical capacitive CV response have been found for both case. The voltammograms are observed to be near-ideal rectangular shape in the slow scan rates. It has been reported that the redox reaction of $Fe(CN)_6^{3-}$/ $Fe(CN)_6^{4-}$ occurs at both the outer and interior surface of the CNTs, and the electrode behaves as a three-dimensional structure.[255] As scan rate increases, the voltammogram gradually lose its rectangular shape.

As shown in Figure 5.9b, a broad ferrocyanide oxidation peak is observed at ca. +0.25 V (*vs.* Ag/AgCl). The peak current increased linearly with the square root of the scan rate (Regression data show in Figure 5.9c: oxidative current = 307.2 *(square root scan rate) – 13.6, R^2 =0.999), which shows the ferrocyanide oxidation at CNT-Au-glass electrode is diffusion controlled. In addition, the peak to peak separation is identified with a value of ca. 0.063 V *vs*. Ag/AgCl at a scan rate of 0.01 V/s, which also become wider as scan rate increases. Comparison experiments of ferrocyanide oxidation have also been conducted on a gold electrode on glass wafer with and without adhesive film (both without CNT forest). The data obtained from pure gold electrode is shown in Figure 5.9d, which illustrates a well-shaped CV curves with separation

peak of ca. 0.071 V *vs*. Ag/AgCl. Furthermore, the peaks remain at the same potential and the oxidation and reduction peak is of identical magnitude with varying scan rate, showing a reversible reaction at the gold electrode. Figure 5.9e illustrates the cyclic voltammetric response of the same reaction at a gold electrode with adhesive film on its surface with varying scan rates. The difference between this electrode and the CNT-Au-glass electrode is no CNT forest structure. The figure shows that merely no capacitive response has been found for the electrode, confirming the previous capacitive data is solely from the CNT structure. Moreover, the peak to peak separation is found to be wider than that of CNT-Au-glass electrode.

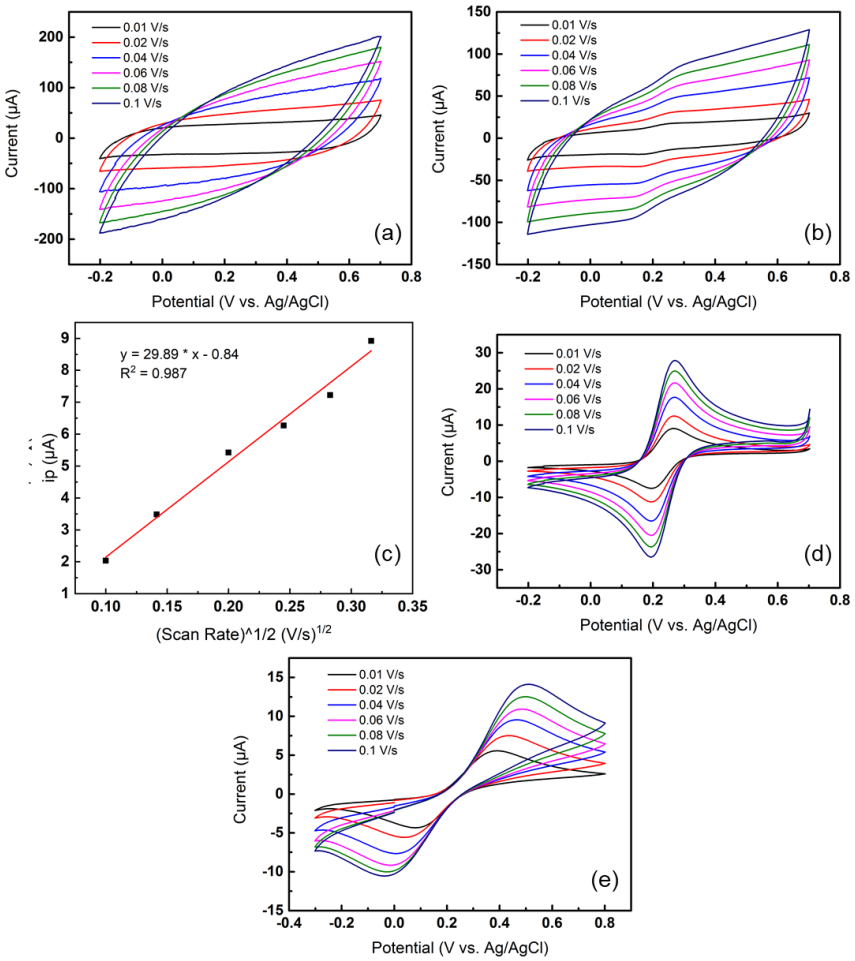

Figure 5.9 Cyclic voltammograms of 0.5 M KCl solution in the absence (a) and presence (b, d, e) of 2 mM ferrocyanide recorded on a CNT-Au-glass electrode (a, b) or gold electrode (d) or gold electrode with adhesive film (e) at various scan rates of 0.01 V s^{-1} to 0.1 V s^{-1}; (c) Regression data showing peak current *vs.* SQRT (scan rate) for oxidation peak in (b).

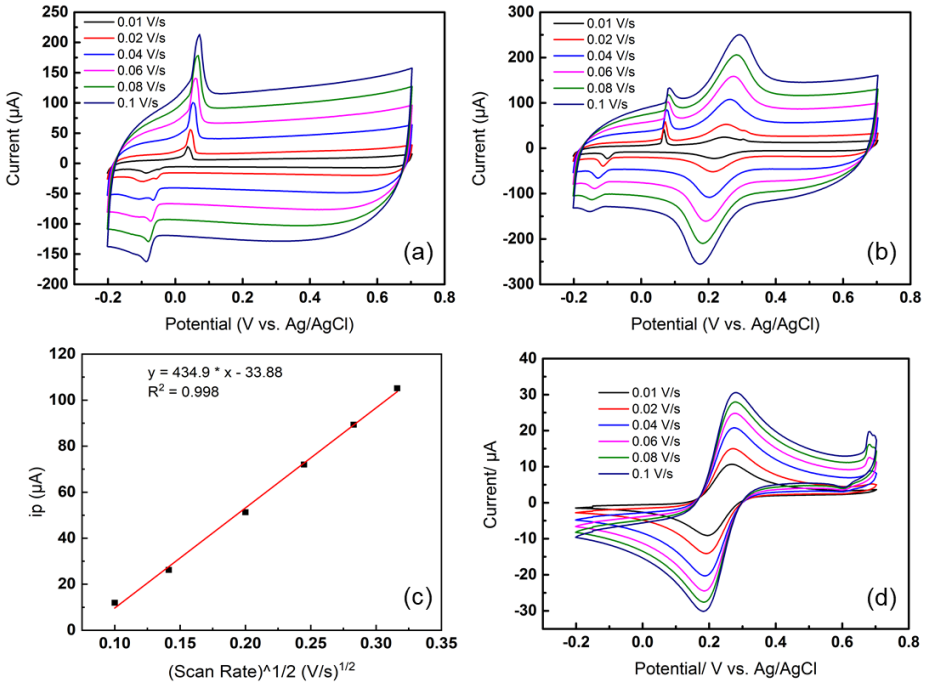

Figure 5.10 Cyclic voltammograms of 0.5 M KCl solution in the absence (a) and presence (b, d) of 2 mM ferrocyanide recorded on a CNT-Au-FSi electrode (a, b) or catalyst-Au-FSi electrode (d) at various scan rates of 0.01 V s^{-1} to 0.1 V s^{-1} and potential range of -0.2 to +0.7 V. (c) Regression data showing peak current *vs.* SQRT (scan rate) for oxidation peak in (b).

Figure 5.10 details the electrochemical response of a CNT-Au-FSI electrode in a solution consisting of 0.5 M KCl in the absence (a) and presence (b) of 2 mM ferrocyanide at varying scan rates of 0.01 to 0.1 V/s. Compared to the responses in Figure 5.9a, more rectangular voltammograms have been found. The voltammogram remains rectangular even at high scan rates. The ferrocyanide oxidation peak occurs at a potential of +0.25 V *vs*. Ag/AgCl for the slowest scan rate and gradually shifts to more positive values as the scan rate increases. However, another redox couple has been found before the ferrocyanide oxidation for both voltammograms. The new oxidation peak is observed at +0.07 V *vs*. Ag/AgCl, and the corresponding reduction peak at -0.10 V *vs*. Ag/AgCl. However, the redox species causing this oxidation and reduction peaks have not been expected. Thus it is necessary to verify whether the peaks emerges from the catalyst used during the CVD process for synthesising CNT forest. A further experiment of the ferrocyanide oxidation has therefore been undertaken on a gold electrode with catalyst on its surface. The result is presented in Figure 5.10d, which only shows

a typical ferrocyanide oxidation with no peak found at potential of ca. +0.07 V *vs*. Ag/AgCl. This then suggests that the new redox couple does not arise from the catalyst for CNT forest synthesis. The occurrence of the first peak remains an unknown, but is suggested from the contamination of the evaporator by silver particles. Therefore the fabrication of CNT forest was taken place on gold electrode on silicon wafers for the following results.

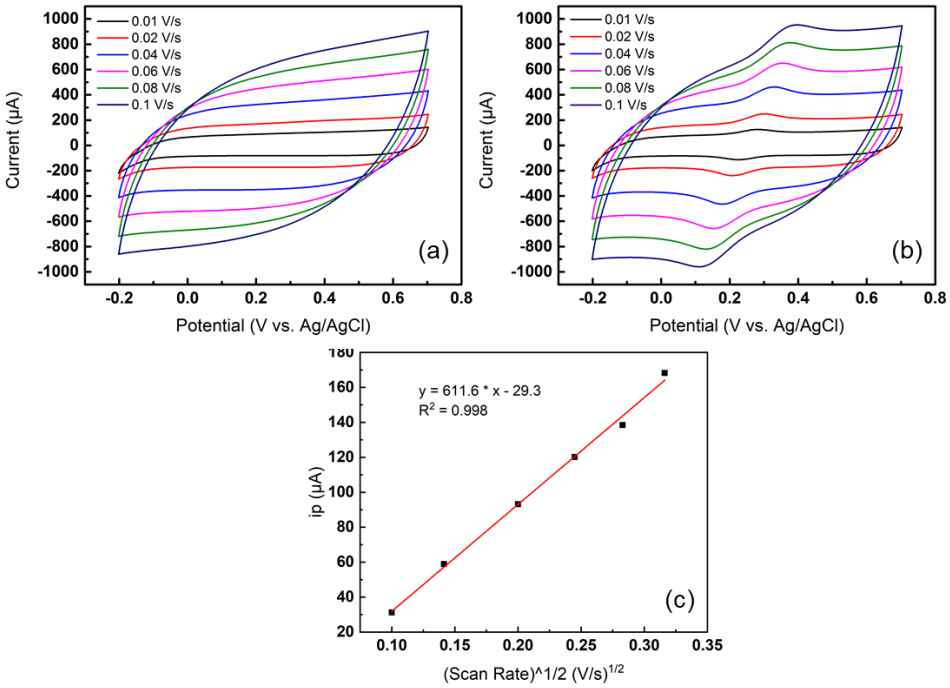

Figure 5.11 Cyclic voltammograms of 0.5 M KCl solution in the absence (a) and presence (b) of 2 mM ferrocyanide recorded on a CNT-Au-Si electrode at various scan rates of 0.01 V s^{-1} to 0.1 V s^{-1} and potential range of -0.2 to +0.7 V. (c) Regression data showing peak current *vs.* SQRT (scan rate) for oxidation peak in (b)

Figure 5.11 indicates cyclic voltammetric response of a CNT-Au-Si electrode in an electrolyte of 0.5 M KCl with (a) and without (b) 2 mM ferrocyanide at varying scan rates. Similar to the previous two electrodes, rectangular voltammograms have been obtained at each scan rate. In addition, the peak current response appears in CNT-Au-Si electrode is three times larger than that of the CNT-Au-glass and CNT-Au-FSi electrodes. When ferrocyanide is introduced into the system, oxidation peak potential at +0.28 V *vs*. Ag/AgCl is found for the slowest scan rate, and it shifts to more anodic with increasing scan rate. Then the peak to peak separation also enlarges with scan rate becoming larger, which indicates that the reaction on the CNT-Au-Si

electrode is more reversible at slow scan rate. The peak analysis of the oxidation currents against square root of scan rates reveals a liner relationship, indicating a diffusion controlled electrode reaction (regression data shown in Figure 5.11c). Therefore, the CNT forest directly grown on gold electrode on a silicon substrate shows a significantly enhanced performance than the other two electrodes. It was decided that this method of preparing the electrode being used for later studies on the electrochemical applications of the CNT forest.

5.5.3 Ferrocyanide Oxidation for CNT-Au-Si electrode

This section describes a further electrochemical study of CNT-Au-Si electrode by CV and FTACV. The voltammetric response at varying scan rates (0.01 – 0.1 V/s) for an electrolyte containing 0.5 M KCl and 2 – 10 mM ferrocyanide at a CNT-Au-Si electrode is shown in Figure 5.12. For the curves obtained at different concentrations of ferrocyanide, the shape indicates well established voltammogram with capacitive characteristics. In all conditions, the current response increases as scan rate increases, with larger current responses recorded at higher concentrations. Figure 5.12f illustrates a linear relationship between peak current and square root of scan rate for 10 mM ferrocyanide oxidation, with fitted regression data shown in the graph. The result indicates a diffusion controlled process at the CNT-Au-Si electrode even at high concentration of ferrocyanide. Additionally, the shift of the peak position towards positive potential is minimal at low concentration (2 mM). However, the amount of shift becomes significant at higher concentrations of ferrocyanide. This can be rationalised through the disrupted diffusion process at high concentration, thus extra potential is required to compensate the disruption and re-establish mass transport. Next the data in Figure 5.12 is reconstructed to give the voltammograms shown in Figure 5.13. This figure clearly depicts the variations of the current responses upon the change of ferrocyanide concentration at different scan rates.

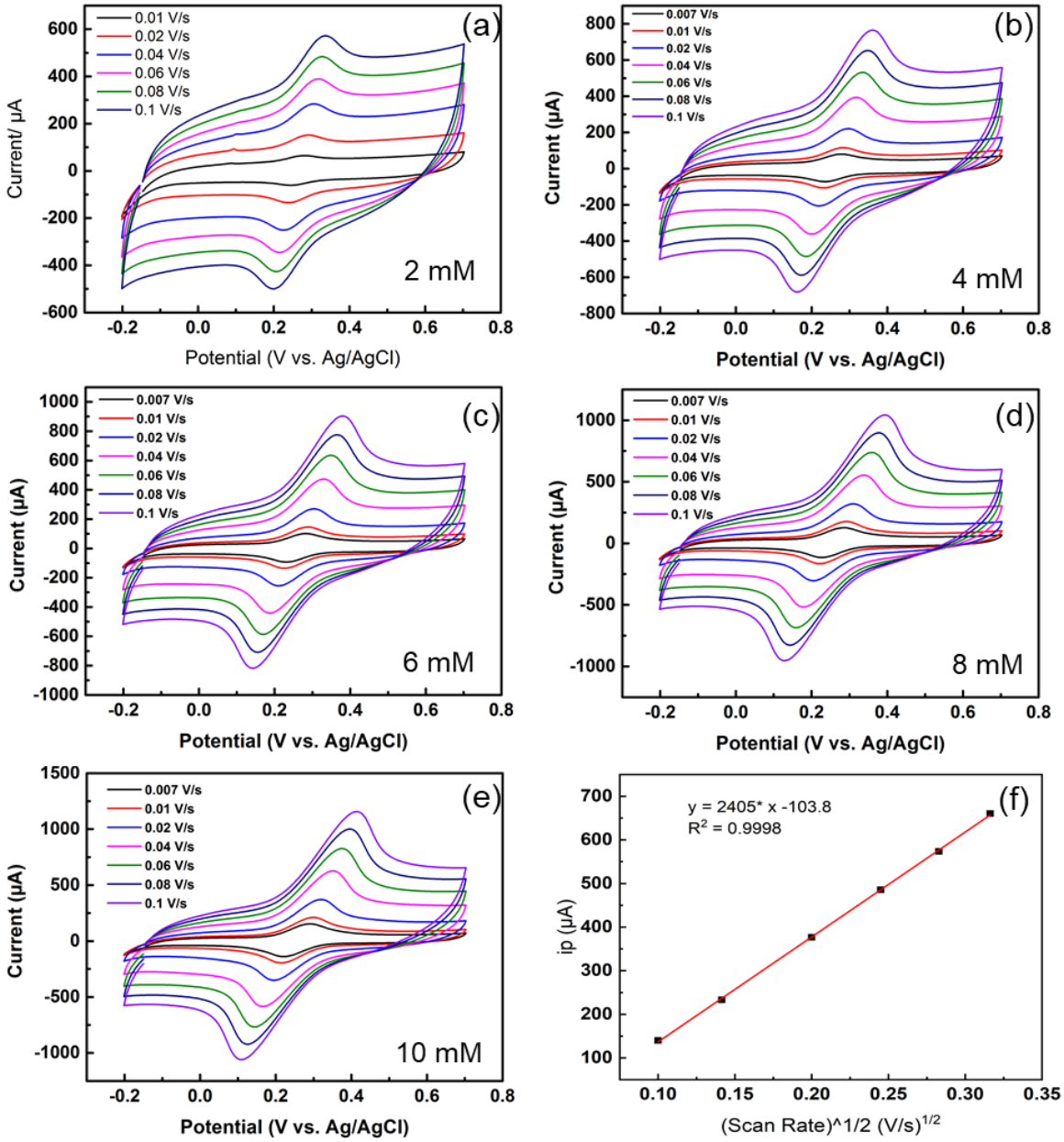

Figure 5.12 (a) - (e) Cyclic voltammograms of 2 mM to 10 mM ferrocyanide in 0.5 M KCl recorded on a CNT-Au-Si electrode at various scan rates of 0.01 V s^{-1} to 0.1 V s^{-1} and potential range of -0.2 to +0.7 V *vs*. Ag/AgCl; (f) Regression data of anodic peak current *vs.* SQRT(scan rate) for (e).

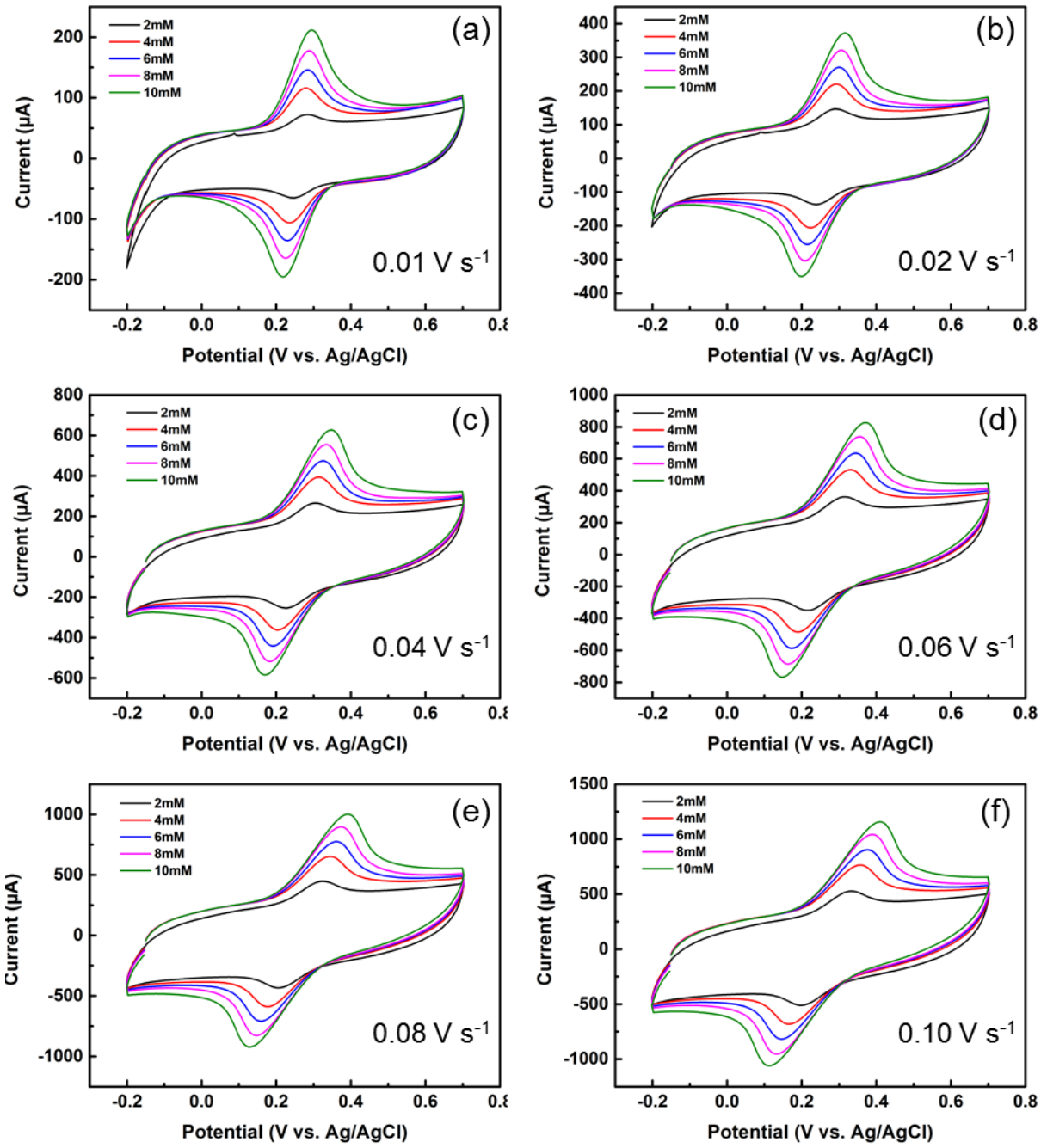

Figure 5.13 (a)-(f) Cyclic voltammograms of 2 mM to 10 mM ferrocyanide in 0.5 M KCl recorded on a CNT-Au-Si electrode at various scan rates of 0.01 V s^{-1} to 0.1 V s^{-1} and potential range of -0.2 to +0.7 V. Figures plotted using same data from Figure 5.12 to show the voltammograms with varying concentration.

FTACV Investigation of the CNT-Au-Si Electrode

The technique of FTACV is also utilised to study the ferrocyanide reaction on the CNT-Au-Si electrode. To the best of our knowledge, it is the first study of vertically aligned CNT forest using FTACV technique. Preliminary FTACV measurements were carried out at above electrode using the following experimental parameters: potential window of -0.1 to 0.5 V (*vs*. Ag/AgCl), scan rate (v) of 7 mV s^{-1} and ac superimposition amplitude (ΔE) of 100 mV with varying frequency (f) of 1 to 5 Hz. Figure 5.14a shows the extracted dc component of FTACV applied on a solution of 2 - 10 mM ferrocyanide supported with 0.5 M KCl on a CNT-Au-Si working electrode. The dc responses are similar to the CV results, with typical capacitive voltammograms illustrated. The data reveals oxidative and reductive peaks at +0.28 V *vs*. Ag/AgCl and +0.24 V *vs*. Ag/AgCl for the 2 mM ferrocyanide curve, slight peak shift is found for higher concentrations. A linear relationship between the ferrocyanide concentration and the anodic peak current has been observed (Regression data: anodic peak current (µA) = 14.98 * ferrocyanide concentration (mM) + 38.45 (µA), R^2 = 0.997).

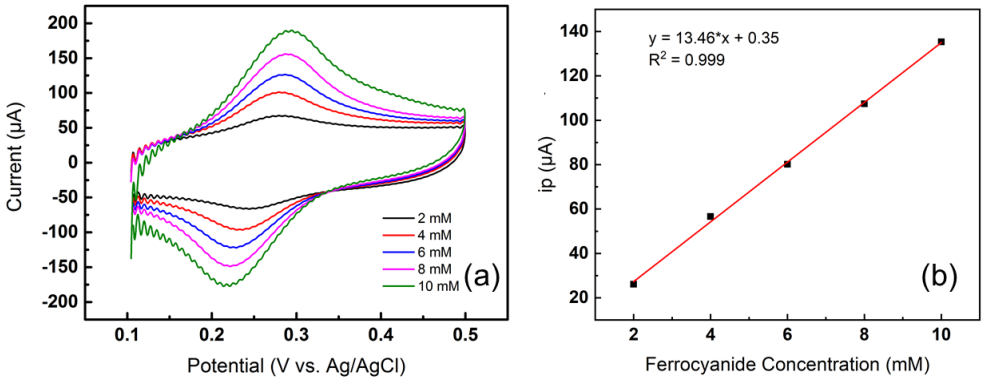

Figure 5.14 (a) The dc responses for the redox reaction of 2 to 10 mM Ferrocyandie in 0.5 M KCl electrolyte on a CNT-Au-Si electrode. Parameters: ΔE = 100 mV, f = 5 Hz, v = 7 mV s^{-1}. (b) Regression data showing anodic peak current *vs.* ferrocyanide concentration for (a).

After that, the harmonic components of the FTACV are examined to extract additional information. Figure 5.15 illustrates the fundamental and second ac harmonic components for 2 mM ferrocyanide in 0.5 M KCl supported electrolyte on a CNT-Au-Si working electrode. For the fundamental harmonics, two clear current peaks can be observed, corresponding to the

oxidative and reductive processes. The bell-shaped peaks of ferrocyanide oxidation and reduction lie symmetrically with midpoint potentials (E_m) of 0.2 V *vs*. Ag/AgCl, which is in good agreement with the extracted dc signals. The oxidative and reductive peaks are of equal height, revealing the reversibility of the ferrocyanide/ferricyanide redox couple at the sweep rate and ac frequencies on the CNT-Au-Si electrode surface. As frequency increases, the background signal in the fundamental harmonic also increases since the fundamental component is sensitive to both Faradaic current and capacitance of the electrode.

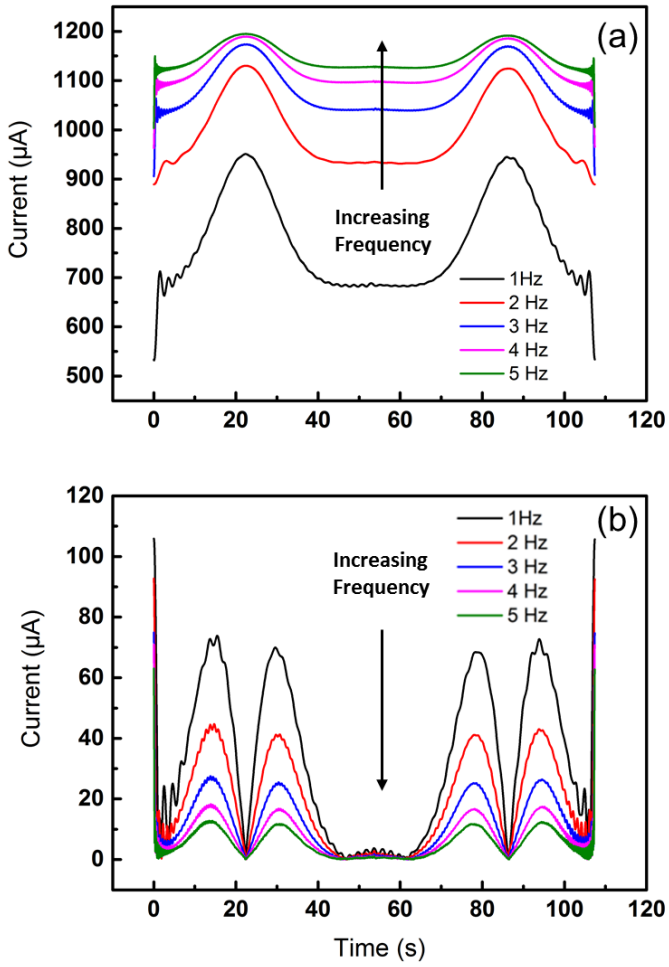

Figure 5.15 The fundamental (a) and second (b) ac harmonic responses for the redox reaction of 2 mM ferrocyanide in 0.5 M KCl electrolyte on a CNT-Au-Si electrode. Parameters: ΔE = 100 mV, f = 1 – 10 Hz, v = 7 mV s^{-1}.

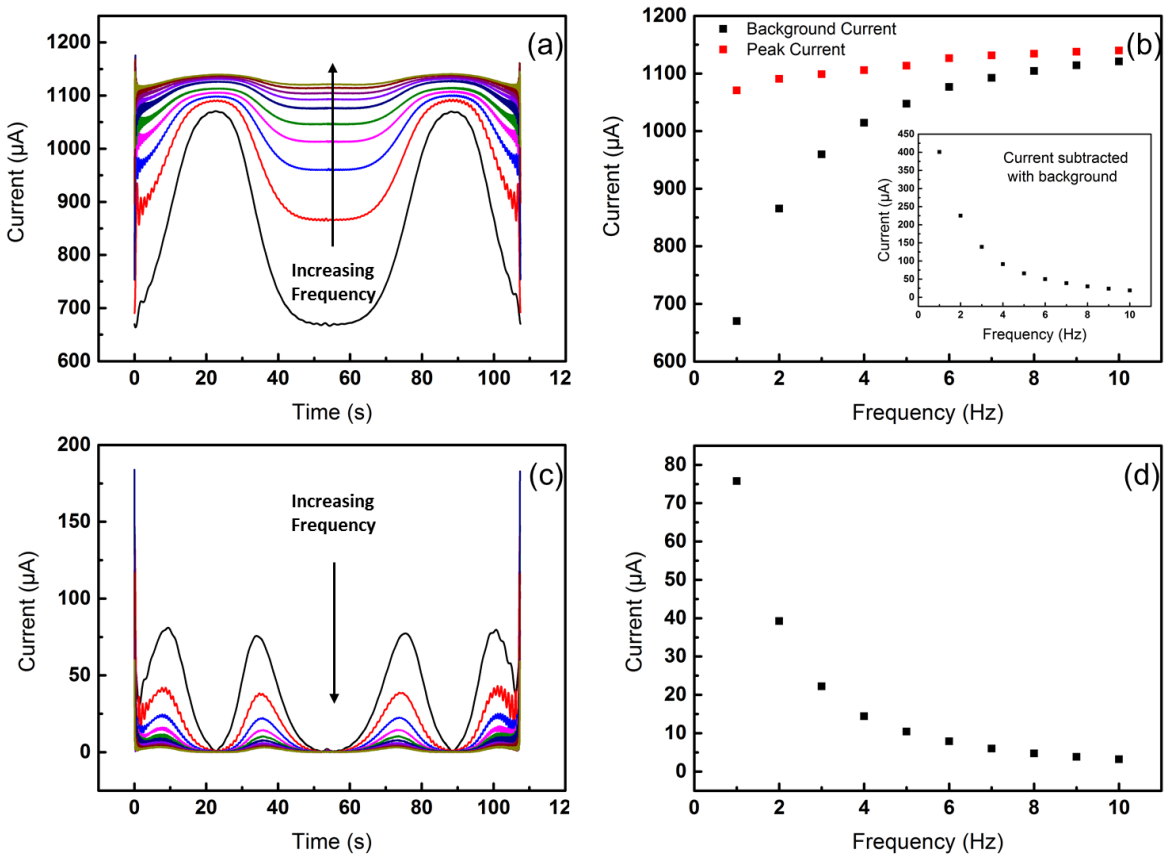

Figure 5.16 The fundamental (a) and second (c) ac harmonic responses for the redox reaction of 10 mM ferrocyanide in 0.5 M KCl electrolyte on a CNT-Au-Si electrode. Parameters: ΔE = 100 mV, f = 1 – 10 Hz, v = 7 mV s^{-1}. (b), (d) Current *vs*. Frequency analysis for (a) and (b) respectively.

Figure 5.16 illustrates a further FTACV measurement for 10 mM ferrocyanide under same conditions with varying frequency. In the fundamental harmonics, similar trends of the background current has been found with the increment of frequency. The peak current subtracted with background current at 1 Hz reaches a value of ca. 400.8 μA, compared with a value of ca. 265.4 μA for 2 mM ferrocyanide case. Figure 5.16b indicates the variation of overall peak current and background current against frequency. The results show that the peak current changes slowly upon the increment of frequency, while background current varies significantly. The inset graph shows that the subtracted current gradually decreases with frequency in a non-linear way. In the second harmonics (Figure 5.16c), a similar shift of the peak position as in CV has been discovered, which can also be attributed to disordered diffusion process at high concentration. There is a small difference for current magnitudes of the peaks

in 10 mM and 2 mM ferrocyanide. The peak current also varies with the frequency in a non-linear manner.

5.5.4 Anthraquinone Deposited CNT Forest Gold Electrode for pH Sensing

Scheme 5.2 (a) The electrochemical redox reaction of the immobilised anthraquinone. (b) Illustration of the covalent immobilisation of anthrqauinone onto CNT structure.

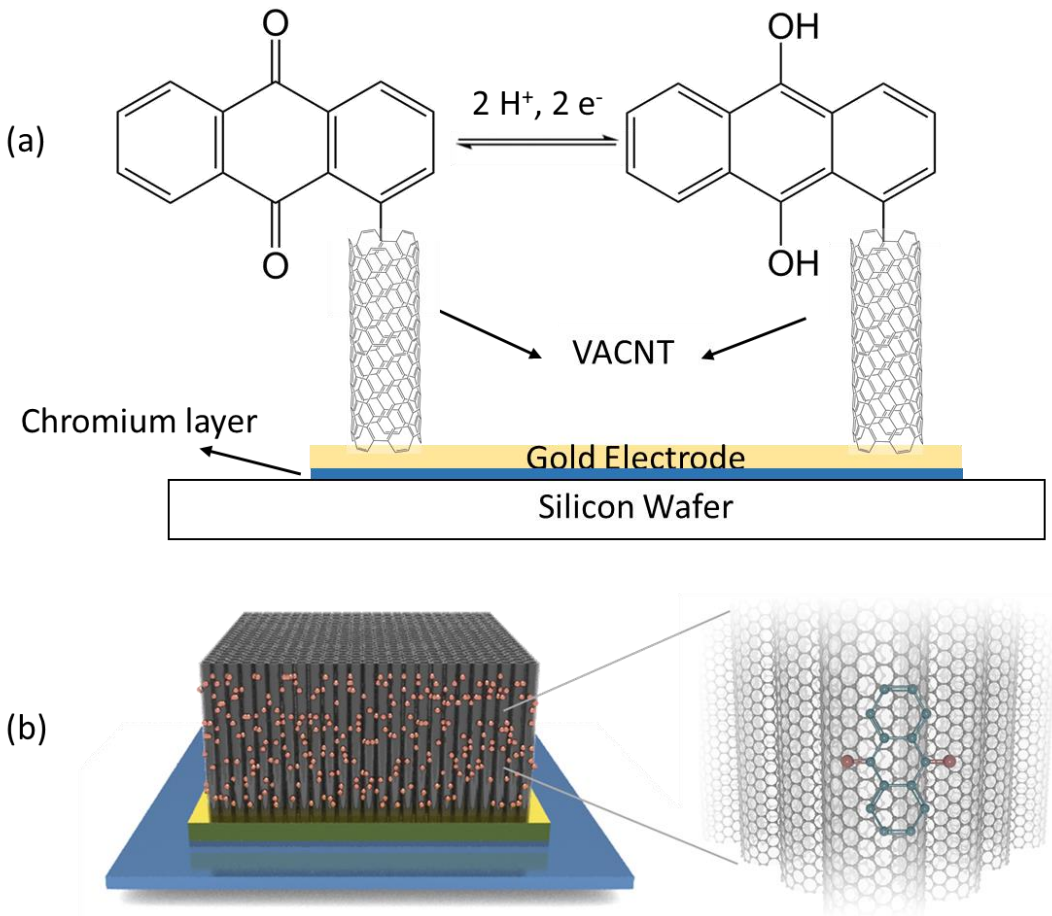

After the preliminary electrochemical characterisation of the CNT-Au-Si electrode, functionalisation of the CNT forests was further conducted by immobilising anthraquinone onto their surface. The immobilisation method has been described in the experimental section. This chemical is adopted as the active material to sense the concentration of hydrogen ion in the solution due to the pH dependence of its redox process. Scheme 5.2 illustrates the electrochemical redox reaction of the anthraquinone on the prepared CNT structure. The

electrode was examined at a range of pH values under several voltammetric techniques, including CV, SWV and FTACV.

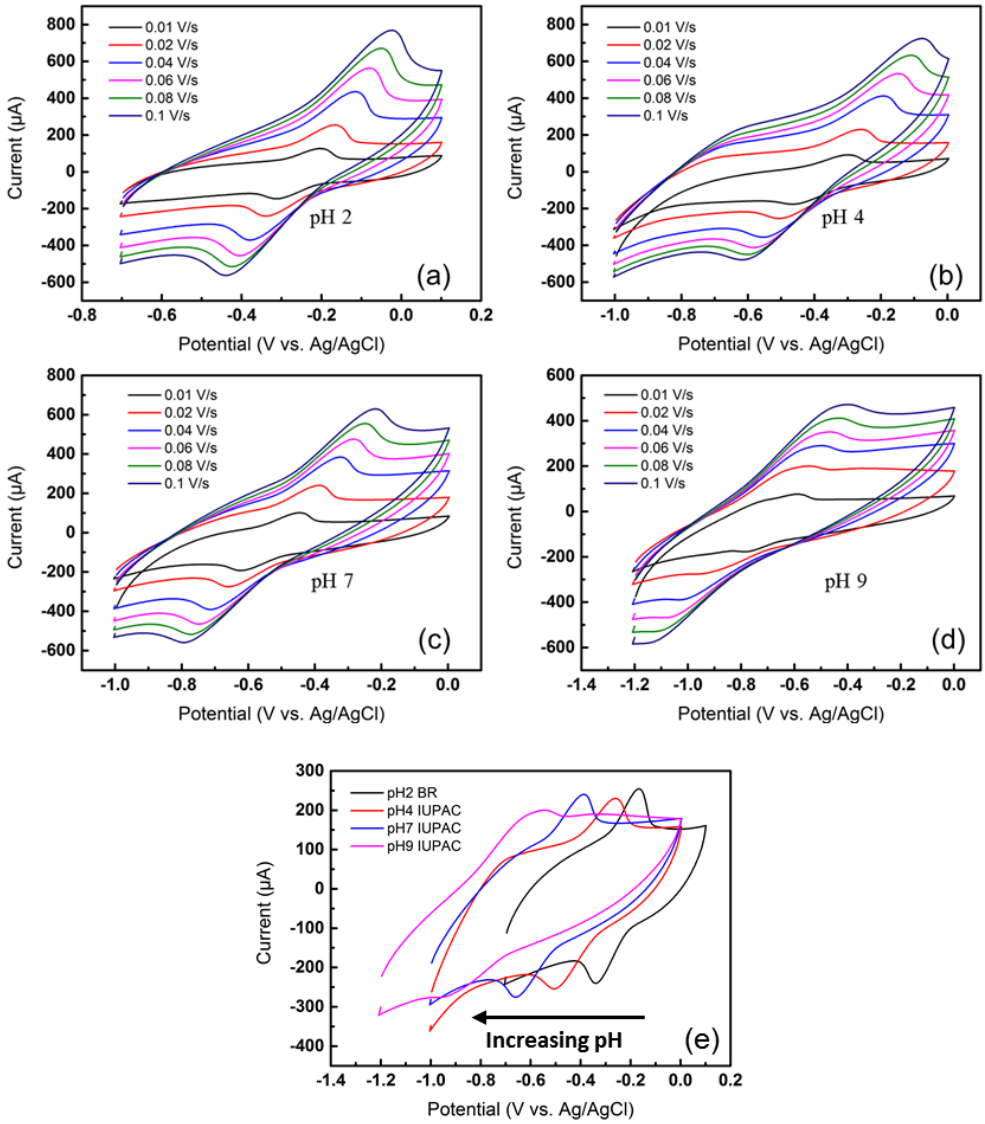

Figure 5.17 Cyclic voltammograms recorded at an AQ-CNT-Au-Si electrode in (a) pH 2 Britton-Robinson, (b) pH 4 citrate, (c) pH 7 phosphate and (d) pH 9.2 borate buffer solutions supported with 0.1 M KCl at various scan rates of 0.01 V s^{-1} to 0.1 V s^{-1}. (e) Comparison of the voltammograms at the scan rate of 0.02 V s^{-1}.

The fabricated AQ-CNT-Au-Si electrode was first subjected to cyclic voltammetric analysis using different pH buffer solutions at various scan rates in the voltage range of -0.7 to +0.1 V (*vs.* Ag/AgCl). The voltammetric responses are shown in Figure 5.17. At the slowest scan rate

of 0.01 V/s in a pH 2 BR buffer solution, an oxidation peak at ca. -0.204 V *vs.* Ag/AgCl followed by a reduction peak at ca. -0.311 V *vs.* Ag/AgCl were recorded. The peak to peak potential separation is then calculated with a value of 0.106 V. For all the voltammograms at different pH values, the peak potential shifts to more positive values as the scan rate increases. In the meanwhile, peak to peak separation also enlarges with the increment of scan rate. A comparison graph showing the transformation of voltammogram upon the changing of pH values is also plotted in Figure 5.17a. The graph clearly shows that both oxidation and reduction peak positions shift to more negative values upon the increment of pH values.

Furthermore, in order to verify the anthraquinone is attached to the CNT forest, the buffer solution was replaced after the varying scan rate experiment and additional measurement has been carried out. The resulted voltammogram was found to overlay that of the previous voltammogram, thus confirming the attachment of the anthraquinone species on the CNT forest.

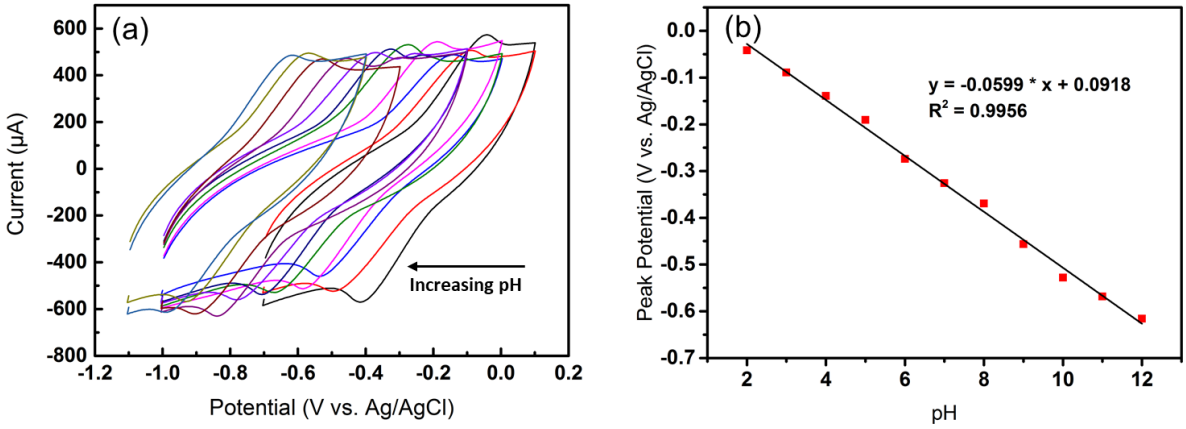

Figure 5.18 (a) Cyclic voltammograms recorded at an AQ-CNT-Au electrode in pH 2 to pH 12 BR buffer solutions supported with 0.1 M KCl at a scan rate of 0.05 V s^{-1}; (b) Plot of anodic peak potential against pH for (a).

Next, in order to prove that this AQ-CNT-Au electrode can be used to probe pH, the voltammetric response of AQ-CNT-Au electrode was investigated over a pH range from 2 to 12 in Britton-Robinson buffer solutions at room temperature, and the result shown in Figure 5.18a. The peak potential moves negatively as the pH increases, thereby making the reduction of the anthraquinone species more difficult. The plot of peak potential against pH indicates a good linear relationship in the pH range of 2 to 12. The regression data in Figure 5.18b shows

a sensitivity of 59.9 mV per pH unit within the above pH range. For the redox reaction of anthraquinone shown in Scheme 5.2, the theoretical variation of peak potential would be 58.1 mV per pH unit at 20 °C, as can be derived from the Nernst Equation (1.2).[281]

In the studies detailed below, square wave voltammetry (SWV) was utilised as the electrochemical probe of the system. This technique owns substantial advantages to the conventional cyclic voltammetry. It can produce a well-defined voltammetric peak in a single sweep due to the reversibility of the anthraquinone redox couple.[295] Consequently, the technique assists the resolution of the anthraquinone reduction wave, especially at higher pH values where oxygen reduction competes at similar potential position. The corresponding square wave voltammograms (shown in Figure 5.19a) were recorded for the AQ-CNT-Au electrode in pH 2 to pH 12 BR buffer solutions. The voltammograms indicate that as the pH increases, the peak potential shifts towards more negative values as similar to the cyclic voltammograms. Figure 5.19b shows the corresponding regression plot of peak potential against pH. This reveals an extremely linear response from pH 2 to 12 with a gradient of ca. 56.8 mV per pH unit, which is consistent with studies of anthraquinone derivatised carbon powder.[281] In conclusion, a wide pH probe range has been discovered for the AQ-CNT-Au electrode in buffer solution with excellent linearity and sensitivity.

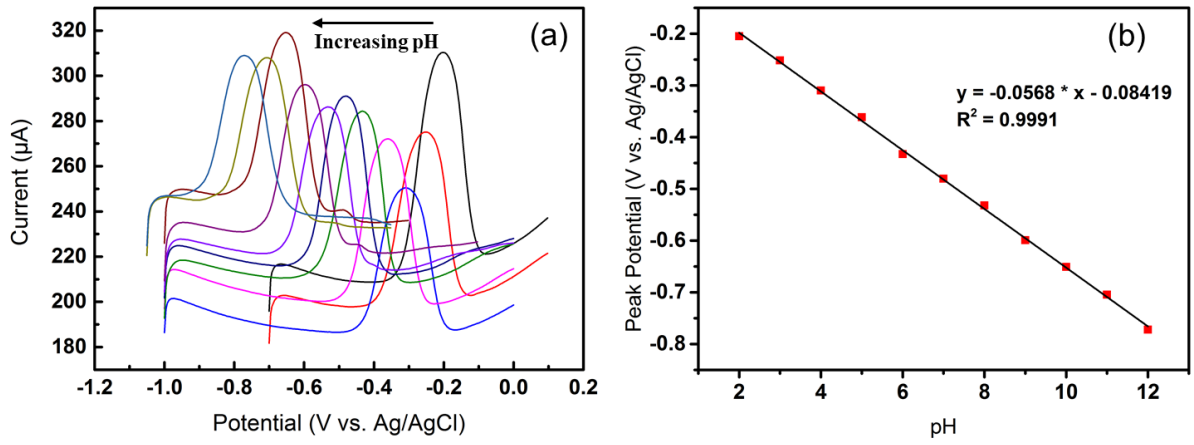

Figure 5.19 (a) Square wave voltammograms recorded at an AQ-CNT-Au electrode in pH 2 to pH 12 BR buffer solutions supported with 0.1 M KCl at a scan rate of 0.05 V s^{-1}; (b) Plot of peak potential against pH for (a).

FTACV Investigation of the AQ-CNT-Au Electrode

After the AQ-CNT-Au electrode in buffer solutions was examined by the CV and SWV, the electrode was subjected to the more advanced FTACV technique. The FTACV measurements were carried out in pH 2 BR buffer solution with the following conditions: potential range of -0.7 to 0.1 V (*vs.* Ag/AgCl reference electrode), scan rate of 15 mV/s, frequency of 1 Hz and ac superimposition (ΔE) of 40 to 100 mV.

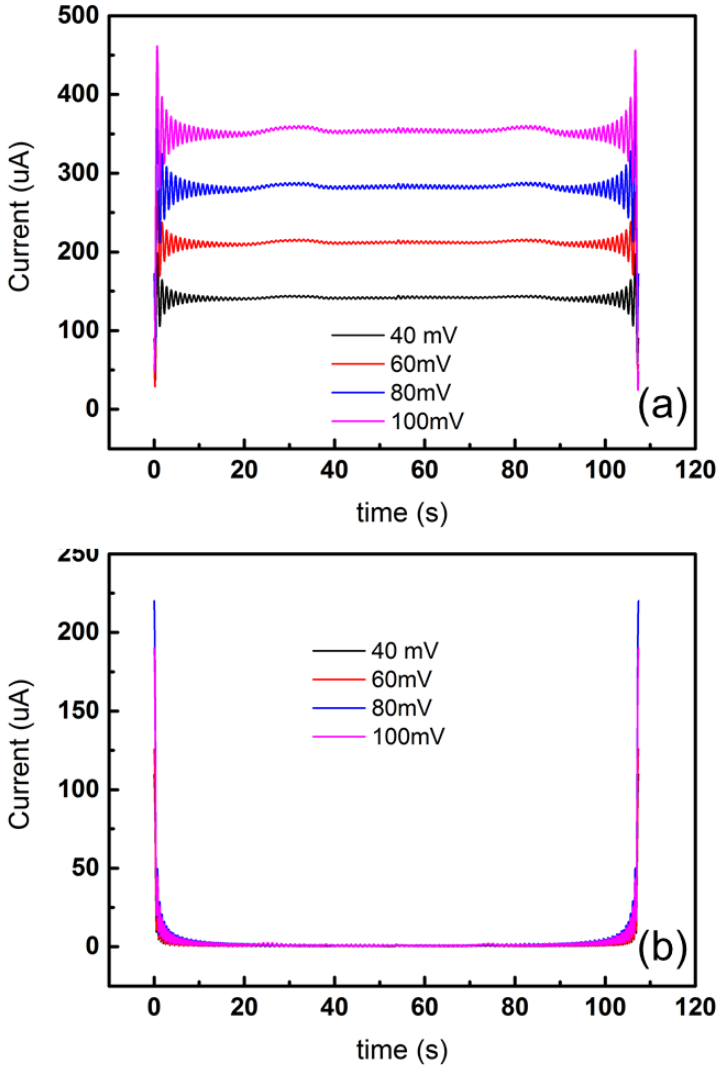

Figure 5.20 The fundamental (a) and second (b) ac harmonic responses recorded at an AQ-CNT-Au electrode in pH 2 BR buffer solutions supported with 0.1 M KCl electrolyte. Parameters: ΔE = 40 to 100 mV, f = 1 Hz, v = 14 mV s^{-1}.

Figure 5.20 shows the fundamental and second ac harmonic components for AQ-CNT-Au electrode recorded in pH 2 BR buffer solution supported with 0.1 M KCl electrolyte. In the fundamental harmonics, four symmetric voltammograms have been recorded with E_m of -0.4 V. Moreover, as amplitude increases from 40 to 100 mV, the background current also increases. However, only small faradaic peaks can be observed, which is unexpected as the SWV responses illustrate large peaks. These decreased peaks are likely to be caused by the resistance from the CNT structure. Therefore, additional work has to be designed and conducted to explain the reason why the FTACV peaks are not distinguishing. For the second harmonics, capacitive background current and faradaic current have all been disappeared.

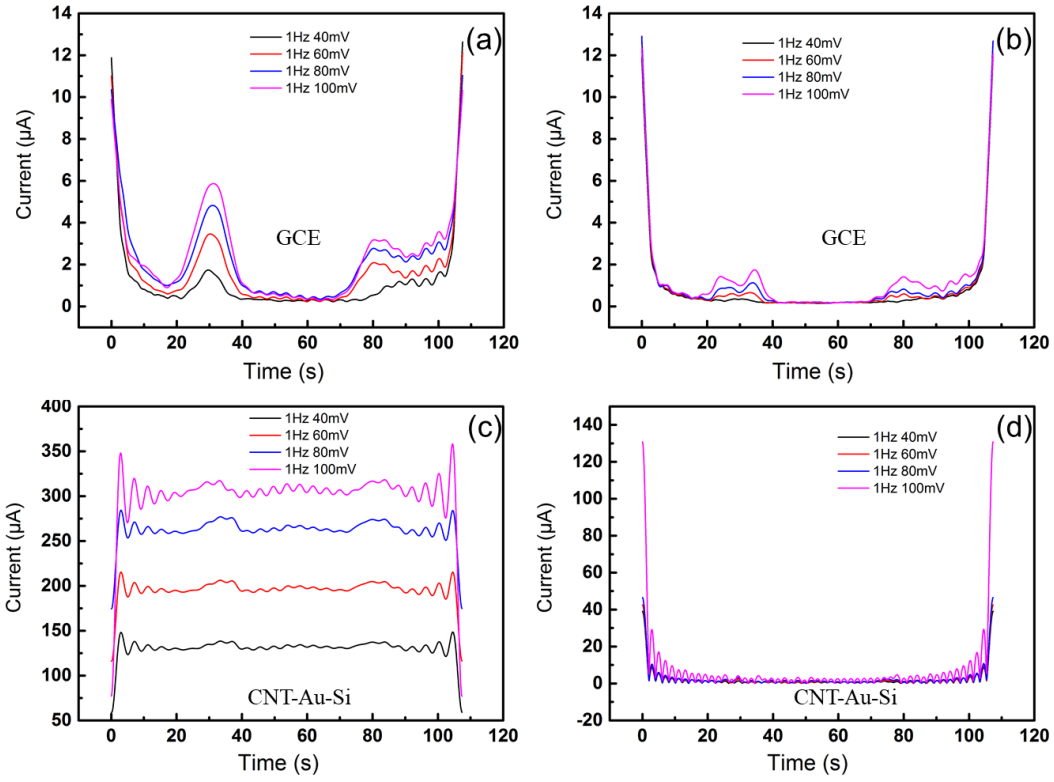

Figure 5.21 The fundamental (a, c) and second (b, d) ac harmonic responses recorded at a GCE (a, b) and an AQ-CNT-Au electrode (c, d) in pH 2 BR buffer solutions supported with 0.1 M KCl electrolyte. Parameters: ΔE = 40 to 100 mV, f = 1 Hz, v = 14 mV s^{-1}.

Next, in order to explain the above phenomenon of small FTACV responses of AQ-CNT-Au electrode, further comparison measurements have been applied on a GCE. FTACV measurements with same parameters were conducted in a pH 2 buffer solution of 1 mM AQ

supported with 0.1 M KCl at a GCE and a CNT-Au-Si electrode. For the fundamental harmonics recorded on a GCE shown in Figure 5.21a, two sets of small peaks have been found for oxidation (2 – 6 mV) and reduction (1 – 4 mV) of AQ, respectively. The unequal equal heights of the peaks may be resulted from the quasi-reversible characteristic of AQ in slow sweep rates.[281] The responses in second harmonics reveals a smaller current signal as expected, with peaks hardly identified.

Figure 5.21c&d illustrate the fundamental and second ac harmonic components for 1 mM AQ in pH 2 BR buffer solution on a CNT-Au-Si electrode. Large capacitive background currents can also be observed, which is in consistent with the responses recorded on the AQ-CNT-Au electrode. Similarly, small peak currents can be found in the first harmonic, and the current signals of both faradaic and capacitive diminishes in the second harmonics. From the comparison of the voltammograms obtained at GCE and CNT-Au-Si electrode,

5.6 Conclusion

This chapter describes the synthesis of vertically aligned CNT forests and preparation of CNT forests on gold electrode. The vertically aligned CNT structure is a desired organised CNT arrangement, which is believed to give better electrochemical responses. The electrode has been characterised by several techniques, including SEM, FTIR and Raman Spectrometry. Various electrochemical characterisations of the electrode have also been carried out, including CV, SWV and FTACV.

Functionalisation of CNT forest has also been attempted by covalently immobilising anthraquinone onto the CNT structure. The fabricated functionalised CNT forest electrode was then examined as a pH sensor using voltammetric methods. In CV measurements, a linear response of ca. 59.9 mV per pH unit has been obtained in the pH range of 2 to 12, while the sensitivity in SWV responses is ca. 56.8 mV per pH unit. The electrode used as a pH sensor in both technique indicates an excellent sensitivity. However, small FTACV responses of the electrode were detected, and a comparison experiment on GCE also revealed small signals. Thus, examining the reason behind the phenomenon would be appealing for future work.

Chapter 6 Conclusion and Future Work

Although the applications investigated in this thesis are varied, spanning from gelation process, hydrogen evolution reaction, to carbon nanotubes sensors, they also share common features, examined by voltammetry techniques and utilised for electrochemical applications.

Chapter 3 has highlighted the formation of hydrogel on electrode surface. The mechanism study of catechol oxidation and subsequent polymerisation through crosslinking with D-glucosamine or Chitosan has also been conducted by voltammetry measurements. The Hydrogel formation has been confirmed by rheological measurements. The chemical system of catechol and D-glucosamine has been determined to follow an EC mechanism. The voltammetric profiling of the process can be used to monitor the degree of crosslinking. An additional FTACV study on the chemical system was also successfully conducted with clear responses.

Chapter 4 illustrates the synthesis of a series of carbon microsphere supported molybdenum disulfide nanocatalysts with and without doping metals (Co or Ni). Various characterisations of the samples were performed and analysed. The catalysts have been examined for the catalytic HER process in acidic media. Traditional LSV and advanced FTACV techniques have been adopted to evaluate their performances. In particular, the FTACV technique has produced extra information than the dc polarisation curve. It is argued that the technique reveals the Volmer reaction and Heyrovsky reaction from the harmonic data. The higher harmonic data could also potentially be used to elucidate HER process with additional simulation work. Furthermore, these samples have been utilised for the catalytic thermal decomposition of hydrogen sulfide, which exhibit higher conversion rates than commercial catalysts. For future work, the FTACV can be further exploited to study HER process and to reveal the inherent mechanisms associated with the process.

Chapter 5 has investigated the direct growth of vertically aligned CNT forests on gold electrodes. The fabricated electrodes have been tested with ferrocyanide as the redox species by several voltammetric techniques. Furthermore, covalent bonding of anthraquinone onto a CNT forest was also attempted and utilised as a pH sensor. The sensor has been tested by both CV and SWV in the pH range of 2 to 12, which indicate well correlated pH-potential relationships. For future developments, the stabilisation of the CNT structure is necessary to enhance the durability of the sensor. Also, the currently unusual lack for a voltammetric responses of the FTACV investigation of the anthraquinone immobilised CNT structure could be further studied.

Reference

[1] A. J. Bard and L. R. Faulkner, *Electrochemical Methods: Fundamentals and Applications*. Wiley, 2000.

[2] A. C. Fisher, *Electrode Dynamics*. New York: Oxford University Press, 1996.

[3] A. Heller and B. Feldman, "Electrochemical glucose sensors and their applications in diabetes management," *Chem Rev*, vol. 108, no. 7, pp. 2482–2505, 2008.

[4] A. Richter, G. Paschew, S. Klatt, J. Lienig, K.-F. Arndt, and H.-J. P. Adler, "Review on Hydrogel-based pH Sensors and Microsensors," *Sensors*, vol. 8, no. 1, pp. 561–581, 2008.

[5] J. Voldman, M. L. Gray, M. Toner, and M. A. Schmidt, "A microfabrication-based dynamic array cytometer," *Anal. Chem.*, vol. 74, no. 16, pp. 3984–3990, 2002.

[6] V. Mehta and J. S. Cooper, "Review and analysis of PEM fuel cell design and manufacturing," *J. Power Sources*, vol. 114, no. 1, pp. 32–53, Feb. 2003.

[7] J. Wang, *Analytical Electrochemistry, Third Edition*. 2006.

[8] R. G. Compton and C. E. Banks, *Understanding voltammetry*. World Scientific, 2011.

[9] A. M. Bond, *Modern polarographic methods in analytical chemistry*, vol. 4. CRC Press, 1980.

[10] A. M. Bond *et al.*, "An integrated instrumental and theoretical approach to quantitative electrode kinetic studies based on large amplitude Fourier transformed a.c. voltammetry: A mini review," *Electrochem. commun.*, vol. 57, pp. 78–83, 2015.

[11] P. T. Kissinger and W. R. Heineman, "Cyclic voltammetry," *J. Chem. Educ*, vol. 60, no. 9, p. 702, 1983.

[12] R. S. Nicholson, "Theory and Application of Cyclic Voltammetry for Measurement of Electrode Reaction Kinetics," *Anal. Chem.*, vol. 37, no. 11, pp. 1351–1355, 1965.

[13] M. A. Rahman, P. Kumar, D.-S. Park, and Y.-B. Shim, "Electrochemical sensors based on organic conjugated polymers," *Sensors*, vol. 8, no. 1, pp. 118–141, 2008.

[14] "Linear Sweep and Cyclic Voltametry: The Principles." [Online]. Available: https://www.ceb.cam.ac.uk/research/groups/rg-eme/teaching-notes/linear-sweep-and-cyclic-voltametry-the-principles. [Accessed: 20-Jul-2018].

[15] I. L. Barker, G. C.Jenkins, "Square-Wave Polarography," *Analyst*, no. 920, 1952.

[16] V. Mirceski, S. Komorsky-Lovric, and M. Lovric, *Square-wave voltammetry: theory and application*. Springer Science & Business Media, 2007.

[17] V. Mirceski, R. Gulaboski, M. Lovric, I. Bogeski, R. Kappl, and M. Hoth, "Square-Wave Voltammetry: A Review on the Recent Progress," *Electroanalysis*, vol. 25, no. 11, pp. 2411–2422, 2013.

[18] R. Gulaboski and V. Mirceski, "New aspects of the electrochemical-catalytic (EC') mechanism in square-wave voltammetry," *Electrochim. Acta*, vol. 167, pp. 219–225, 2015.

[19] H. Beitollahi, H. Karimi-Maleh, and H. Khabazzadeh, "Nanomolar and selective determination of epinephrine in the presence of norepinephrine using carbon paste electrode modified with carbon nanotubes and novel 2-(4-oxo-3-phenyl-3, 4-dihydro-quinazolinyl)-N′-phenyl-hydrazinecarbothioamide," *Anal. Chem.*, vol. 80, no. 24, pp. 9848–9851, 2008.

[20] C. Dai, P. Song, J. D. Wadhawan, A. C. Fisher, and N. S. Lawrence, "Screen Printed Alizarin-Based Carbon Electrodes: Monitoring pH in Unbuffered Media," *Electroanalysis*, vol. 27, no. 4, pp. 917–923, 2015.

[21] J. G. Osteryoung and R. A. Osteryoung, "Square wave voltammetry," *Anal. Chem.*, vol. 57, no. 1, p. 101A--110A, 1985.

[22] S. Sarker, A. J. S. Ahammad, H. W. Seo, and D. M. Kim, "Electrochemical impedance spectra of dye-sensitized solar cells: Fundamentals and spreadsheet calculation," *Int. J. Photoenergy*, vol. 2014, 2014.

[23] R. K. Singh, R. Devivaraprasad, T. Kar, A. Chakraborty, and M. Neergat, "Electrochemical impedance spectroscopy of oxygen reduction reaction (ORR) in a rotating disk electrode configuration: effect of ionomer content and carbon-support," *J. Electrochem. Soc.*, vol. 162, no. 6, pp. F489--F498, 2015.

[24] J.-Y. Park and S.-M. Park, "DNA Hybridization Sensors Based on Electrochemical Impedance Spectroscopy as a Detection Tool," *Sensors*, vol. 9, no. 12, pp. 9513–9532, 2009.

[25] N. Ben Messaoud, M. E. Ghica, C. Dridi, M. Ben Ali, and C. M. A. Brett, "Electrochemical sensor based on multiwalled carbon nanotube and gold nanoparticle modified electrode for the sensitive detection of bisphenol A," *Sensors Actuators B Chem.*, vol. 253, pp. 513–522, 2017.

[26] A. M. Bond, N. W. Duffy, S.-X. Guo, J. Zhang, and D. Elton, "Changing the Look of Voltammetry," *Anal. Chem.*, vol. 77, no. 9, p. 186 A-195 A, 2005.

[27] S. Guo, J. Zhang, D. M. Elton, and A. M. Bond, "Fourier Transform Large-Amplitude Alternating Current Cyclic Voltammetry of Surface-Bound Azurin," *Anal. Chem.*, vol. 76, no. 1, pp. 166–177, 2004.

[28] D. J. Gavaghan and A. M. Bond, "A Complete numerical simulation of the techniques of alternating current linear sweep and cyclic voltammetry: analysis of a reversible process by conventional and fast Fourier transform methods," *J. Electroanal. Chem.*,

vol. 480, no. 1–2, pp. 133–149, 2000.

[29] T. G. McCord and D. E. Smith, "Alternating current polarography: an extension of the general theory for systems with coupled first-order homogeneous chemical reactions," *Anal. Chem.*, vol. 40, no. 13, pp. 1959–1966, 1968.

[30] T. G. McCord and D. E. Smith, "Alternating current polarography: theoretical predictions for systems with first-order chemical reactions preceding the charge transfer step," *Anal. Chem.*, vol. 41, no. 1, pp. 116–130, 1969.

[31] Y. Tan *et al.*, "Designer based Fourier transformed voltammetry: A multi-frequency, variable amplitude, sinusoidal waveform," *J. Electroanal. Chem.*, vol. 634, no. 1, pp. 11–21, 2009.

[32] C. Y. Lee, J. P. Bullock, G. F. Kennedy, and A. M. Bond, "Effects of coupled homogeneous chemical reactions on the response of large-amplitude AC voltammetry: Extraction of kinetic and mechanistic information by fourier transform analysis of higher harmonic data," *J. Phys. Chem. A*, vol. 114, no. 37, pp. 10122–10134, 2010.

[33] D. J. Gavaghan, D. Elton, and A. M. Bond, "A comparison of sinusoidal, square wave, sawtooth, and staircase forms of transient ramped voltammetry when a reversible process is analysed in the frequency domain," *J. Electroanal. Chem.*, vol. 513, no. 2, pp. 73–86, 2001.

[34] S. O. Engblom, J. C. Myland, and K. B. Oldham, "Must ac voltammetry employ small signals?," *J. Electroanal. Chem.*, vol. 480, no. 1–2, pp. 120–132, 2000.

[35] B. Lertanantawong, A. P. O'Mullane, J. Zhang, W. Surareungchai, M. Somasundrum, and A. M. Bond, "Investigation of mediated oxidation of ascorbic acid by ferrocenemethanol using large-amplitude fourier transformed ac voltammetry under quasi-reversible electron-transfer conditions at an indium tin oxide electrode," *Anal. Chem.*, vol. 80, no. 17, pp. 6515–6525, 2008.

[36] A. P. O'Mullane, J. Zhang, A. Brajter-Toth, and A. M. Bond, "Higher harmonic large-amplitude fourier transformed alternating current voltammetry: Analytical attributes derived from studies of the oxidation of ferrocenemethanol and uric acid at a glassy carbon electrode," *Anal. Chem.*, vol. 80, no. 12, pp. 4614–4626, 2008.

[37] A. A. Sher *et al.*, "Resistance, capacitance, and electrode kinetic effects in fourier-transformed large-amplitude sinusoidal voltammetry: Emergence of powerful and intuitively obvious tools for recognition of patterns of behavior," *Anal. Chem.*, vol. 76, no. 21, pp. 6214–6228, 2004.

[38] J. Zhang, S.-X. Guo, and A. M. Bond, "Discrimination and evaluation of the effects of uncompensated resistance and slow electrode kinetics from the higher harmonic components of a Fourier transformed large-amplitude alternating current voltammogram," *Anal. Chem.*, vol. 79, no. 6, pp. 2276–2288, 2007.

[39] B. D. Fleming, N. L. Barlow, J. Zhang, A. M. Bond, and F. A. Armstrong, "Application

of power spectra patterns in Fourier transform square wave voltammetry to evaluate electrode kinetics of surface-confined proteins," *Anal. Chem.*, vol. 78, no. 9, pp. 2948–2956, 2006.

[40] E. Mashkina *et al.*, "Estimation of electrode kinetic and uncompensated resistance parameters and insights into their significance using Fourier transformed ac voltammetry and e-science software tools," *J. Electroanal. Chem.*, vol. 690, pp. 104–110, 2013.

[41] Y. Zhang *et al.*, "Direct Detection of Electron Transfer Reactions Underpinning the Tin-Catalyzed Electrochemical Reduction of CO2using Fourier-Transformed ac Voltammetry," *ACS Catal.*, vol. 7, no. 7, pp. 4846–4853, 2017.

[42] C. G. Bell, C. A. Anastassiou, D. O'Hare, K. H. Parker, and J. H. Siggers, "Theory of large-amplitude sinusoidal voltammetry for reversible redox reactions," *Electrochim. Acta*, vol. 56, no. 24, pp. 8492–8508, 2011.

[43] P. Song *et al.*, "Fourier transform large amplitude alternating current voltammetry investigations of the split wave phenomenon in electrocatalytic mechanisms," *Phys. Chem. Chem. Phys.*, vol. 19, pp. 24304–24315, 2017.

[44] J. C. Myland and K. B. Oldham, "The excess current in cyclic voltammetry arising from the presence of an electrode edge," *J. Solid State Electrochem.*, vol. 18, no. 12, pp. 3259–3269, 2014.

[45] A. M. Bond, E. A. Mashkina, and A. N. Simonov, "A critical review of the methods available for quantitative evaluation of electrode kinetics at stationary macrodisk electrodes," *Dev. Electrochem. Sci. Inspired by Martin Fleischmann*, pp. 21–47, 2014.

[46] A. N. Simonov, E. Mashkina, P. J. Mahon, K. B. Oldham, and A. M. Bond, "Determination of diffusion coefficients from semiintegrated d.c. and a.c. voltammetric data: Overcoming the edge effect at macrodisc electrodes," *J. Electroanal. Chem.*, vol. 744, pp. 110–116, 2015.

[47] G. P. Morris *et al.*, "A comparison of fully automated methods of data analysis and computer assisted heuristic methods in an electrode kinetic study of the pathologically variable [Fe(CN)6]3-/4- process by AC voltammetry," *Anal. Chem.*, vol. 85, no. 24, pp. 11780–11787, 2013.

[48] E. A. Mashkina, A. N. Simonov, and A. M. Bond, "Optimisation of windowing for harmonic recovery in large-amplitude Fourier transformed ac voltammetry," *J. Electroanal. Chem.*, vol. 732, pp. 86–92, 2014.

[49] B. D. Fleming, J. Zhang, D. Elton, and A. M. Bond, "Detailed analysis of the electron-transfer properties of azurin adsorbed on graphite electrodes using dc and large-amplitude Fourier transformed ac voltammetry," *Anal. Chem.*, vol. 79, no. 17, pp. 6515–6526, 2007.

[50] C.-Y. Lee *et al.*, "Theoretical and experimental investigation of surface-confined two-

center metalloproteins by large-amplitude Fourier transformed ac voltammetry," *J. Electroanal. Chem.*, vol. 656, no. 1–2, pp. 293–303, 2011.

[51] A. N. Simonov *et al.*, "New insights into the analysis of the electrode kinetics of flavin adenine dinucleotide redox center of glucose oxidase immobilized on carbon electrodes," *Langmuir*, vol. 30, no. 11, pp. 3264–3273, 2014.

[52] J. Zhang, S. X. Guo, A. M. Bond, and F. Marken, "Large-amplitude fourier transformed high-harmonic alternating current cyclic voltammetry: Kinetic discrimination of interfering faradaic processes at glassy carbon and at boron-doped diamond electrodes," *Anal. Chem.*, vol. 76, no. 13, pp. 3619–3629, 2004.

[53] "Cyclic Voltammetry: The Investigation Of Electrolysis Mechanisms." [Online]. Available: https://www.ceb.cam.ac.uk/research/groups/rg-eme/teaching-notes/cyclic-voltammetry-the-investigation-of. [Accessed: 20-Jul-2018].

[54] Y. Yan, B. Xia, Z. Xu, and X. Wang, "Recent development of molybdenum sulfides as advanced electrocatalysts for hydrogen evolution reaction," *ACS Catal.*, vol. 4, no. 6, pp. 1693–1705, 2014.

[55] R.L. McCreery, "Advanced carbon electrode materials for molecular electrochemistry," *Chem. Rev.*, vol. 108, no. 7, pp. 2646–2687, 2008.

[56] R. L. McCreery, "Carbon electrodes: structural effects on electron transfer kinetics," *Electroanal. Chem.*, vol. 17, pp. 221–374, 1991.

[57] T. J. Davies, C. E. Banks, and R. G. Compton, "Voltammetry at spatially heterogeneous electrodes," *J. Solid State Electrochem.*, vol. 9, no. 12, pp. 797–808, 2005.

[58] C. E. Banks and R. G. Compton, "Edge plane pyrolytic graphite electrodes in electroanalysis: an overview," *Anal. Sci.*, vol. 21, no. 11, pp. 1263–1268, 2005.

[59] K. Jurkschat, X. Ji, A. Crossley, R. G. Compton, and C. E. Banks, "Super-washing does not leave single walled carbon nanotubes iron-free," *Analyst*, vol. 132, no. 1, pp. 21–23, 2006.

[60] C. E. Banks, A. Crossley, C. Salter, S. J. Wilkins, and R. G. Compton, "Carbon nanotubes contain metal impurities which are responsible for the 'electrocatalysis' seen at some nanotube-modified electrodes," *Angew. Chemie Int. Ed.*, vol. 45, no. 16, pp. 2533–2537, 2006.

[61] M. Pumera and H. Iwai, "Multicomponent metallic impurities and their influence upon the electrochemistry of carbon nanotubes," *J. Phys. Chem. C*, vol. 113, no. 11, pp. 4401–4405, 2009.

[62] M. Pumera and H. Iwai, "Metallic impurities within residual catalyst metallic nanoparticles are in some cases responsible for 'electrocatalytic' effect of carbon nanotubes," *Chem. Asian J.*, vol. 4, no. 4, pp. 554–560, 2009.

[63] A. Chou, T. Böcking, N. K. Singh, and J. J. Gooding, "Demonstration of the importance

of oxygenated species at the ends of carbon nanotubes for their favourable electrochemical properties," *Chem. Commun.*, no. 7, pp. 842–844, 2005.

[64] C. E. Banks, R. R. Moore, T. J. Davies, and R. G. Compton, "Investigation of modified basal plane pyrolytic graphite electrodes: definitive evidence for the electrocatalytic properties of the ends of carbon nanotubes," *Chem. Commun.*, no. 16, pp. 1804–1805, 2004.

[65] M. Pumera, "The electrochemistry of carbon nanotubes: fundamentals and applications," *Chem. Eur. J.*, vol. 15, no. 20, pp. 4970–4978, 2009.

[66] J. Liu, A. Chou, W. Rahmat, M. N. Paddon-Row, and J. J. Gooding, "Achieving direct electrical connection to glucose oxidase using aligned single walled carbon nanotube arrays," *Electroanalysis*, vol. 17, no. 1, pp. 38–46, 2005.

[67] I. Heller, J. Kong, H. A. Heering, K. A. Williams, S. G. Lemay, and C. Dekker, "Individual single-walled carbon nanotubes as nanoelectrodes for electrochemistry," *Nano Lett.*, vol. 5, no. 1, pp. 137–142, 2005.

[68] N. Karousis, N. Tagmatarchis, and D. Tasis, "Current progress on the chemical modification of carbon nanotubes," *Chem. Rev.*, vol. 110, no. 9, pp. 5366–5397, 2010.

[69] K. F. E. Schafthaul, "Gelehrte Anzeigen Bayer," *Akad., 20, 557*, vol. 593, 1845.

[70] K. Byrappa and M. Yoshimura, *Handbook of hydrothermal technology*. William Andrew, 2012.

[71] M. S. Whittingham, J.-D. Guo, R. Chen, T. Chirayil, G. Janauer, and P. Zavalij, "The hydrothermal synthesis of new oxide materials," *Solid State Ionics*, vol. 75, pp. 257–268, 1995.

[72] M. Bedewy, E. R. Meshot, M. J. Reinker, and A. J. Hart, "Population growth dynamics of carbon nanotubes," *ACS Nano*, vol. 5, no. 11, pp. 8974–8989, 2011.

[73] M. L. Terranova, V. Sessa, and M. Rossi, "The world of carbon nanotubes: an overview of CVD growth methodologies," *Chem. Vap. Depos.*, vol. 12, no. 6, pp. 315–325, 2006.

[74] J. Prasek *et al.*, "Methods for carbon nanotubes synthesis," *J. Mater. Chem.*, vol. 21, no. 40, pp. 15872–15884, 2011.

[75] S. Liatard, K. Benhamouda, A. Fournier, R. Ramos, C. Barchasz, and J. Dijon, "Vertically-aligned carbon nanotubes on aluminum as a light-weight positive electrode for lithium-polysulfide batteries," *Chem. Commun.*, vol. 51, no. 36, pp. 7749–7752, 2015.

[76] S. Ahmad, D. Copic, C. George, and M. De Volder, "Hierarchical Assemblies of Carbon Nanotubes for Ultraflexible Li-Ion Batteries," *Adv. Mater.*, vol. 28, no. 31, pp. 6705–6710, 2016.

[77] W. Z. Li *et al.*, "Large-scale synthesis of aligned carbon nanotubes," *Science (80-.).*,

vol. 274, no. 5293, pp. 1701–1703, 1996.

[78] G. D. Nessim, "Properties, synthesis, and growth mechanisms of carbon nanotubes with special focus on thermal chemical vapor deposition," *Nanoscale*, vol. 2, no. 8, pp. 1306–1323, 2010.

[79] M. De Volder, S. Park, S. Tawfick, and A. J. Hart, "Strain-engineered manufacturing of freeform carbon nanotube microstructures," *Nat. Commun.*, vol. 5, p. 4512, 2014.

[80] G. D. Nessim *et al.*, "Precursor gas chemistry determines the crystallinity of carbon nanotubes synthesized at low temperature," *Carbon N. Y.*, vol. 49, no. 3, pp. 804–810, 2011.

[81] D. A. Skoog, F. J. Holler, and S. R. Crouch, *Principles of instrumental analysis*. Cengage learning, 2017.

[82] E. J. W. Crossland, "Block Copolymer Patterning of Functional Materials," vol. 101, no. 5, pp. 3053–725, 2008.

[83] P. C. Tiemeijer, M. Bischoff, B. Freitag, and C. Kisielowski, "Using a monochromator to improve the resolution in TEM to below 0.5 {Å}. Part II: application to focal series reconstruction," *Ultramicroscopy*, vol. 118, pp. 35–43, 2012.

[84] E. Stauffer, J. A. Dolan, and R. Newman, *Fire Debris Analysis*. Elsevier Science, 2007.

[85] J. W. Niemantsverdriet, *Spectroscopy in catalysis*. John Wiley & Sons, 2007.

[86] J. Rouquerol, F. Rouquerol, P. Llewellyn, G. Maurin, and K. S. W. Sing, *Adsorption by powders and porous solids: principles, methodology and applications*. Academic press, 2013.

[87] S. K. Shukla, A. K. Mishra, O. a. Arotiba, and B. B. Mamba, "Chitosan-based nanomaterials: A state-of-the-art review," *Int. J. Biol. Macromol.*, vol. 59, pp. 46–58, 2013.

[88] J. Zhang *et al.*, "Chitosan modification and pharmaceutical/biomedical applications," *Mar. Drugs*, vol. 8, no. 7, pp. 1962–1987, 2010.

[89] N. Mano, F. Mao, and A. Heller, "A Miniature Membrane-less Biofuel Cell Operating at+ 0.60 V under Physiological Conditions," *ChemBioChem*, vol. 5, no. 12, pp. 1703–1705, 2004.

[90] N. Mano, J. E. Yoo, J. Tarver, Y.-L. Loo, and A. Heller, "An electron-conducting cross-linked polyaniline-based redox hydrogel, formed in one step at pH 7.2, wires glucose oxidase," *J. Am. Chem. Soc.*, vol. 129, no. 22, pp. 7006–7007, 2007.

[91] S. A. Merchant, T. O. Tran, M. T. Meredith, T. C. Cline, D. T. Glatzhofer, and D. W. Schmidtke, "High-sensitivity amperometric biosensors based on ferrocene-modified linear poly (ethylenimine)," *Langmuir*, vol. 25, no. 13, pp. 7736–7742, 2009.

[92] N. Mano and A. Heller, “Bioelectrochemical propulsion,” *J. Am. Chem. Soc.*, vol. 127, no. 33, pp. 11574–11575, 2005.

[93] A. Heller, “Electron-conducting redox hydrogels: design, characteristics and synthesis,” *Curr. Opin. Chem. Biol.*, vol. 10, no. 6, pp. 664–672, 2006.

[94] C. Dispenza, C. Lo Presti, C. Belfiore, G. Spadaro, and S. Piazza, “Electrically conductive hydrogel composites made of polyaniline nanoparticles and poly (N-vinyl-2-pyrrolidone),” *Polymer (Guildf).*, vol. 47, no. 4, pp. 961–971, 2006.

[95] L. Tan *et al.*, “Stimuli-induced gel--sol transition of multi-sensitive supramolecular $β$-cyclodextrin grafted alginate/ferrocene modified pluronic hydrogel,” *Soft Matter*, vol. 8, no. 21, pp. 5746–5749, 2012.

[96] A. Heller and B. Feldman, “Electrochemistry in diabetes management,” *Acc. Chem. Res.*, vol. 43, no. 7, pp. 963–973, 2010.

[97] D. Zhai *et al.*, “Highly sensitive glucose sensor based on Pt nanoparticle/polyaniline hydrogel heterostructures,” *ACS Nano*, vol. 7, no. 4, pp. 3540–3546, 2013.

[98] S. Brahim, D. Narinesingh, and A. Guiseppi-Elie, “Polypyrrole-hydrogel composites for the construction of clinically important biosensors,” *Biosens. Bioelectron.*, vol. 17, no. 1, pp. 53–59, 2002.

[99] L. Chen *et al.*, “One-step synthesis of polyhydroquinone--graphene hydrogel composites for high performance supercapacitors,” *J. Mater. Chem. A*, vol. 3, no. 31, pp. 16033–16039, 2015.

[100] M. N. V. R. Kumar, R. A. A. Muzzarelli, C. Muzzarelli, H. Sashiwa, and A. J. Domb, “Chitosan chemistry and pharmaceutical perspectives,” *Chem. Rev.*, vol. 104, no. 12, pp. 6017–6084, 2004.

[101] R. A. A. Muzzarelli and C. Muzzarelli, “Chitosan chemistry: relevance to the biomedical sciences,” in *Polysaccharides I*, Springer, 2005, pp. 151–209.

[102] G. Berth, H. Dautzenberg, and M. G. Peter, “Physico-chemical characterization of chitosans varying in degree of acetylation,” *Carbohydr. Polym.*, vol. 36, no. 2, pp. 205–216, 1998.

[103] K. Roy, H.-Q. Mao, S.-K. Huang, and K. W. Leong, “Oral gene delivery with chitosan--DNA nanoparticles generates immunologic protection in a murine model of peanut allergy,” *Nat. Med.*, vol. 5, no. 4, pp. 387–391, 1999.

[104] T. Sato, T. Ishii, and Y. Okahata, “In vitro gene delivery mediated by chitosan. Effect of pH, serum, and molecular mass of chitosan on the transfection efficiency,” *Biomaterials*, vol. 22, no. 15, pp. 2075–2080, 2001.

[105] J.-K. F. Suh, H. W. . T. Matthew, J.-K. Francis Suh, and H. W. . T. Matthew, “Application of chitosan-based polysaccharide biomaterials in cartilage tissue engineering: a review,” *Biomaterials*, vol. 21, no. 24, pp. 2589–2598, Dec. 2000.

[106] S. A. Agnihotri, N. N. Mallikarjuna, and T. M. Aminabhavi, "Recent advances on chitosan-based micro-and nanoparticles in drug delivery," *J. Control. release*, vol. 100, no. 1, pp. 5–28, 2004.

[107] L. Fan, H. Yang, J. Yang, M. Peng, and J. Hu, "Preparation and characterization of chitosan/gelatin/PVA hydrogel for wound dressings," *Carbohydr. Polym.*, vol. 146, pp. 427–434, 2016.

[108] J. H. Cho *et al.*, "Chondrogenic differentiation of human mesenchymal stem cells using a thermosensitive poly (N-isopropylacrylamide) and water-soluble chitosan copolymer," *Biomaterials*, vol. 25, no. 26, pp. 5743–5751, 2004.

[109] N. Bhattarai, H. R. Ramay, J. Gunn, F. A. Matsen, and M. Zhang, "PEG-grafted chitosan as an injectable thermosensitive hydrogel for sustained protein release," *J. Control. Release*, vol. 103, no. 3, pp. 609–624, 2005.

[110] Y. Hong, H. Song, Y. Gong, Z. Mao, C. Gao, and J. Shen, "Covalently crosslinked chitosan hydrogel: properties of in vitro degradation and chondrocyte encapsulation," *Acta Biomater.*, vol. 3, no. 1, pp. 23–31, 2007.

[111] Y. Hong, Z. Mao, H. Wang, C. Gao, and J. Shen, "Covalently crosslinked chitosan hydrogel formed at neutral pH and body temperature," *J. Biomed. Mater. Res. Part A*, vol. 79, no. 4, pp. 913–922, 2006.

[112] B. G. Amsden, A. Sukarto, D. K. Knight, and S. N. Shapka, "Methacrylated glycol chitosan as a photopolymerizable biomaterial," *Biomacromolecules*, vol. 8, no. 12, pp. 3758–3766, 2007.

[113] M.-S. Kim, Y.-J. Choi, I. Noh, and G. Tae, "Synthesis and characterization of in situ chitosan-based hydrogel via grafting of carboxyethyl acrylate," *J. Biomed. Mater. Res. Part A*, vol. 83, no. 3, pp. 674–682, 2007.

[114] J. He, A. Zhang, Y. Zhang, and Y. Guan, "Novel redox hydrogel by in situ gelation of chitosan as a result of template oxidative polymerization of hydroquinone," *Macromolecules*, vol. 44, no. 7, pp. 2245–2252, 2011.

[115] E. Kim *et al.*, "Redox-Cycling and H 2 O 2 Generation by Fabricated Catecholic Films in the Absence of Enzymes," pp. 880–888, 2011.

[116] P. S. Yavvari and A. Srivastava, "Robust, self-healing hydrogels synthesised from catechol rich polymers," *J. Mater. Chem. B*, vol. 3, no. 5, pp. 899–910, 2015.

[117] J. March, *Advanced organic chemistry: reactions, mechanisms, and structure*. John Wiley & Sons, 1992.

[118] P. W. Milligan and M. M. Häggblom, "Biodegradation of resorcinol and catechol by denitrifying enrichment cultures," *Environ. Toxicol. Chem.*, vol. 17, no. 8, pp. 1456–1461, 1998.

[119] N. Schweigert, a. J. B. Zehnder, and R. I. L. Eggen, "Chemical properties of catechols

and their molecular modes of toxic action in cells, from microorganisms to mammals," *Environ. Microbiol.*, vol. 3, no. 2, pp. 81–91, 2001.

[120] H. S. Mason, E. Spencer, and I. Yamazaki, "Identification by electron spin resonance spectroscopy of the primary product of tyrosinase-catalyzed catechol oxidation," *Biochem. Biophys. Res. Commun.*, vol. 4, no. 3, pp. 236–238, 1961.

[121] Q. Lin, Q. Li, C. Batchelor-McAuley, and R. G. Compton, "Two-Electron, Two-Proton Oxidation of Catechol: Kinetics and Apparent Catalysis," *J. Phys. Chem. C*, vol. 119, no. 3, pp. 1489–1495, 2015.

[122] L. Papouchado, G. Petrie, and R. N. Adams, "Anodic oxidation pathways of phenolic compounds: Part I. Anodic hydroxylation reactions," *J. Electroanal. Chem. Interfacial Electrochem.*, vol. 38, no. 2, pp. 389–395, 1972.

[123] A. Kiani, J.-B. Raoof, D. Nematollahi, and R. Ojani, "Electrochemical study of catechol in the presence of dibuthylamine and diethylamine in aqueous media: Part 1. Electrochemical investigation," *Electroanalysis*, vol. 17, no. 19, pp. 1755–1760, 2005.

[124] R. Ojani, J.-B. Raoof, R. Hosseinzadeh, and A. Alinezhad, "Electrochemical oxidation of catechol in the presence of dimethyl chloromalonate and its digital simulation," *Asian J. Chem.*, vol. 20, no. 8, p. 5863, 2008.

[125] S. Mu, "Catechol sensor using poly (aniline-co-o-aminophenol) as an electron transfer mediator," *Biosens. Bioelectron.*, vol. 21, no. 7, pp. 1237–1243, 2006.

[126] L. Su and L. Mao, "Gold nanoparticle/alkanedithiol conductive films self-assembled onto gold electrode: Electrochemistry and electroanalytical application for voltammetric determination of trace amount of catechol," *Talanta*, vol. 70, no. 1, pp. 68–74, 2006.

[127] B. Nasr, G. Abdellatif, P. Cañizares, C. Sáez, J. Lobato, and M. a. Rodrigo, "Electrochemical oxidation of hydroquinone, resorcinol, and catechol on boron-doped diamond anodes," *Environ. Sci. Technol.*, vol. 39, no. 18, pp. 7234–7239, 2005.

[128] M. R. Deakin, P. M. Kovach, K. J. Stutts, and R. M. Wightman, "Heterogeneous mechanisms of the oxidation of catechols and ascorbic acid at carbon electrodes," *Anal. Chem.*, vol. 58, no. 7, pp. 1474–1480, 1986.

[129] P. Zanello, *Inorganic electrochemistry: theory, practice and applications*. Royal Society of Chemistry, 2003.

[130] C.-M. Che, K.-Y. Wong, and F. C. Anson, "Effects of electrode surface pretreatments on the electrochemistry of a macrocyclic dioxoruthenium (VI) complex," *J. Electroanal. Chem. interfacial Electrochem.*, vol. 226, no. 1, pp. 211–226, 1987.

[131] Y.-K. Lai and K.-Y. Wong, "Electrochemistry of bis (2, 2′-bipyridine)-diammineruthenium (II) complex in aqueous media at edge-plane pyrolytic graphite electrodes," *J. Electroanal. Chem.*, vol. 374, no. 1, pp. 255–261, 1994.

[132] M. H. V Huynh and T. J. Meyer, "Proton-coupled electron transfer," *Chem. Rev.*, vol.

107, no. 11, pp. 5004–5064, 2007.

[133] J. Poon, Q. Lin, C. Batchelor-McAuley, C. Salter, C. Johnston, and R. G. Compton, "Altered Electrochemistry at Graphene- or Alumina-Modified Electrodes: Catalysis vs Electrocatalysis in Multistep Electrode Processes," *J. Phys. Chem. C*, p. 150604132011002, 2015.

[134] S. M. Matthews *et al.*, "Attributes of direct current aperiodic and alternating current harmonic components derived from large amplitude fourier transformed voltammetry under microfluidic control in a channel electrode," *Anal. Chem.*, vol. 84, no. 15, pp. 6686–6692, 2012.

[135] M. H. Kim, "Analysis of the first-order EC process by direct current and derivative polarography," *Anal. Chem.*, vol. 59, no. 17, pp. 2136–2144, 1987.

[136] Q. S. Lin, Sin Rhu and Feng, "Determination of Chemical Reaction Rate Constants Preceding or Following Electron Transfer by Mechanical Square Wave Polarography," *Anal. Chem.*, vol. 54, no. 8, pp. 1362–1367, 1982.

[137] J. A. Dean and N. A. Lange, *Lange's handbook of chemistry*. McGraw-Hill, 1992.

[138] J. Zak and T. Kuwana, "Electrooxidative catalysis using dispersed alumina on glassy carbon surfaces," *J. Am. Chem. Soc.*, vol. 104, no. 20, pp. 5514–5515, 1982.

[139] J. Zak and T. Kuwana, "Chemically modified electrodes and electrocatalysis," *J. Electroanal. Chem. Interfacial Electrochem.*, vol. 150, no. 1–2, pp. 645–664, 1983.

[140] D. Nematollahi, M. Alimoradi, and S. W. Husain, "Cyclic voltammetric study of the oxidation of catechols in the presence of cyanide ion," *Electroanalysis*, vol. 16, no. 16, pp. 1359–1365, 2004.

[141] M. D. Ryan, "The Electrochemical Oxidation of Substituted Catechols," *J. Electrochem. Soc.*, vol. 127, no. 7, p. 1489, 1980.

[142] D. Nematollahi and M. Rafiee, "Electrochemical oxidation of catechols in the presence of acetylacetone," *J. Electroanal. Chem.*, vol. 566, no. 1, pp. 31–37, 2004.

[143] R. T. Kachoosangi, G. G. Wildgoose, and R. G. Compton, "Using capsaicin modified multiwalled carbon nanotube based electrodes and p-chloranil modified carbon paste electrodes for the determination of amines: Application to benzocaine and lidocaine," *Electroanalysis*, vol. 20, no. 23, pp. 2495–2500, 2008.

[144] S.-X. Guo, A. M. Bond, and J. Zhang, "Fourier Transformed Large Amplitude Alternating Current Voltammetry: Principles and Applications," *Rev. Polarogr.*, vol. 61, no. 1, pp. 21–32, 2015.

[145] S. A. Bonke, A. M. Bond, L. Spiccia, and A. N. Simonov, "Parameterization of Water Electrooxidation Catalyzed by Metal Oxides Using Fourier Transformed Alternating Current Voltammetry," *J. Am. Chem. Soc.*, vol. 138, no. 49, pp. 16095–16104, 2016.

[146] J. Zhang *et al.*, "Efficient hydrogen production on MoNi4 electrocatalysts with fast water dissociation kinetics," *Nat. Commun.*, vol. 8, no. May, p. 15437, 2017.

[147] A. J. Bard and M. A. Fox, "Artificial photosynthesis: solar splitting of water to hydrogen and oxygen," *Acc. Chem. Res.*, vol. 28, no. 3, pp. 141–145, 1995.

[148] D. Das and T. N. Veziroğlu, "Hydrogen production by biological processes: a survey of literature," *Int. J. Hydrogen Energy*, vol. 26, no. 1, pp. 13–28, 2001.

[149] A. Haryanto, S. Fernando, N. Murali, and S. Adhikari, "Current status of hydrogen production techniques by steam reforming of ethanol: A review," *Energy and Fuels*, vol. 19, no. 5, pp. 2098–2106, 2005.

[150] Z. Chen, Y. Yan, and S. S. E. H. Elnashaie, "Catalyst deactivation and engineering control for steam reforming of higher hydrocarbons in a novel membrane reformer," *Chem. Eng. Sci.*, vol. 59, no. 10, pp. 1965–1978, 2004.

[151] R. C. Timpe, "Hydrogen production from fossil fuels and other regionally available feedstocks," in *Fuel and Energy Abstracts*, 1997, vol. 4, no. 38, p. 228.

[152] J. D. Holladay, J. Hu, D. L. King, and Y. Wang, "An overview of hydrogen production technologies," *Catal. Today*, vol. 139, no. 4, pp. 244–260, 2009.

[153] N. S. Lewis, "Research opportunities to advance solar energy utilization," *Science (80-.).*, vol. 351, no. 6271, p. aad1920, 2016.

[154] K. Zeng and D. Zhang, "Recent progress in alkaline water electrolysis for hydrogen production and applications," *Prog. Energy Combust. Sci.*, vol. 36, no. 3, pp. 307–326, 2010.

[155] S. A. Grigoriev, V. I. Porembsky, and V. N. Fateev, "Pure hydrogen production by PEM electrolysis for hydrogen energy," *Int. J. Hydrogen Energy*, vol. 31, no. 2, pp. 171–175, 2006.

[156] J. Ivy, "Summary of electrolytic hydrogen production: milestone completion report," 2004.

[157] R. F. De Souza, J. C. Padilha, R. S. Gonçalves, M. O. De Souza, and J. Rault-Berthelot, "Electrochemical hydrogen production from water electrolysis using ionic liquid as electrolytes: towards the best device," *J. Power Sources*, vol. 164, no. 2, pp. 792–798, 2007.

[158] M. K. Bates, Q. Jia, N. Ramaswamy, R. J. Allen, and S. Mukerjee, "Composite Ni/NiO-Cr2O3 catalyst for alkaline hydrogen evolution reaction," *J. Phys. Chem. C*, vol. 119, no. 10, pp. 5467–5477, 2015.

[159] S. A. Vilekar, I. Fishtik, and R. Datta, "Kinetics of the hydrogen electrode reaction," *J. Electrochem. Soc.*, vol. 157, no. 7, pp. B1040--B1050, 2010.

[160] D. B. Levin, L. Pitt, and M. Love, "Biohydrogen production: prospects and limitations

to practical application," *Int. J. Hydrogen Energy*, vol. 29, no. 2, pp. 173–185, 2004.

[161] W. A. Amos, "Biological Water-gas Shift Conversion of Carbon Monoxide to Hydrogen: Milestone Completion Report," 2004.

[162] J. M. Norbeck, J. W. Heffel, T. D. Durbin, B. Tabbara, J. M. Bowden, and M. C. Montano, *Hydrogen fuel for surface transportation*, vol. 160. 1996.

[163] M. S. Opu, "Effect of operating parameters on performance of alkaline water electrolysis," *Int. J. Therm. Environ. Eng*, vol. 9, pp. 53–60, 2015.

[164] J. Kubisztal, A. Budniok, and A. Lasia, "Study of the hydrogen evolution reaction on nickel-based composite coatings containing molybdenum powder," *Int. J. Hydrogen Energy*, vol. 32, no. 9, pp. 1211–1218, 2007.

[165] J. R. McKone, S. C. Marinescu, B. S. Brunschwig, J. R. Winkler, and H. B. Gray, "Earth-abundant hydrogen evolution electrocatalysts," *Chem. Sci.*, vol. 5, no. 3, pp. 865–878, 2014.

[166] M. Zeng and Y. Li, "Recent advances in heterogeneous electrocatalysts for the hydrogen evolution reaction," *J. Mater. Chem. A*, vol. 3, no. 29, pp. 14942–14962, 2015.

[167] C. C. L. McCrory, S. Jung, J. C. Peters, and T. F. Jaramillo, "Benchmarking heterogeneous electrocatalysts for the oxygen evolution reaction," *J. Am. Chem. Soc.*, vol. 135, no. 45, pp. 16977–16987, 2013.

[168] E. J. Kelly and H. R. Bronstein, "Kinetics and mechanism of the hydrogen evolution reaction on titanium in acidic media," *J. Electrochem. Soc.*, vol. 131, no. 10, pp. 2232–2238, 1984.

[169] J. Bockris and E. C. Potter, "The mechanism of the cathodic hydrogen evolution reaction," *J. Electrochem. Soc.*, vol. 99, no. 4, pp. 169–186, 1952.

[170] Y. Xu and B. Zhang, "Recent advances in porous Pt-based nanostructures: synthesis and electrochemical applications," *Chem. Soc. Rev.*, vol. 43, no. 8, pp. 2439–2450, 2014.

[171] J. Zhang and C. M. Li, "Nanoporous metals: fabrication strategies and advanced electrochemical applications in catalysis, sensing and energy systems," *Chem. Soc. Rev.*, vol. 41, no. 21, pp. 7016–7031, 2012.

[172] J. Greeley, T. F. Jaramillo, J. Bonde, I. B. Chorkendorff, and J. K. Nørskov, "Computational high-throughput screening of electrocatalytic materials for hydrogen evolution," *Nat. Mater.*, vol. 5, no. 11, p. 909, 2006.

[173] D. M. F. Santos, C. A. C. Sequeira, and J. L. Figueiredo, "Hydrogen production by alkaline water electrolysis," *Qu{\'i}mica Nov.*, vol. 36, no. 8, pp. 1176–1193, 2013.

[174] D. M. Soares, O. Teschke, and I. Torriani, "Hydride effect on the kinetics of the hydrogen evolution reaction on nickel cathodes in alkaline media," *J. Electrochem. Soc.*, vol. 139, no. 1, pp. 98–105, 1992.

[175] I. A. Raj and K. I. Vasu, "Transition metal-based hydrogen electrodes in alkaline solution—electrocatalysis on nickel based binary alloy coatings," *J. Appl. Electrochem.*, vol. 20, no. 1, pp. 32–38, 1990.

[176] B. Hinnemann *et al.*, "Biomimetic hydrogen evolution: MoS2 nanoparticles as catalyst for hydrogen evolution," *J. Am. Chem. Soc.*, vol. 127, no. 15, pp. 5308–5309, 2005.

[177] T. F. Jaramillo, K. P. Jørgensen, J. Bonde, J. H. Nielsen, S. Horch, and I. Chorkendorff, "Identification of active edge sites for electrochemical H2 evolution from MoS2 nanocatalysts," *Science (80-.).*, vol. 317, no. 5834, pp. 100–102, 2007.

[178] M. a. Lukowski, A. S. Daniel, F. Meng, A. Forticaux, L. Li, and S. Jin, "Enhanced hydrogen evolution catalysis from chemically exfoliated metallic MoS2 nanosheets," *J. Am. Chem. Soc.*, vol. 135, no. 28, pp. 10274–10277, 2013.

[179] W.-F. Chen, J. T. Muckerman, and E. Fujita, "Recent developments in transition metal carbides and nitrides as hydrogen evolution electrocatalysts," *Chem. Commun.*, vol. 49, no. 79, pp. 8896–8909, 2013.

[180] C. Wan, Y. N. Regmi, and B. M. Leonard, "Multiple phases of molybdenum carbide as electrocatalysts for the hydrogen evolution reaction," *Angew. Chemie - Int. Ed.*, vol. 53, no. 25, pp. 6407–6410, 2014.

[181] N. Daems, X. Sheng, I. F. J. Vankelecom, and P. P. Pescarmona, "Metal-free doped carbon materials as electrocatalysts for the oxygen reduction reaction," *J. Mater. Chem. A*, vol. 2, no. 12, pp. 4085–4110, 2014.

[182] P. Patnaik, *A comprehensive guide to the hazardous properties of chemical substances*. John Wiley & Sons, 2007.

[183] B. Meyer, "Sulfur," *Energy Environ. Elsevier Sci. Publ. Amsterdam, Netherlands*, 1977.

[184] S. BAYKARA, E. FIGEN, A. KALE, and T. NEJATVEZIROGLU, "Hydrogen from hydrogen sulphide in Black Sea," *Int. J. Hydrogen Energy*, vol. 32, no. 9, pp. 1246–1250, Jun. 2007.

[185] A. N. Startsev *et al.*, "Low temperature catalytic decomposition of hydrogen sulfide into hydrogen and diatomic gaseous sulfur," *Top. Catal.*, vol. 56, no. 11, pp. 969–980, 2013.

[186] R. Adewale, D. J. Salem, A. S. Berrouk, and S. Dara, "Simulation of hydrogen production from thermal decomposition of hydrogen sul fi de in sulfur recovery units," *J. Clean. Prod.*, vol. 112, pp. 4815–4825, 2016.

[187] J. Zaman and A. Chakma, "Production of Hydrogen and Sulfur from Hydrogen-Sulfide," *Fuel Process. Technol.*, vol. 41, no. 2, pp. 159–198, 1995.

[188] V. E. Kaloidas and N. G. Papayannakos, "Hydrogen production from the decomposition of hydrogen sulphide. Equilibrium studies on the system H2S/ H2/Si, (i = 1,…,8) in the gas phase," *Int. J. Hydrogen Energy*, vol. 12, no. 6, pp. 403–409, 1987.

[189] A. Pietro Reverberi, J. J. Klemeš, P. S. Varbanov, and B. Fabiano, "A review on hydrogen production from hydrogen sulphide by chemical and photochemical methods," *J. Clean. Prod.*, vol. 136, pp. 72–80, 2016.

[190] T. C. and C. LAU, "The Thermal Decomposition of Hydrogen Sulfide Over Vanadium and Molybdenum Sulfides and Mixed Sulfide Catalysts in Quartz and Thermal Diffusion Column Reactors," *Int. J. Hydrog. Energy*, no. 4, 1987.

[191] K. Fukuda, M. Dokiya, T. Kameyama, and Y. Kotera, "Catalytic Decomposition of Hydrogen Sulfide," *Ind. Eng. Chem. Fundam.*, vol. 17, no. 4, pp. 243–248, 1978.

[192] M. Moghiman, S. M. Javadi, A. R. Moghiman, and S. B. Hosseini, "A numerical study on thermal dissociation of H2S," in *World Academy of Science, Engineering and Technology 62 2010*, 2010.

[193] M. E. D. Raymont, "Make hydrogen from hydrogen sulfide.[Non-oxidative thermal cracking of H/sub 2/S]," *Hydrocarb. Process. States)*, vol. 54, no. 7, 1975.

[194] V. E. Kaloidas and N. G. Papayannakos, "Kinetic Studies on the Catalytic Decomposition of Hydrogen Sulfide in a Tubular Reactor," *Ind. Eng. Chem. Res.*, vol. 1923, pp. 664–670, 1991.

[195] Y. Yin, R. M. Rioux, C. K. Erdonmez, S. Hughes, G. A. Somorjai, and A. P. Alivisatos, "Formation of hollow nanocrystals through the nanoscale Kirkendall effect," *Science (80-.).*, vol. 304, no. 5671, pp. 711–714, 2004.

[196] P. M. Arnal, M. Comotti, and F. Schüth, "High-temperature-stable catalysts by hollow sphere encapsulation," *Angew. Chemie*, vol. 118, no. 48, pp. 8404–8407, 2006.

[197] J. Feng and H. C. Zeng, "Reduction and reconstruction of Co3O4 nanocubes upon carbon deposition.," *J. Phys. Chem. B*, vol. 109, no. 36, pp. 17113–9, 2005.

[198] P. J. F. Harris and S. C. Tsang, "A simple technique for the synthesis of filled carbon nanoparticles," *Chem. Phys. Lett.*, vol. 293, no. 1, pp. 53–58, 1998.

[199] D. Merki and X. Hu, "Recent developments of molybdenum and tungsten sulfides as hydrogen evolution catalysts," *Energy Environ. Sci.*, vol. 4, no. 10, p. 3878, 2011.

[200] Z. Zhang *et al.*, "3D Interconnected Porous Carbon Aerogels as Sulfur Immobilizers for Sulfur Impregnation for Lithium-Sulfur Batteries with High Rate Capability and Cycling Stability," *Adv. Funct. Mater.*, vol. 24, no. 17, pp. 2500–2509, 2014.

[201] K. T. Lee, Y. S. Jung, and S. M. Oh, "Synthesis of tin-encapsulated spherical hollow carbon for anode material in lithium secondary batteries," *J. Am. Chem. Soc.*, vol. 125, no. 19, pp. 5652–5653, 2003.

[202] J. Dou and H. C. Zeng, "Preparation of Mo-embedded mesoporous carbon microspheres for friedel-crafts alkylation," *J. Phys. Chem. C*, vol. 116, no. 14, pp. 7767–7775, 2012.

[203] X. W. Lou, J. S. Chen, P. Chen, and L. A. Archer, "One-pot synthesis of carbon-coated

SnO2 nanocolloids with improved reversible lithium storage properties," *Chem. Mater.*, vol. 21, no. 13, pp. 2868–2874, 2009.

[204] Y. Tian *et al.*, "Synthesis of amorphous MoS 2 nanospheres by hydrothermal reaction," *Mater. Lett.*, vol. 60, no. 4, pp. 527–529, 2006.

[205] H. Zhang, H. Lin, Y. Zheng, Y. Hu, and A. MacLennan, "Understanding of the effect of synthesis temperature on the crystallization and activity of nano-MoS2 catalyst," *Appl. Catal. B Environ.*, vol. 165, pp. 537–546, 2015.

[206] F. Rashidi, T. Sasaki, A. M. Rashidi, A. N. Kharat, and K. J. Jozani, "Ultradeep hydrodesulfurization of diesel fuels using highly efficient nanoalumina-supported catalysts: impact of support, phosphorus, and/or boron on the structure and catalytic activity," *J. Catal.*, vol. 299, pp. 321–335, 2013.

[207] L. Yang *et al.*, "Porous metallic MoO2-supported MoS2 Nanosheets for enhanced electrocatalytic activity in hydrogen evolution reaction," *Nanoscale*, vol. 7, pp. 5203–5208, 2015.

[208] T. K. T. Ninh, L. Massin, D. Laurenti, and M. Vrinat, "A new approach in the evaluation of the support effect for NiMo hydrodesulfurization catalysts," *Appl. Catal. A Gen.*, vol. 407, no. 1–2, pp. 29–39, 2011.

[209] S. Eijsbouts, J. J. L. Heinerman, and H. J. W. Elzerman, "MoS2 structures in high activity hydrotreating catalysts. II. Evolution of the active phase during the catalyst life cycle. Deactivation model," *Appl. Catal. A Gen.*, vol. 105, no. 1, pp. 69–82, 1993.

[210] J. D. Benck, Z. Chen, L. Y. Kuritzky, A. J. Forman, and T. F. Jaramillo, "Amorphous molybdenum sulfide catalysts for electrochemical hydrogen production: insights into the origin of their catalytic activity," *Acs Catal.*, vol. 2, no. 9, pp. 1916–1923, 2012.

[211] X. Dai *et al.*, "Co-Doped MoS2 Nanosheets with the Dominant CoMoS Phase Coated on Carbon as an Excellent Electrocatalyst for Hydrogen Evolution," *ACS Appl. Mater. Interfaces*, vol. 7, no. 49, pp. 27242–27253, 2015.

[212] D. Laurenti *et al.*, "Intrinsic potential of alumina-supported CoMo catalysts in HDS: Comparison between γc, γt, and δ-alumina," *J. Catal.*, vol. 297, pp. 165–175, 2013.

[213] P. A. Nikulshin, D. I. Ishutenko, A. A. Mozhaev, K. I. Maslakov, and A. A. Pimerzin, "Effects of composition and morphology of active phase of CoMo/Al 2 O 3 catalysts prepared using Co 2 Mo 10--heteropolyacid and chelating agents on their catalytic properties in HDS and HYD reactions," *J. Catal.*, vol. 312, pp. 152–169, 2014.

[214] B. Guichard, M. Roy-Auberger, E. Devers, C. Legens, and P. Raybaud, "Aging of Co (Ni) MoP/Al 2 O 3 catalysts in working state," *Catal. Today*, vol. 130, no. 1, pp. 97–108, 2008.

[215] A. F. Lamic, A. Daudin, S. Brunet, C. Legens, C. Bouchy, and E. Devers, "Effect of H2S partial pressure on the transformation of a model FCC gasoline olefin over

unsupported molybdenum sulfide-based catalysts," *Appl. Catal. A Gen.*, vol. 344, no. 1–2, pp. 198–204, 2008.

[216] Y. R. Liu *et al.*, "Facile one-pot synthesis of CoS2-MoS2/CNTs as efficient electrocatalyst for hydrogen evolution reaction," *Appl. Surf. Sci.*, vol. 384, pp. 51–57, 2016.

[217] Y. Li, H. Wang, L. Xie, Y. Liang, G. Hong, and H. Dai, "MoS2 nanoparticles grown on graphene: An advanced catalyst for the hydrogen evolution reaction," *J. Am. Chem. Soc.*, vol. 133, no. 19, pp. 7296–7299, 2011.

[218] R. Subbaraman *et al.*, "Enhancing hydrogen evolution activity in water splitting by tailoring Li+-Ni (OH) 2-Pt interfaces," *Science (80-.).*, vol. 334, no. 6060, pp. 1256–1260, 2011.

[219] Y. Zheng, Y. Jiao, M. Jaroniec, and S. Z. Qiao, "Advancing the electrochemistry of the hydrogen- Evolution reaction through combining experiment," *Angew. Chemie - Int. Ed.*, vol. 54, no. 1, pp. 52–65, 2015.

[220] Y. Yu, S. Y. Huang, Y. Li, S. N. Steinmann, W. Yang, and L. Cao, "Layer-dependent electrocatalysis of MoS2 for hydrogen evolution," *Nano Lett.*, vol. 14, no. 2, pp. 553–558, 2014.

[221] F. Safizadeh, E. Ghali, and G. Houlachi, "Electrocatalysis developments for hydrogen evolution reaction in alkaline solutions - A Review," *Int. J. Hydrogen Energy*, vol. 40, no. 1, pp. 256–274, 2015.

[222] S. A. Bonke, A. M. Bond, L. Spiccia, and A. N. Simonov, "Parameterization of Water Electrooxidation Catalyzed by Metal Oxides Using Fourier Transformed Alternating Current Voltammetry," *J. Am. Chem. Soc.*, vol. 138, no. 49, pp. 16095–16104, 2016.

[223] N. O. Guldal, H. E. Figen, and S. Z. Baykara, "New catalysts for hydrogen production from H2S : Preliminary results," *Int. J. Hydrogen Energy*, vol. 40, no. 24, pp. 7452–7458, 2015.

[224] A. V Pashigreva, G. A. Bukhtiyarova, O. V Klimov, Y. A. Chesalov, G. S. Litvak, and A. S. Noskov, "Activity and sulfidation behavior of the CoMo / Al2O3 hydrotreating catalyst : The effect of drying conditions," *Catal. Today*, vol. 149, pp. 19–27, 2010.

[225] H. Bashiri and S. Mohamadi, "Hydrogen sulfide decomposition on Ni surface : A kinetic Monte Carlo study," *Appl. Catal. A Gen.*, vol. 509, pp. 105–110, 2016.

[226] M. Argyle and C. Bartholomew, "Heterogeneous Catalyst Deactivation and Regeneration: A Review," *Catalysts*, vol. 5, no. 1, pp. 145–269, 2015.

[227] S. Iijima, "Helical microtubules of graphitic carbon," *Nature*, vol. 354, no. 6348, p. 56, 1991.

[228] M. F. L. De Volder, S. H. Tawfick, R. H. Baughman, and A. J. Hart, "Carbon Nanotubes: Present and Future Commercial Applications," *Science (80-.).*, vol. 339, no. 6119, pp.

535–539, 2013.

[229] P. M. Ajayan, “Nanotubes from carbon,” *Chem. Rev.*, vol. 99, no. 7, pp. 1787–1800, 1999.

[230] N. S. Lawrence and J. Wang, “Chemical adsorption of phenothiazine dyes onto carbon nanotubes: Toward the low potential detection of NADH,” *Electrochem. commun.*, vol. 8, no. 1, pp. 71–76, 2006.

[231] C. B. Jacobs, M. J. Peairs, and B. J. Venton, “Review: Carbon nanotube based electrochemical sensors for biomolecules,” *Anal. Chim. Acta*, vol. 662, no. 2, pp. 105–127, 2010.

[232] J. Wang, M. Li, Z. Shi, N. Li, and Z. Gu, “Electrocatalytic oxidation of norepinephrine at a glassy carbon electrode modified with single wall carbon nanotubes,” *Electroanalysis*, vol. 14, no. 3, pp. 225–230, 2002.

[233] J. Wang and M. Musameh, “Carbon nanotube/teflon composite electrochemical sensors and biosensors,” *Anal. Chem.*, vol. 75, no. 9, pp. 2075–2079, 2003.

[234] H. Luo, Z. Shi, N. Li, Z. Gu, and Q. Zhuang, “Investigation of the electrochemical and electrocatalytic behavior of single-wall carbon nanotube film on a glassy carbon electrode,” *Anal. Chem.*, vol. 73, no. 5, pp. 915–920, 2001.

[235] N. S. Lawrence, R. P. Deo, and J. Wang, “Electrochemical determination of hydrogen sulfide at carbon nanotube modified electrodes,” *Anal. Chim. Acta*, vol. 517, no. 1–2, pp. 131–137, Jul. 2004.

[236] J. Wang, M. Li, Z. Shi, N. Li, and Z. Gu, “Electrochemistry of DNA at single-wall carbon nanotubes,” *Electroanalysis*, vol. 16, no. 1–2, pp. 140–144, 2004.

[237] M. L. Pedano and G. A. Rivas, “Adsorption and electrooxidation of nucleic acids at carbon nanotubes paste electrodes,” *Electrochem. commun.*, vol. 6, no. 1, pp. 10–16, 2004.

[238] M. Pumera, A. Merkoçi, and S. Alegret, “Carbon nanotube-epoxy composites for electrochemical sensing,” *Sensors Actuators, B Chem.*, vol. 113, no. 2, pp. 617–622, 2006.

[239] P. Yáñez-Sedeño, J. M. Pingarrón, J. Riu, and F. X. Rius, “Electrochemical sensing based on carbon nanotubes,” *TrAC - Trends Anal. Chem.*, vol. 29, no. 9, pp. 939–953, 2010.

[240] H. Hiura, T. W. Ebbesen, and K. Tanigaki, “Opening and purification of carbon nanotubes in high yields,” *Adv. Mater.*, vol. 7, no. 3, pp. 275–276, 1995.

[241] A. Miodek, G. Castillo, T. Hianik, and H. Korri-Youssoufi, “Electrochemical aptasensor of human cellular prion based on multiwalled carbon nanotubes modified with dendrimers: A platform for connecting redox markers and aptamers,” *Anal. Chem.*, vol. 85, no. 16, pp. 7704–7712, 2013.

[242] F. Patolsky, Y. Weizmann, and I. Willner, "Long-range electrical contacting of redox enzymes by SWCNT connectors," *Angew. Chemie - Int. Ed.*, vol. 43, no. 16, pp. 2113–2117, 2004.

[243] Y. Lin, F. Lu, Y. Tu, and Z. Ren, "Glucose Biosensors Based on Carbon Nanotube Nanoelectrode Ensembles," *Nano Lett.*, vol. 4, no. 2, pp. 191–195, 2004.

[244] P. J. Britto, K. S. V Santhanam, and P. M. Ajayan, "Carbon nanotube electrode for oxidation of dopamine," *Bioelectrochemistry Bioenerg.*, vol. 41, no. 1, pp. 121–125, 1996.

[245] C. E. Banks, G. G. Wildgoose, C. G. R. Heald, and R. G. Compton, "Oxygen reduction catalysis at anthraquinone centres molecularly wired via carbon nanotubes," *J. Iran. Chem. Soc.*, vol. 2, no. 1, pp. 60–64, 2005.

[246] S. B. Hočevar, J. Wang, R. P. Deo, M. Musameh, and B. Ogorevc, "Carbon nanotube modified microelectrode for enhanced voltammetric detection of dopamine in the presence of ascorbate," *Electroanalysis*, vol. 17, no. 5–6, pp. 417–422, 2005.

[247] C. Deng, J. Chen, X. Chen, C. Xiao, L. Nie, and S. Yao, "Direct electrochemistry of glucose oxidase and biosensing for glucose based on boron-doped carbon nanotubes modified electrode," *Biosens. Bioelectron.*, vol. 23, no. 8, pp. 1272–1277, 2008.

[248] M. M. Rahman, A. Umar, and K. Sawada, "Development of amperometric glucose biosensor based on glucose oxidase co-immobilized with multi-walled carbon nanotubes at low potential," *Sensors Actuators B Chem.*, vol. 137, no. 1, pp. 327–333, 2009.

[249] K. Ramachandran, K. J. Babu, and others, "Ni-Co bimetal nanowires filled multiwalled carbon nanotubes for the highly sensitive and selective non-enzymatic glucose sensor applications," *Sci. Rep.*, vol. 6, p. 36583, 2016.

[250] R. Akter, M. A. Rahman, and C. K. Rhee, "Amplified electrochemical detection of a cancer biomarker by enhanced precipitation using horseradish peroxidase attached on carbon nanotubes," *Anal. Chem.*, vol. 84, no. 15, pp. 6407–6415, 2012.

[251] L. Ji *et al.*, "Ultrasensitive sandwich-type electrochemical immunosensor based on a novel signal amplification strategy using highly loaded palladium nanoparticles/carbon decorated magnetic microspheres as signal labels," *Biosens. Bioelectron.*, vol. 68, pp. 757–762, 2015.

[252] H. Cui, C. Hong, A. Ying, X. Yang, and S. Ren, "Ultrathin gold nanowire-functionalized carbon nanotubes for hybrid molecular sensing," *ACS Nano*, vol. 7, no. 9, pp. 7805–7811, 2013.

[253] J. Li, G. Liu, W. Zhang, W. Cheng, H. Xu, and S. Ding, "Competitive detection of pregnancy-associated plasma protein-A in serum using functional single walled carbon nanotubes/chitosan-based electrochemical immunosensor," *J. Electroanal. Chem.*, vol. 708, pp. 95–100, 2013.

[254] A. Profumo *et al.*, "Multiwalled carbon nanotube chemically modified gold electrode for inorganic as speciation and Bi (III) determination," *Anal. Chem.*, vol. 78, no. 12, pp. 4194–4199, 2006.

[255] J. Li, A. Cassell, L. Delzeit, J. Han, and M. Meyyappan, "Novel three-dimensional electrodes: Electrochemical properties of carbon nanotube ensembles," *J. Phys. Chem. B*, vol. 106, no. 36, pp. 9299–9305, 2002.

[256] S. Sotiropoulou and N. A. Chaniotakis, "Carbon nanotube array-based biosensor," *Anal. Bioanal. Chem.*, vol. 375, no. 1, pp. 103–105, 2003.

[257] X. Yu, D. Chattopadhyay, I. Galeska, F. Papadimitrakopoulos, and J. F. Rusling, "Peroxidase activity of enzymes bound to the ends of single-wall carbon nanotube forest electrodes," *Electrochem. commun.*, vol. 5, no. 5, pp. 408–411, 2003.

[258] X. Yu *et al.*, "Carbon nanotube amplification strategies for highly sensitive immunodetection of cancer biomarkers," *J. Am. Chem. Soc.*, vol. 128, no. 34, pp. 11199–11205, 2006.

[259] B. S. Munge, J. Fisher, L. N. Millord, C. E. Krause, R. S. Dowd, and J. F. Rusling, "Sensitive electrochemical immunosensor for matrix metalloproteinase-3 based on single-wall carbon nanotubes," *Analyst*, vol. 135, no. 6, pp. 1345–1350, 2010.

[260] J. J. Gooding *et al.*, "Protein electrochemistry using aligned carbon nanotube arrays," *J. Am. Chem. Soc.*, vol. 125, no. 30, pp. 9006–9007, 2003.

[261] C. V Nguyen, L. Delzeit, A. M. Cassell, J. Li, J. Han, and M. Meyyappan, "Preparation of nucleic acid functionalized carbon nanotube arrays," *Nano Lett.*, vol. 2, no. 10, pp. 1079–1081, 2002.

[262] J. Koehne *et al.*, "The fabrication and electrochemical characterization of carbon nanotube nanoelectrode arrays," *J. Mater. Chem.*, vol. 14, no. 4, pp. 676–684, 2004.

[263] G. Liu, Y. Lin, Y. Tu, and Z. Ren, "Ultrasensitive voltammetric detection of trace heavy metal ions using carbon nanotube nanoelectrode array," *Analyst*, vol. 130, no. 7, pp. 1098–1101, 2005.

[264] D. Cai *et al.*, "A molecular-imprint nanosensor for ultrasensitive detection of proteins," *Nat. Nanotechnol.*, vol. 5, no. 8, p. 597, 2010.

[265] I. Taurino, S. Carrara, M. Giorcelli, A. Tagliaferro, and G. De Micheli, "Comparing sensitivities of differently oriented multi-walled carbon nanotubes integrated on silicon wafer for electrochemical biosensors," *Sensors Actuators B Chem.*, vol. 160, no. 1, pp. 327–333, 2011.

[266] D. Sun, X. Xie, Y. Cai, H. Zhang, and K. Wu, "Voltammetric determination of Cd2+ based on the bifunctionality of single-walled carbon nanotubes--Nafion film," *Anal. Chim. Acta*, vol. 581, no. 1, pp. 27–31, 2007.

[267] C. Wang and C. K. Chan, "Carbon Nanotube--Based Electrodes for Detection of Low--

ppb Level Hexavalent Chromium Using Amperometry," *ECS J. Solid State Sci. Technol.*, vol. 5, no. 8, pp. M3026--M3031, 2016.

[268] I. Dumitrescu, P. R. Unwin, and J. V Macpherson, "Electrochemistry at carbon nanotubes: perspective and issues," *Chem. Commun.*, no. 45, pp. 6886–6901, 2009.

[269] N. R. Stradiotto, H. Yamanaka, and M. V. B. Zanoni, "Review Electrochemical Sensors : A Powerful Tool in Analytical Chemistry," *J.Braz.Chem.Aoc.*, vol. 14, no. 2, pp. 159–173, 2003.

[270] P. Jiang, H. Xia, Z. He, and Z. Wang, "Design of a water environment monitoring system based on wireless sensor networks," *Sensors*, vol. 9, no. 8, pp. 6411–6434, 2009.

[271] X. Shi and X. Zhu, "Biofilm formation and food safety in food industries," *Trends Food Sci. Technol.*, vol. 20, no. 9, pp. 407–413, 2009.

[272] L. Wang *et al.*, "Imaging acidosis in tumors using a pH-activated near-infrared fluorescence probe," *Chem. Commun.*, vol. 48, no. 95, pp. 11677–11679, 2012.

[273] S. Schreml, R.-M. Szeimies, S. Karrer, J. Heinlin, M. Landthaler, and P. Babilas, "The impact of the pH value on skin integrity and cutaneous wound healing," *J. Eur. Acad. Dermatology Venereol.*, vol. 24, no. 4, pp. 373–378, 2010.

[274] R. G. Sawyer, M. D. Spengler, R. B. Adams, and T. L. Pruett, "The peritoneal environment during infection. The effect of monomicrobial and polymicrobial bacteria on pO2 and pH.," *Ann. Surg.*, vol. 213, no. 3, p. 253, 1991.

[275] D. W. Kimmel, G. Leblanc, M. E. Meschievitz, and D. E. Cliffel, "Electrochemical sensors and biosensors," *Anal. Chem.*, vol. 84, no. 2, pp. 685–707, 2012.

[276] A. Bratov, N. Abramova, and A. Ipatov, "Recent trends in potentiometric sensor arrays—A review," *Anal. Chim. Acta*, vol. 678, no. 2, pp. 149–159, 2010.

[277] G. Korotcenkov, *Chemical Sensors: Comprehensive Sensor Technologies Volume 5: Electrochemical and Optical Sensors*, vol. 5. Momentum Press, 2011.

[278] H. Freiser, "Coated wire ion-selective electrodes. Principles and practice," *J. Chem. Soc. Faraday Trans. 1 Phys. Chem. Condens. Phases*, vol. 82, no. 4, pp. 1217–1221, 1986.

[279] T. Akiyama, Y. Ujihira, Y. Okabe, T. Sugano, and E. Niki, "Ion-sensitive field-effect transistors with inorganic gate oxide for pH sensing," *IEEE Trans. Electron Devices*, vol. 29, no. 12, pp. 1936–1941, 1982.

[280] Y. Ohno, K. Maehashi, Y. Yamashiro, and K. Matsumoto, "Electrolyte-gated graphene field-effect transistors for detecting pH and protein adsorption," *Nano Lett.*, vol. 9, no. 9, pp. 3318–3322, 2009.

[281] G. G. Wildgoose, M. Pandurangappa, N. S. Lawrence, L. Jiang, T. G. J. Jones, and R. G. Compton, "Anthraquinone-derivatised carbon powder: Reagentless voltammetric pH electrodes," *Talanta*, vol. 60, no. 5, pp. 887–893, 2003.

[282] R. T. Kennedy, L. Huang, M. A. Atkinson, and P. Dush, "Amperometric monitoring of chemical secretions from individual pancreatic. beta.-cells," *Anal. Chem.*, vol. 65, no. 14, pp. 1882–1887, 1993.

[283] M. A. Makos, D. M. Omiatek, A. G. Ewing, and M. L. Heien, "Development and characterization of a voltammetric carbon-fiber microelectrode pH sensor," *Langmuir*, vol. 26, no. 12, pp. 10386–10391, 2010.

[284] B. Brunetti, P. Ugo, L. M. Moretto, and C. R. Martin, "Electrochemistry of phenothiazine and methylviologen biosensor electron-transfer mediators at nanoelectrode ensembles," *J. Electroanal. Chem.*, vol. 491, no. 1–2, pp. 166–174, 2000.

[285] R. Koncki and M. Mascini, "Screen-printed ruthenium dioxide electrodes for pH measurements," *Anal. Chim. Acta*, vol. 351, no. 1–3, pp. 143–149, 1997.

[286] K. Lee, J. H. Kwon, S. ll Moon, W. S. Cho, B. K. Ju, and Y. H. Lee, "pH sensitive multiwalled carbon nanotubes," *Mater. Lett.*, vol. 61, no. 14–15, pp. 3201–3203, 2007.

[287] D. Wang and L. Chen, "Temperature and pH-responsive single-walled carbon nanotube dispersions," *Nano Lett.*, vol. 7, no. 6, pp. 1480–1484, 2007.

[288] D. Jung, M. E. Han, and G. S. Lee, "PH-sensing characteristics of multi-walled carbon nanotube sheet," *Mater. Lett.*, vol. 116, pp. 57–60, 2014.

[289] P. G. Collins, A. Zettl, H. Bando, A. Thess, and R. E. Smalley, "Nanotube nanodevice," *Science (80-.).*, vol. 278, no. 5335, pp. 100–102, 1997.

[290] K. Kostarelos *et al.*, "Cellular uptake of functionalized carbon nanotubes is independent of functional group and cell type," *Nat. Nanotechnol.*, vol. 2, no. 2, p. 108, 2007.

[291] N. Nakayama-Ratchford, S. Bangsaruntip, X. Sun, K. Welsher, and H. Dai, "Noncovalent functionalization of carbon nanotubes by fluorescein- polyethylene glycol: supramolecular conjugates with pH-dependent absorbance and fluorescence," *J. Am. Chem. Soc.*, vol. 129, no. 9, pp. 2448–2449, 2007.

[292] L. Zhao, T. Nakayama, H. Tomimoto, Y. Shingaya, and Q. Huang, "Functionalization of carbon nanotubes with a pH-responsive molecule to produce a pH sensor," *Nanotechnology*, vol. 20, no. 32, 2009.

[293] P. Li, C. M. Martin, K. K. Yeung, and W. Xue, "Dielectrophoresis aligned single-walled carbon nanotubes as ph ensors," *Biosensors*, vol. 1, no. 1, pp. 23–35, 2011.

[294] Y. Miyata, K. Mizuno, and H. Kataura, "Purity and Defect Characterization of Single-Wall Carbon Nanotubes Using Raman Spectroscopy," *J. Nanomater.*, vol. 2011, no. Cvd, pp. 1–7, 2011.

[295] E. H. Seymour, N. S. Lawrence, and R. G. Compton, "Reaction with N, N-Diethyl-p-phenylenediamine: A Procedure for the Sensitive Square-Wave Voltammetric Detection of Chlorine," *Electroanalysis*, vol. 15, no. 8, pp. 689–694, 2003.

[296] Á. Mechler, J. Kokavecz, P. Heszler, and R. Lal, "Surface energy maps of nanostructures: atomic force microscopy and numerical simulation study," *Appl. Phys. Lett.*, vol. 82, no. 21, pp. 3740–3742, 2003.

[297] H. Baltruschat and A. Wieckowski, "Interfacial Electrochemistry: Theory, Experiment, and Application." Marcel Dekker, Inc., New York, 1999.

[298] M. Monthioux and V. L. Kuznetsov, "Who should be given the credit for the discovery of carbon nanotubes?" Pergamon, 2006.

[299] R. Zhang, Y. Zhang, Q. Zhang, H. Xie, W. Qian, and F. Wei, "Growth of half-meter long carbon nanotubes based on Schulz--Flory distribution," *ACS Nano*, vol. 7, no. 7, pp. 6156–6161, 2013.

[300] R. Zhang, Y. Zhang, and F. Wei, "Horizontally aligned carbon nanotube arrays: growth mechanism, controlled synthesis, characterization, properties and applications," *Chem. Soc. Rev.*, 2017.

[301] Z. Liu, L. Jiao, Y. Yao, X. Xian, and J. Zhang, "Aligned, Ultralong Single-Walled Carbon Nanotubes: From Synthesis, Sorting, to Electronic Devices," *Adv. Mater.*, vol. 22, no. 21, pp. 2285–2310, 2010.

[302] X. Zhou, J.-Y. Park, S. Huang, J. Liu, and P. L. McEuen, "Band structure, phonon scattering, and the performance limit of single-walled carbon nanotube transistors," *Phys. Rev. Lett.*, vol. 95, no. 14, p. 146805, 2005.

[303] S. Berber, Y.-K. Kwon, and D. Tománek, "Unusually high thermal conductivity of carbon nanotubes," *Phys. Rev. Lett.*, vol. 84, no. 20, p. 4613, 2000.

[304] A. Thess *et al.*, "Crystalline ropes of metallic carbon nanotubes," *Science (80-.).*, vol. 273, no. 5274, pp. 483–487, 1996.

[305] D. Takagi, H. Hibino, S. Suzuki, Y. Kobayashi, and Y. Homma, "Carbon nanotube growth from semiconductor nanoparticles," *Nano Lett.*, vol. 7, no. 8, pp. 2272–2275, 2007.

[306] K. Hata, D. N. Futaba, K. Mizuno, T. Namai, M. Yumura, and S. Iijima, "Water-assisted highly efficient synthesis of impurity-free single-walled carbon nanotubes," *Science (80-.).*, vol. 306, no. 5700, pp. 1362–1364, 2004.

[307] M. De Volder *et al.*, "Diverse 3D microarchitectures made by capillary forming of carbon nanotubes," *Adv. Mater.*, vol. 22, no. 39, pp. 4384–4389, 2010.

[308] P. J. F. Harris, *Carbon nanotube science: synthesis, properties and applications*. Cambridge university press, 2009.

Appendix A

A.1 Physical Properties of Carbon Based Materials

Graphite

Graphite is composed of a series of parallel planar planes (basal-planes). Graphite has a perfect hexagonal, crystallographic structure that is defect free. Two forms of stacking have been found for the basal-plane in graphite, which are –ABAB– (hexagonal) and –ABCABC– (rhombohedral) sequence (shown in Figure A.1). Hexagonal sequence is the most common stacking order in graphite, superimposing the carbon atoms of alternating basal-planes.

Figure A.1 Schematic illustrations of hexagonal and rhombohedral graphite stacking arrangements.[55]

The basal layer of graphitic crystal has two faces, zig-zag or arm-chair (shown in Figure A.2), depending on the orientation of the basal-plane. It is reported that the two configurations display different conductivities.[55] Another term edge-plane is in line with the basal-plane, it is formed via the termination sites around the perimeter of the basal-plane layers. It is reported that basal-plane and edge-plane sites of graphite exhibit significantly different surface energies, which are 0.11 J/m^2 and 5 J/m^2.[296] Therefore, the reaction rate of a reaction at the edge-plane is believed to be faster than that at the basal-plane. Then it is desirable that the working

electrode surface should contain some percentage of edge-plane-like sites/defects to achieve fast electrocatalytic reactions.

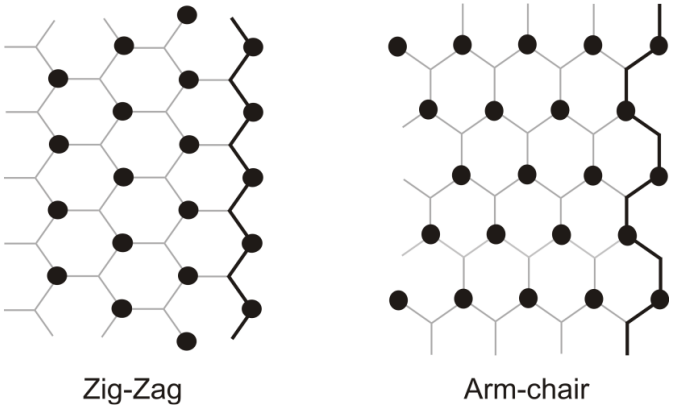

Figure A.2 Schematic representation of zig-zag and arm-chair graphitic crystal formations.

Another commonly used sp^2 hybridised carbon material is the pyrolytic graphite. This type of material is prepared by graphitisation heat treatment of pyrolytic carbon. Then high oriented pyrolytic graphite (HOPG) is produced by the hotworking of pyrolytic graphite by annealing under compressive stress along the c-axis at high temperature. A schematic illustration of HOPG is shown in Figure A.3, which depicts the edge plane bands and basal plane islands. Defects along the surface occur in the form of steps exposing the edges of the graphite layers. It has been reported that the electrochemical reactivity of an electrode reaction on edge planes are faster than that of the basal planes. In addition, graphite's layered structure tenders low resistivity along the plane (ca. 2.5 to 5 × 10–6 Ω·m), conversely through (perpendicular to) the plane, resistivity values approach close to ca. 3000 × 10–6 Ω·m.

Edge-plane and basal-plane pyrolytic graphite electrodes (EPPG and BPPG respectively) can be fabricated from HOPG. As shown in Figure A.3c, EPPG can be produced by cutting the HOPG electrode surface to form perpendicular lined graphite layers. In comparison, BPPG can be fabricated from HOPG by cutting the surface to obtain parallel graphite layers.

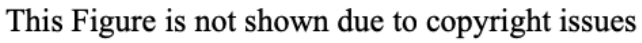

Figure A.3 a) A commercially available slab of HOPG. (b) A schematic illustration of a HOPG surface showing the discrete basal plane and edge plane islands. (c) A schematic representation of the side on view of a HOPG surface, highlighting its basal plane and edge plane like-sites/defects which exhibit contrasting behaviours in terms of electrochemical activity. (d) A typical STM image of a HOPG surface with the corresponding fragment of the graphene structure is superimposed.

Glassy Carbon

Glassy carbon (GC) offers unique properties compared with other types of carbon materials. It includes a structure of interwoven ribbons of the graphite structure (Figure 1.23 inset) that is essentially non-porous. This structure is resulted from the random crystallite arrangement (no long-range order) of the material, which also gives the material isotropic characteristic. These makes the material much harder and impermeable to liquids and gases, while it is also free from defects. These properties of GC are attributed to the organic precursors used in the fabrication process. The material is made from polymeric resins such as polyacrylonitrile (PAN) or phenol/formaldehyde polymers. As can be seen from Scheme A.1, the atoms of hydrogen, nitrogen and oxygen in the precursor polymer are released during the reactions of forming GC. This give rise to an extensively conjugated sp^2 carbon structure with original polymeric

backbone remains intact. The values of L_a and L_c for GC are typically 50 Å and 15 Å respectively.[297]

Scheme A.1 A simplified reaction pathway of sp^2 carbon fabrication from polyacrylonitrile.[56]

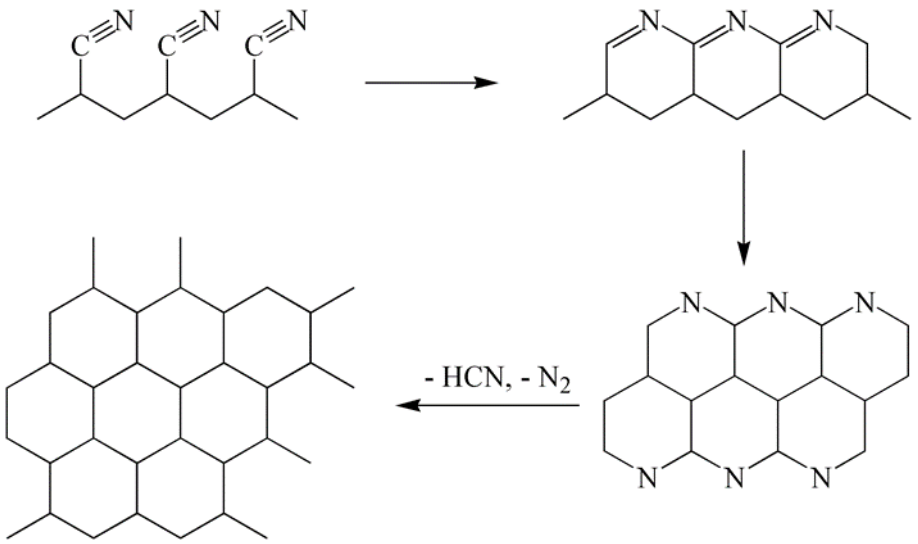

Additionally, sp^2 and sp^3 structures are existed in the material due to the variable bond energies, which are caused from the twisted and crosslinked aromatic rings. The partial diamond structure (sp^3) is believed to give the GC its high strength and hardness properties. Also, the structure makes the material does not graphitize under high temperature of 3000 °C and is highly resistant to chemical attack.[56]

Carbon Nanotubes

Carbon nanotubes (CNTs) are materials of superstrong but extremely lightweight. Though hollow carbon nanofilaments were discovered as early as the 1950s,[298] the research on CNTs has attracted much attention since the publication of Iijima's scientific report in 1991.[227] As shown in Figure A.4, CNTs are seamless cylinders of one or more layers of graphene, denoted as single-wall (SWCNTs) or multiwall (MWCNTs). Typical diameters of 0.8 to 2 nm can be found for SWCNTs and 5 to 20 nm for MWCNTs. [228] The length of both depend on the synthesis method and can range from less than 100 nm to 0.5 m.[299] CNTs are composed of sp^2 hybrid C-C bond, which is the strongest chemical bond, thus providing CNTs with

remarkable mechanical strength. The weight-specific strength of CNTs is four hundred times higher than that of steel. In addition, CNTs are a type of Dirac material (carbon materials have Dirac nodes in the spectrum), which provides CNTs extraordinary mechanical, electrical, and thermal properties.[300] Therefore, CNTs are of great potential for numerous applications, including actuators, nanoelectronics, sensors, filters, ultrafast photonics, *etc*.[301] In terms of the ability to carry current density, CNTs can reach a value up to 10^9 A/cm^2, which is 1000 times higher than that of noble metals. Also, SWCNTs can achieve field-effect nobilities up to 10^4 cm^2 V^{-1} s^{-1}.[302] Moreover, the thermal conductivity of SWCNTs is reported to reach 6600 W m^{-1} K^{-1},[303] which is three times higher than that of diamond.

This Figure is not shown due to copyright issues

Figure A.4 The Connection between the structures of HOPG, graphene, SWCNTs and MWCNTs.[268]

A number of methods have been developed for the synthesis of CNTs. The initial CNTs reported by Iijima were fabricated by an arc-discharge fullerene reactor.[298] Other techniques include the laser ablation[304], [305] and chemical vapour deposition (CVD).[306], [307] Arc-discharge utilises a chamber filled with helium gas (also others such as H_2, CH_4, ethanol, acetone or hexane may be used) and two graphite electrodes. A direct-current arc-discharge applied across the electrodes can generate MWCNTs on the electrode. The yield, purity and crystallinity can be modified by controlling the pressure and gas type. In order to produce SWCNTs, addition of metal catalysts of Fe, Co or Ni is necessary.[74] The second technique, laser ablation, shares a similar principle with arc-discharge. A graphite pellet containing some catalysts (typically Ni or Co) is ablated with pulsed laser to form CNTs.[74] The formation of CNTs is affected by the composition and structure of the pellet and the laser properties. This technique is able to produce SWCNTs of high quality and purity, however, it is hard to scale up and its running cost is high. The third technique, CVD, utilises a carbon species such as methane, acetylene, carbon monoxide or a liquid hydrocarbon as a carbon source, and can

produce large volumes of CNTs. The advantages of the technique involve simple scalability, affordable feedstock and high yield. A larger fraction of defect sites can be found for the CNTs formed by CVD than the other two processes.[308] This technique is discussed in detail in chapter 2.